Neutron Diffraction Studies of Frustrated and Correlated Electron Systems

Lewis Thomas Edwards

Cardiff University

A thesis submitted for the degree of

Doctor of Philosophy

July 2022

Abstract

A new algorithm for the WISH diffractometer is discussed, in particular, its utility as extended to the solution and refinement of structures from single crystal data. Further, this algorithm finds itself applicable to structural and magnetic diffuse scattering, where it allows for the presentation of combined reciprocal space data and symmetrized planes.

A correspondence between short range magnetic order and plateaus of the magnetization is established in the one-dimensional Ising system, α-CoV_2O_6, in which we measure the co-existence of short-range $\langle \hat{T}^3 \rangle$ and $\langle \hat{T}^4 \rangle$ orders manifest only for a non-zero component of magnetic field applied out of the easy plane. When the magnetic field is applied along the easy axis, only $\langle \hat{T}^3 \rangle$ long range order is observed.

We also describe a new method for the preparation of out-of-equilibrium, monopole rich states in $Dy_2Ti_2O_7$ spin ice — a pulse heating/cooling method that relies upon the high cooling power of a dry dilution refrigerator. This includes the Bluefors refrigerator at Cardiff University — in which we tested our set-up — and the E18 refrigerator at ISIS, in which we planned to conduct our investigation of the spin correlations. Prior to our measurements on

the WISH diffractometer, we achieved a very fast cooling rate of 150 mK/s in Cardiff — much faster than that previously reported in previous studies where rich monopole populations were prepared. Due to factors beyond our control, however, we had to modify our set-up in order for it to work in a standard dilution insert refrigerator, which severely limited the cooling rate and thereby the density of monopoles frozen in. As a result of these restrictions, we did not observe any appreciable change to the spin correlations, as compared to the equilibrium state; consequently, we placed a lower bound on the cooling rate spin freezing transition of $9.5\,\mathrm{mK\,s^{-1}}$ before changes to the spin correlations are manifest.

Acknowledgments

Firstly, I would like to thank my supervisor, Sean Giblin, based at Cardiff. Secondly, I would like to thank my co-supervisor, Pascal Manuel, based on the WISH diffractometer at ISIS; I would like to extend my gratitude to the other instrument scientists on WISH, namely Fabio Orlandi and Dimitiry Khalyavin. I would also like to thank my collaborators at Edinburgh, Chris Stock, Harry Lane and Manila Songvilay (now at CNRS). I would also like to thank fellow members of my group, my family, and Cheryl. Finally I would like to thank Cardiff University, the Center for Doctoral Training in Data Intensive Science, and ISIS/STFC for financial support over the course of this degree.

Cardiff, July 2022

Publications

- L. Edwards, H. Lane, F. Wallington, A. M. Arevalo-Lopez, M. Songvilay, et al., Phys. Rev. B **102**, 195136 (2020).

Conferences, presentations and posters

- ISIS Student Meeting: Milton Hill House, Harwell (October, 2019). Presentation & Poster: Short range magnetic order in anisotropic spin-chain system α-CoV_2O_6.
- CDT Data Intensive Physics, Industrial Partner Meeting: The Watershed, Bristol (March, 2019). Presentation: Magnetic structure solution from single-crystal on WISH.
- Frontiers in Condensed Matter Physics Conference: Bristol University (January, 2019). Presentation & Poster: Field-induced spin orders in α-CoV_2O_6.
- PCG Intensive School in Physical Crystallography: The Cosener's House, Abingdon (June, 2018). Poster: Investigating the defect structure in spin ice via diffuse scattering.

List of Figures

List of Tables

Table of Contents

Chapter 1

Introduction

In this thesis, we explore the rich physics of long and short-range ordered phases in frustrated and correlated electron systems using modern single-crystal neutron scattering techniques. Neutron diffraction is an elegant experimental technique with deep principles of symmetry at its core, and is the primary technique by which we investigate the emergent properties of the magnetic materials discussed herein. Part of this thesis is dedicated to the development of the WISH diffractometer [1] on the second target station at the ISIS Pulsed Neutron and Muon Source, expanding its scope to deal more routinely with single-crystal diffraction experiments. The layout of this thesis is presented as follows.

Chap. 2 opens with a discussion of historical developments related to the discovery of the neutron, and subsequently, its use as a scattering probe of condensed matter. Acknowledging the pivotal roles that key figures have played in advancing the field of neutron scattering, we describe the progresses made in neutron instrumentation and measurement techniques over the past

century that have laid the foundations for modern-day neutron scattering techniques, which — with dedicated specialist facilities worldwide — support a broad and diverse scientific community of neutron beam users. Of fundamental importance is a discussion of the elementary physical properties of neutrons apropos to their role as a scattering probe of condensed matter. Then, we discuss symmetry analysis, group representations, and scattering theory as foundational tools used implicitly throughout this thesis. This discussion of theoretical matters then segues into a discussion of instrumentation — specifically of the triple-axis and time-of-flight spectrometers — and finally, of bulk property measurements.

Chap. 3 is concerned with a treatment of goniometer rotations, and subsequently, quantitative structural characterizations from single-crystal on the WISH beamline, which, as previously mentioned, is located at the ISIS facility, established in 1984 at the Rutherford Appleton Laboratory of the Science and Technology Facilities Council in Didcot, Oxfordshire. This chapter is tripartite. We open with a discussion of the properties of cold neutrons, before considering the time-of-flight diffractometer in further detail. We then describe the characteristics of pulsed neutron sources, highlighting the versatility of the WISH beamline. Lastly, we discuss the ramifications of the strengths afforded by its intrinsic qualities on the field of single-crystal diffraction.

The second part of this chapter focuses on practical aspects of data reduction salient to the treatment of single-crystal time-of-flight diffraction data.

We consider Vanadium as a normalization standard for neutron scattering, discuss peak detection, and importantly, describe the orientation matrix formalism. This is followed by a discussion of peak integration and the dynamical theory of diffraction, owing to its importance in correcting for the effects of extinction and multiple scattering, which is ubiquitous in single-crystal diffraction. Then, we discuss the main contribution of the chapter, namely a novel algorithm `LinkedUBs`. This algorithm allows for the derivation of a set of mutually consistent orientation matrices, thereby facilitating quantitative structural characterization from single-crystal data on WISH, traditionally and foremost a powder instrument.

The final part of this chapter discusses results from single-crystal refinement, along with supporting visualizations, taking the form of symmetrized reciprocal space planes; these were obtained from the implementation of a method for combining data with different statistical weights in reciprocal space, as described in Ref. [2]. These are especially useful in the analysis of diffuse scattering datasets, where spectral weight is distributed over large volumes in reciprocal space. Specifically, present an investigation of the crystal structure of the garnet $Ca_3Ga_2Ge_3O_{12}$, which displays interesting optical properties, as well the as rutile-type MnF_2, in which antiferromagnetic order with a $\vec{k} = 0$ type propagation wavevector is stabilized below T_N. Finally, as a testament to the additional utility of WISH unlocked by the `LinkedUBs` algorithm, we present diffuse scattering results obtained in a study of the germinate spinel $GeNi_2O_4$; our results provide novel microscopic insight into

the nature of the short-range magnetic correlations in this material.

In Chap. 4, we present an investigation of short-range magnetic correlations in the insulating $j_{\text{eff}} = \frac{1}{2}$ Ising-chain material α-CoV_2O_6. Interestingly, an $M/M_s = \frac{1}{3}$ plateau is stabilized in applied fields below T_N, with the appearance of additional fine structure as temperature is decreased [3–9]. Such behavior typically appears in frustrated systems with a triangular geometry, and as such, much effort has been dedicated to developing a greater understanding of this unexpected behavior over recent years. In general, the presence of plateaus in the magnetization implies the existence of a gap to magnetic excitations. The presence of plateaus in this $j_{\text{eff}} = \frac{1}{2}$ Ising magnet appears, therefore, to conflict with Haldane's conjecture, which posits that the spectrum of magnetic excitations is gapless in half-integer spins [10, 11].

In an effort to resolve this difficulty, we sought to conduct neutron diffraction experiments in applied magnetic fields to measure the equilibrium structure factor $S(\vec{Q}) \equiv \int S(\vec{Q}, \omega)\, \mathrm{d}\omega$, and thereby elucidate the nature of the magnetic magnetic correlations in the vicinity of the plateaus. We characterized the crystal structure and magnetic ground state in neutron diffraction experiments on single-crystals and powders below T_N using the WISH beamline (ISIS, UK) and MORPHEUS instrument at the SINQ Spallation Neutron Source (PSI, Switzerland). After concretizing our understanding of the ground state, we proceeded to characterize the magnetization at the Institut Néel (Grenoble, France), using a single-crystal sample and measuring down to $T = 0.85\,\mathrm{K}$ using a SQUID magnetometer in a Physical Properties Measure-

ment System (PPMS). Our measurements at dilution temperatures revealed the the emergence of new plateaus not present at higher temperatures, and in particular, a prominent plateau at $M/M_{\mathrm{s}} = \frac{1}{4}$.

Guided by our magnetization measurements, we conducted single-crystal neutron diffraction experiments in applied magnetic fields on the WISH diffractometer to characterize the temperature and field dependence of the magnetic correlations between 0.1 K and 4.5 K. Owing to kinematic constraints of the vertical field on WISH, it was not possible to apply the magnetic field wholly along the easy c-axis; to achieve adequate coverage, it was necessary to apply a small component of field out of the ac-plane along the b-axis. In the vicinity of the magnetization plateaus, we found no evidence of long-range translational symmetry breaking; instead rich short-range ordered states were found to evolve between the propagation wavevectors $\vec{k} = (1, 0, \frac{1}{2})$, $\vec{k} = (\frac{1}{2}, 0, \frac{1}{4})$, and $\vec{k} = (\frac{2}{3}, 0, \frac{4}{3})$. The diffuse scattering was characterized by the broadening of peaks along the direction of the Néel wavevector, and is similar in nature to the correlations manifest in the case of antiphase domains.

We investigated the directional dependence of the applied field on $S(\vec{Q})$ using the RITA triple-axis spectrometer at PSI. With magnetic field applied strictly along the c-axis in a horizontal magnetic field, we found no evidence of the $\vec{k} = (\frac{1}{2}, 0, \frac{1}{4})$ propagation wavevector. This stands in contrast to the results obtained on WISH. To resolve this discrepancy, we conducted neutron powder diffraction in applied magnetic fields on the TASP triple-axis-spectrometer at PSI, finding complex behavior involving all propagation

wavectors, owing to the isotropic nature of applied field among grains. Finally, with no change to the long-range magnetic structure evidenced, we resolve the conflict with Haldane's conjecture by appeal to the Lieb-Schultz-Mattis theorem [12], which states that a gap can emerge in half-integer spins without breaking translational symmetry if the magnetization per spin satisfies $(S-m) \in \mathbb{Z}$. Our results therefore demonstrate a correspondence between local translational symmetry breaking and the stabilization of magnetization plateaus.

Finally, in Chap. 5 we present an investigation of the nature of the magnetic correlations in far-from-equilibrium states in the frustrated spin-ice material $Dy_2Ti_2O_7$ by neutron diffraction. Using a BlueFors dilution refrigerator at Cardiff University, we developed a novel avalanche-quench cooling protocol which delivers a pulse of heat to the sample, thereby inducing thermally activated spin-flip excitations, followed by rapid cooling through the spin-ice freezing transition $T_\mathrm{f} \sim 0.65\,\mathrm{K}$, at which the system falls out of equilibrium. The rapid cooling through T_f traps in an enhanced monopole population which has been shown to be stable on the order of neutron scattering timescales through direct measurement of the monopole density using a similar cooling protocol involving polarizing magnetic fields, at a rate of $70\,\mathrm{mK\,s^{-1}}$ [13].

Such monopole-rich states have the potential to harbor non-trivial types of correlations; in the testing of our beamline-compatible protocol, we achieved cooling rate of $\sim 150\,\mathrm{mK\,s^{-1}}$, sufficient to enhance the monopole density.

We therefore sought to implement our quench-cooling protocol on the WISH beamline (ISIS, UK), preparing a non-equilibrium monopole-rich state, before measuring the equilibrium structure factor $S(\vec{Q})$ which, in the equilibrium state, is characterized by pinch point singularities as well as significant zone-boundary scattering. We used an isotopically enriched $^{162}Dy_2Ti_2O_7$ sample in our neutron scattering experiment on account of its $I = 0$ nuclear spin state; this removes the complicating effects of the hyperfine interaction, which has been shown to facilitate magnetic relaxation via quantum tunneling processes [14].

We performed both quench-cooling and conventional slow-cooling protocols at $T = 0.35\,\mathrm{K}$ and at $T = 10\,\mathrm{K}$; the high temperature dataset was collected to serve as a background subtraction, necessary to reveal the magnetic diffuse scattering in the absence of polarization analysis. We planned to use the cryogen-free E18 dilution refridgerator on the beamline since its mixing chamber has a sufficient cooling power to support our quench-cooling protocol. However, due to issues beyond our control, we were required to adapt our protocol to work with the lesser powered Kelvinox dilution refridgerator insert, thereby severely limiting the rate of cooling through T_f, and consequently, the degree of monopole enrichment. Our data revealed no significant changes in the features of the diffuse scattering, up to a maximum achieved cooling rate of $9.5\,\mathrm{mK\,s^{-1}}$; as such, we place a lower bound on the cooling rate necessary to influence magnetic correlations through manipulation of the monopole density.

Chapter 2

Experimental techniques

2.1 Introduction

The neutron was discovered by Chadwick in 1932 [15]. In 1935, he was awarded the Nobel prize in physics, and one year later, the first evidence for the diffraction of neutrons was found in experiments using radioisotope driven (α, n) sources [16, 17]. Soon after its discovery, Bloch [18] and Schwinger [19] would demonstrate that the magnetic scattering of neutrons could, in principle, be observed in experiments. Meitner and Hahn later discovered nuclear fission in 1938 [20–22] — a crucial step in the early development of neutron scattering as they established a feasible means to access free neutrons en masse. Shortly after, Fermi arrived in the United States and joined teams at Columbia University pursuing the development of chain-reacting exponential 'piles' which, at the time, comprised Uranium oxide powder in a graphite matrix [23, 24]. While commissioned on the Manhattan project in 1942, Fermi and colleagues at the University of Chicago built the first nuclear reac-

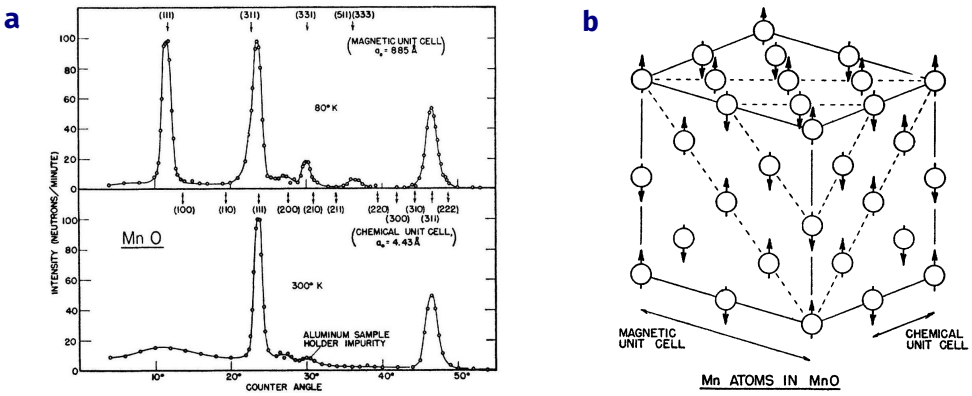

Figure 2.1: The magnetic neutron diffraction profiles of MnO collected by Shull and Smart in 1949 at Oak Ridge is shown in (a) with the determined magnetic structure shown in (b). The top panel of (a) shows the profile below the ordering temperature for $T < T_c$. The broad in $\vec{Q}$ scattering observed for $T > T_c$ (shown in the bottom panel) is redistributed among sharp satellite reflections for $T < T_c$ as symmetry is broken and long-range magnetic order is established. From Ref. [28].

tor which used high-purity graphite to moderate the velocity of fission neutrons, thereby promoting a self-sustaining chain reaction. This technology made possible the production of high-flux beams of 'slow' neutrons; reactors were subsequently built at the Oak Ridge National Laboratory, United States [25, 26], and at Chalk River Laboratories, Canada [27].

In 1944, Wollan submitted a proposal to the director of research at Oak Ridge requesting funding for neutron diffraction experiments on the graphite X-10 pile reactor. After the acceptance of this, he proceeded to establish the technique with a series of measurements on powder samples. Later working in collaboration with Shull, they developed a two-axis neutron diffractome-

ter, applying it to crystal structure determination. In 1949, Shull and Smart measured satellite reflections associated with ordered antiferromagnetism in MnO [28] for the first time. Their powder data collected above and below the ordering transition, which clearly demonstrate the shift of spectral weight below the Néel temperature T_{N}, is shown in Fig. 2.1(a). The new peaks observed below T_{N} are consistent with a $\vec{k} = (\frac{1}{2}, \frac{1}{2}, \frac{1}{2})$ propagation wavevector; this corresponds to a magnetic unit cell which is doubled along all the principal axes of the parent nuclear cell, and is shown in Fig. 2.1(b). With these measurements, they had established the use of neutrons for the investigation of magnetic structure; this elegant experimental technique has symmetry at its core, and is used extensively in this thesis.

While most early work focused on the elastic scattering of neutrons, at the NRX reactor, Chalk River, Brockhouse worked on the development of the triple-axis spectrometer (TAS). He shared his first results on the energy spectrum of phonon modes in Vanadium [29], and subsequently, Aluminum [30], in 1955, and completed the construction of the instrument in earnest in 1956. This allowed him to obtain the first measurements of the collective spin wave excitations in magnetite Fe_3O_4 [31] at Chalk River in 1957. In these measurements, the Néel mode was investigated, allowing the spin-wave number as a function of energy transfer to be extracted. The invention of the TAS made possible the controlled measurement of the dynamic structure factor $S(\vec{Q}, \omega)$ at any point in $(\vec{Q}, E)$ space. For this, and the groundbreaking experiments he subsequently performed establishing neutrons as a probe of dynamic prop-

erties in condensed matter, he was awarded the 1994 Nobel prize in physics jointly with Shull, who was recognized for his seminal work on the neutron diffraction technique.

Advances in neutron instrumentation and measurement techniques have continued at pace to the present day, with neutrons now used by a diverse scientific community for the benefit of society. Reactor sources were soon built specifically for the purpose of neutron scattering, the first of which being the the high-flux beam reactor at Brookhaven National Laboratory, United States [32] in operation between 1965 and 1996. This was followed by the Institut Laue-Langevin, Grenoble [33], in 1971, founded by France and Germany, with the UK joining as a major partner in 1973. Through continual development in collaboration with its numerous associated European member countries, it maintains its position as providing the most intense steady flux of neutrons in the world.

The ISIS facility, UK [34], was first approved in 1977 and produced its first neutrons in 1984 by spallation — a bombardment process in which an abundance of neutrons are generated when a highly accelerated proton beam is collided with a heavy metal target. The two experimental halls associated with the first and second target stations at ISIS are shown in Fig. 2.2, hosting a wide range of advanced beamlines. Here, world leading innovation of the time-of-flight (TOF) technique — an alternative method that facilitates the measurement of four dimensional volumes of $(\vec{Q}, E)$ space — took place. Other sources, including the SNS Facility at Oak Ridge [35] followed suit,

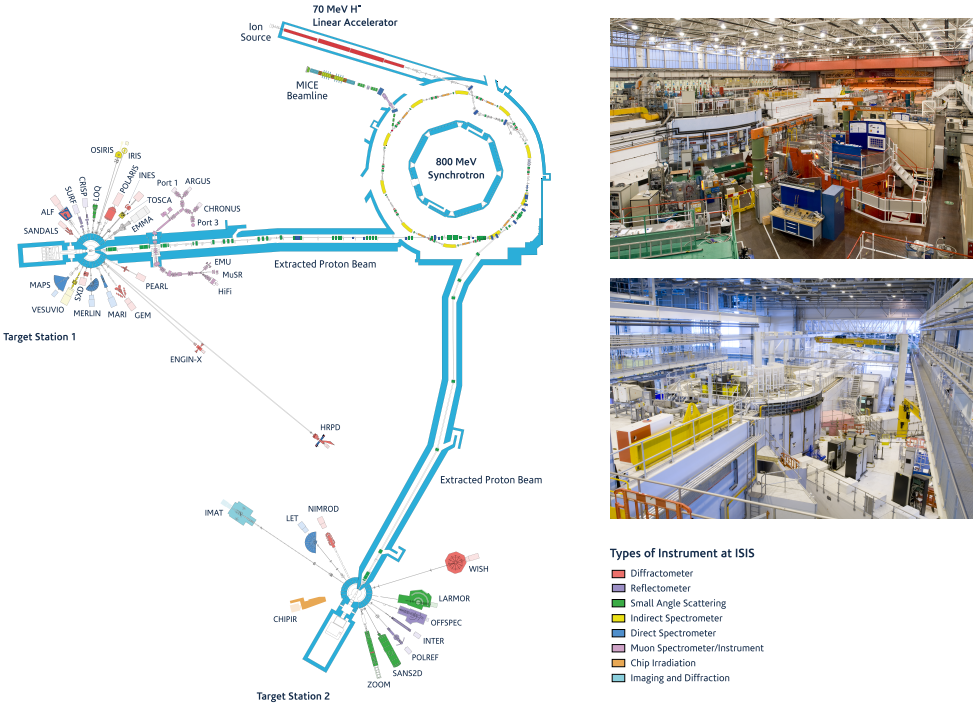

Figure 2.2: The 70 MeV linear accelerator and 800 MeV snychotron at the heart of the ISIS Pulsed Spallation Neutron Source in Didcot, UK. The first (top) and second (bottom) target stations house different moderators, providing thermal and cold neutrons to the beamlines respectively, each configured to a particular science case. Schematic from Ref. [36]. Images from `http://ftp.nd.rl.ac.uk/ISISmedia/`.

taking advantage of the improved efficiency afforded by the white beam and its numerous constituent wavelengths which serve to illuminate multiple Brillouin zones with the same in-plane wavevector.

The advent of spallation sources, hosting suites of instruments with large arrays of position sensitive detectors, has presented new challenges for the

reduction and analysis of data. To meet the increasingly difficult challenge of analyzing the complex datasets generated in TOF scattering experiments, ISIS manages the `IDAaaS` computing cluster that provides the user community access to virtual machines with up to `14CPU` and `128GB RAM` [37]. Environments of this capacity are necessary for the most intensive of reduction tasks, such as the treatment of single-crystal diffuse scattering data. The `mantid` analysis framework [38] is standard at the ISIS and SNS sources; it is under active development by teams at both facilities, while also benefiting from external contributions, since its code base is open source [39]. It provides a comprehensive set of algorithms and workflows that serve to introduce a degree of standardization for the reduction of TOF data — a valuable asset to the neutron community that greatly reduces the complexity of data analysis. Currently under construction, the much anticipated next generation European Spallation Source (ESS), Sweden [40], will use `mantid` as standard on site for data reduction; with enhanced flux, the latest detector technology, and a suite of advanced instruments, the facility promises a bright future for neutron science in Europe.

2.2 Neutron properties

The neutron is a massive, charge neutral particle. In Table 2.1, we list the elementary physical properties apropos to its role as a scattering probe of condensed matter. It is a composite fermion and carries a nuclear spin

Table 2.1: Elementary physical properties of the neutron, relevant to the description of their scattering by condensed matter. Values have been compiled from Refs. [41–43].

Quantity	Value
Electronic charge (q_n)	$0\,\mathrm{e}$
Rest mass (m_n)	$939.57\,\mathrm{MeV/c^2}$
Nuclear spin (I_n)	1/2
Mean lifetime (τ_n)	$885.7(8)\,\mathrm{s}$
Geometric ratio (γ_n)	1.913

$\sigma_\mathrm{n} = \hbar/2$. After their initial liberation from bound nuclear states, and with appropriate moderation, it is possible to prepare a flux of 'slow' neutrons having a de Broglie wavelength $\lambda_\mathrm{n} = h/m_\mathrm{n}v \sim$ Å with an associated energy $E = hc/\lambda_\mathrm{n} \sim$ meV. The long-wavelength, low-energy nature of the neutron is related to its appreciable rest mass $m_\mathrm{n} \approx 939.57\,\mathrm{MeV/c^2}$. This wavelength is well matched to both the length-scale of typical interatomic spacings, and to the energy-scale of elementary collective excitations in condensed matter systems. With isospin $I_\mathrm{n} \neq 0$, the neutron directly probes the magnetic degrees of freedom in matter. Carrying a nuclear moment $\mu_\mathrm{n} = -\gamma_\mathrm{n}\mu_\mathrm{N}\sigma_\mathrm{n} \ll \mu_\mathrm{e}$, with a gyromagnetic ratio $\gamma_\mathrm{n} = 1.913$, the neutron interacts through the dipolar interaction with the magnetic fields generated by the localized moments of unpaired electrons in the scattering system.

Both nuclear and magnetic interactions admit elastic and inelastic kinematical scattering processes, thereby providing a means of measuring both the static and dynamical properties of matter. The classification of slow

Table 2.2: Classification of neutrons by their energy, velocity, de Broglie wavelength, and associated temperature. Values have been compiled from Refs. [41–43].

	E [meV]	λ [Å]	v [m/s]	T [K]
Ultra-cold	$< 3 \times 10^{-4}$	> 520	5	2×10^{-3}
Cold	$0.1 - 20$	5	800	40
Thermal	25	1.8	2200	300
Hot	$40 - 10^3$	0.7	5700	2000
Fission	2×10^9	2×10^{-4}	2×10^7	2×10^{10}

neutrons by their energies, velocities, de Broglie wavelengths, and associated temperatures is presented in Table 2.2. The neutron-magnetic interaction is a leading order effect and can give rise to strong magnetic scattering with measured intensities often comparable to those obtained for nuclear scattering. By contrast, the much weaker non-resonant magnetic x-ray cross section is obtained only by the inclusion of perturbations up to fourth order in the electron interaction Hamiltonian [44]. The relative simplicity and accessibility afforded by neutrons is not without drawbacks, however; unlike the case of x-ray scattering, it is often not possible to separate the contribution of orbital correlations in the magnetic cross-section directly.

Unlike nuclear scattering which concerns interactions with point-like atoms, the magnetic scattering cross-section is limited by the fall-off of the magnetic form factor $f(\vec{Q})$ with increasing momentum transfer $\vec{Q}$. This follows from the Heisenberg uncertainty principle, from which the spatial distribution of the electron is understood to be intrinsically diffuse. In the dipole approxi-

mation where $Q = |\vec{Q}|$ is large compared to the mean radius of the orbital wavefunctions, the $\vec{Q}$-dependence of the magnetic form-factor is well approximated by the expression [45]

$$f(\vec{Q}) = \langle j_0(\vec{Q})\rangle + (2g^{-1} - 1)\langle j_2(\vec{Q})\rangle. \tag{2.1}$$

The $j_l(s)$ terms in this expression are lth-order Bessel functions, with the leading order isotropic term $\langle j_0(\vec{Q})\rangle$ dominant at low momentum transfer, accounting for spin-only contribution. The $l > 0$ terms are relevant in accounting for orbital contributions; in this case, the $\vec{Q}$-dependence of the form-factor is dependent on the orbital state of the magnetic ion and can be expressed through the piecewise relation [46]

$$\langle j_l(\vec{Q})\rangle = \begin{cases} A\,\exp(-a\vec{Q}^2) + B\,\exp(-b\vec{Q}^2) + C\,\exp(-c\vec{Q}^2) + D & l = 0, \\ A\,\exp(-a\vec{Q}^2) + B\,\exp(-b\vec{Q}^2) + C\,\exp(-c\vec{Q}^2) + D\vec{Q}^2 & l \neq 0. \end{cases} \tag{2.2}$$

This magnetic form-factor describes the Fourier transform of the magnetization density of a single magnetic atom; the fall-off at large momentum transfer is a reflection of the probabilistic distribution of electrons in orbitals and bands around the ion.

The erratic variation of the nuclear coherent scattering length with increasing atomic number Z is advantageous since this often results in a good degree of contrast in materials containing atoms with similar Z. Free neutrons are weakly interacting and unobstructed by Coulomb barriers as they

travel through matter. The neutron-matter interaction is well described by the application of the Born approximation in which incident and final states are treated as spherically symmetric plane waves [47], with neutrons a probe of the linear response regime whereby correlation functions are determined by equilibrium fluctuations. With a lifetime $\tau_{\mathrm{n}} \approx 886\,\mathrm{s}$ and a typical mean free path of order $\sim$ cm, neutrons are an excellent bulk probe, providing the unique opportunity to investigate matter under extreme conditions, including at high pressures, low temperatures, and high magnetic fields — a challenging set of environmental conditions to maintain, requiring extensive sample environment material in the path of the beam, inaccessible to x-rays on account of considerable beam attenuation.

2.3 Symmetry and reciprocal space

Having now reviewed some relevant properties of the neutron and understood its efficacy as a scattering probe of nuclear and magnetic degrees of freedom, we consider the general symmetry properties of the scattering system. Broadly concerning the many-electron problem, the investigation of emergent magnetic phases in crystalline solids is central to the work presented in this thesis, and draws implicitly on the formalism presented in this section.

The crystal structure of these materials is characterized by a fundamental, repeating atomic configuration called the unit cell. By definition, the crystal system must possess, at the least, discrete translational symmetry under the

n linearly independent vectors that constitute the basis, thereby spanning the vector space $\mathbb{E}^n$. In most cases, the structure is additionally invariant under a number of rigid-body symmetry operations. These transformations preserve the dot product between vectors $\in \mathbb{R}^n$, corresponding to the preservation of distances and angles. These symmetry elements are members of the affine group $\mathcal{A}_n$ of mappings, defined by the combination of an orthogonal linear component $h \in GL_n(\mathbb{R})$ satisfying $h^{\mathrm{T}} = h^{-1}$ and a translation $\vec{\tau} \in \mathbb{R}^n$. We express the isometries of the space group $g \in G$ using Seitz notation [48, 49], which we illustrate by the action of the symmetry element on some vector $\vec{v} \in \mathbb{R}^n$, according to $\{h|\vec{\tau}\}(\vec{v}) := h \cdot \vec{v} + \vec{\tau}$. This set of isometries define the crystal space group $\mathcal{G}$[1].

The set of translations $T := \{\{e|\vec{\tau}\} \mid \vec{\tau} \in \mathbb{R}^n\}$ is an abelian (commutative) subgroup of the space group, denoted by $\mathcal{T} \leq \mathcal{G}$; this defines the crystal lattice. A selection of lattice types with various centering conditions are illustrated in Fig. 2.3. The factor group of $\mathcal{G}$ by the normal subgroup $\mathcal{T} \triangleleft \mathcal{G}$ is isomorphic to the group of point operations $\mathcal{G}/\mathcal{T} \cong \mathcal{P}$, describing the symmetries of the crystal with one point fixed. We will discuss the symmetry of the scattering system from the perspective of group theory, as presented here, and additionally using representation theory in Sec. 2.3.1.

Each atom in the crystal basis is specified by a set of fractional coordinates, together with a thermal displacement parameter U and site occupancy factor

[1] The true definition of the space group requires much more rigorous formalism, referring to the theorems of Bieberbach [50, 51], but, while interesting, is beyond the scope of this discussion.

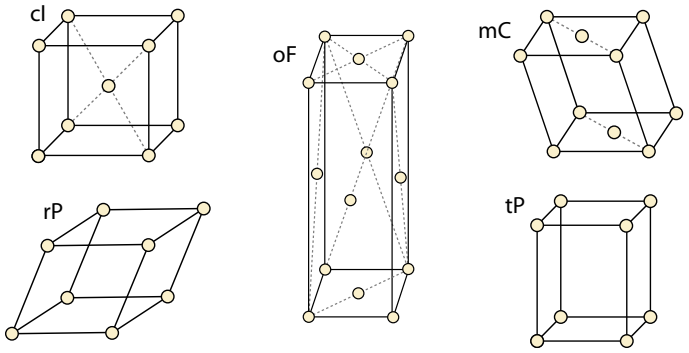

Figure 2.3: The cubic (c), monoclinic (m), orthorhombic (o), and tetragonal (t) Bravais lattice types. The labels P, C, F, and I describe the lattice centering type. The P-cell by definition has only primitive centering vectors.

B. Each atomic position is associated with a Wyckoff position specifying the point group $\mathcal{P}$ (stabilizer) of the site[2]. The geometry of the crystal lattice in real (direct) space is defined by three noncollinear unit-vectors $\vec{a}_1, \vec{a}_2, \vec{a}_3 \in \mathbb{E}^3$. We denote these by $\vec{a}_1 = \vec{a}$, $\vec{a}_2 = \vec{b}$, $\vec{a}_3 = \vec{c}$, with lengths a, b, c respectively, known as the lattice parameters. The cell angles are denoted by α, β, γ, where $\alpha = \vec{b} \measuredangle \vec{c}$, $\beta = \vec{c} \measuredangle \vec{a}$, $\gamma = \vec{a} \measuredangle \vec{b}$. General positions in the lattice are denoted by the vector $\vec{R}_{ij} = \vec{\tau} + \vec{r}_j$ where $\vec{\tau} = u\vec{a} + v\vec{b} + w\vec{c}$ $(u, v, w \in \mathbb{Z})$ and $\vec{r}_j = x\vec{a} + y\vec{b} + z\vec{c}$ $(x, y, z \in \mathbb{R})$. There exist 14 distinct Bravais classes which describe the full set of unit cell metrics in 3D, imposing constraints on the relationships between cell lengths and angles.

We define the metric tensor of the lattice by $\mathsf{G}_{ij} = \vec{a}_i \cdot \vec{a}_j$, facilitating the cal-

[2] An infinite set of symmetry equivalent sites, known as the crystallographic orbit, is generated under the action of elements $p \in \mathcal{P} \subset \mathcal{G}$.

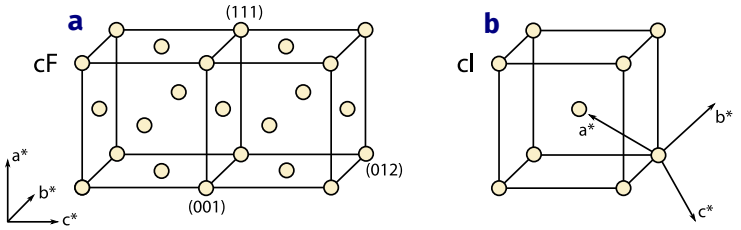

Figure 2.4: The face-centered cubic (cF) lattice in direct space is shown in (a) and its dual in reciprocal space, the body-centered cubic (cI) lattice, is shown alongside in (b), with the reciprocal space basis vectors indicated.

culation of inner products via $\langle \vec{u}, \vec{v} \rangle = \vec{u} \cdot \vec{v} = \mathsf{G}_{ij} u^i \vec{v}^j$. We can define a dual basis with $\vec{b}^i = 2\pi \vec{a}_k (\mathsf{G}^{-1})^{ki}$ having the property $\vec{a}_i \cdot \vec{b}^j = \vec{a}_i \cdot \vec{a}_k (\mathsf{G}^{-1})^{kj} = 2\pi \delta_i^j$. The basis vectors $\vec{b}^i$ are contravariant and linearly independent; any vector on the new basis can be expressed $\vec{Q} = q_i \vec{b}^i$, where the coordinates q_i are not necessarily covariant. The vectors $\vec{b}^i$ have units of inverse length and define the reciprocal space of the system [52] — a vector space on $\mathbb{E}^3$ dual to the direct space. The dot product between position vectors in real space and reciprocal space is a dimensionless quantity $\vec{Q} \cdot \vec{v} = 2\pi q_i x^i$, since reciprocal space is dual to direct space. The reciprocal metric tensor is $\tilde{\mathsf{G}} = (2\pi)^2 \mathsf{G}^{-1}$. For two reciprocal-space vectors $\vec{Q}$ and $\vec{r}$, the dot product takes the form $\vec{Q} \cdot \vec{r} = \tilde{\mathsf{G}}^{ij} q_i r_j$. The basis vectors of the reciprocal lattice are given by

$$\vec{a}^1 = \frac{2\pi}{V} \vec{a}_2 \times \vec{a}_3, \qquad \vec{a}^2 = \frac{2\pi}{V} \vec{a}_3 \times \vec{a}_1, \qquad \vec{a}^3 = \frac{2\pi}{V} \vec{a}_1 \times \vec{a}_2, \tag{2.3}$$

where $V = \vec{a}_1 \cdot (\vec{a}_2 \times \vec{a}_3)$ is the unit cell volume. We denote these by $\vec{a}^1 = \vec{a}^*$,

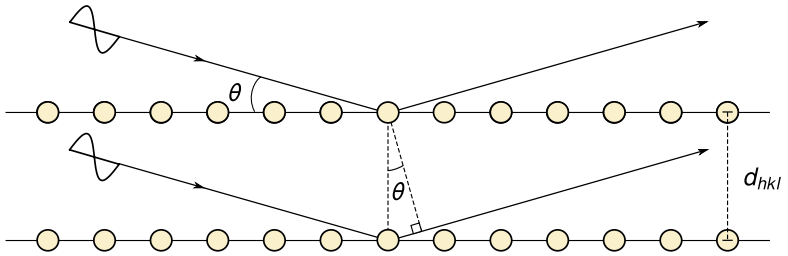

Figure 2.5: Bragg's law — an incident neutron approaches at an angle θ to a lattice plane and is diffracted at an angle 2θ when the path difference between lattice planes is integral multiple n of the wavelength λ.

$\vec{a}^2 = \vec{b}^*$, $\vec{a}^3 = \vec{c}^*$ and define the angles $\alpha^*, \beta^*, \gamma^*$ in a manner analogous to that of the direct lattice angles. The mapping between direct and reciprocal bases is depicted in Fig. 2.4, showing the face-centered cubic (cF) lattice in direct space and its dual, the body-centered cubic (cI) lattice in reciprocal space, with basis vectors indicated.

Considering atomic planes through the direct lattice, if their mutual separation $d \sim$ Å is an integral multiple of the neutron incident wavelength, then coherent interference of the neutron plane wave is manifest with elastic kinematics. This is summarized by the Bragg law [53],

$$2d \sin\theta = n\lambda \quad \text{for} \quad n \in \mathbb{N}, \tag{2.4}$$

with the kinematics of the diffraction from lattice planes depicted in Fig. 2.5. Noting the matter-wave properties of the neutron expressed through the de Broglie relation, in the limit of the Born approximation, the neutron incident

upon the scattering system takes the form of a spherically symmetric wave $\psi_i = b\ \exp(i[\vec{k}_i \cdot \vec{r} - \omega t])$. After the scattering event, the outgoing scattered wave can be expressed in the form $\psi_f = F(b/r)\ \exp(i[\vec{k}_f \cdot \vec{r} - \omega t])$. The canonical response observed is one of sharp Bragg peaks, each corresponding to the reflection of neutrons from a set of reciprocal lattice planes, indexed by Miller indices h, k, l. Each member of the triple corresponds to the inverse intersection of some lattice plane (h, k, l) on the direct basis vectors.

The elastic scattering is characterized by a delta-function type response, peaked at $\hbar\omega = 0$, and given by the expression

$$I(\vec{Q}) = \frac{1}{V}\frac{(2\pi)^3}{N}\sum_{\vec{\tau}} |F(\vec{\tau})|^2 \delta(\vec{Q} - \vec{\tau}), \tag{2.5}$$

where the momentum transfer Q is defined as the difference between incoming and outgoing neutron wavevectors $\vec{Q} = \vec{k}_i - \vec{k}_f$. From this definition, a basic condition for diffraction follows, given by $|\vec{Q}| = |\vec{\tau}|$ for $\vec{\tau} \in \mathsf{R}_{uvw}$, the set of lattice vectors. The term $F(\vec{\tau})$ is the structure factor, given by the expression $F(\vec{\tau}) = \sum_l \bar{b}_l W_l(\vec{\tau})\ \exp(i\vec{\tau} \cdot \vec{r}_l)$, where $\bar{b}$ is the nuclear scattering length and W_l is the Debye-Waller factor describing the isotropic displacement of atoms about their equilibrium positions with a Q dependence $W_l(Q) =\ \exp(-U_l^{\text{iso}} Q^2/2)$ and U_l^{iso} determined by refinement.

Analogous to the direct unit cell, the first Brillouin Zone (BZ), sometimes referred to as the Wigner–Seitz cell, serves as the primitive cell in reciprocal space and can be constructed by Voronoi decomposition. Alternatively,

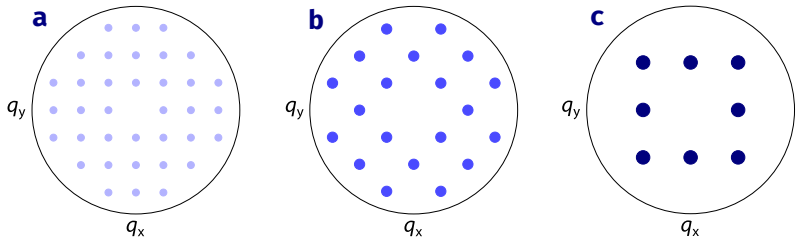

Figure 2.6: Systematic absences due to centering translations for primitive (P) cell is shown in (a), the body-centered (I) cell in (b), and face-centered (F) cell in (c). Diffraction shown is from a crystal with one-atom basis on position $(0, 0, 0)$ in space groups $P23$, $I23$, and $F23$, with respective Patterson symmetries indicated. Absences are manifest in the structure factor due to an exact cancellation of terms, with conditions on the relevant Miller indices.

we can define the nth zone as the set of points in the neighborhood of the origin that can be reached while crossing exactly $(n - 1)$ Bragg planes. The diffraction patterns manifest in the case of a primitive, body-centered, and face-centered cubic cell are shown in Fig. 2.6, with centering vectors in the direct space basis listed in Table 2.3. Non-primitive lattices are invariant under a larger set of translation vectors, as compared to the case of a primitive lattice; these additional centerings give rise to systematic absences in the diffraction pattern where the Fourier components of some reflections cancel exactly, explaining the differences in the diffraction patterns among Fig. 2.6(a-c). Systematic absences are useful in the analysis of diffraction patterns — especially in the study of phase transitions where symmetries are often broken leading to the development of intensity at nominally extinct positions. The conditions on the h, k, l for allowed reflections and systematic absences are tabulated for

Table 2.3: The centering vectors for the base-centered (C), face-centered (F), body-centered (I), and rhombohedral (R) lattice systems are shown as rational fractions of the lattice vectors $\vec{a}, \vec{b}, \vec{c}$. As noted previously, the P-cell by definition has centering vector $[0, 0, 0]$.

Lattice type	Centering translations
C	$[\frac{1}{2}, \frac{1}{2}, 0]$
F	$[\frac{1}{2}, \frac{1}{2}, 0]$, $[\frac{1}{2}, 0, \frac{1}{2}]$, $[0, \frac{1}{2}, \frac{1}{2}]$
I	$[\frac{1}{2}, \frac{1}{2}, \frac{1}{2}]$
R	$[\frac{1}{3}, \frac{2}{3}, \frac{2}{3}]$, $[\frac{2}{3}, \frac{1}{3}, \frac{1}{3}]$

each space group type, for example in Ref. [54].

For an atom j in the crystal basis, denoting the scattering length by $b_j \in \mathbb{R}$, we can write for $\overline{Q} = (\overline{h}, \overline{k}, \overline{l})$ the Fourier amplitude satisfies the relation $F(-\vec{Q}) = \sum_j f_j \exp(-i\vec{Q} \cdot \vec{R}_j) = F^*(\vec{Q})$. This is the case since the measured intensity is related to the absolute square of the Fourier amplitude $I(\vec{Q}) \propto |F(\vec{Q})|^2 = F(\vec{Q})F^*(\vec{Q})$; consequently the intensity of the reflection $\vec{Q} = (h, k, l)$, and its image under inversion $\overline{Q}$ are equal. This phenomenon is known as Friedel's law and gives rise to the appearance of centrosymmetric pairs $(Q, \overline{Q})$ in the diffraction pattern, known as Friedel pairs. These occur even when space group lacks a center of inversion symmetry. If $\vec{Q}$ is close to a resonance, however, Friedel's law is violated; the anomalous part of the scattering length $b = b' - ib''$ can be used to determine the symmetry and understand the nature of chiral structures, traditionally difficult to solve on account of the Friedel law. In this case, with the lattice assumed to be lacking of a center of inversion symmetry $i \notin \mathsf{G}$, the structure factor satisfies

Table 2.4: The 11 Laue classes which result from the combination of rotational elements of point group symmetries of each crystal system with Friedel's law. Each Laue class has a number of compatible point group symmetries; for instance, the Orthorhombic class permits 222, $mm2$, and mmm point group symmetries of the diffraction pattern.

Crystal system	Laue class
Triclinic	$\overline{1}$
Monoclinic	$2/m$
Orthorhombic	mmm
Tetragonal	$4/m$, $4/mmm$
Trigonal	$\overline{3}$, $\overline{3}/m$
Hexagonal	$6/m$, $6/mmm$
Cubic	$m3$, $m\overline{3}m$

$F(-\vec{Q}) = \sum_j f_j \exp(-i\vec{Q}\cdot\vec{R}_j) \neq F^*(\vec{Q})$.

The combination of Friedel's law with the rotational component of the point group symmetry elements of the generating space group results in 11 Laue classes, listed in Table 2.4, defining the symmetry of the diffraction pattern. For $g = \{h|\vec{\tau}\} \in \mathcal{G}$, improper rotations are those arising from the combination of a rotational symmetry element h with a lattice translation $\vec{\tau} \neq 0$. These symmetries are perhaps more subtle, but their presence can have important consequences on the material properties manifest. Consider a non-symmorphic crystal system with space group $\mathcal{G}$. In the following, we show how the presence of these symmetries can be inferred from diffraction measurements by considering the systematic absences that arise from two particular classes of improper rotations, often relevant for the stabilization

of special, or functional, physical properties. A motivating example for the analysis of Fourier amplitudes we present here concerns the deduction of a ferroaxial coupling mechanism in multiferroic $Ca_3Mn_7O_{12}$ from neutron diffraction, in which a large ferroelectric polarization constrained to 3-fold axis of the rhombohedral crystal structure is induced by an incommensurate helical magnetic structure [55].

We first consider the case of a screw-axis symmetry element given by $g = 2_1 \parallel \vec{b} \in \mathcal{G}$. The image of the general position (x_j, y_j, z_j) under the action of the symmetry element g is given by $(-x_j, \frac{1}{2} + y_j, -z_j)$, while the unit cell structure factor reduces to $F(h,k,l) = \sum_j f_j \exp(2\pi i[hx_j + ky_j + lz_j]) + \sum_j f_j \exp(2\pi i[-hx_j + k(\frac{1}{2} + y_j) - lz_j])$. For the $(0k0)$ zone, the structure factor takes the form $F(0k0) = [1 + (-1)^k] \sum_j f_j \exp(2\pi iky_j)$ and therefore generates an extinction condition for $(0k0)$ type reflections if $k = 2n + 1$, for $n \in \mathbb{Z}$. We now consider the case where g represents a c-axis glide element $\perp b \in \mathcal{G}$. Under the action of g, the general position (x_j, y_j, z_j) is mapped onto the position $(x_j, -y_j, \frac{1}{2} + z_j)$; in this case, the unit cell structure factor takes the form $F(h,k,l) = \sum_j f_j \exp(2\pi i[hx_j + ky_j + lz_j]) + \sum_j f_j \exp(2\pi i[hx_j - ky_j + l(\frac{1}{2} + z_j)])$. The structure factor for $(h0l)$ type reflections hence takes the form $F(h0l) = [1 + (-1)^l] \sum_j f_j \exp(2\pi i[hx_j + lz_j])$ and generates an extinction condition for $(h0l)$ if $l = 2n + 1$, for $n \in \mathbb{Z}$.

2.3.1 Symmetry groups

Symmetry analysis provides an elegant and systematic means of simplifying and understanding the stabilization of phase transitions in correlated and functional materials. In the following exposition, we discuss the algebraic properties of groups, sufficient to utilize its extensions in the description of subgroup structures stabilized in phase transitions. Here, we draw upon Refs. [56–64], which offer a more complete description. Consider a set $G = \{g_1, g_2, \ldots, g_n\}$ with n elements — the size of G is referred to as the order, denoted by $|G| = n$. We endow this set with a binary operation $*$ specifying the rule for the composition elements $g_i, g_j \in G$. In short-form we write $g_i * g_j = g_i g_j$. The set G has the algebraic structure of a group, notated $\mathcal{G} = (G, *)$, if the following axioms hold true.

1. Closure. The group $\mathcal{G}$ must be closed under the composition of elements such that $g_i g_j = g_k \in \mathcal{G}$ for all $g_i, g_j, g_k \in \mathcal{G}$.

2. Identity. The group $\mathcal{G}$ must contain an identity element $e \in \mathcal{G}$ such that $eg = ge = g$ for all $g \in \mathcal{G}$.

3. Inverse. The group $\mathcal{G}$ must contain an appropriate set of inverse elements; that is, for all $g \in \mathcal{G}$ require that $\exists g^{-1} \in \mathcal{G}$ such that $g^{-1}g = gg^{-1} = e$ holds true.

4. Associativity. The composition of elements must be associative; that is for elements $g_i, g_j, g_k \in \mathcal{G}$, the relation $(g_i g_j)g_k = g_i(g_j g_k)$ must hold.

If the subset $H \subseteq G$ satisfies the group axioms, then it is a subgroup $\mathcal{H} \leq \mathcal{G}$. Further, if there exist elements $g \in \mathcal{G}$ that do not appear in $\mathcal{H}$, then it is a proper subgroup $\mathcal{H} < \mathcal{G}$. Commutative groups are those that satisfy $g_i g_j = g_j g_i$ for all $g_i, g_j \in \mathcal{G}$ and are termed abelian. In the context of crystallography, the Bravais lattice is an abelian group $\mathcal{T}$ of translations with $\text{rank}(\mathcal{T}) = 3$, referring to the smallest order of the possible generating sets for $\mathcal{G}$. Due to the translational symmetry of the Bravais lattice, it is a normal subgroup of the space group $\mathcal{T} \triangleleft \mathcal{G}$ since it is invariant under conjugation by all members of the space group $g\vec{\tau}g^{-1} \in \mathcal{T}$ for all $g \in \mathcal{G}$ and $\vec{\tau} \in \mathcal{T}$.

Considering, now, the group structure and mappings between groups, we introduce the concept of a homeomorphism — a bijective mapping between two groups $\phi : \mathcal{G}_1 \mapsto \mathcal{G}_2$ which preserves multiplication of domain elements in the codomain $\phi(g_i g_j) = \phi(g_i)\phi(g_j)$ for all $g_i, g_j \in \mathcal{G}$. Homeomorphic mappings that preserve the structure of the group (most easily intuited by considering the group multiplication table) are termed isomorphisms. These establish a kind of equivalence between groups $\mathcal{G}_1$ and $\mathcal{G}_2$. Isomorphic groups have the same order and possess an identical group structure; in the parlance of algebra, we call such groups similar and the conjugacy relation between the $\mathcal{G}_1$ and $\mathcal{G}_2$ is termed a similarity transformation.

Space groups for which the symmetry elements have no combination of rotational, mirror, or inversion operations with non-primitive translations $g = \{h|0\} \in \mathcal{G}$ are symmorphic and account for 73 of the total 230 unique space groups in 3D. The remaining groups are non-symmorphic, having glide

planes and screw axes resulting from the combination of translation with a mirror element and rotation element respectively. Symmetry elements of the crystal g constitute a linear mapping h on $\mathbb{R}^n$ and a translation $\vec{\tau}$ on $\mathbb{R}^n$, defined by $\{h|\vec{\tau}\}\vec{v} := h \cdot \vec{v} + \vec{\tau}$, expressed in Seitz notation. Of interest to us are affine symmetry elements g for which the linear map h on $\mathbb{R}^n$ is an isometry, satisfying $h(\vec{v})h(\vec{w}) = \vec{v} * \vec{w}$ for all $\vec{v}, \vec{w} \in \mathbb{R}^n$; equivalently, we require that $h^{\mathrm{T}} = h^{-1}$ in the matrix representation, such that h belongs to the Euclidean group $\mathcal{E}_n$ of orthogonal matrices.

Consider the subgroup $\mathcal{H} = \{h_1, h_2, \ldots\} < \mathcal{G}$ where $g_i \in \mathcal{G}$ and $g_i \notin \mathcal{H}$. The quantities $g_i\mathcal{H} = \{g_i h_1, g_i h_2, \ldots\}$ and $\mathcal{H}g_i = \{h_1 g_i, h_2 g_i, \ldots\}$ are termed the left and right cosets of $\mathcal{H}$ respectively. Lagrange's theorem states that for some finite group $\mathcal{G}$, the order of every subgroup of $\mathcal{G}$ divides the order of $\mathcal{G}$ and it is therefore the case that all cosets of a subgroup have the same order. Further, each $g \in \mathcal{G}$ appears in exactly one coset of a subgroup, therefore partitioning $\mathcal{G}$. Consequently, the order of $\mathcal{H}$ in $\mathcal{G}$, written $[\mathcal{H} : \mathcal{G}]$, must be integral $[\mathcal{H} : \mathcal{G}] = |\mathcal{H}|/|\mathcal{G}| = m \in \mathbb{Z}$. We draw upon this construction later in Sec. 2.3.2 where we discuss the symmetry of the magnetic propagation wavevector under the rotational elements of the space group.

Subgroups of the 230 space groups can be divided among two broad categories, namely Translationengleiche (t-type) and Klassengleiche (k-type). The t-subgroups are those with a point group of reduced order and an identical set of translations. By contrast, the k-subgroups are those for which the order of the point group is unchanged, but are accompanied by a reduction

of translational symmetry. In the case where a k-subgroup $\mathcal{H}$ belongs to the same affine space group type as $\mathcal{G}$, it is an isomorphic subgroup. Meanwhile, the non-isomorphic subgroups are divided into two distinct types. Subgroups belonging to the type-I classification are characterized by a reduction of centering translations only, while those belonging to type-II have an enlarged unit cell only, when compared to the parent structure.

2.3.2 Modulated structures

The propagation wavevector $\vec{k}$ establishes a correspondence between the parent lattice and that of the magnetic subgroup structure, while the basis vectors $\vec{m}_j = \Psi_j$ encode the projection of the magnetic moment along principal directions of the reciprocal lattice. It is typical for multiple basis vectors to be involved in a phase transition, so we write $\Psi_j = \sum_\nu C_\nu \psi_\nu$, where the ψ_ν terms represent the ν components of Ψ_j for a given propagation wavevector $\vec{k}$ in the zeroth crystallographic unit cell. If more than one propagation wavevector is involved in the transition to the ordered phase, then it is necessary to sum over all the contributions to the moment projections $\vec{m}_j$ arising from these, which can lie at any point on or within the first BZ, as follows

$$\vec{m}_j = \sum_{\vec{k}} \Psi_j^{\vec{k}} \exp(-2\pi i \vec{k} \cdot \vec{\tau}). \tag{2.6}$$

From this follows a classification of the subgroup lattice. A commensurable lattice Λ', in direct space, is related to its parent lattice $\Lambda \in \mathbb{R}^n$ modulo some

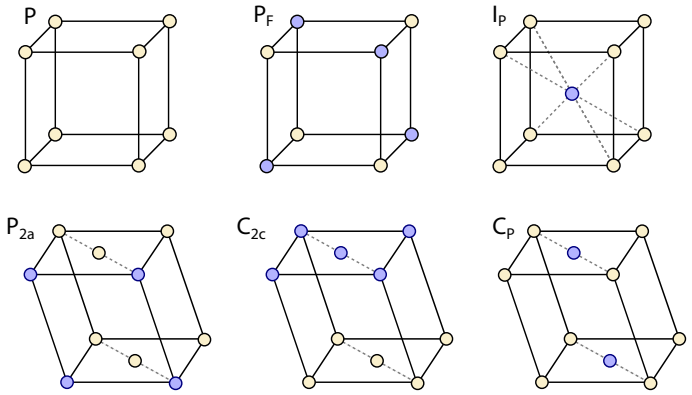

Figure 2.7: A subset of the magnetic Bravais lattices illustrating the notion of a colored lattice. Shown here are examples of colored cubic and monoclinic Bravais lattices types, with primitive (P), body-centered (I) and base-centered (C) cells, equipped with both translation and anti-translation, denoted by yellow and blue sites respectively.

integral number of primitive cells along each of the principal lattice directions; this correspondence is summarized by stating that all the components of $\vec{k}$ can be expressed as rational fractions of whole numbers $p/q \in \mathbb{Q}$. This gives rise to a change in the overall symmetry of the structure, with some examples of so-called colored lattices given in Fig. 2.7. Consequent from this is a redistribution of spectral weight among sharp Bragg reflections at rational positions in reciprocal space, manifest in experiments as satellite reflections, as illustrated in Fig. 2.8.

On the other hand, superstructures induced by the presence of a wavevector with irrational components have no simple relationship between nuclear and magnetic cells; these aperiodic structures are incommensurate, and give

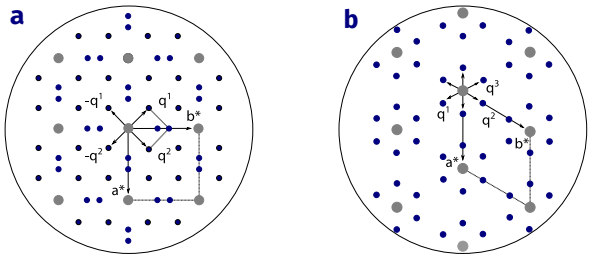

Figure 2.8: Development of satellite reflections below the T_c, associated with a reduction of symmetry $\mathcal{G} < \mathcal{G}_0$. In magnetic systems approaching a transition, critical scattering is manifest as paramagnetic background which is then increasingly redistributed in reciprocal space among positions specified by the $\vec{k}$-actives involved in the transition. In (a), the diffraction is manifest from two arms of the star of $\vec{k}$ while in (b), the diffraction results from three arms of the star of $\vec{k}$. Based on Fig. 1.12 of Ref. [65].

rise to the development of intensity at irrational positions in reciprocal space. The lack of translational symmetry induced by an incommensurate modulation results in a supercell of infinite size, although while it is the case that incommensurable structures are nominally aperiodic, they can be recast as the embedding of a $(3+n)$-D space group in which the structure is periodic.

Consider some scattering system with space group $\mathcal{G}$ and propagation wavevector $\vec{k}$. We need only consider the action of the rotational component of the symmetry element h, since $\vec{k}$ is invariant modulo some linear combination of primitive translations. Lattice translations do not affect $\vec{k}$, when operated on by the rotational component $h \in \mathcal{G}$, therefore the propagation wavevector $\vec{k}$ is either left invariant, or is mapped onto the inequivalent

wavevector $\vec{k}' = kh$. The action of the rotation operator will generally give rise to a number of such distinct wavevectors, providing a means by which to partition the symmetry elements of $\mathcal{G}$ into cosets. The first coset $\vec{G}_{\vec{k}}$ is made up of the elements that do not change $\vec{k}$, the second coset (g_2) transforms $\vec{k}$ into the inequivalent wavevector $\vec{k}' = \vec{k}_2$, and so on. The full set of inequivalent wavevectors obtained in this manner defines the star of $\vec{k}$, with each inequivalent wavevector representing a separate arm of the star, which is typically made up from a number of arms satisfying $l_{\vec{k}} < |\mathcal{G}_{\vec{k}}| < |\mathcal{G}_0|$.

The symmetry elements of $\mathcal{G}_0$ leaving $\vec{k}$ invariant are those of the first coset and form the little-group $\mathcal{G}_{\vec{k}}$, with elements of the form $\vec{k}h = \vec{k} + \vec{\tau}$. Magnetic ordering typically involves one propagation wavevector, generating single-$\vec{k}$ structures described within the remit of a single propagation wavevector. In cases where appreciable higher order exchange terms are manifest in the Hamiltonian of the scattering system, it is possible to observe quadrupolar ordering in which several arms of the star are involved in the magnetic structure, which is then termed multi-$\vec{k}$. These types of magnetic structure are rare, but domain structure can give rise to Bragg scattering that is indistinguishable; to determine whether the structure is multi-$\vec{k}$ or comprising $\vec{k}$-domains, it is necessary to test environmental conditions of the scattering system such as temperature, pressure, or magnetic field, to investigate whether there is a favoring of some $\vec{k}$-domain manifest in the response.

The magnetic moment can be expressed $\vec{m}_j = \Psi_j^{\vec{k}}[\cos(2\pi\vec{k}\cdot\vec{\tau}) + i\sin(2\pi\vec{k}\cdot\vec{\tau})]$ in general. The simplest case occurs when the basis vectors $\Psi_j^{\vec{k}}$ are purely real

or purely imaginary. Propagation wavevectors with such basis vectors can result in simple ferromagnetic, antiferromagnetic, or ferrimagnetic structures, with $\vec{m}_j = \Psi_j^{\vec{k}} \cos(2\pi\vec{k}\cdot\vec{\tau})$. In the case where $\Psi_j^{\vec{k}}$ is real with a nonzero sine component, given that $\vec{m}_j$ must be real, the magnetic moment requires a contribution from both $\vec{k}$ and $-\vec{k}$. In this case, the moment can be expressed by $\vec{m}_j = \Psi_j^{\vec{k}} \exp(2\pi i\vec{k}\cdot\vec{\tau}) + \Psi_j^{-\vec{k}} \exp(-2\pi i\vec{k}\cdot\vec{\tau})$ where we have $\Psi_j^{-\vec{k}} = \Psi_j^{\vec{k}*}$. Since $\vec{m}_j$ is real, it can be expressed simply as $\vec{m}_j = 2\mathfrak{Re}(\Psi_j^{\vec{k}}) \cos(2\pi\vec{k}\cdot\vec{\tau})$, since the imaginary part $2\mathfrak{Re}(\Psi_j^{\vec{k}}) \sin(2\pi\vec{k}\cdot\vec{\tau})$ is zero. Magnetic structures with basis vectors requiring $(\vec{k}, -\vec{k})$ admit a cosine modulation of the magnetic moments and the presence of both wavevectors gives rise to a modulation of the size of the magnetic moment in what is often called a spin density wave.

Incommensurate structures also require a contribution from both $(\vec{k}, -\vec{k})$, with the moment given by $\vec{m}_j = 2\mathfrak{Re}(\Psi_j^{\vec{k}}) \cos(2\pi\vec{k}\cdot\vec{\tau}) + 2\mathfrak{Im}(\Psi_j^{\vec{k}}) \sin(2\pi\vec{k}\cdot\vec{\tau})$. When the real and imaginary components of the basis functions are equal in magnitude and lie in the plane $\perp \vec{k}$, a helical magnetic structure is manifest in which a cosine modulation is accompanied by a transverse sine modulation. The two components are separated by a phase of $\pi/2$, and since the real and imaginary components are equal in magnitude, the projection of the helix is circular with no variation of the moment size — only its direction in the crystal. When these are not of equal magnitude, an elliptical helix is formed. If the basis vectors have components $\parallel \vec{k}$ then a cycloid is formed in which the components of the basis vector change direction and sign along the modulation axis, meaning the moments twist in the direction of $\vec{k}$.

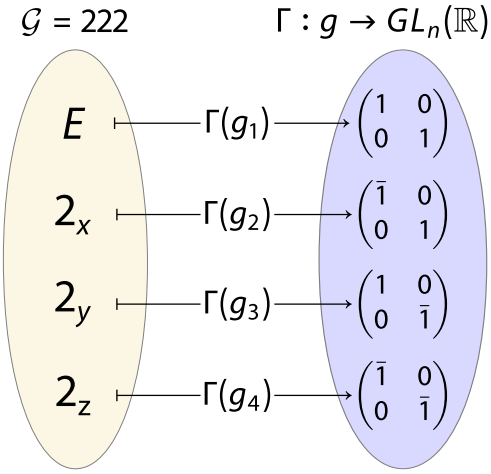

Figure 2.9: Matrix representation of the point group $\mathcal{P} = 222$. Each of the rotational symmetry elements h of the point group $\mathcal{P}$ are mapped onto corresponding invertible 2×2 matrices, belonging to the general linear group $GL_2(\mathbb{R})$ of order 2.

2.3.3 Group representations

In this section, we draw partly on the relevant expositionary material presented in Ref. [66]. The concept of a group representation is illustrated in Fig. 2.9, showing the mapping of elements of the little group $g \in \mathcal{G}_{\vec{k}}$ onto matrices R belonging to $GL_n(\mathbb{R})$, the general linear group of order n. We note that both the atomic position and the direction of magnetic moment are exposed to the action of a symmetry element $g \in \mathcal{G}_{\vec{k}}$, when operating on some magnetic site in the crystal basis. The magnetic moment is an axial vector, distinct from that of the usual polar vector. Both of these are invariant under the action of inversion, and transform similarly under rotations. They differ

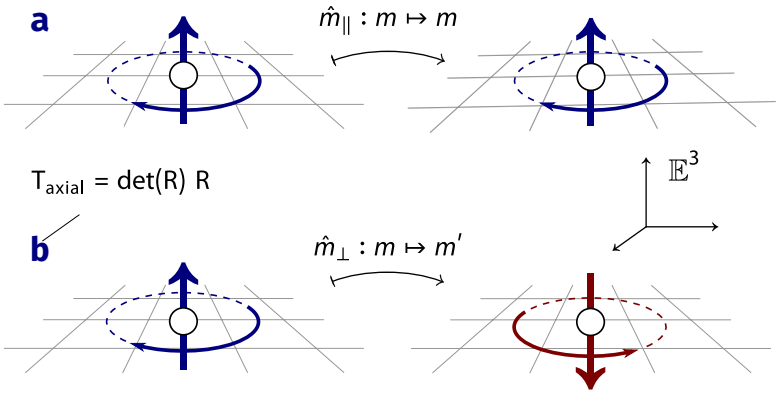

Figure 2.10: Transformation properties of the axial vector under mirror symmetry elements both parallel and perpendicular to the moment direction. Identifying the magnetic moment with a current loop, the action of a mirror plane perpendicular to the moment axis, as in (a) leaves the moment unchanged, while the action of mirror plane parallel to the moment axis, as in (b) reverses the sense of rotation of the current loop, and hence the moment direction.

in their response to mirror symmetry elements, however; the action of mirror elements both perpendicular to and parallel to the moment direction for axial is compared to that of polar vectors in Fig. 2.10. Axial vectors are relevant in the description magnetic structures, while polar vectors are relevant to the case of atomic distortions, or in the study of phonon modes.

Written in matrix form, the set of symmetry elements belonging to the little group of $\vec{k}$ define the group representation of $\mathcal{G}_{\vec{k}}$. We can transform this into a more convenient form, in which the matrices are all mutually orthogonal — this is known as the irreducible representation of $\mathcal{G}_{\vec{k}}$. The structure transforms, in general, as $R(g)\,|\psi\rangle = \chi(g)\,|\psi\rangle$, where χ is the character of

$g \in \mathcal{G}_{\vec{k}}$, which is in general a complex quantity and given simply by the trace of the matrix $R(g)$ corresponding to the symmetry element $g \in \mathcal{G}_{\vec{k}}$. The symmetry elements $g \in \mathcal{G}_{\vec{k}}$ have the action of permuting the set of atomic positions such that $g\vec{x}_i = \vec{x}_j$. We note that since the effect of polar and axial operations are independent, their effects on the system are independent and are therefore considered separately. When a symmetry element maps an atom to a position beyond the boundary of the unit cell, we can account for this by invoking a phase factor $\exp[i\vec{k} \cdot (\vec{u}_j - \vec{u}_i)]$, allowing us to represent its image within the the zeroth cell. The matrix that accounts for the permutation of atom labels and the introduction of a phase term, discussed previously, is the permutation representation $\Gamma_{\text{perm}}(g)$.

The magnetic vector associated with an atom $\vec{\mu} = (\mu_a, \mu_b, \mu_c)$ transforms according to $\vec{\mu}' = |R(g)|R(g)\vec{\mu}$, where $|R(g)|$ is the determinant of the matrix $R(g)$, required in order to conserve the symmetry of the axial vector under improper rotations. The axial representation $\Gamma_{\text{axial}}(g)$ is a 3×3 matrix that characterizes the transformation of the magnetic moment vector. The character of the permutation and axial vector representations are given simply by the trace of their respective matrices. The magnetic representation $\Gamma_{\text{mag}}(g)$ is given simply by the product of the permutation and axial representations, since they are independent. It is, in general, a tensor quantity defined by

$$\begin{aligned} \Gamma_{\text{mag}}(g) &= \Gamma_{\text{perm}}(g) \times \Gamma_{\text{axial}}(g), \\ \chi_{\text{mag}}(g) &= \chi_{\text{perm}}(g)\chi_{\text{axial}}(g), \end{aligned} \tag{2.7}$$

where $\Gamma_{\rm mag}(g)$ has dimension $3N \times 3N$. Noting that the matrices $\Gamma_\nu(g)$ act only upon a subspace of the $3N$-spin components μ_{Γ_ν}, a block-diagonal form of the magnetic representation can be obtained by summation over all the irreducible representations $\Gamma_\nu(g)$, as follows

$$\Gamma_1\mu_1 + \Gamma_2\mu_2 + \cdots + \Gamma_\nu\mu_\nu = \begin{pmatrix} \Gamma_1 & 0 & \cdots & 0 \\ 0 & \Gamma_2 & \cdots & 0 \\ \vdots & \vdots & \ddots & \vdots \\ 0 & 0 & \cdots & \Gamma_\nu \end{pmatrix} \begin{pmatrix} \mu_{\Gamma_1} \\ \mu_{\Gamma_2} \\ \vdots \\ \mu_{\Gamma_\nu} \end{pmatrix}. \tag{2.8}$$

With n_ν defining the number of distinct basis vectors involved in each irreducible representation, the magnetic representation is described as,

$$\Gamma_{\rm mag}(g) = \sum_\nu n_\nu \Gamma_\nu(g), \tag{2.9}$$

$$n_\nu = \frac{1}{n(\mathcal{G}_{\vec{k}})} \sum_{g \in \mathcal{G}_{\vec{k}}} \chi_{\rm mag}(g)\chi_{\Gamma_\nu}(g)^*. \tag{2.10}$$

One strategy for the calculation of basis vectors ψ the projection operator method, in which trial functions $\vec{m}_a = (1,0,0)$, $\vec{m}_b = (0,1,0)$, and $\vec{m}_c = (0,0,1)$ along the crystallographic axes are used in conjunction with the projection operator formula to find the basis vector ψ for magnetic representation $\Gamma_\nu(g)$. The projection operator is given by

$$\psi_{\alpha\nu} = \sum_{g \in \mathcal{G}_{\vec{k}}} \chi^*_\nu(g) \sum_n \delta_{n,g_n} |R(g)| R(g)\, \vec{m}_\alpha, \tag{2.11}$$

where $\chi(g)$ is the character of $g \in \mathcal{G}_{\vec{k}}$. Any linear combination of basis vectors will, in the general case, have the same symmetry as that of the irreducible representation. The moment distribution $\vec{M}_j$ of jth atom expressed as the Fourier transform of the linear combination of basis vectors $\Psi_j = \sum_\alpha C_\alpha \psi_\alpha$ is given by

$$\vec{M}_j = \sum_{\vec{k}} \sum_{\alpha} C_\alpha \psi_\alpha \exp(-i\vec{k} \cdot \vec{\tau}), \tag{2.12}$$

where C_α is a mixing coefficient, describing the weighted contribution of the basis vectors. In general, this is a complex quantity with the summation taken over all possible propagation vectors $\vec{k}$.

In order for a result to be physical, the moment must be real. In accordance with this, the basis vectors can be brought into a completely real form by constructing linear combinations of basis vectors with their complex conjugates, given by $-\vec{k}$. As deduced from the projection of test functions, the moment distribution takes the form [64, 67]

$$\vec{M}_j = \sum_{\alpha} C_\alpha \psi_\alpha \exp(-i\vec{k} \cdot \vec{\tau}) + C^*_\alpha \psi^*_\alpha \exp(+i\vec{k} \cdot \vec{\tau}). \tag{2.13}$$

This can be expressed equivalently in the form

$$\vec{M}_j = 2 \sum_{\alpha} |C_\alpha| \hat{v} \cos(\vec{k} \cdot \vec{\tau} + \omega_\alpha + \theta_\alpha). \tag{2.14}$$

The basis vectors along direction $\hat{v}$, can be expressed as $\psi = \exp(-i\omega)\hat{v}$, with the complex coefficient written in the form $C = |C| \exp(-i\theta)$; here, θ is a

free parameter, while the phase contribution ω is restricted by the symmetry of the space group.

2.4 Scattering theory

Like most scattering techniques, the fundamental quantities measured in neutron experiments are the incident and final states of the wavevectors and energies. The angle and intensity of scattering is recorded on position sensitive detectors and it is possible to transfer these quantities to the reciprocal lattice frame using geometrical and kinematical transformations. The conservation of momentum and energy can be expressed as

$$\begin{aligned} \vec{Q} &= \vec{k}_i - \vec{k}_f, \\ E_T &= E_i - E_f = \frac{\hbar^2}{2m_\mathrm{n}}(\vec{k}_i^2 - \vec{k}_f^2), \end{aligned} \tag{2.15}$$

where $\vec{Q}$ is the momentum transfer and E_T is the energy transfer.

2.4.1 Geometry and kinematics

Summarizing from Refs. [68–71], we denote the neutron flux as Φ_0 and assume the detectors to be perfectly efficient. The total scattered intensity is given by the product of the flux with the cross-section $I_\mathrm{tot} = \sigma_\mathrm{tot} \times \mathrm{d}^2\sigma/\mathrm{d}\Omega_f \mathrm{d}E_f$. The quotient term in this expression is the partial differential cross-section

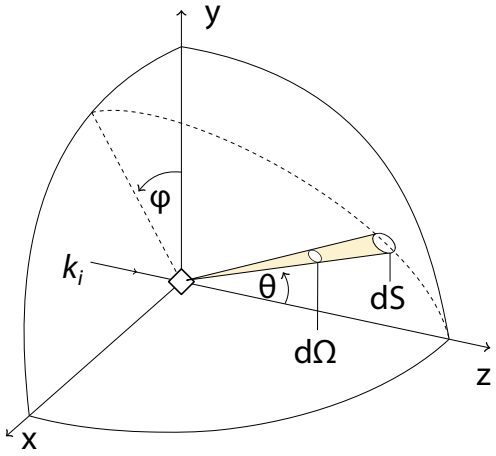

Figure 2.11: The geometry of the scattering experiment expressed in spherical coordinates (r, θ, ϕ). The neutron beam, with incoming wavevector $\vec{k}_i$ is along the $\hat{z}$-axis of the scattering frame, with $\hat{y}$ vertically upwards and $\hat{x}$ lying in the horizontal scattering plane. The angle element $\mathrm{d}\Omega$ encodes the direction of the final wavevector $\vec{k}_f$ incident on the detectors in terms of (θ, ϕ). Based on Fig. 1.2 in Ref. [68].

$I_{\mathrm{tot}}/\sigma_{\mathrm{tot}}$, which is a sum of incoherent and coherent components

$$\frac{\mathrm{d}^2\sigma}{\mathrm{d}\Omega_f \mathrm{d}E_f} = \left.\frac{\mathrm{d}^2\sigma}{\mathrm{d}\Omega_f \mathrm{d}E_f}\right|_{\mathrm{inc}} + \left.\frac{\mathrm{d}^2\sigma}{\mathrm{d}\Omega_f \mathrm{d}E_f}\right|_{\mathrm{coh}}, \tag{2.16}$$

and intrinsically contains the direction of the scattered neutrons in terms of (θ, ϕ) through the angle element $\mathrm{d}\Omega_f$, along with the final neutron energy E_f. The geometry of the scattering experiment is shown in Fig. 2.11. The incoherent component of the scattering cross-section arises when there exists a distribution of isotopes or nuclear spins in the system.

2.4.2 Scattering lengths, interactions and cross-section

Consider a system with i atomic species each having a set of set of uncorrelated scattering lengths $b_{i'}$. Summarizing from Refs. [46, 72], the neutron has spin σ_{n} and the nucleus has spin s. In the case where the target nucleus has non-zero spin, the neutron scattering length is spin-dependent. Upon colliding with the target nucleus, the neutron can be scattered or absorbed; in the latter case, photons or α-particles are produced. The scattering length can be written as a complex quantity $b = b' + ib''$. The total bound cross-section takes the form $\sigma_s = 4\pi\langle|b|^2\rangle$, where $\langle\dots\rangle$ denotes a statistical average over neutron and nuclear spins.

The absorption cross-section takes the form $\sigma_a = (4\pi/k)\langle b''\rangle$, where $k = 2\pi/\lambda$ is the wavevector of the incident neutron with wavelength λ. The macroscopic absorption cross-section takes the form $\Sigma = N_A\rho_j\sigma_j/A_j$ and relates the area of the nucleus seen by the incident neutron to the resultant beam attenuation. In the case of unpolarized neutrons and unpolarized nuclei, the bound scattering cross-section is of the sum of coherent and incoherent cross sections $\sigma_s = \sigma_c + \sigma_i = 4\pi(|b_c|^2 + |b_i|^2)$. The coherent cross-section is the thermal average, $b_c = \langle b\rangle$, therefore the absorption cross-section is given by $\sigma_a = (4\pi/k)b_c''$. There is a small ($\leq$ 0.5 %) electrostatic contribution to b_c from the neutron polarizability. This contribution, b_e, is due to the neutron-electron electron interaction with the Coulomb field of bound nuclei.

Summarizing from Ref. [72], the neutron-electron interaction potential can be written as follows: $\hat{V}_{\mathrm{E}}(\vec{r}) = \hat{V}_{\mathrm{SO}}(\vec{r}) + \hat{V}_{\mathrm{F}}(\vec{r})$. The first term gives rise

to Schwinger scattering with a potential given by $\hat{V}_{\mathrm{SO}} = -\gamma_{\mathrm{n}}\mu_{\mathrm{N}}(mc^2)^{-1}\sigma \cdot (\vec{E} \times \vec{p})$, arising from the coupling of the electric field of the moving neutron magnetic moment with the charge-density of the scattering system via the spin-orbit interaction [73]. The second term gives rise to scattering by the Foldy interaction, which has potential $\hat{V}_{\mathrm{F}} = \hbar\gamma_{\mathrm{n}}\mu_{\mathrm{N}}(2mc^2)^{-1}\nabla \cdot \vec{E}$, and arises from the relativistic *Zitterbewegung* motion of the neutron moment. This gives rise to an anomalous moment as the neutron rapidly oscillates to and from its dissociated state (comprising a proton and π^- meson), which in turn provides a separation of charge [74].

The Schwinger scattering gives a purely imaginary cross-section while the Foldy contribution is $b_{\mathrm{F}} = -1.486 \times 10^{-3}$ fm [46, 75]. These Coulombic contributions to the neutron scattering length will henceforth be considered negligible. The scattering is spherically symmetric because the Fermi interaction potential is valid over very short ranges, and gives rise to s-wave type scattering. Neutrons are sensitive only to the component of the magnetic moment perpendicular to $\vec{Q}$, and unlike the nuclear case, the scattering is anisotropic. The probability of scattering is given by application of Fermi's golden rule, resulting in the matrix element

$$\left.\frac{\mathrm{d}^2\sigma}{\mathrm{d}\Omega_f \mathrm{d}E_f}\right|_{\lambda_i \to \lambda_f} = \frac{k_f}{k_i}\left[\frac{m_{\mathrm{n}}}{2\pi\hbar^2}\right] |\langle \vec{k}_f \lambda_f | \hat{V} | \vec{k}_f \lambda_i \rangle|^2 \, \delta(\hbar\omega + E_i - E_f). \qquad (2.17)$$

The potential $\hat{V}$ in Eq. (2.17) is the Fermi pseudo-potential, given by

$$\hat{V}_{\mathrm{n}}(\vec{r}) = \delta(\vec{r})\frac{2\pi\hbar^2}{m_{\mathrm{n}}}b. \tag{2.18}$$

In general, the interaction potential for magnetic scattering is

$$V(\vec{r}) = 2\mu_{\mathrm{B}}\ \gamma\mu_{\mathrm{N}}\ \sigma \cdot \left[\nabla \times \left(\frac{\vec{s}\times\hat{\vec{R}}}{R^2}\right) + \frac{1}{\hbar}\frac{\vec{r}\times\hat{\vec{R}}}{R^2}\right], \tag{2.19}$$

the first term due to spin, and the second due to the orbital motion of the electron. The cross-section comprises matrix elements $\left\langle \vec{k}_1\sigma_1\lambda_1 \middle| V \middle| \vec{k}_0\sigma_0\lambda_0 \right\rangle$. The magnetic interaction potential for magnetic neuron scattering is $V_M(\vec{r}) = -\vec{\mu}_{\mathrm{n}} \cdot \vec{B}(\vec{r})$, where $\vec{B}$ is the local magnetic field around localized moments of the electrons in the crystal structure. Invoking a Fourier transformation, from Maxwell's laws, one can write the magnetic interaction potential as

$$\begin{aligned} V(\vec{Q}) &= -\mu_{\mathrm{n}}\vec{B}(\vec{Q}) = -\mu_0\mu_{\mathrm{n}} \cdot \vec{M}_{\perp}(\vec{Q}), \\ \vec{M}_{\perp}(\vec{Q}) &= \hat{\vec{Q}} \times [\vec{M}(\hat{\vec{Q}}) \times \hat{\vec{Q}}], \end{aligned} \tag{2.20}$$

where $\vec{M}_{\perp}(\vec{Q})$ is the perpendicular projection of the magnetization. In the dipole approximation, one can simply write

$$\vec{M}(\vec{Q}) = -g\vec{\mu}_{\mathrm{B}}f(\vec{Q})\vec{S} = f(\vec{Q})\vec{\mu}. \tag{2.21}$$

Now considering the incoherent scattering from a distribution of isotopic

abundances, the average isotopic states for each atomic species can be defined by their relative frequency $f_{i'}$ through the relations

$$\overline{b}_i = \sum_{i'} f_{i'} b_i \quad \text{and} \quad \overline{b_i^2} = \sum_{i'} f_{i'} b_i^2. \tag{2.22}$$

The incoherent elastic cross-section then takes the form

$$\left.\frac{\mathrm{d}^2\sigma}{\mathrm{d}\Omega \mathrm{d}E_f}\right|_{\mathrm{inc}} = \sum_i (\overline{b_i^2} - \overline{b}_i^2). \tag{2.23}$$

This component of the cross-section provides a measurement of the autocorrelation function for a particular atom in the system. That is, the probability that a particular atom is located at position $\vec{r}'$ at time t' given an initial position $\vec{r} = 0$ at $t = 0$. Since the incoherent scattering does not arise from collective interference, it contains no structural information. In experiments, the incoherent scattering is typically treated as a parasitic contribution to the background and its minimization is sought with careful choice of materials used for sample environment and mounting. The second term in Eq. (2.16) describes the collective interference of scattered neutrons from atomic centers in the sample. For a system with atomic species i, j and instantaneous displacement between their equilibrium positions $\vec{r}_{ij} = \vec{r}_j - \vec{r}_i$, the coherent elastic cross-section takes the form

$$\left.\frac{\mathrm{d}^2\sigma}{\mathrm{d}\Omega \mathrm{d}E_f}\right|_{\mathrm{coh}} = \frac{1}{N} \sum_{ij} \overline{b}_i \overline{b}_j \langle \exp(i\vec{Q} \cdot \vec{r}_{ij}) \rangle, \tag{2.24}$$

and in the case of powder diffraction, it is given by

$$I_{\mathrm{el}}^{\mathrm{coh}}(\vec{Q}) = \frac{1}{N}\sum_i \bar{b}_i^2 + \frac{1}{N}\sum_{i\neq j} \bar{b}_i \bar{b}_j \left\langle \frac{\sin qr_{ij}}{qr_{ij}} \right\rangle . \tag{2.25}$$

2.4.3 Correlation functions and diffuse scattering

Consider the magnetic susceptibility $\vec{M} = \chi\vec{H}$. If $\vec{H}$ is constant in spatial and temporal variables, then we measure the zero frequency, uniform susceptibility, i.e. the $(\vec{Q},\omega) = 0$ response. On the other hand, if the applied field has a varying spatial and temporal dependence, then we measure the generalized dynamic susceptibility $\chi(\vec{Q},\omega)$. In the case where the system responds linearly to the applied magnetic field, the susceptibility is $\vec{M}_\alpha(\vec{Q},\omega) = \chi_{\alpha\beta}(\vec{Q},\omega)H_\beta(\vec{Q},\omega)$. In general, there is a phase factor between $\vec{M}$ and $\vec{H}$, so χ is a complex quantity and can be written in the two component form $\chi(\vec{Q},\omega) = \chi'(\vec{Q},\omega) - i\chi''(\vec{Q},\omega)$.

Since the neutron is weakly interacting, the system responds linearly within the remit of the fluctuation-dissipation theorem. Then, between pairs of spins, one can define the spin-pair correlation function. The imaginary component of the generalized susceptibility is related to the dynamic structure factor through the relation

$$S^{\alpha\beta}(\vec{Q},\omega) = [1 + n(\omega)]\frac{1}{\pi}\chi''(\vec{Q},\omega), \tag{2.26}$$

where the factor $n(\omega) = [\exp(\hbar\omega\ k_{\mathrm{B}}T) - 1]^{-1}$ is required on account of de-

tailed balance. In terms of the perpendicular component of the spin, the dynamic structure factor takes the form

$$S(\vec{Q},\omega) = (2\pi N)^{-1} \int \sum_{ij} \exp[i(\vec{Q}\cdot r_{ij} - \omega t)] \langle \vec{S}_i^{\perp}(0) \cdot \vec{S}_j^{\perp}(0) \rangle. \tag{2.27}$$

The self-pair correlation function measures correlations between the position of the same particle at different times, so quantifies the incoherent nuclear scattering,

$$S_i(\vec{Q},\omega) = A'' \iint \exp(i[\vec{Q}\cdot\vec{r} - \omega t]) G_s(\vec{r},t)\,\mathrm{d}\vec{r}\,\mathrm{d}t, \tag{2.28}$$

where $G_s(\vec{r},t)$ is the self-pair correlation function. For a scattering system with a single magnetic ion species, an electron density distributed isotropically around atomic positions, no magnetoelastic coupling, and only isotropic harmonic atomic displacements $T = T^{\mathrm{iso}}$, the magnetic scattering is

$$I_{\mathrm{mag}}(\vec{Q},\omega) = \frac{k_f}{k_i} \left(\frac{\vec{\mu}_0}{4\pi} \frac{\gamma_{\mathrm{n}} e^2}{2m_{\mathrm{e}}} \right)^2 T^2 [g f(\vec{Q})]^2 S^{\alpha\beta}(\vec{Q},\omega). \tag{2.29}$$

The magnetic scattering obeys sum rules, which assumes that the spin value S is constant, leading to the expression

$$\int S(\vec{Q}) = \frac{2}{3} S(S+1) \int \mathrm{d}\vec{Q}, \tag{2.30}$$

with the factor of 2/3 due to the projection of the spin perpendicular to $\vec{Q}$.

The dynamic structure factor contains information on the distribution of spectral weight in reciprocal space. Magnetic dynamics such as dispersion relations and spectral weight distributions can be calculated from linear response theory. In such a linear system, the response $R(\vec{x},t)$ that is induced by a small perturbation $H(\vec{x},t)$ is proportional to this perturbation to first order $R(\vec{x},t) = \chi(\vec{x},t) \cdot H(\vec{x},t)$

$$\chi'^{\alpha\beta} = -\frac{2\omega}{\pi} p \int_0^\infty \mathrm{d}\omega' \frac{\chi'(\vec{Q},\omega')}{\omega'^2 - \omega^2}. \tag{2.31}$$

In fact, for any neutron scattering process, a continuity relation must hold, defined by the condition $S(\vec{Q},-\omega) = \exp(\hbar\omega/k_\mathrm{B}T)S(\vec{Q},\omega)$, relating the neutron energy gain $S(\vec{Q},-\omega)$ to the neutron energy loss $S(\vec{Q},\omega)$.

The average crystallographic structure of a material, as we have seen, gives rise to sharp [$\delta(\vec{Q}) \otimes$ resolution function] Bragg reflections; the intensity between these is the diffuse scattering, arising from local distortions and correlated disorder. The lead-oxide class of relaxor ferroelectric materials are a classic diffuse scattering material with extraordinary piezoelectric properties, with their configurations of correlated disorder producing vivid and striking patterns of diffuse intensity in reciprocal space, as illustrated in Fig. 2.12. The magnitude of intensities arising from diffuse scattering are typically orders of magnitude lower than the Bragg contribution. The separation of diffuse scattering from background signal is highly non-trivial and is a longstanding challenge. On account of their weak nature, diffuse features are often uncov-

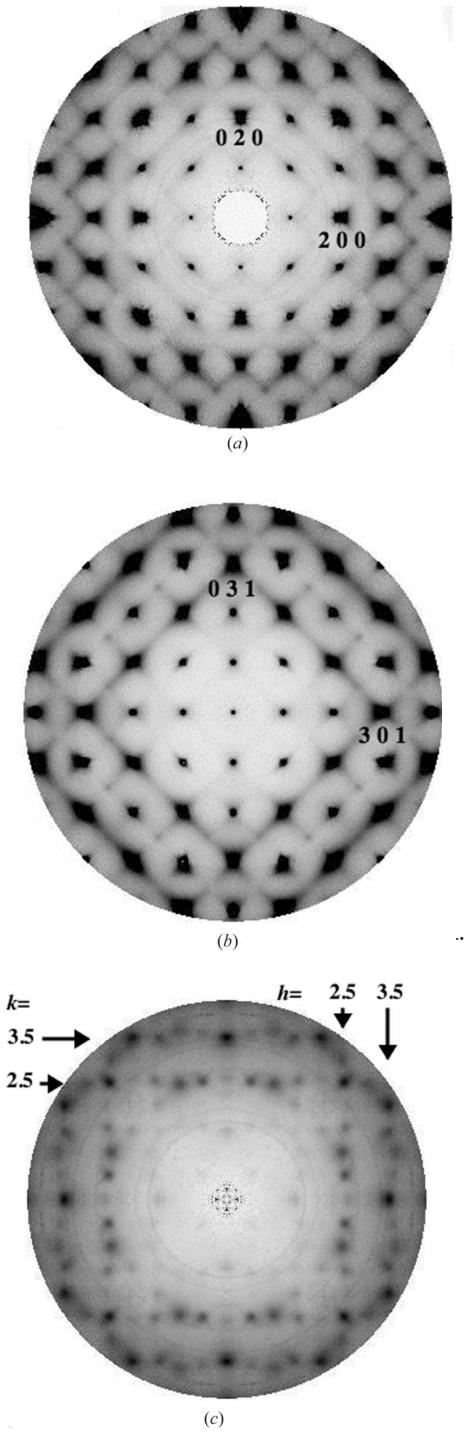

Figure 2.12: Neutron diffuse scattering in relaxor ferroelectrics, showing broad in $\vec{Q}$ correlations spread throughout reciprocal space, indicating the presence of correlated disorder. Adapted from Ref. [76].

ered only after careful, properly normalized background subtraction. Small local distortions in direct space give rise to a broad-in-momentum response in reciprocal space since $Q = 2\pi/d$. In the kinematic approximation, the coherent neutron cross section is

$$I(\vec{Q}) = \frac{1}{N}\sum_{jk}\langle b_j b_k \ \exp[i\vec{Q}\cdot(\vec{r}_j - \vec{r}_k)]\rangle, \tag{2.32}$$

where b_j is the coherent scattering length of atom j. The scattered intensity from a crystal is the sum of Bragg and diffuse contributions. $I(\vec{Q})$ can be can be separated into these, as follows,

$$\begin{aligned} I(\vec{Q}) &= I_{\text{Bragg}}(\vec{Q}) + I_{\text{diffuse}}(\vec{Q}) \\ &= \frac{1}{N}|\langle F(\vec{Q})\rangle|^2 + \frac{1}{N}\langle|F(\vec{Q}) - \langle F(\vec{Q})\rangle|^2\rangle, \end{aligned} \tag{2.33}$$

where $F(\vec{Q})$ is the unit cell structure factor, a discrete Fourier transform of the direct lattice unit cell, given by $F(\vec{Q}) = \sum_{j=1}^{N} b_j \ \exp(i\vec{Q}\cdot\vec{r}_k)$.

Before the advent of Pair Distribution Function (PDF) and Reverse Monte Carlo (RMC) methods [77] of interpretation, problems in diffuse scattering were largely approached by symmetry analysis and physical intuition for disorder mechanisms used to propose models, allowing for direct Monte Carlo simulation of the equilibrium structure factor $S(\vec{Q}) \equiv S(\vec{Q}, 0)$ in packages such as the DISCUS suite [78, 79] to be compared against measurements. The algorithm simulates thermalization under each system configuration in

which random perturbations are introduced to the phase-space Hamiltonian $\mathcal{H}(\phi)$. 'Moves' are accepted if they lower the configuration energy with some probability. The partition function of the canonical ensemble, and the thermal operator of some operator $\hat{O}$, are given by the relations

$$\mathcal{Z} = \int D\phi \ \ \exp[-\mathcal{H}(\phi)/k_{\mathrm{B}}T], \tag{2.34}$$

$$\langle \hat{O}(\phi) \rangle = \mathcal{Z}^{-1} \int D\phi \ \hat{O}(\phi) \ \ \exp[-\mathcal{H}(\phi)/k_{\mathrm{B}}T], \tag{2.35}$$

where $\mathcal{H}(\phi)$ is the configuration energy. The Metropolis method of phase-space exploration imposes the transition probability between configuration states as

$$W(\phi \rightarrow \phi') = C \times \begin{cases} \exp(\delta H/k_{\mathrm{B}}T) & \text{if} \delta H > 0, \\ 1 & \text{otherwise.} \end{cases} \tag{2.36}$$

Summarizing from Ref. [80], which presents a new method for calculation of diffuse scattering patterns by fast Fourier transform, the ordering wavevector $\vec{k}$ with components $k_\alpha \in \mathbb{R}$ defines a supercell such that Bragg positions are $\vec{G} = \vec{H} + \vec{k}$, with $\vec{H} = H_1\vec{a}^* + H_2\vec{b}^* + H_3\vec{c}^*$ and $H_\alpha \in \mathbb{Z}$. Let $\vec{r}_{\mu i}$ denote the average position of site μ in the unit cell and $\vec{u}_{\vec{R}\mu i}$ denote the local displacement of atom i at site μ and lattice point $\vec{R}$. The structure factor can the be expressed as

$$F(\vec{G}) = \sum_{\vec{R}\mu i} \delta_{\vec{R}\mu i} b_{\mu i} \ \ \exp[i\vec{G} \cdot (\vec{r}_\mu + \vec{u}_{\vec{R}\mu i})] \exp(i\vec{k} \cdot \vec{R}), \tag{2.37}$$

where $\delta_{\vec{R}\mu i}$ is 1 if site μ at lattice point $\vec{R}$ is occupied by atom of element i, and zero otherwise. The deviation from average occupancy is $a_{\vec{R}\mu i} = [\delta_{\vec{R}\mu i} - c_{\mu i}]/c_{\mu i}$, in which $c_{\mu i}$ is the average occupancy of site μ by atom of type i. This separates the structure factor into an average component and a local modulation. Since the structure factor is now in terms of an average component and a local modulation, it can be written in terms of a Bragg and diffuse contribution, given by

$$F(\vec{Q}) = \sum_{\mu i} [\mathsf{U}_{\vec{k}\mu i}(\vec{G}) + \mathsf{A}_{\vec{k}\mu i}(\vec{G})] c_{\mu i} b_{\mu i} \ \exp(i\vec{G} \cdot \vec{r}_\mu). \tag{2.38}$$

The terms $\mathsf{U}_{\vec{k}\mu i}(\vec{G})$ and $\mathsf{A}_{\vec{k}\mu i}(\vec{G})$ are a pair of Fourier transforms for each site μ and element i, defined by the relations

$$\mathsf{U}_{\vec{k}\mu i}(\vec{G}) = \sum_{\vec{R}} \ \exp(i\vec{G} \cdot \vec{u}_{\vec{R}\mu i}) \ \exp(i\vec{k} \cdot \vec{R}), \tag{2.39}$$

$$\mathsf{A}_{\vec{k}\mu i}(\vec{G}) = \sum_{\vec{R}} a_{\vec{R}\mu i} \ \exp(i\vec{G} \cdot \vec{u}_{\vec{R}\mu i}) \ \exp(i\vec{k} \cdot \vec{R}). \tag{2.40}$$

The Bragg structure factor therefore takes the form

$$\langle F(\vec{Q}) \rangle = n_1 n_2 n_3 \delta_{\vec{G}\vec{H}} \sum_{\mu i} T_{\mu i}(\vec{Q}) c_{\mu i} b_{\mu i} \ \exp(i\vec{G} \cdot \vec{r}_\mu), \tag{2.41}$$

where n_1, n_2, n_3 denote the number of units cells, and with the Debye-Waller

(temperature) factor given by

$$T_{\mu i}(\vec{G}) = \frac{1}{n_1 n_2 n_3} \sum_{\vec{R}} \langle (1 + a_{\vec{R}\mu i}) \ \exp(i\vec{G} \cdot \vec{u}_{\vec{R}\mu i}) \rangle. \tag{2.42}$$

Laue monotonic scattering from random population of defect sites appears as incoherent background scattering. The magnetic cross section is

$$F_{\mathrm{mag}}(\vec{G}) = \sum_{\mu i} f_{\mu i}^{\mathrm{mag}}(|\vec{G}|) T_{\mu i}(\vec{G}) \vec{M}_{\vec{k}\mu i} \ \exp(i\vec{G} \cdot \vec{r}_{\mu}), \tag{2.43}$$

where $f_{\mu i}^{\mathrm{mag}}(|\vec{G}|)$ is the magnetic form factor, and the Fourier component of the magnetic moment is given by

$$\vec{M}_{\vec{k}\mu i} = \sum_{\vec{R}} \vec{M}_{\vec{R}\mu i} \ \exp(i\vec{k} \cdot \vec{R}). \tag{2.44}$$

The measured intensity then takes the form $I_{\mathrm{mag}}(\vec{G}) = (C/N)\langle |F_{\mathrm{mag}}^{\perp}(\vec{G})|^2 \rangle$, with the constant $C = (\gamma_n r_0/2)^2 = 0.07265$ barn. This is the case because the neutron interacts with the perpendicular component of the magnetic moment, $F_{\mathrm{mag}}^{\perp} = \hat{G} \times F_{\mathrm{mag}} \times \hat{G}$, where $\hat{G} = \vec{G}/|\vec{G}|$.

2.5 Instrumentation

In this section, we draw partly on the relevant expositionary material presented in Refs. [66, 81]. Neutron scattering is a flux-limited technique. In a neutron scattering experiment, one generally aims to measure some volume

element of the dynamical structure factor $S(\vec{Q},\omega)$. In the case of neutron diffraction, measurements are energy integrated, so one measures instead the static structure factor $S(\vec{Q}) \equiv \int S(\vec{Q},\omega)\,\mathrm{d}\omega$. Depending on the aims of the experiment, one selects an instrument and beamline configuration in the planning stage that takes into account the equipoised relationship between beam flux and instrument resolution.

It is generally the case that a higher brilliance — the neutron current normalized to the source area and solid angle of emission — comes at the cost of resolution, since higher resolutions typically require a greater degree of beam shaping, thereby giving rise to a greater degree of beam attenuation. Due to the bounded nature of instrument resolution, there are always a distribution of wavevectors $\vec{k}_i$ and energies E_i around their nominal values in scattering experiments. The intensity $I(\vec{Q},\omega)$, as measured on the detectors in experiments, is directly proportional to a function which encodes the $(\vec{Q},E)$ dependence of the instrument resolution.

Owing to the complexities of accounting for the effect of all neutronics, resolution effects are not usually easy to calculate; the resolution function itself manifests as an anisotropic ellipsoid in $(\vec{Q},E)$ space, and is often approximated to a reasonable degree of accuracy by a 4D multivariate Gaussian distribution. We denote the wavevector spread of the incident and scattered beam $\vec{k}_i$ and $\vec{k}_f$ by the vector $\tilde{Q} = \vec{Q} - \vec{Q}_0$, and notate the spread of frequencies by $\tilde{\omega} = \vec{\omega} - \vec{\omega}_0$. Then, the measured intensities vary according to the

relation

$$I(\tilde{Q},\tilde{\omega}) \propto \iint R(\tilde{Q},\tilde{\omega}) S(\vec{Q},\omega)\, \mathrm{d}^3\vec{Q}\, \mathrm{d}\omega. \tag{2.45}$$

The resolution function $R(\tilde{Q},\tilde{\omega})$ is peaked at $(\vec{Q}_0,\omega_0)$, and is the inverse of the covariance matrix describing a 4D Gaussian distribution in $(\vec{Q},E)$ space of the form [82]

$$R(\tilde{Q},\tilde{\omega}) = \frac{1}{(2\pi)^2}|C|^{1/2}\, \exp(-\frac{1}{2}\mathsf{X}^{\mathrm{T}}\mathsf{C}\mathsf{X}), \tag{2.46}$$

where X is a column vector with elements $(\tilde{Q},\tilde{\omega})$ and the integral of R is normalized to unity. Here, C is the resolution matrix, which in general is not diagonal — that is, the eigenvectors are not oriented along the axes of the $(\vec{Q},\omega)$ coordinate system.

2.5.1 Triple-axis spectrometer

Affording the experimenter granular control of the incident neutron momentum $\vec{k}_i$ and energy E_i, the triple-axis spectrometer is well known for its high resolution and versatility, and has enjoyed decades of success in condensed matter physics, as discussed in Sec. 2.1. The instrument is particularly effective when applied to the study of collective excitations, including phonons and magnons. A schematic representation of the instrument is shown in Fig. 2.13. An incident wavevector $\vec{k}_i$ is selected from the polychromatic incident beam by a single-crystal monochromator. This operates on the basis of Bragg's law by varying the angle $2\theta_{\mathrm{M}}$ alike the analyzer crystal; by varying the angle

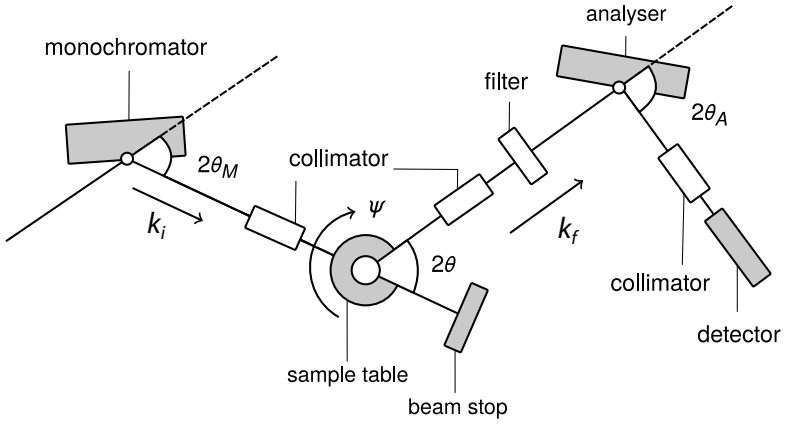

Figure 2.13: Schematic diagram of the triple-axis spectrometer. The white beam is filtered by the crystal monochromator, selecting an incident wavevector $\vec{k}_i$. There are many options for the installation of collimation or filtration modules on both the incident and scattered side of the beam, affording much flexibility. Upon scattering with the sample, the scattered beam is directed to an analyzer crystal where the final wavevector $\vec{k}_f$ is selected before the beam is directed to the detector tube and its counts recorded.

$2\theta_{\mathrm{A}}$, the final wavevectors of the scattered neutrons $\vec{k}_f$ are selected. Both monochromator and analyzer are typically made from Pyrolytic graphite, though sometimes also from Cu, Si, or Heusler alloys.

Meanwhile, low efficiency detectors known as monitors are situated along the length of the beam for diagnostic purposes; they additionally serve as a proxy for the incident flux, therefore allowing for the normalization of raw detector panel data. High energy neutrons contaminate the beam and contribute to the background, and can be removed via the insertion of Be or graphite filters along the length of the beam on either side of the sample

table. Fig. 2.13, a schematic representation of the instrument, shows the layout of the monochromator, sample, and analyzer tables, which rotate about their respective axes. When combined with sample orientation, these degrees of freedom allow for a variety of instrument configurations, and afford the experimenter the opportunity to measure any region of reciprocal space.

The measurements of a given $(\vec{Q}, E)$ point can be performed in an infinite number of ways due to the flexibility of the instrument configuration. In reality, however, not all configurations are equivalent as they lead to different intensity or resolution characteristics. The quantity which we measure in neutron scattering experiments is the double-differential cross-section with respect to solid angle Ω and scattered neutron energy E_f,

$$\frac{\mathrm{d}^2\sigma}{\mathrm{d}\Omega \mathrm{d}E_f} = \frac{k_i}{k_f} S(\vec{Q}, E), \tag{2.47}$$

where the response function $S(\vec{Q}, E)$ is the physical quantity of the sample which we wish to extract in neutron scattering experiments. Generally, the final wavevector k_f is held fixed and k_i is allowed to vary. This can be accounted for by the following: often varying k_i results in a decreasing incident neutron flux on the sample; in qualitative analysis of the integrated intensities in constant-Q scans, the intensity is also proportional to the factor $F(k_f)$ which is given as [71],

$$F(k_f) = R_A(k_f) k_f^3 \cot\theta_A, \tag{2.48}$$

where R_A is the reflectivity of the analyzer and θ_A is the scattering angle, defined in Fig. 2.13. This factor accounts for the changes in analyzer response and resolution volume as a function of k_f; in the instrument setup where k_f is varied, a significant k_f-dependent correction must be accounted for.

Over a large range of k_f, the analyzer reflectivity will also become important. The variable-k_f mode is useful in measurements which require a very low background as higher-order neutrons can be filtered out of the incident beam [71]. By contrast, in the fixed-k_f scattering mode — which is more frequently used — the factor $F(k_f)$ becomes constant. That is not to say that the resolution volume is not changing; rather, as the incident beam monitor efficiency is inversely proportional to k_i, the neutron count rate normalized to the monitor counts is then directly proportional to the response function $S(\vec{Q}, E)$, from Eq. (2.47).

2.5.2 Time-of-flight spectrometer

Unlike the case of the TAS which probes a specific point in $(\vec{Q}, E)$ space, the TOF technique is capable of collecting many energy spectra simultaneously for a wide range of wavevectors by using PSD arrays. Pulsed sources are therefore ideally suited to TOF techniques, although a reactor source can be adopted to use TOF if the source beam is pulsed through the use of a series of choppers. The TOF measurements can be made in the following geometry settings. Firstly, the direct geometry spectrometer, where the incident neutron energy E_i is defined by a crystal or a chopper, and the final energy

E_f is found from TOF. Secondly, the indirect geometry spectrometer, where the sample is illuminated by a polychromatic beam and E_f is defined by a crystal or filter, where the incident energy E_i is determined by TOF. Only a direct geometry spectrometer has been used in the work presented in this thesis, and will be discussed further.

In the classical limit where the neutron wavelength is much smaller than the slits the neutron encounters along its path, neutrons can be treated as an ensemble of particles of mass m_{n} traveling with a velocity v for a time interval of t. The velocity of thermal neutrons is of order of $\mathrm{km\,s^{-1}}$; consequently, their energy can be determined by measuring their TOF over a distance of a few meters. The manner by which this is achieved is as follows.

Fig. 2.14 shows a typical TOF setup using the WISH instrument at ISIS as an example; an initial pulse of neutrons from the spallation source contains neutrons with velocities $\langle v \rangle \pm \delta v$, where $\langle v \rangle$ represents the average velocity, and the velocity distribution is denoted by δv. As the neutrons propagate, the pulse width will increase. To reduce the initial background, choppers are used to block fast neutrons produced in the instant of proton spallation, and a Fermi chopper is then placed to monochromate the incident beam further. The chopper is a rotating drum synchronized to the neutron pulse which consists of layers of highly absorbing (such as B) and transparent material (such as Al). Only a narrow range of neutrons with desired energy are allowed to pass, with the remainder of neutrons absorbed by the chopper. The energy width of the pulse is varied by adjusting the frequency of the rotation of the

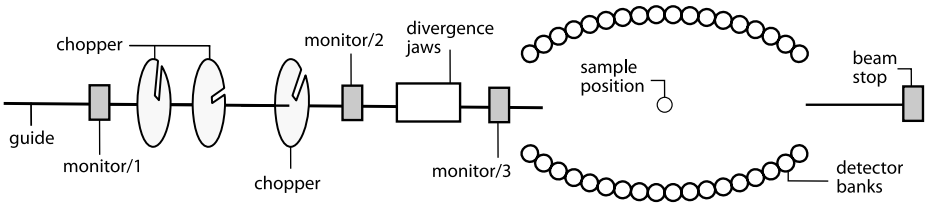

Figure 2.14: Schematic diagram of WISH diffractometer at ISIS — an example of a TOF instrument. The initial neutron beam is pulsed, and two choppers are used to select a particular incident wavevector k_i. The scattered neutrons are recorded by a large array of position sensitive detectors located some distance away from the sample. Monitors are placed before background chopper, after the Fermi chopper, and at very end of the beam after the detectors.

chopper — using a higher frequency will improve the energy resolution but reduce the beam intensity.

The monochromatic beam is then incident on the sample and will be scattered into the position sensitive detector banks. The neutron position can be determined to within about 1 cm, and the neutron arrival time is measured to a precision of around 1 ns. With the chopper–sample and sample–detector distances denoted by L_1 and L_2 respectively, and the neutron traverses this distance in a time interval of t_{12}, the final energy can be found by solving

$$t_{12} = (m_{\mathrm{n}}/n)^{1/2}(L_1/E_i^{1/2} + L_2/E_f^{1/2}), \tag{2.49}$$

and since the position of the detector is known, the scattering wavevector can be calculated. However, unlike in the triple-axis experiments, the momentum and energy transfer are coupled. Resolving the scattering wavevector parallel

and perpendicular to k_i as $(Q_\parallel, Q_\perp)$, it can be shown that

$$E = -\frac{\hbar^2}{2m_\mathrm{n}}(Q_\parallel^2 + Q_\perp^2 + 2Q_\parallel Q_\perp \cot 2\theta), \tag{2.50}$$

where 2θ is the angle between $\vec{k}_i$ and $\vec{k}_f$. Therefore, for a given $Q_\perp$, the predetermined values of E_i and E_f can be used to calculate $Q_\parallel$. The variation of $Q_\parallel$ with E does not present issues when analyzing two-dimensional systems, but when the dispersion is three-dimensional, rotation of the crystal about the axis perpendicular to the scattering plane is necessary, and software is available to reconstruct the full (Q, E) excitation spectrum, including the `Horace` suite in `Matlab`.

The resolution function given in Eq. (2.45) also holds for TOF spectrometers. However, a good approximation to the energy dependent part of the resolution can be calculated using the width of the elastic line, and in doing so, treating the wavevector and energy resolutions separately. At a fixed detector position, the uncertainty in the energy transfer can be expressed as

$$\delta E = \frac{\partial E}{\partial E_i}\,\delta E_i + \frac{\partial E}{\partial E_f}\frac{\partial E_f}{\partial E_i}\,\delta E_i. \tag{2.51}$$

In order for neutrons to arrive at the same time t_{12}, from Eq. (2.49), it is the case that E_i and E_f are coupled. Using the width of the elastic line, δE_0, we can eliminate δE_e from Eq. (2.51) to obtain

$$\delta E = \frac{\delta E_0}{1 + L_1/L_2}[1 + (L_1/L_2)(E_f/E_i)^{3/2}]. \tag{2.52}$$

The wavevector resolution is mainly dependent on the beam divergence $\delta\phi$; for an incident neutron of energy E_i, the wavevector broadening can be approximated as $\delta|\vec{Q}| \approx k_i\delta\phi$. Another advantage of TOF measurements is that the excitation spectrum can be readily converted into absolute units, which can then be compared to theoretical models. This can be achieved by comparing the data measured to a standard V/Nb calibration dataset with the same instrument parameters employed.

2.6 Bulk property measurements

In this section, we draw partly on the relevant expositionary material presented in Refs. [66, 83]. Magnetization measurements are an ubiquitous bulk probe of magnetic materials, and are employed in the work presented in Chap. 4. The magnetization $\vec{M}$ is a measure of the total magnetic moment of a sample; it is an aggregate measurement probing the overall response manifest due to the collective behavior of the constituent magnetic ions. This quantity is typically normalized by the sample volume, but sometimes also by the sample mass [84]. These measurements are useful in the characterization of the bulk magnetic response of materials as a function of temperature and applied magnetic field. Combining these measurements with the microscopic information obtained from neutron scattering measurements is often useful, as it provides a more comprehensive understanding of the material properties, thereby allowing for the identification and understanding of phase transitions.

In the case where the constituent magnetic moments are unpolarized — that is, with $\langle \vec{M} \rangle = 0$ representing a random distribution of moments — they cancel out over the sample volume on average, and result in zero net magnetization $\vec{M} = 0$. When this is the case, and in the absence of magnetizing applied fields $\vec{H}$, the material is known as a paramagnet; in the presence of applied fields, however, spontaneous symmetry breaking occurs. The continuous rotational symmetry of the $\langle \vec{M} \rangle = 0$ state is broken and a polarization direction is chosen, at random, as the spins align along a common axis; in doing so, a net $\vec{M} > 0$ is generated.

For small applied magnetic fields, the relationship between magnetization and applied field is often linear and related by a constant of proportionality. This is called the magnetic susceptibility, denoted by χ. The susceptibility facilitates a second definition of a paramagnetic material, defined by the case where $\chi > 0$. For an ideal paramagnetic material, the relationship between $\vec{M}$ and $\vec{H}$ is governed by the Brillouin function — contingent on the temperature, the number of atoms per unit volume, and their total angular momentum J — as given by [84]

$$B_J(x) = \frac{2J+1}{2J} \coth\left(\frac{2J+1}{2J}x\right) - \frac{1}{2J}\coth\left(\frac{1}{2J}x\right), \tag{2.53}$$

where x is the ratio of the Zeeman energy of the magnetic moment in the external magnetic field to the thermal energy $k_{\mathrm{B}}T$, that is $x = Jg\mu_{\mathrm{B}}B/k_{\mathrm{B}}T$. In the case of $\chi < 0$, upon application of a magnetic field $\vec{H}$, the magnetic

moments align in opposition to the applied field. This phenomenon is known as diamagnetism, and arises as a purely quantum mechanical effect that is present in all materials.

There exist a class of materials — ferromagnets — in which the application of a applied field $\vec{H}$ is not necessary to give rise to the onset and stabilization of long range magnetic order; this leads to a situation in which the system has a positive net magnetization $\vec{M} > 0$. This net magnetization can be the result of an applied field that was subsequently removed, giving rise to spontaneous co-alignment of magnetic moments in the case where the sample temperature is cooler than its Curie temperature $T < T_{\mathrm{C}}$; these materials exhibit hysteretic phenomena between $\vec{M}$ and $\vec{H}$, and it is therefore the case that the susceptibility χ is not well defined. On the other hand, long-range magnetic order can also be realized in materials for which $\vec{M} = 0$, and is known as antiferromagnetism; in this case, the magnetic moments align on two opposing sublattices, such that neighboring spins are aligned anti-parallel to one another. This phenomenon often occurs in insulators, and can occur spontaneously when the sample is cooled below its Néel temperature $T < T_{\mathrm{N}}$.

The magnetization and magnetic susceptibility can be measured using a superconducting quantum interference device (SQUID); later in the thesis, we present results using a commercial instrument — a Quantum Design MPMS3 — for which operation and data acquisition are computer-controlled. The SQUID magnetometer is highly sensitive to small magnetic fields and operates on the principle of the Josephson junction, fundamentally measuring

trapped flux quanta. The dynamic magnetic susceptibility, as measured by neutrons, can be directly related to the static susceptibility χ'_0, as measured in a SQUID magnetometer by the relation [85]

$$\chi'_0 = \lim_{\vec{Q}\to 0} \frac{1}{\pi} \int_{-\infty}^{\infty} \chi''(\vec{Q}, E) \frac{1}{E} \, \mathrm{d}E. \tag{2.54}$$

The Kramers-Kronig relation has been used in this expression to connect the real and imaginary parts of the generalized susceptibility [45], as discussed in Sec. 2.4.3. The SQUID is capable of measuring the magnetic susceptibility of samples from 400 K to a base temperature of 2 K, and static magnetic field measurements from ~ 10 G up to a maximum of 70000 G.

SQUID measurements are based principally on sensors comprising an isolation transformer and a second-derivative detector array. The sample is placed inside a set of detection loops and configured as a highly-balanced coil set, with coils made from superconducting wire. Here, pairs of coils are wound in opposite directions to give rise to a cancellation of mutually induced fields, thereby reducing noise in the detection unit; the pick-up coils, in which the current signal induced from the sample is manifest, are isolated within the SQUID loop by the transformer for a reduction in noise. This superconducting transformer features a small heating element which drives the SQUID input circuit back into the normal state, eliminating persistent currents that arise in the pick-up loops that result from changing the applied magnetic field. The application of heat drives the quenching of the magnet in a chain

reaction as it enters the normal state, with remnant fields less than 2 G. As previously mentioned, the SQUID device measures trapped flux quanta; a constant biasing current is maintained in the device such that the measured voltage oscillates with changes in the phase between two Josephson junctions which, in turn, depend on the change in the magnetic flux, thus facilitating a sensitive measurement.

The sample magnetization can be measured in its vicinity, and has the effect of inducing a net magnetic moment in the sample. This represents a sufficient condition for the magnetization to be measured since the moment induces a current in the detector coils of the SQUID, with the output voltage directly proportional to the current induced by the magnetization. Field-cooled measurements are presented in Chap. 4, and are defined by measuring from room temperature with a small measuring (excitation) field, typically of order 100 Oe, applied to the sample, which is then cooled to base temperature. Measurements are then made on increasing temperature, covering the full temperature range of the SQUID. Zero-field-cooled measurements are defined by first cooling from room temperature to base temperature with zero applied magnetic field; a small measuring field is then applied at base temperature in the SQUID, and measurements can be made again on increasing temperature. The resulting measurements of the magnetization $\vec{M}$ can then be converted to units of emu/mol.

There are several techniques which can be employed to measure the sample magnetization. One such method is the reciprocating sample option (RSO),

and another, the direct current (DC) method. In RSO measurements, the sample is subject to oscillations from the center of the main sensing coils, while in the case of the DC method, the sample itself is moved through the detector coils. In both methods, the output of the SQUID is measured as a function of the position of the sample, which is then fitted to a theoretical curve for a point-like sample geometry. The sample magnetization is then taken as the amplitude of the recorded voltage signal, with the sample typically mounted within a plastic straw. A benefit running the instrument in this configuration is that the movement of the sample through the detector coils has the effect of nullifying the background contribution that arises from the straw mount. It is generally the case that the RSO method is more sensitive than the DC method; the former is therefore preferred over the latter, especially for the measurement of small or subtle effects.

Chapter 3

Magnetic structure from single-crystal on WISH

3.1 Chapter summary

WISH is a cold neutron time-of-flight (TOF) diffractometer on the second target station (TS-2) at the ISIS Pulsed Neutron and Muon Source, UK. Noted for its excellence in neutron powder diffraction, the beamline delivers a high-flux of long-wavelength neutrons at the sample position with low intrinsic background and good resolution over a wide $\vec{Q}$-range. Well suited to the investigation of magnetostructural phenomena, the beamline excels in the measurement of subtle effects manifest in small samples, in the presence of strongly absorbing elements, and in the measurement of small magnetic moments. The beamline is modular and highly flexible, with neutronics that can be simply reconfigured programmatically to fulfill its secondary role in single-crystal diffraction. There is considerable appetite within the user base

and broader scientific community for the study of quantum and topological materials. Given that the growth of large, high-quality crystal samples is generally challenging for these types of materials, WISH is uniquely positioned to facilitate scientific insights in this area where observed signals may be weak.

In this chapter we report on a novel algorithm, `LinkedUBs` [86], created to assist in the generation of a consistent set of orientation matrices (UBs) for a set of single-crystal runs, associated with a corresponding set of goniometer configurations. It is necessary to combine runs on account of the limited $\pm 15^{\circ}$ out-of-plane coverage of the instrument. As described in Sec. 3.4, the strategy operates principally on the transfer of a reference UB between runs, and is followed by the subsequent refinement of the U matrix. This second step operates on the basis of a peak matching algorithm, and compares a set of observed reflections for a given run to those predicted from the contiguous rotation of a reference UB. By applying the algorithm to a sequence of single-crystal runs, a corresponding set of UBs can be obtained; taken together, these define a connected reciprocal space. Related by continuous rotations and preserving the directionality of the vectors expressing the reference UB, the resultant set of UB matrices obtained in this manner are self-consistent. This is a necessary condition that must be met before reflections can be integrated, collated, and subsequently used for structural refinement.

We present additionally the implementation of a method from Ref. [2] for the combination of data with different statistical weights in reciprocal space (presented Sec. 3.3.1), which thereby allows for the visualization and sym-

metrization of reciprocal space volumes. This feature is particularly useful for diffuse scattering experiments where intensity is often distributed over large volumes of reciprocal space. Using these tools, we present the results of commissioning experiments conducted on WISH for a number of well studied materials — namely, the crystal structure of the garnet $Ca_3Ga_2Ge_3O_{12}$ (presented in Sec. 3.5.1) and the commensurate antiferromagnetic magnetic structure of rutile-type MnF_2 (presented in Sec. 3.5.2). Finally, we investigate short-range magnetic correlations in the spinel $GeNi_2O_4$ (presented in Sec. 3.5.3), highlighting the versatility of the WISH beamline unlocked by the `LinkedUBs` algorithm, as applied to single-crystal diffraction.

The contributions to this chapter are as follows. Prototype goniometer and low temperature fully motorized goniometer were designed and tested by Pascal Manuel (ISIS), Fabio Orlandi (ISIS), and Dimitiry Khalyavin (ISIS) — hereafter referred to as the WISH team. Measurement strategy and analysis methodology developed by the WISH team. Novel `LinkedUBs` algorithm was designed, tested, and implemented by Lewis Edwards (Cardiff). Collection of $Ca_3Ga_2Ge_3O_{12}$ and MnF_2 datasets was carried out by Lewis Edwards (Cardiff) and WISH team (ISIS). Collection of $GeNi_2O_4$ dataset was carried out by the WISH team (ISIS). Reduction and analysis of $Ca_3Ga_2Ge_3O_{12}$, MnF_2 and, $GeNi_2O_4$ data was carried out by Lewis Edwards (Cardiff).

3.2 Introduction

Powerful and highly flexible, the WISH beamline [1] is equipped for the detailed investigation of magnetostructural phenomena under a wide array of extreme sample environment conditions[1]. The beamline facilitates the measurement of small magnetic moments down to at least $\sim 0.47\ \mu_B$ [99] — and much smaller in 1-2-10 compounds — as well as small samples down to at least ~ 20 mg [100]. While primarily optimized for powder diffraction experiments, the instrument has excellent characteristics for single-crystal diffraction, as evidenced by an impressive program of experiments already carried out[2]. The development of this secondary capability is the central focus of this chapter.

The spallation process begins with the acceleration of H^- ions to 70 MeV in a linear accelerator through high intensity radio frequency fields. The accelerated beam is then passed through 0.3 µm thick graphite foil, stripping its outer electrons, before it is directed along the 26 m radius of a synchrotron and restructured into bunches. As it circulates, the beam is focused by quadrupole magnets and is subsequently accelerated to 800 MeV before irradiating the primary target [101], which constitutes a cylindrical core of Tungsten clad in an outer layer of Tantalum[3]. The target operates at a power

[1] While magnetism experiments account for ~ 85 % of those awarded beamtime on WISH, high-impact work has been carried out in the investigation of large-unit cell systems, metal-organic frameworks [87–98].

[2] Single-crystal experiments represent ~ 20 % of those approved on the WISH beamline and correspond to ~ 40 % of allocated beamtime.

[3] While Tantalum produces ~ 10 % less neutrons by spallation than Tungsten, it is an inert and durable material; its presence prevents the accumulation of radioactive material over the course of its operation by water-damage/degradation.

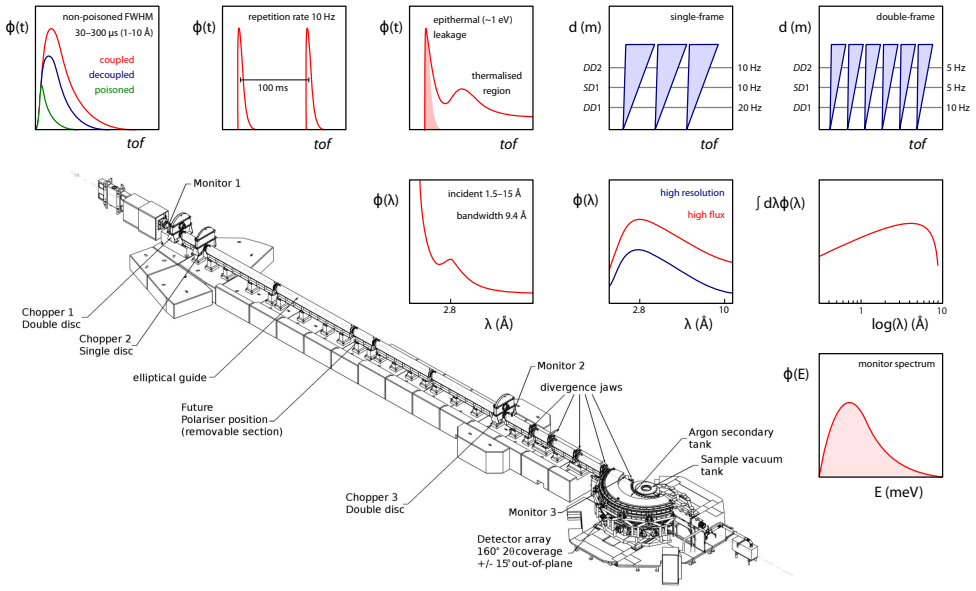

Figure 3.1: The WISH beamline on the second target station. A schematic view of the beamline is reproduced from Ref. [1]. Characteristics of the solid methane moderator are illustrated along with the repetition rate of successive pulses and the time-structure of a single-frame. The main aspects of beamline neutronics are shown, illustrating chopper phasing in single- and double-frame operation. The brilliance of the solid-methane moderator is illustrated through plots of the λ-dependent flux in high-resolution and high-flux divergence modes.

of 48 kW (corresponding to a beam current of 40 μA h^{-1}) with the beamline viewing the broad-side of a dedicated solid methane moderator. The moderator is cooled to 40 K, and is responsible for the thermalization of a highly brilliant Maxwellian distribution[4] of cold neutrons ($0-0.025$ eV) with a peak flux of 2.8 Å and a wide natural bandwidth of 8 Å. In addition to this, the

[4] A small number of high energy neutrons are inevitably thermalized in the moderator. These give rise to an epithermal tail in the neutron flux profile, as shown in Fig. 3.1.

pulse width of 10 Hz results in a high resolution at long d-spacing — an invaluable characteristic for the study of aperiodic structures and long-wavelength modulations. Over the course of operation, the moderator experiences a pressure build up from H_2 [102]. This affords a data-collection time window of $\sim 17 - 18$ hours between refilling.

The thermalized neutron beam is directed along the primary flight path ($L_1 = 40\,\mathrm{m}$) within a supermirror[5] guide, beginning 1.7 m from the source and ending 0.5 m from the sample position, with a tuneable exit opening. A schematic diagram of the beamline is shown in Fig. 3.1 from Ref. [1], and is supplemented with illustrations of the neutronic characteristics described henceforth. At the expense of increased divergence, the elliptical profile of the guide in the horizontal and vertical planes promotes an increased acceptance angle for internal reflection, and results in an increased flux transported by the guide. A continuum of reflected neutrons are transported along its length up to a critical wavevector $\vec{Q}_\mathrm{c}$, determined by the shortest bilayer period in the $m = 2$ supermirror array[6]. Noting the λ-distribution transported along the guide and the 10 Hz repetition rate of TS-2, by adjustment of their relative phases or frequencies, the selection of a wavelength bandpass can be made;

[5] Supermirror guides are made from repeating bilayers of, for instance, Ni/Ti. The bilayer spacing decreases with depth and gives rise to a variable Bragg condition, while the critical wavevector $\vec{Q}_\mathrm{c}$ transported by the guide depends on the shortest bilayer spacing. Supermirror guides are generally characterized by an m value, which describes the ratio of $\vec{Q}_\mathrm{c}$ to that of a pure Ni guide [82].

[6] WISH has Aluminum choppers measuring 1.2 m in diameter. Neutrons pass through a window on the radius of the disk while beam-blocking portions are coated in highly absorbing ^{10}B.

crucially, this also prevents the overlap of successive frames.

In single-frame operation, the counter-rotating double-disk chopper and single-disk chopper located within the first few meters of the guide are run at frequencies of 20 and 10 Hz respectively, with a second counter-rotating double-disk chopper run at 10 Hz further along the guide. In double-frame mode, the chopper frequencies are halved — the accessible $\vec{Q}$-range at each diffraction angle is doubled, giving rise to a factor-2 reduction in flux as half of the frames are discarded. Further to the modification of angular frequencies, the introduction of relative phase-shifts allows for specific wavelength frames to be selected. An oscillating radial collimator[7] (described in Ref. [103]) operating at frequencies below 5 Hz — with Gd_2O_3 painted Mylar blades separated by 0.75° — surrounds the sample environment and removes the effect of scattering from Aluminum sample environment, while a secondary argon tank removes the effect of air scattering. These features contribute to the low intrinsic background of the instrument, increasing the signal to noise ratio for the detection of weak features in the energy integrated structure factor $S(Q) \equiv \int S(Q,\omega)\,\mathrm{d}\omega$. An adjustable system of piezoelectric slits are located along the last 8 m of the guide, and allow for the control of the horizontal and vertical components of beam divergence. With the slits fully open, the full divergence is transported by the guide, whereas 0.4° and 0.2° divergence is transported for medium and high resolution configurations respectively.

[7] The oscillation of the collimator produces a uniform distribution of detector shadowing that is accounted for by normalization to V/Nb standard.

For single-crystal measurements, the slits are operated in medium-resolution mode, with choppers phased to access the full frame such that flux is maximized while good $\vec{Q}$-resolution is maintained.

The moderator produces frames with a time resolution that varies from a full-width at half-maximum (FWHM) of $\Delta t = 30\,\mu s$ at $1\,\text{Å}$ to $300\,\mu s$ at $10\,\text{Å}$. The profile function for TOF diffraction is well approximated by a Pseudo-Voigt function, including asymmetry, convolved with an impulse function comprised of back-to-back exponentials. With $G(x)$ and $L(x)$ representing Gaussian and Lorentzian functions respectively, and the constant $\eta \in [0, 1]$, the profile function is given by

$$\begin{aligned} pV(x) &= \eta G(x) + (1-\eta)L(x), \\ \Omega\,(x) &= pV(x) \otimes E(x) = \int_{-\infty}^{\infty} pV(x-t)E(t)\,\mathrm{d}t. \end{aligned} \tag{3.1}$$

The impulse function $E(x)$ is parameterized by a rising (α) and falling (β) component, with the requirement that $N = \alpha\beta/2(\alpha+\beta)$, satisfying

$$\begin{aligned} E(t) &= 2N \exp(t) \qquad t \leq 0, \\ E(t) &= 2N \exp(-t) \qquad t > 0. \end{aligned} \tag{3.2}$$

Many approximations of the neutron TOF pulse shape have been introduced. The Ikeda-Carpenter function [104], for instance, captures the steep onset of the pulse very well — much better than an impulse constructed solely from back-to-back exponentials. However, the model has a large number of pa-

rameters that require accurate characterization of moderator and neutronic characteristics, either through careful measurements or by Monte-Carlo ray-tracing simulations using programs such as `McStas` [105].

In general terms, the wavelength spread $\Delta\lambda$ can be obtained by differentiation of the Bragg equation with respect to λ and θ, followed by adding these terms in quadrature, leading to [82]

$$\left(\frac{\Delta\lambda}{\lambda}\right)^2 = \left(\frac{\Delta d}{d}\right)^2 + \left(\Delta\theta\cot\theta\right)^2. \tag{3.3}$$

From this we see that as $\theta \to 90°$, the resolution is increasingly dominated by the Δd contribution. Noting the relationship between the TOF t, and the distance traveled along the total flight path $L = L_1 + L_2$, the wavelength obtained from the Bragg condition and d-spacing can be expressed as

$$\lambda = \frac{ht}{m_{\mathrm{n}}L} \quad \text{and} \quad d = \frac{1}{2\sin\theta}\frac{ht}{m_{\mathrm{n}}L}. \tag{3.4}$$

Finally, the resolution function can be recast in terms of the TOF and total flight path as

$$\left(\frac{\Delta d}{d}\right)^2 = \left(\frac{\Delta t}{t}\right)^2 + \left(\frac{\Delta L}{L}\right)^2 + \left(\Delta\theta\cot\theta\right)^2. \tag{3.5}$$

Continuous arrays of position-sensitive ^{3}He gas detectors surround the sample position, providing access to a wide $\vec{Q}$-range via 320° of coverage in the horizontal scattering plane, as well as ±15° of coverage out-of-plane. While

the detector resolution $\Delta\theta_{\mathrm{det}}$ decreases along the length of the tube out of the horizontal scattering plane, they are well suited to our purposes since slow neutrons do not have sufficient energy to create charged particles by collision, operating on the principle

$$n + {}^{3}\mathrm{He} \rightarrow {}^{3}\mathrm{He} + p + 0.764\,\mathrm{MeV}. \tag{3.6}$$

The large number of isotropic pixels without gaps between adjacent detectors is especially important for single-crystal measurements, where continuous $\vec{Q}$-coverage is essential. The instrument has 10 detector banks which can be grouped by average scattering angle for a factor-2 enhancement of statistics in powder diffraction. The detector array comprises a total of 1520 tubes, each having 128 pixels of dimension 8 mm × 8 mm. WISH collects TOF data in each frame between 6000 and 99000 µs, with 4500 logarithmically binning time channels per pixel, with each run generating unprocessed data files of size 20 GB. Finally, we note the growing use of WISH for single-crystal studies and the associated development of its single-crystal program. This is evidenced in Refs. [106–120], with examples shown in Fig. 3.2.

3.3 Reduction of single-crystal TOF data

Over the course of a measurement, the TOF spectra of each pixel are saved to disk. This is facilitated by a system of data acquisition electronics which focuses the spectra into histogram data before writing to `*.raw` file — a bi-

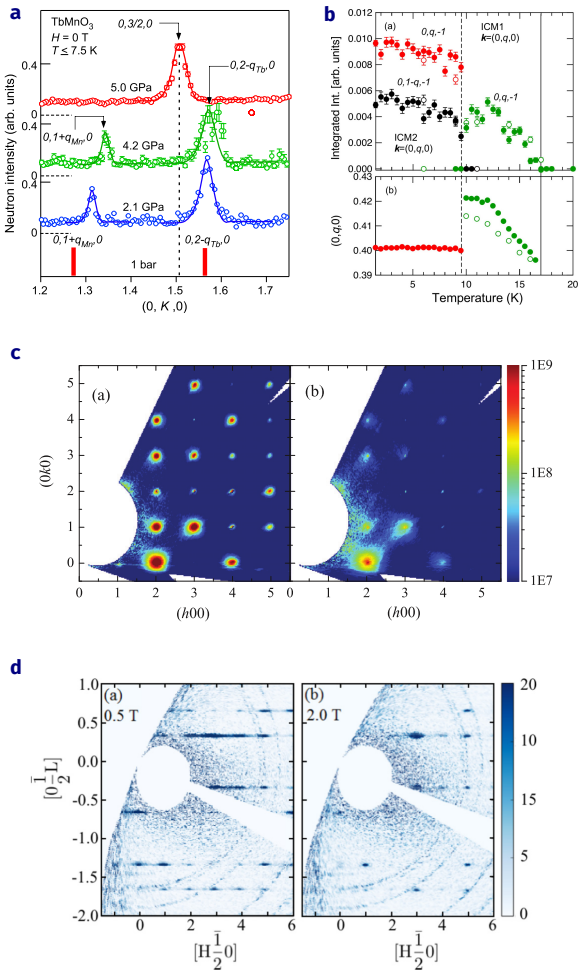

Figure 3.2: WISH single-crystal experiments under extreme conditions. A great asset to its magnetism program, the beamline boasts a dedicated 14 T superconducting magnet that can be used in combination with a dilution refrigerator insert [121]. High pressure [122] studies on WISH, with restricted geometry in α-$TbMnO_3$ (panel a) and $AgFeO_2$ (panel b) from Ref. [111] and from Ref. [116] respectively. Magnetic diffuse scattering in $SrHo_2O_4$ (panel c) and in $SrDy_2O_4$ (panel d) in applied fields from Ref. [106] and Ref. [112] respectively.

nary format that provides 4-factor compression. Relevant metadata and sample/instrument logs are saved in `*.log` format accompanying the `*.raw` detector panel and monitor data, and are indexed together by beam operation cycle and run number. The `JournalViewer` program [123] is used to search the data repository and query metadata/sample logs, while the `mantid` framework [38, 124] is used for the processing and normalization of data. This is carried out on performant virtual machines hosted on the `IDAaaS` cluster[8]. With a substantial allocation of `CPU` and `RAM`, these provide the high work capacity required to execute the intensive calculations and transformations involved in the treatment of the volumetric single-crystal data.

Once loaded into memory, the `*.raw` data is is stored in a `Workspace2D` container. This is equipped with the instrument and detector geometry and relevant beamline parameters, as specified by an underlying instrument definition file in `*.xml` format. The `Workspace2D` container is a subclass of the more general data structure, the `MatrixWorkspace`, which holds, by definition, one or more spectra in histogram format defined by an independent variable (e.g. TOF) along with the signal and its associated error. In the case where data depends on more than one independent variable, it is contained within an `MDWorkspace`; this multi-dimensional data structure has the capacity to store a dataset dependent with up to 9 independent variables. Following appropriate transformations of the `Workspace2D` — as described below in Sec. 3.3.1 — it is frequently used in the analysis of the 3D volumetric

[8]The `IDAaaS` cluster supersedes its recently retired predecessor, the `ISIScompute` cluster.

datasets generated in single-crystal experiments.

3.3.1 Vanadium normalization

With a negligible coherent scattering cross-section, the scattering response in $V_{0.95}Nb_{0.05}$ is concentrated almost entirely in the incoherent channel; accordingly, it is widely used as a standard for the normalization of single-crystal neutron diffraction data. In a scattering experiment, each pixel of the multi-bank detector array records an intensity based on the neutron count rate, and is proportional to the detector solid angle efficiency. These Niobium doped Vanadium (V/Nb) datasets intended for use as a normalization standard are usually collected at the start of each beam operation cycle in order to accurately account for the neutronic and detector characteristics relevant to forthcoming experiments, with separate datasets collected for the different modes of beamline operation. Long counting times are employed to achieve excellent statistics; where possible, samples are sanded into spheres to mitigate the effects of beam attenuation, and to facilitate straightforward absorption corrections.

Single-crystal experiments are limited most severely by the effects of restricted detector coverage, with the additional complication that different segments of the measured reciprocal space volume are distinguished by their non-uniform counting statistics; an optimal normalization procedure must take this into account and provide appropriate weightings based on the angular setting of the sample. This is accomplished with the method described

in Ref. [2], which imposes an appropriate statistical averaging of overlapping volume elements in reciprocal space. The treatment of volumetric data in this manner is especially relevant for diffuse scattering experiments where spectral weight arising from local distortions is redistributed over large regions of reciprocal space in one, two, or three $\vec{Q}$-dimensions, as demonstrated in Fig. 3.3.

The intensities measured by the arrays of position-sensitive detectors in experiments are fundamentally driven by the number of registered neutron counts; consequently, the associated errors are independent and identically distributed and — in the limiting case — are described by a Poisson distribution. Following the derivation in presented in Ref. [2], recall the definition of the differential cross-section $\mathrm{d}\sigma/\mathrm{d}\Omega = \sum_i N_i/[\sum_i(\Phi_i \mathrm{d}\Omega_i)]$. Spectral weight is distributed isotropically throughout reciprocal space for the V/Nb standard, with a spherically symmetric signal measured on the detector banks. The summation over all detectors and configurations that contribute to the scattering in reciprocal space volume element $\mathrm{d}\vec{Q}$ is given by the quantity $\mathrm{d}\sigma/\mathrm{d}\Omega = \sigma_\mathrm{I}/4\pi$, where σ_I is the incoherent scattering cross-section.

With V_i being the counts recorded from the diffraction of the V/Nb sample, and assuming the sample is measured under identical conditions — namely, with orientation and flux at the same 2θ-position where the instrument flux profile is identical — then $\sum_i \Phi_i \mathrm{d}\Omega_i = \sum_i V_i \cdot (\sigma_i/4\pi)^{-1}$. The calculation of the sum yields the quantity $\mathrm{d}\sigma/\mathrm{d}\Omega = (\sigma_I/4\pi)\sum_i N_i/[\sum_i V_i]$, where it is understood that the values N_i and V_i are to be corrected for sample and

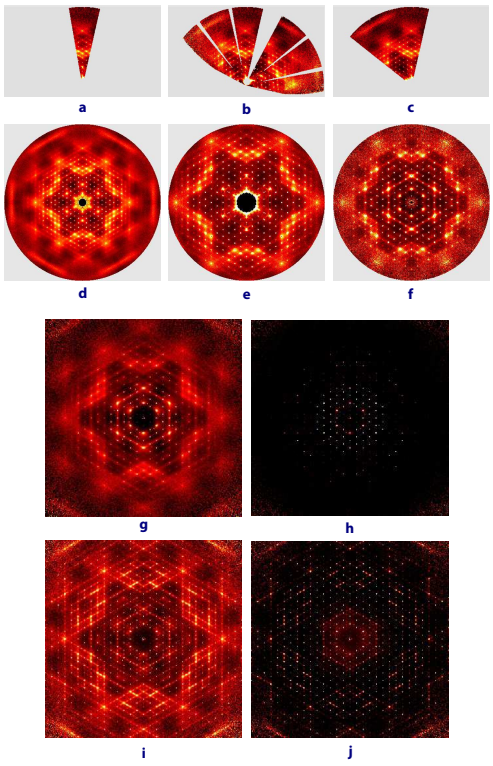

Figure 3.3: Diffuse scattering in Benzil. The $(h, k, 0)$ zone is shown for measurements from the SXD single-crystal instrument (TS-1, ISIS) [125] in (a-f). (a) shows the results from 1 crystal orientation and a single detector bank (No. 1), while (b) shows the results from using one crystal orientation and all six equatorial detector banks (Nos. 3, 2, 1, 6, 5, 4). In (c) the results from using three different crystal orientations with a single detector bank (No. 1) are presented, while in (d) the results obtained using three crystal orientations and four detector banks (Nos. 1, 2, 5, 6) with $3m$ symmetry applied. (e) and (f) show the data at lower values of Q; specifically in (e) data is shown using detector bank 1 with three different crystal orientations and finally, (f) shows the data using detector bank 3 with three different crystal orientations. The $(h, k, 0)$ zone is also shown as measured from the Corelli instrument (SNS, ORNL) [126, 127] in (g-j), which has elastic discrimination from its cross-correlation chopper system. The same color scheme is used as for the SXD data for the purposes of comparison. (g) presents the total scattering (elastic plus inelastic) at 300 K, while (h) presents the elastic scattering only at 300 K. In (i), the total scattering (elastic plus inelastic) is shown at 100 K, while in (j) the elastic scattering only is shown at 100 K. Adapted from Ref. [128].

Vanadium absorption. Next, we perform an average weighted by the number of counts of incoherent scatter in the same region of reciprocal space $w_i = V_i$,

$$\frac{\mathrm{d}\sigma}{\mathrm{d}\Omega} = \frac{\sigma_I}{4\pi}\frac{\sum_i V_i N_i/V_i}{\sum_i V_i} = \frac{\sigma_I}{4\pi}\frac{\sum_i w_i N_i/V_i}{\sum_i w_i}. \tag{3.7}$$

Departing from the usual convention of adding up intensity around a peak — as is done for the calculation of integrated intensities of ungrouped runs for structural refinement — the number of scattered neutrons from a particular Bragg peak can be represented by the integral over the solid angle of the detector multiplied by the integrated flux,

$$I_c = \int N(\lambda)\mathrm{d}\Omega_f \frac{\mathrm{d}\sigma_c}{\mathrm{d}\Omega}\,\mathrm{d}\lambda. \tag{3.8}$$

After a change of coordinate system, it can be shown that

$$I_c = \frac{V N(\lambda)\lambda^4 |F(\vec{G})|^2}{2v_c^2 \sin^2(\theta)}, \tag{3.9}$$

where the sample volume is given by $V = Nv_c$. The structure factor is therefore related to the integrated intensity by $|F(\vec{G})|^2 \propto I_c \sin^2(\theta/2)/N(\lambda)\lambda^4$, which is composed of the product of the spectrum correction and Lorentz correction (described in Sec. 3.3.3); by similar means, for the incoherent scatterer, it can be found that the flux and Lorentz terms are identical, leading to $|F(\vec{G})|^2 = cI_c/I_i$, where c is a λ and detector-independent constant.

3.3.2 Peak detection and orientation matrix

In single-crystal experiments, the orientation matrix defines a transformation from the instrument frame to the reciprocal lattice of the diffracting sample, derived by Busing and Levy in 1967 [129]. Writing both these vector spaces in an orthogonal basis with common handedness means the mapping between them is a rotation in SO(3). The B matrix orthogonalizes the contravariant reciprocal basis, while the U matrix provides a mapping onto the instrument frame; the product of these quantities is the UB matrix [129, 130]. In the context of the `mantid` framework, the UB matrix can be attached to a `Workspace2D` in the instrument frame, allowing for the transformation to an `MDWorkspace` in the reciprocal lattice frame.

A suitable right-handed basis can be constructed from the following projections of the reciprocal lattice vector $\vec{Q}_{hkl}/2\pi = h\vec{a}^* + k\vec{b}^* + l\vec{c}^*$. In this thesis, the crystallography convention is assumed, where factors of 2π do not appear in the definition of $\vec{Q}_{hkl}$. Following the derivation set out in the `mantid` documentation [38], we first choose $\vec{e}_1$ to lie along the component of $\vec{Q}_{hkl} \parallel \vec{a}^*$, then require $\vec{e}_2$ to lie along the component of $\vec{Q}_{hkl} \perp \vec{a}^*$ in the $(\vec{a}^*\vec{b}^*)$ plane; with $\vec{e}_3$ along the direction of $\vec{e}_1 \times \vec{e}_2$, the resulting basis set is orthogonal. The matrix representation of this basis transformation has upper triangular

form and defines the B matrix, given by

$$\mathsf{B} = \begin{pmatrix} a^* & b^* \cos\gamma^* & c^* \cos\beta^* \\ 0 & b^* \sin\gamma^* & -c^* \sin\beta^* \cos\alpha \\ 0 & 0 & 1/c \end{pmatrix}. \tag{3.10}$$

This quantity is related to the reciprocal metric tensor[9] $\mathsf{G}^* = \mathsf{B}^{\mathrm{T}}\mathsf{B} = \mathsf{G}$ which facilitates the straightforward calculation of the inner product for two vectors $\vec{p}, \vec{q}$ in the reciprocal lattice basis via $\langle \vec{p}, \vec{q} \rangle = \sum_{ij} p_i \mathsf{G}^* q_j$. It is conventional in `mantid` to define the instrument frame with $\hat{y}$ vertical, $\hat{z} \parallel$ beam direction and with a horizontal $\hat{x} \perp (yz)$ plane, with the incident wavevector $\vec{k}_i$ along the incoming beam direction. The instrument geometry is shown in Fig. 3.4, with θ the angle between incident and final wavevector, and ϕ' the inclination of the final wavevector out of the horizontal scattering plane. The second axis $\vec{u}_\phi(\omega, \chi)$ is oriented at an angle χ to $\vec{u}_\phi(\omega)$ — its definition is therefore dependent upon the angle ω.

Designed and tested by the WISH team, the prototype single-crystal goniometer, suitable for high-temperature measurements, features a manual ω axis and motorized ϕ axis inclined at $\chi = 54°$. By contrast, the new fully motorized goniometer developed by the WISH team used in this work has the ϕ-axis inclined at an angle of $\chi = 45°$, and is compatible with

[9] Calculations involving the metric tensor are implemented in `mantid` as methods of the `mantid.geometry.UnitCell` class. For instance, after importing the `UnitCell` class from `mantid.geometry` the d-spacing of a given reflection can be calculated by `UnitCell.d(h,k,l)`. Furthermore, the two reflections can be calculated using another method of the class by `UnitCell.recAngle(`$\mathtt{h}_1$`,` $\mathtt{k}_1$`,` $\mathtt{l}_1$`,` $\mathtt{h}_2$`,` $\mathtt{k}_2$`,` $\mathtt{l}_2$`)`.

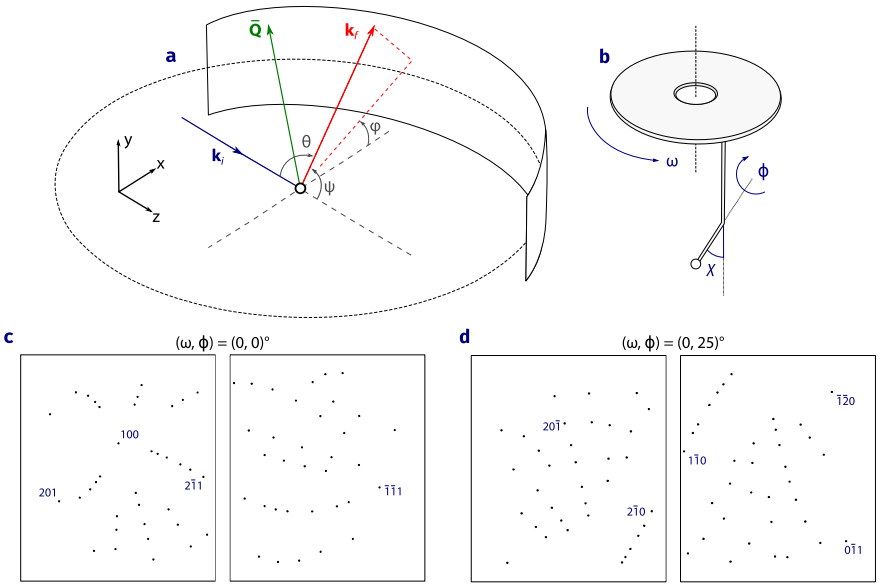

Figure 3.4: Instrument frame geometry on WISH. (a) shows half of the detector banks on WISH, covering 160° of the horizontal scattering plane and ±15° out of the plane. The incident wavevector is parallel to the $\hat{z}$-axis of right handed Cartesian basis, with the $\hat{y}$-axis vertical and the $\hat{x}$-axis in the horizontal plane. (b) illustrates the rotation axes of the WISH single-crystal goniometer. In the same Cartesian system discussed previously, the in-plane angle ω has axis $\parallel$ to the $\hat{y}$-axis. The ϕ-axis is inclined at an angle χ from the vertical direction and is given by $\vec{u}' = \vec{u}(0, \chi) = [0, \sin\chi, -\cos\chi]^{\mathrm{T}}$. The Laue projection (along the $\hat{y}$-axis) for all detector banks is shown for two goniometer configurations in panels (c-d).

the cryostats used on WISH — a top-loading cryostat for low temperature measurements[10] between 1.25 and 300 K described in Refs. [131, 132]. The prototype goniometer enabled rough measurements at room temperature to be taken in the development of the data collection methodology, but suffered from systematic corrections due to the hand-turned, non-motorized ϕ-axis. The new fully motorized goniometer, however, enables data collection at lower temperatures and without considerable systematic error in the goniometer settings. We define a general rotation of the sample about the $\vec{u}(\omega, \phi, \chi)$ axis in which the vector describing the $\vec{u}_\phi(\omega, \chi)$ rotation axis is defined by convention at $\omega = 0°$. We express this as the vector $\vec{u}' = \vec{u}(0, \chi) = [0, \sin\chi, -\cos\chi]^{\mathrm{T}}$; for varying ω, the recalculation of the axis is achieved by premultiplication of the axis defined at $\omega = 0°$ by the $\mathsf{R}(\omega)$ matrix. This definition of goniometer axes is compatible with the `SetGoniometer` algorithm in `mantid`, which reads the angles ω and ϕ — whose attribute names are `ccrPos` and `ewaldPos` respectively — as entries of the sample log metadata for the given run. Rotations about the $\vec{u}_\phi(\omega, \chi)$ axis by an angle ϕ are given by $\vec{u}(\omega, \chi) = \mathsf{R}_\omega(\omega)\ \vec{u}' = \mathsf{R}_\omega(\omega)[0, \sin\chi, -\cos\chi]^{\mathrm{T}}$. For brevity, we define $\sin'\psi = (1 - \sin\psi)$ and $\cos'\psi = (1 - \cos\psi)$; the most general rotation around a direction $\vec{v} = (v_x, v_y, v_z)$ with $v_x^2 + v_y^2 + v_z^2 = 1$ by angle ψ is the

[10] With its high cooling power ~ 0.23 W at 1.9 K, a dilution refrigerator insert can be used in the continuous regime of the cryostat facilitating measurements down to 0.5 K. We note that this is not currently compatible with the motorized goniometer design for single-crystal measurements at variable angular configurations. The width of the device is around 100 mm so the sample stays in the center of the instrument, and there is a large thermal leak from the goniometer at cold temperatures o the motor.

matrix

$$\mathsf{R}(\psi) = \begin{pmatrix} \cos\psi + v_x^2 \cos'\psi & v_x u_y \cos'\psi - v_z \sin'\psi & v_x v_z \cos'\psi + v_y \sin\psi \\ v_y v_x \cos'\psi + v_z \sin\psi & \cos\psi + v_y^2 \cos'\psi & v_y v_z \cos'\psi - v_x \sin\psi \\ v_z v_x \cos'\psi - v_y \sin\psi & v_z v_y \cos'\psi + v_x \sin\psi & \cos\psi + v_z^2 \cos'\psi \end{pmatrix} \tag{3.11}$$

satisfying $\mathsf{R}^{-1}(\psi) = \mathsf{R}(-\psi) = \mathsf{R}^{\mathrm{T}}(\psi)$. This R is a member of the rotation group. It provides an affine transformation between orthonormal bases $\in \mathbb{R}^3$ and satisfies the relation $\mathsf{R}\mathsf{R}^{\mathrm{T}} = \mathsf{R}^{\mathrm{T}}\mathsf{R} = \mathsf{I}$. This rotation matrix belongs to the special orthogonal group SO(3), a subgroup of the orthogonal matrices for which $\det \mathsf{R}^{\mathrm{T}} = \det \mathsf{R}$, and consequently, $(\det \mathsf{R})^2 = \pm 1$. For an n-axis goniometer with corresponding rotation matrices $\mathsf{R}_1, \mathsf{R}_2, \ldots, \mathsf{R}_n \in \mathrm{SO}(3)$, by writing $\mathsf{R} = \prod_i^n \mathsf{R}_i$, the momentum transfer in the instrument frame $\vec{Q}_{\mathrm{lab}} = \Delta\vec{p}/\hbar = (\vec{k}_i - \vec{k}_f)$ can be related to the momentum transfer $\vec{Q}_{hkl}/2\pi$ in the reciprocal basis as follows,

$$\vec{Q}_{\mathrm{lab}} = \begin{pmatrix} -k_f \sin\theta \ \cos\phi' \\ -k_f \sin\theta \ \sin\phi' \\ k_i - k_f \cos\theta \end{pmatrix} = 2\pi \mathsf{R}\mathsf{U}\mathsf{B}\vec{Q}_{hkl}, \tag{3.12}$$

where the angle θ is between $\vec{k}_i$ and $\hat{z}$, and $\phi' = \pi - \phi$ is the angle between the $\hat{x}$ axis and the projection of $\vec{k}_f$ in the (xy) plane (shown as the angle $\phi = \pi - \phi'$ between $-\hat{x}$ and $\vec{k}_f$ in Fig. 3.4). This definition of $\vec{Q}_{\mathrm{lab}}$ ensures

that the neutron energy loss is a positive quantity,

$$\Delta E = \frac{\hbar^2}{2m}(k_i^2 - k_f^2) = \hbar\omega > 0 \tag{3.13}$$

identified with the wavevector transferred to the sample, so is widely used by convention in inelastic scattering. By writing $\vec{Q} = [h, k, l]^{\mathrm{T}}$, we can express the momentum transfer in a Cartesian frame associated with the reciprocal lattice of the sample via $\vec{Q}_c = 2\pi \mathsf{B}\vec{Q}$.

The U matrix is a simple rotation matrix which maps $\vec{Q}_c$ onto the axes of the Cartesian lab frame, thus yielding the momentum transfer in the lab frame $\vec{Q}_l$. The rotations of the goniometer axes are encoded in the product of rotation matrices $\mathsf{R} = \mathsf{R}_\omega(\omega) \cdot \mathsf{R}_\phi(\phi)$; finally, for a general goniometer setting, the relation between lab and reciprocal lattice frame can be written as $\vec{Q}_l = 2\pi \mathsf{RUB}\vec{Q}$. The samples studied on WISH are typically well characterized, with known lattice parameters, Laue symmetry, and space group. As such, the B matrix is typically known to a first approximation in advance of the experiment, and it is therefore usually possible to identify some reflections based on attributes such their as d-spacing and the angles between them. After the deduction of the indices of three non-coplanar reflections by their d-spacing, the U matrix can be calculated; further refinement[11] of the B matrix

[11] We report on a recent algorithm incorporated in `mantid`, namely `FindGlobalBMatrix`, to refine the B matrix over a set of runs with distinct U matrices while preserving indexation.

is, however, preferable. By first expressing these reflections in the form

$$\begin{aligned} \vec{Q}_1 &= 2\pi \mathsf{R}(\omega_1)\, \mathsf{UB}\vec{v}_1 \\ \vec{Q}_2 &= 2\pi \mathsf{R}(\omega_2)\, \mathsf{UB}\vec{v}_2, \end{aligned} \tag{3.14}$$

the rotation matrix that describes the rotation between $\vec{Q}$-vectors is the U matrix, which facilitates the rotation of $\mathsf{B}\vec{v}_1$ and $\mathsf{B}\vec{v}_2$ onto $\mathsf{R}^{-1}(\omega_1)\,\vec{Q}_1/2\pi$ and $\mathsf{R}^{-1}(\omega_2)\,\vec{Q}_2/2\pi$ respectively.

Due to errors in the angular settings of the goniometer or in the calculated B matrix, it is often not possible to find a matrix that simultaneously satisfies these two equations. This can be overcome by constructing two orthogonal coordinate systems related to one another by the U matrix, in which the unit vectors are defined by $\hat{t}_{1\mathrm{c}} = \mathsf{B}\vec{v}_1/\left|\mathsf{B}\vec{v}_2\right|$, $\hat{t}_{3\mathrm{c}} = (\mathsf{B}\vec{v}_1) \times (\mathsf{B}\vec{v}_2) \,/\, \left|(\mathsf{B}\vec{v}_1) \times (\mathsf{B}\vec{v}_2)\right|$, and $\hat{t}_{2\mathrm{c}} = \hat{t}_{3c} \times \hat{t}_{1\mathrm{c}}$. A set of three orthogonal unit vectors can subsequently be obtained from the vectors $\mathsf{R}^{-1}(\omega_1)\,\vec{Q}_1/2\pi$ and $\mathsf{R}^{-1}(\omega_2)\,\vec{Q}_2/2\pi$ — labeled $\hat{t}_{1\nu}$, $\hat{t}_{2\nu}$, and $\hat{t}_{3\nu}$ — where the subscript ν indicates that the system is tied to the inner axis of the goniometer. Noting that the relationships $\hat{t}_{1\nu} = \mathsf{U}\hat{t}_{1\mathrm{c}}$, $\hat{t}_{2\nu} = \mathsf{U}\hat{t}_{2\mathrm{c}}$, and $\hat{t}_{3\nu} = \mathsf{U}\hat{t}_{3\mathrm{c}}$ hold true, they can be recast in terms of the matrices T_ν with columns $\hat{t}_{1\nu}$, $\hat{t}_{2\nu}$, and $\hat{t}_{3\nu}$, and T_c with columns $\hat{t}_{1\mathrm{c}}$, $\hat{t}_{2\mathrm{c}}$, and $\hat{t}_{3\mathrm{c}}$. When expressed in this form, it follows that $\mathsf{T}_\nu = \mathsf{U}\mathsf{T}_\mathrm{c}$ which immediately yields

$$\mathsf{U} = \mathsf{T}_\nu \mathsf{T}_c^{-1} = \mathsf{T}_\nu \mathsf{T}_\mathrm{c}^{\mathrm{T}}. \tag{3.15}$$

3.3.3 Intensity corrections and peak integration

After the positions and indices of the Bragg peaks have been characterized by the UB matrix, what remains is to determine their intensity in a process called integration, summarized by

$$\begin{aligned} I &= \Sigma N_{\text{model}} \\ \sigma^2 &= N\Sigma_{\text{obs}} + N\Sigma_{\text{bg}} + \frac{\Sigma N_{\text{obs}}(N_{\text{obs}} - N_{\text{model}})^2}{\Sigma N_{\text{obs}}}. \end{aligned} \tag{3.16}$$

Bragg reflections are complex 3D profiles of intensity, and can be integrated in detector space or in reciprocal space; there exist a number of standard algorithms in `mantid` to make these computations. For the structures presented in this work, spherical integration in $\vec{Q}$ is sufficient, but we note that in the case of modulated structures with low symmetry, the reciprocal space can be very dense and present challenges with peak overlap. This is, however, beyond the scope of the discussion at hand. Integration can be carried out upon either a `FindSXPeaks` workspace or instead upon a `PredictPeaks` workspace. The latter case affords the inclusion of peaks missed by imperfect peak finding routines; it is also most useful, as with an accurate UB matrix, weak reflections can be conveniently located according to their predicted position and subsequently integrated. A comparison of integration schemes in `mantid` is described in more detail in Refs. [133, 134].

In order to refine single-crystal data, we must consider corrections of the measured intensity using the results of the dynamical theory of diffraction,

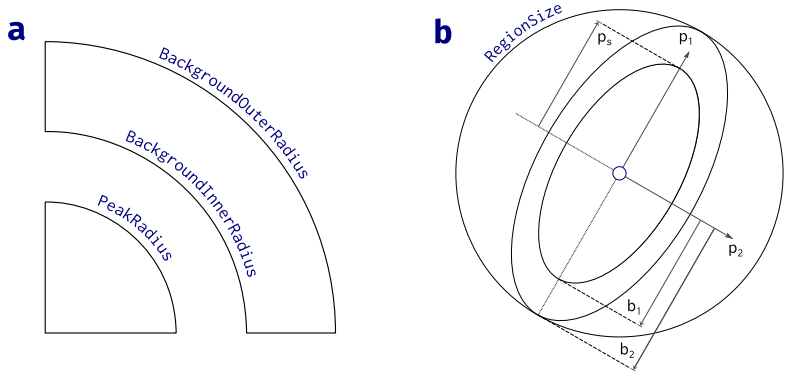

Figure 3.5: (a) spherical integration conventions in `mantid`, showing a section of the cross-section through spherical regions centered on an observed Bragg reflection. Shown are the radius of integration and the definition of the shell used to estimate background under peak which is subsequently subtracted from the integrated intensity. The inner and outer radii of the shell are shown as `BackgroundOuterRadius` and `BackgroundInnerRadius` respectively. (b) elliptical integration conventions in `mantid`, within a sphere of radius `RegionSize`. The principal ellipsoid axes are denoted by variables $\mathtt{p_1}$ and $\mathtt{p_2}$ respectively. The peak size is denoted $\mathtt{p_s}$. The `BackgroundOuterSize` and `BackgroundInnerSize` denoting the elliptical shell used to estimate background under the peak are denoted $\mathtt{b_1}$ and $\mathtt{b_2}$, respectively. Figure made with reference to `mantid` documentation [38].

where the neutron optical phenomena manifest due to interactions between the incident and scattered beam are taken into account. This approach goes beyond the Born approximation, where the scattering amplitude is given simply by the Fourier transform of the scattering potential. The kinematical theory is generally valid only for small sample volumes or weak scattering; the more general dynamical theory that takes account of multiple scattering and beam attenuation is required for the interpretation of Bragg intensities

observed in single-crystal diffraction experiments.

The Lorentz correction considers the wavelength dependent TOF flux profile, and takes the amount of a time a given reflection remains in the diffraction condition into account [135–137]. Owing to resolution effects, the surface of the Ewald sphere in fact has some thickness; effects such as the non-zero wavelength spread, divergence of the incident beam, and the mosaicity of the sample — as shown in Fig. 3.6 — all contribute to this [82]. As the crystal orientation is varied across a set of runs, some reflections intercept the surface of the Ewald sphere at more or less oblique angles. This results in unequal measuring times for such reflections, and is a systematic source of intensity error. This procedure is important for the combination of data at different crystal spatial orientations, and is briefly outlined in Ref. [2]. The number of neutrons scattered from a particular Bragg peak is

$$I_c = \int \mathrm{d}\lambda N(\lambda) \mathrm{d}\Omega_f \frac{\mathrm{d}\sigma_c}{\mathrm{d}\Omega}, \tag{3.17}$$

while the Jacobian of the transformation from $\vec{Q}$ to spherical coordinates of $\vec{k}_f$ is the quantity $\mathcal{J} = k^2 \sin\theta[-2\sin^2(\theta/2)]$. As noted in Ref. [2], this allows computation of the volume element in $\vec{Q}$ as the quantity

$$\mathrm{d}\vec{Q} = [-2\sin^2(\theta/2)]k^2 \,\mathrm{d}k\, \sin\theta \,\mathrm{d}\theta \,\mathrm{d}\phi,$$

with the last three terms on the right-hand side representing the solid angle

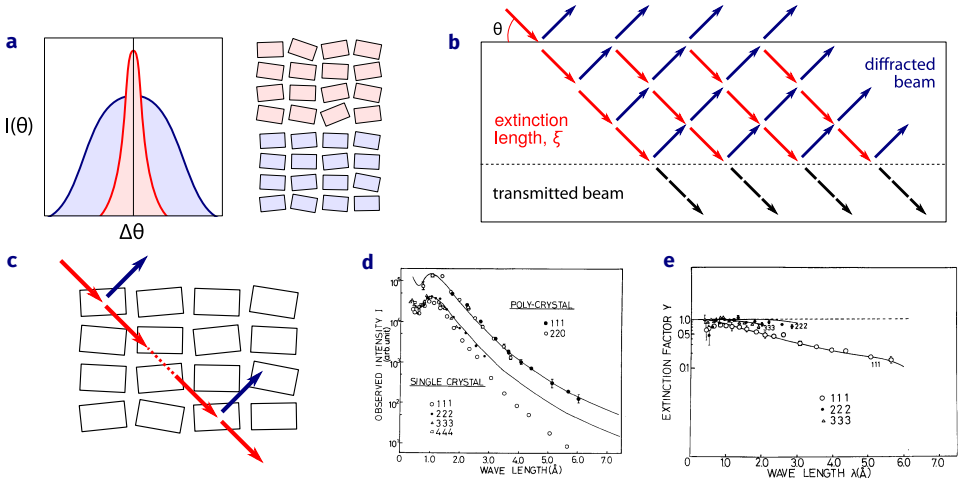

Figure 3.6: (a) Crystal mosaicity and rocking curve profiles as a function of the Bragg angle, with reference to Fig. 1 of Ref [138]. (b) Primary and (c) secondary extinction effects, with reference to Fig. 4.1 of Ref. [139] and Fig. 6 of Ref. [140] respectively. The extinction effect for TOF diffraction is illustrated in (d) and (e), reproduced from Ref. [141].

of scattering $\mathrm{d}\Omega_f$. This yields the Bragg intensity as

$$I_c = VN(\lambda)\frac{\lambda^4|F(\vec{\tau})|^2}{2v_c^2\sin^2(\theta/2)}, \tag{3.18}$$

where the sample volume is given by $V = Nv_c$. As discussed in Ref. [2], the structure factor is then related to the integrated intensity through the relation

$$|F(\vec{\tau})|^2 \propto I_c\frac{1}{N(\lambda)}\frac{\sin^2(\theta/2)}{\lambda^4}, \tag{3.19}$$

which describes a spectrum correction (contained within the first term) and the Lorentz correction (contained within the second term).

The mosaic model was proposed in 1922 by Darwin [142] and, as described in Ref. [82], views the crystal as an array of perfect domains that have some mutual misalignment making up the crystal volume as we see it, with the boundaries between these domains not taken into account. The degree of domain structure can be accessed through the rocking curve, in which the angular distribution of intensity around a Bragg position is measured. The individual blocks are themselves perfect and are slightly misorientated with respect to each other. These blocks are small enough that the integrated intensities of their reflections are proportional to their volume Δv, such that $\rho = Q\Delta v$, where $Q = N^2\lambda^3(e^2/mc^2)^2|F|^2(1+\cos^2 2\theta)/(2\sin 2\theta)$. The dynamical theory always predicts Bragg intensities that are lower than those obtained from the kinematical theory. A major contribution is the extinction effect, illustrated in Fig. 3.6, which is most severe for large samples.

The extinction length ξ is related to the Pendellösung period, and defines the volume element of an infinite crystal (namely, within the extinction length) that contributes to the diffraction. Following Ref. [82], primary extinction concerns the coherent multiple scattering (also known as the Renninger effect) within a single mosaic block, which occurs when two or more sets of crystal planes satisfy the Bragg condition for a given incident wavevector. Meanwhile, secondary extinction occurs when the diffracted beam from one mosaic block is rescattered by other mosaic blocks [82]. Primary extinction is only appreciable if the individual mosaic blocks are larger than the

extinction length. The extinction effect is illustrated in Fig. 3.6.

$$\xi = \frac{\pi v_0 \cos\theta}{\lambda |F_{\mathrm{N}}(\vec{G})|}, \tag{3.20}$$

which is one period of the Pendellösung interference pattern.

Following Ref. [143] (and Refs. therein), the model for extinction [144, 145] considers the integrated intensity P_k of the Bragg reflection according to the kinematical theory that can be approximated from the intensity of the incident beam I_0 and the irradiated volume v. The integrated intensity is given by $P_k = I_0 v Q$, where Q is the average scattering cross-section per unit volume $Q = |aFK/V|^2 \lambda^3 / \sin 2\theta$ with F the structure factor, K the polarization factor (1 for neutron or synchrotron radiation), V the unit cell volume, θ the Bragg angle, and λ the wavelength of the radiation. The constant factor is given by $a = 10^{-12}$ m for neutrons. The influence of secondary extinction can be expressed by a factor y, through $P = P_k \cdot y$. The mosaicity, or angular distribution of domains, W is approximated by either Gaussian or Lorentzian profiles with width g,

$$\begin{aligned} W_G(\epsilon) &= \sqrt{2} g \exp\left(-2\pi^2 g^2 \epsilon^2\right) \\ W_L(\epsilon) &= 2g/(1 + 4\pi^2 \epsilon^2 g^2). \end{aligned} \tag{3.21}$$

For secondary extinction, the correction for y can be approximated by [145]

$$y(x,\theta) = \left[1 + \xi_{G,L} x + \frac{A(\theta) x^2}{1 + B(\theta) x}\right]^{-1/2} \qquad x = \frac{2}{3} Q \alpha_{G,L} \bar{t} \tag{3.22}$$

$$\begin{aligned} \alpha_G &= \overline{\alpha}/(1+\overline{\alpha}^2/2g^2)^{1/2} \qquad \xi_G = 2.12 \\ \alpha_L &= \overline{\alpha}/(1+2\overline{\alpha}/3g)^{1/2} \qquad \xi_L = 2. \end{aligned} \tag{3.23}$$

The parameter $\overline{\alpha} = (3r/2\lambda)\sin 2\theta = (3\rho/2)\sin 2\theta$, where r is the particle size. The primary and secondary extinction coexist and are assumed to be independent, in which case $y = y_{\rm p}y_{\rm s}$, where $y_{\rm s}$ and $y_{\rm p}$ are the coefficients for primary and secondary extinction respectively. In the case of a spherical crystal containing idealized spherical crystal blocks, both can be approximated (see for instance Ref. [82]).

Following Ref. [82], the absorption-weighted mean path through the crystal $\overline{T}$ is given by the expression

$$\overline{T} = \frac{1}{AV}\int_V (L_i + L_f)\exp[-\mu(L_i + L_f)]{\rm d}V. \tag{3.24}$$

The Beer-Lambert law is given by

$$I = I_0\,\exp(-\mu x), \tag{3.25}$$

where the quantity μ is the linear absorption coefficient. Sample transmission is a measure of the variation of path length of the diffracted beam. If the crystal is not spherical, then reflections will have a distribution of flight paths. This leads to the systematic reduction of intensity for some peaks, where the

transmission factor is

$$\mathcal{T} = \frac{1}{V} \int \mathrm{d}\tau \, \exp(\mu L(\vec{r})). \tag{3.26}$$

The Beer-Lambert law describes transmission of neutrons through a sample of uniform thickness; the transmission is defined as the factor by which the count rate is attenuated,

$$A = I(t)/I_0 = \exp(-\mu t), \tag{3.27}$$

where I_0 is the incident intensity, $I(t)$ is the intensity for thickness t, and μ is the linear attenuation coefficient that is assumed to be independent of position such that the sample is homogeneous, as described in Ref. [82]. Attenuation is caused by coherent and incoherent scattering, as well as absorption. One may write $\mu = n(\sigma_\mathrm{s} + \sigma_\mathrm{a})$, where n is the number density of some grouping of atoms such as a formula unit or unit cell, and σ_s and σ_a are the total scattering and absorption cross-sections respectively for the grouping considered.

As described in Ref. [82], the absorption varies as the inverse of neutron speed increases linearly with more time spent in the sample, but there exist resonant excitation energies of the nucleus such that the neutron can be easily captured being close to bound state. With the exception of B, Cd, and, Gd, which have large cross-sections and are used for shielding or to poison moderators, these do not typically coincide with thermal neutron ve-

locities. Proper absorption corrections require knowledge of the average path through the sample, and are usually done for idealized crystal shapes with Monte Carlo simulations. The data refinement software used in this work is `Jana2006` [143] due to its superior treatment of extinction. Integration in `mantid` [133, 134] allows the intensities of the Bragg reflections to be determined. This information is critical for structural refinement, allowing the unit cell composition to be deduced through various methods including Rietveld refinement and charge flipping.

3.4 Linked orientation matrices

The first crucial step towards structural refinement is the accurate prediction of peaks at each goniometer configuration — a series of spatial configurations of the sample in space at goniometer angles (χ, ω, ϕ), as defined in Fig. 3.4. In order to obtain sufficient coverage of reciprocal space, enabling high quality structural refinement, the diffracting crystal must be measured at a number of orientations in the laboratory frame. In general terms, the crystal potential $\rho(\vec{r})$ and its Fourier transform $g(\vec{q})$ are invariant under the symmetry element $h = \{R|\tau\} \in \mathbb{G}$, and transform according to the relations

$$\begin{aligned} \rho(\vec{r}) &= \rho(R\vec{r} + t), \\ g(\vec{q}) &= g(\vec{q}) \exp(2\pi i R\vec{q} \cdot \tau). \end{aligned} \tag{3.28}$$

The interaction of the beam with the crystal is mediated by the potential $V(\vec{r})$, and measurements of the momentum transfer in a diffraction experiment are proportional to the matrix element

$$\left\langle \vec{k}_f \middle| V(\vec{r}) \middle| \vec{k}_i \right\rangle \sim \int \rho(\vec{r}) \exp\left(2\pi i \vec{k} \cdot \vec{r}\right) \mathrm{d}\vec{r} = g(\vec{q}). \tag{3.29}$$

This expression makes clear the Fourier transformation implicit in the scattering process. In the case of missing segments of data, distortions of the reciprocal space volume are manifest in the perpendicular direction; as such, it is crucial that coverage corresponding to at least the asymmetric unit of the space group is collected in a diffraction experiment if these data are to be used for structural refinement.

Methods of UB matrix determination discussed in Sec. 3.3.2 are implemented in `mantid` and exposed to the `Python API` in a number of methods. By deducing and manually setting the indexation (h, k, l) of two Bragg peaks added to a `PeaksWorkspace` by hand, one can calculate a reasonably accurate UB using `CalculateUMatrix`. From this UB, the positions of all peaks on the detectors can be predicted, and one can add more peaks by hand, setting their indices in an iterative procedure of refinement, obtaining a more accurate UB at each step. On the other hand, in the determination of an initial UB one of the auto-indexing methods (including `FindUBUsingLatticeParameters` or `FindUBUsingFFT`) may be used on a `PeaksWorkspace` listing single-crystal Bragg reflections found by invocation of a peak-finding algorithm (includ-

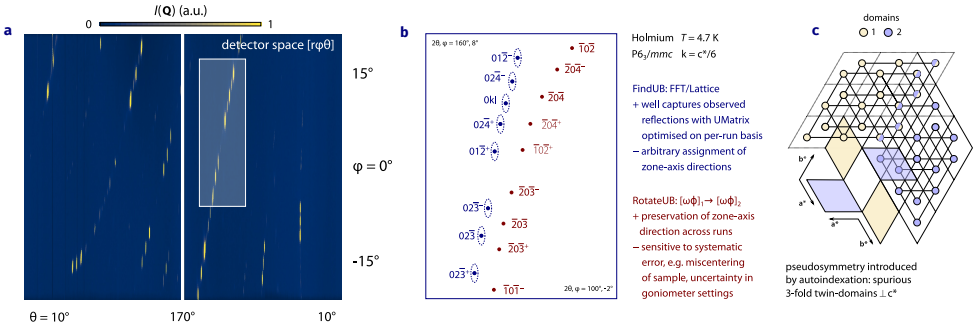

Figure 3.7: Pseudosymmetry introduced by non-unique selection of zone-axes for the commensurate magnetic phase of Holmium with $\vec{k} = \vec{c}^*/6$. In panel (a), the raw panel data is shown, with the highlighted region corresponding to the annotated region in panel (b). The result of rotation of the UB matrix without U matrix correction is compared against the blind indexation of the observed peaks, not consistent with the reference UB. The result of this inconsistent indexing is shown in panel (c) and corresponds to the introduction of a 3-fold pseudosymmetry and gives a false Laue symmetry. Note that in panel (c) only the nuclear structure is shown.

ing `FindSXPeaks` working in detector space and `FindPeaksMD`working in $\vec{Q}$). The determination of UB matrices across goniometer configurations is of paramount importance, and strongly influences subsequent steps of the structural refinement. Without good UB matrices, refinement will not be optimal or, in most cases, even possible at all. It is important therefore, especially in low symmetry or twinned structures, that the determined UB matrices describe a continuous reciprocal space, transforming smoothly between orientations. When one simply applies the auto-indexing methods to separate runs, the above condition is not necessarily met, and one can introduce pseu-

dosymmetry that can distort the structural model. As illustrated in Fig. 3.7, the `LinkedUBs` algorithm presented in this section solves this problem, and is one of the major contributions of the chapter.

Suppose for example that two successive goniometer configurations describing the orientation of the crystal in space share some reflection, (h, k, l). In cubic structures, it is not important whether this is indexed consistently across orientations due to the equivalence in d-spacings,

$$1/d^2 = (h^2 + k^2 + l^2)/a^2. \tag{3.30}$$

However, for lower symmetry structures, such as for the monoclinic system in which $\beta \neq 90°$, the d-spacing is given by

$$1/d^2 = \frac{h^2}{a^2 \sin^2 \beta} + \frac{k^2}{b^2} + \frac{l^2}{c^2 \sin^2 \beta} - \frac{2hl \cos \beta}{ac \sin^2 \beta}. \tag{3.31}$$

While some reflections may be equal in d-spacing, others are not, so it is important for structural refinement that those reflections that occur with equal d-spacing are indexed consistently across detectors, since the indexation of such reflections determines the direction of the UB matrix and may result — if not indexed consistently — in discontinuity between physical rotations of the crystal described by the UB matrices.

This problem is most apparent when auto-indexing algorithms are employed as methods for the determination of the UB matrix. Examples in the `mantid` suite are `FindUBUsingLatticeParameters` and `FindUBUsingFFT`.

These do not take into account the consistency of indexation of reflections across goniometer configurations. In order to solve this problem, an algorithm `LinkedUBs` has been created and incorporated into the `mantid` codebase[12]. The algorithm implements automatic consistent indexation of peaks across orientations using a user-supplied reference UB matrix. The peaks in subsequent orientations are predicted from the starting UB matrix and their d-spacing and $\vec{Q}$ values are compared to sets of found peaks.

This procedure is done iteratively, with a decrementing $\vec{Q}$ envelope and an ordered list in which peaks at long d-spacing are considered first, since these are typically more spread out than those in backscattering, where false matches could occur with many peaks close together and with similar d-spacing. As more iterations are executed, the number of peaks considered increases. This results in more and more peaks being indexed and thus a more accurate UB matrix. This procedure is done for all orientations, resulting in the determination of a complete set of linked UB matrices which can then be used to integrate the peaks. A simple approach might be just to predict peaks at each orientation from the starting UB, and to use those predicted peaks and the UB associated with them (differing only by the R matrix) as linked UBs. In principle this could indeed work; in practice however, the nature of the goniometr means that crystal centering is approximate at best, and is done on the lab bench by eye, as opposed to four-circle x-ray diffractometers which implement a series of cameras to achieve good centering.

[12]L. Edwards, `LinkedUBs`, `mantid/Framework` (2018).

On WISH, the sample is attached to an insert at the end of the goniometer, which sits in the blockhouse, in the beam, with no scope to adjust the position of the sample when it has been mounted. For single-crystal studies, rotations about a miscentered crystal will result in the translation of the peaks on the detectors that predictions of the reflection positions from the goniometer angular settings and UB matrix alone cannot account for. The ω axis is rather more accurate than the ϕ axis which consists of long rod, motor and coupler. The best solution to this problem is to have a single UB matrix for each orientation. What is required is a U matrix correction while preserving the indexing of the peaks. This is done by comparing the predicted peaks to the observed peaks.

The core of the `LinkedUBs` algorithm is as follows. The algorithm requires one to supply a reference UB matrix, from which the peak positions of all subsequent crystal rotations are calculated by goniometer rotations. It is not trivial to do this without the use of an automated algorithm in many cases, since the crystal will not be perfectly centered in the beam when lowered into the blockhouse and rotated in data collection, thereby giving rise to distortions in the U matrix, with subsequent predicted UB matrices not capturing the peak positions. In some cases, this effect can be quite severe, and the manual creation of the UB matrices can be quite time consuming and prone to human error. The algorithm works by comparing the d-spacing and $\vec{Q}$ values of peaks found by a standard search algorithm — such as `FindSXPeaks` — to the predicted peaks. The algorithm searches for matches based on $\vec{Q}$ and

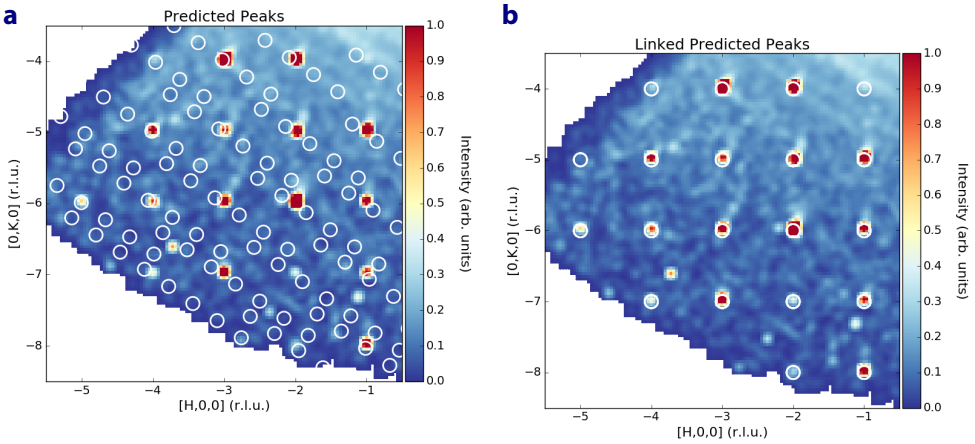

Figure 3.8: Scattering from Ruby, Al_2O_3 showing the predicted peaks from goniometer rotation in panel (a) and the corrected linked peaks in panel (b).

d-spacing tolerance values supplied by the user. Those found peaks, which match within tolerance a predicted peak, inherit the (h, k, l) value; after all peaks have been considered, the UB is forced with `CalculateUMatrix`. This process is done for n interactions, with the tolerance values decrementing at each iteration, as the UB is refined.

The process of linking the peaks is shown in Fig. 3.8 for single-crystal Ruby, Al_2O_3. While having the correct indexing, the goniometer rotated peaks shown in panel (a), are quite far away from capturing the observed peaks shown in panel (b). While it is relatively simple to correct for this by hand for simple structures, the problem becomes much more complicated, time consuming, and prone to error for denser reciprocal spaces characterized by low symmetry or having present some magnetic or structural modulation.

```
...
for i in range(len(qlabs_observed)):
    qx_obs, qy_obs, qz_obs = qlabs_observed[i]
    q_obs = V3D(qx_obs, qy_obs, qz_obs)
    p_obs = linked_peaks.createPeak(q_obs)
    d_obs = dspacings_observed[i]

    for j in range(len(q_ordered)):
        qx_pred, qy_pred, qz_pred = q_ordered[j]
        d_pred = d_ordered[j]

        if (qx_pred - qtol_var <= qx_obs <= qx_pred
                + qtol_var and qy_pred - qtol_var <=
                    qy_obs <= qy_pred
                + qtol_var and qz_pred - qtol_var <=
                    qz_obs <= qz_pred
                + qtol_var and d_pred - self._dtol <=
                    d_obs <= d_pred + self._dtol):
            h, k, l = HKL_ordered[j]
            p_obs.setHKL(h, k, l)
            linked_peaks.addPeak(p_obs)

linked_peaks = FilterPeaks(linked_peaks,
                        FilterVariable="h^2+k^2+l^2",
                        Operator="!=",
                        FilterValue="0")

CalculateUMatrix(PeaksWorkspace=linked_peaks,
                a=self._a,
                b=self._b,
                c=self._c,
                alpha=self._alpha,
                beta=self._beta,
                gamma=self._gamma,
                StoreInADS=False)

linked_peaks_predicted = PredictPeaks(
    InputWorkspace=linked_peaks,
    WavelengthMin=self._wavelength_min,
    WavelengthMax=self._wavelength_max,
    MinDSpacing=self._min_dspacing,
    MaxDSpacing=self._max_dspacing,
    ReflectionCondition=self._reflection_condition,
    StoreInADS=False)
...
```

3.5 Single-crystal results

Solving magnetic structure requires a few main steps. First, the determination of the propagation wavevector, second, the determination of the coupling between magnetic moments, and finally, the determination of the moment directions and their values in Bohr magnetons (μ_B) are determined. In many cases, an unambiguous structure solution cannot be achieved through powder diffraction alone; the propagation wavevector often cannot be determined unambiguously, and peak overlap can be problematic. Single-crystal diffraction, however, facilitates unambiguous determination of the propagation wavevector and does not present major problems concerning peak overlap.

There do exist cases in which single-crystal is not enough for a full structure solution, namely in the case of multi-domain structures, such as multiferroics. In cases of domain structure, magnetic field or uniaxial strain can be provided to the sample to break symmetry and produce single-domain structure. This is especially important in high symmetry structures such as F-centered cubic cells, and will allow one to distinguish magnetic order that involves multiple arms of the star of $\vec{k}$ and a multi-$\vec{k}$ structure involving more than one propagation wavevector. Sometimes, additional polarization analysis is required

to fully solve the structure[13]. In the case of X-ray diffraction, the unit cell structure factor is the Fourier transformation of the electron charge density in the unit cell,

$$\rho(x, y, z) = \sum_{hkl} F(h, k, l) \exp[-2\pi i(hx + ky + kz)]. \tag{3.32}$$

Above, the charge density has been separated into amplitude and phase terms. In diffraction experiments, we measure the square of the structure factor since $I \propto F^2$; the resultant loss of information presents a challenge to structure solution widely known as *the phase problem*. The `superflip` algorithm [146] implements a charge flipping protocol in arbitrary dimension to tackle structure solution, and works by minimization of the difference between observed and calculated electron density. A schematic diagram of the algorithm process is given in Fig. 3.9.

The atoms in the crystal structure are not strictly fixed, but undergo oscillations about their nominal orbits due to thermal motion. With respect to the Fermi length, these displacements are large. The probability of the

[13]Polarization analysis exploits the fermionic nature of the neutron beam to provide additional information from scattering. The $S = 1/2$ beam is split into $|\uparrow\rangle$ and $|\downarrow\rangle$ components in the ratio $P = (N_+ - N_-)/N_+ + N_-$, which can also be expressed $(F-1)/(F+1)$, defining F as the so-called flipping ratio. For uniaxial polarization (longitudinal), the scattered intensity can be separated into the spin-flip and non-spin-flip channels. More complex spherical/vector schemes exist but will not be discussed here, although three-dimensional polarization axes are often required for magnetic structure solution on multi-domain systems.

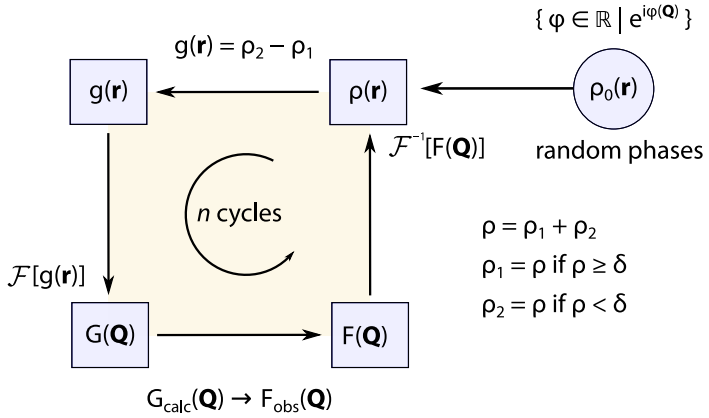

Figure 3.9: Charge flipping algorithm for structure solution from diffraction data [146]. An initial electron density $\rho_0(\vec{r}) = \mathcal{F}^{-1}[F_{\rm obs}(\vec{Q})\,\exp\{i\varphi(\vec{Q})\}]$ is calculated for random set of phases, $\{\varphi(\vec{Q})\}$ satisfying Freidel's law. The low density region of $\rho(\vec{r})$ is flipped in direct space with the modified density $g(\vec{r}) = \rho_1 - \rho_2$, sensitive to the one parameter used in the algorithm — the threshold δ. Temporary structure structure factors are obtained from the modified density $g(\vec{r})$ by Fourier transform. From the temporary structure factors $G(\vec{Q})$, the calculated phases are used to calculate the structure factor for which moduli are replaced by $F_{\rm obs}(\vec{Q})$, with $F(0) = G(0)$ accepted without changes, and the structure factor outside the resolution sphere defined by $Q_{\rm max} = 1/d_{\rm min}$ reset to zero. The grid must satisfy $\Delta r \leq d_{\rm min}/2$. Figure made with reference to Ref. [147].

displacement of the atom by some u is related to the Boltzmann distribution

$$P(u) = \frac{\sum_n \psi_n^2\,\exp(-E_n/k_{\rm B}T)}{\sum_n\,\exp(-E_n/k_{\rm B}T)} = \frac{1}{\sqrt{2\pi\langle u\rangle^2}}\,\exp(-u^2/2\langle u^2\rangle), \qquad (3.33)$$

which describes a Gaussian distribution of atomic displacements. The reciprocal space representation also describes a Gaussian distribution, in which

the probability is given by in terms of u, as varying exponentially according to the relation

$$P(u) = \exp(-u^2Q^2/2) = \exp(-8\pi^2\langle u^2\rangle \sin^2\theta/\lambda^2). \tag{3.34}$$

For isotropic motion, the atomic displacement parameter (ADP) for atom j is $B_j = 8\pi^2\langle u_j^2\rangle$. In the case where the ADP is anisotropic, a multivariate Gaussian distribution is assumed, which — in the most general case — gives rise to 6 independent u_{ij} displacement parameters, and is a second rank tensor. The ADP brings about a dampening of the intensity with increasing momentum transfer. Another effect to consider in refinements is the effect of strain. A phenomenological model for anisotropic strain is described with symmetrical 4^{th} order tensor [143, 148]

$$\sigma^2(hkl) = D^{ijmn}h_ih_jh_mh_n = \sum_{hkl} S_{\text{hkl}}h^{\text{h}}h^{\text{k}}h^{\text{l}}, \tag{3.35}$$

where the landau summation convention is observed and restricted to $h+k+l = 4$. The contribution to the FWHM is $\Gamma_A = [\sigma^2(hkl)]^{1/2}d^2\tan\theta$. The ratio in which the broadening is included in Gaussian and Lorentzian parts is $(1-\zeta)/\zeta$. The weights are calculated from the uncertainties of the profile intensities $w_i = 1/\sigma^2[y_i(\text{obs})]$. The experimental R-factor has n number of profile points and p number of refined parameters. The goodness of fit is GOF $= R_{wp}/R_{\text{exp}}$. The pure profile and weight profile R-factors use the

following background corrected observed and calculated intensities:

$$\begin{aligned} y_i'(\text{obs}) &= y_i(\text{obs}) - b_i, \\ y_i'(\text{calc}) &= y_i(\text{calc}) - b_i. \end{aligned} \tag{3.36}$$

In `Jana2006`, refinements can be made on both the structure factor F and its square F^2. In the former case, the weighting and P factors take the form

$$\begin{aligned} w &= [\sigma^2(|F_{\text{obs}}|) - (uF_{\text{obs}})^2]^{-1} \\ P &= \sum w(|F_{\text{calc}}| - |F_{\text{calc}}|)^2, \end{aligned} \tag{3.37}$$

and the corresponding residuals for F^2 are modified according to the relations

$$\begin{aligned} w' &= w/4F_{\text{obs}}^2 \\ P' &= w'[F_{\text{obs}}^2 - F_{\text{calc}}^2]^2. \end{aligned} \tag{3.38}$$

Here, σ is the estimated standard-deviation (ESD) and u is the so-called instability factor. This parameter should be consistent across all measurements on the same diffractometer. P is the minimized function *i.e.* the R-factor, which is based on F_{obs} and F_{calc} for refinements on both F and F^2.

In `Jana2006`, reflections are counted as observed (from the set of all reflections collected) if $I/\sigma > k$ where k is a chosen real number; a standard choice is $k = 3$. By discounting too many reflections, inaccurate refinements can be obtained, so care is needed. Since it allows for description of anharmonic displacement parameters, as well as for its superior treatment of extinction,

Table 3.1: Reliability factors, `Jana2006` [143].

Reliability factor	Function
R^2_{exp}	$\frac{\sum_i w_i y_i(\text{obs})^2}{n-p}$
R_p	$\frac{\sum_i \lvert y_i(\text{obs}) - y_i(\text{calc})\rvert}{\sum_i y_i(\text{obs})}$
cR_p	$\frac{\sum_i \lvert y'_i(\text{obs}) - y'_i(\text{calc})\rvert}{\sum_i y'_i(\text{obs})}$
R^2_{wp}	$\frac{\sum_i w_i[y_i(\text{obs}) - y_i(\text{calc})]^2}{\sum_i w_i y_i(\text{obs})^2}$
cR^2_{wp}	$\frac{\sum_i w_i[y'_i(\text{obs}) - y'_i(\text{calc})]^2}{\sum_i w_i y'_i(\text{obs})^2}$

`Jana2006` is preferred compared to other refinement software packages such as `FullProf`. The mean path $\overline{T}$ is either recorded in the reflection file and used in numerical absorption correction or, if it is not present, calculated from the equation $\overline{T} = 3R/2$ for a spherical crystal of radius R. The parameter ρ gives the ratio of the particle size in μm to the wavelength in Å.

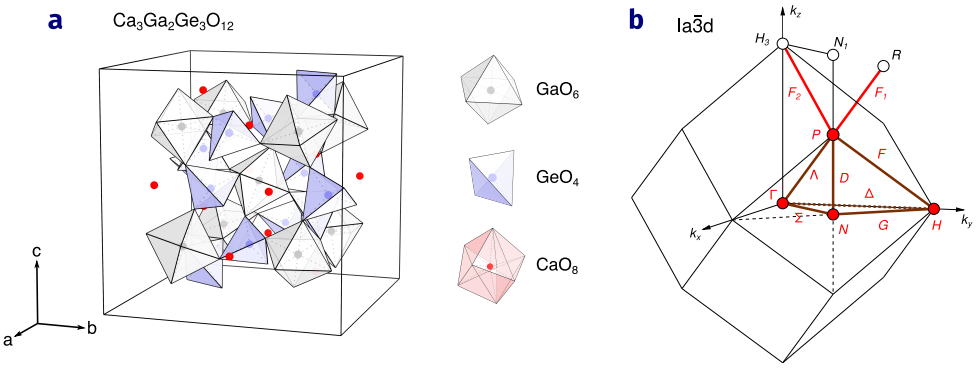

Figure 3.10: Crystal structure of $Ca_3Ga_2Ge_3O_{12}$ (a), drawn using the `VESTA` program [150]. Brillouin-zone associated with Federov group Ia$\bar{3}$d (b) drawn using the `KVEC` program of the Bilbao crystallographic server [151].

3.5.1 Crystal structure of garnet $Ca_3Ga_2Ge_3O_{12}$

The calcium gallium germanium garnet $Ca_3Ga_2Ge_3O_{12}$ is a functional material that has many applications depending on doping. Their optical properties are of particular interest; they are also a component materials of the Earth's crust and mantle. The chemical formula of the garnet structure can be represented as $^{\mathrm{VIII}}[X_3]^{\mathrm{VI}}\{Y_2\}^{\mathrm{IV}}(Z_3)O_{12}$ [149]. A cation in the X site is located in an eightfold triangular dodecahedral coordination site, a cation in the Y site is located in a sixfold octahedral coordination site, and a cation in the Z site is located in a fourfold tetrahedral coordination site.

The garnet structure $Ca_3Ga_2Ge_3O_{12}$ has the symmetry and spatial isometries described by the nonsymmorphic Federov group $Ia\bar{3}d$, with point group $Im\bar{3}m$, and cubic lattice parameter $a = 12.2562(1)$ Åand $Z = 2$. The crystal

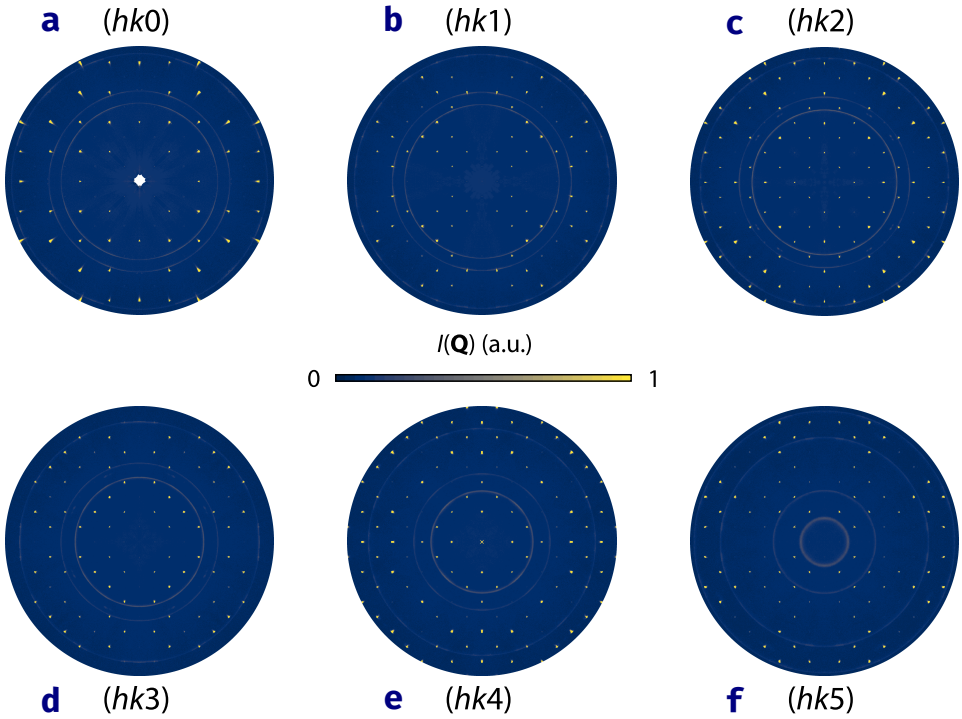

Figure 3.11: Normalized extracted planes, $Ca_3Ga_2Ge_3O_{12}$ ($T = 293\,\mathrm{K}$). Data normalized to incoherent scattering of absorption corrected Vanadium sphere. Symmetrization using the Laue group ($m\bar{3}m$) has been applied to six goniometer configurations representing a redundant volume of reciprocal space, combined using the method described in Ref. [2]. The ends of the detector tubes have been masked to reduce streaks at high Q, and the data have been smoothed using a Gaussian profile function. Powder rings arising from the scattering sample environment components occur at at d-spacing values of $2.338, 2.025, 1.432, \ldots$ Å, with texturing from preferred orientation visible, as well scattering from secondary crystallites.

structure is shown in Fig. 3.10, along with the first Brillouin zone. A high-quality single-crystal was provided by the WISH team, and single crystal neutron diffraction data were collected across several goniometer configurations covering the asymmetric unit of the BZ. This was determined using the `CrystalPlan` program, which optimizes angular settings for maximum coverage in the minimal number of runs. This is the first sample that was tested with the fully motorized, low temperature goniometer. Data were normalized to the incoherent scattering of V/Nb using the `mantid` program; using the `LinkedUBs` algorithm, a full set of consistent UB matrices were refined. Their quality is demonstrated by the joining of datasets to present the reciprocal lattice planes in Fig. 3.11. The quality of the combined volumes is such that texturing can be seen in the powder rings arising from the Aluminum sample environment. Spherical integration of reflections was carried out in reciprocal space and were subsequently combined using `mantid`. The combined integrated intensities were used in the refinement of the crystal structure in `Jana2006` with a type-I extinction correction applied in finding the corrected structure, filtering reflections with $I/\sigma > 3$. The results of the refinement are presented in Table 3.2 and compare favorably with values presented in the literature [152]. The observed and calculated structure factors are compared in Fig. 3.12. The refinement converged with acceptable values for TOF scattering, namely below 10, thereby demonstrating a successful quantitative structural characterization from single-crystal in this material.

Table 3.2: Crystal structure parameters for $Ca_3Ga_2Ge_3O_{12}$ at $T = 293\,\mathrm{K}$ obtained from a refinement of neutron single-crystal diffraction data taken on the WISH instrument, ISIS. Data processing was achieved using the `MantidPlot` framework [38]. Integrated reflections were combined in the refinement of the nuclear structure using `Jana2006` [143], with reflections with $I/\sigma > 3$ discarded. For each atom type, the Wyckoff position (WP) and site symmetry are given, along with its fractional coordinates $(x/a, y/b, z/c)$, isotropic displacement factor (B_{iso}), and site occupation factor (SOF).

Atom	x	y	z	B_{iso}	SOF	WP	Site symmetry
Ge	0.75000	0.12500	0.00000	0.002	1.00	$24d$	$-4..$
Ga	0.75000	0.25000	-0.25000	0.001	1.00	$16a$	$.-3.$
Ca	0.75000	0.37500	0.00000	0.004	1.00	$24c$	2.2 2
O	0.65112	0.03372	0.04997	0.003	1.00	$96h$	1

$G = Ia\bar{3}d$, $a = 12.274(1)$ Å, $V = 1847.284$ Å^3,
GOF $= 9.53\,\%$, $R_{\mathrm{p}} = 6.99\,\%$, $R_{\mathrm{wp}} = 7.73\,\%$

3.5.2 Magnetic structure of rutile-type MnF_2

The insulating transition metal difluoride MnF_2 crystallizes in the rutile structure [153], as shown in Fig. 3.13. The primitive tetragonal unit cell has a metric defined by the lattice constants $a = 4.873$ Å and $c = 3.130$ Å, with appreciable compression perpendicular to the basal ab-plane evident from the ratio $c/a \sim 2/3$. The spatial isometries of the crystal structure are fully described by the nonsymmorphic Federov group $P4_2/mnm$. The space group $\mathcal{G}$ [54] is centrosymmetric, with its origin at the body-center position coincident with an inversion center. With respect to the origin, the crystal is invariant under the group $\mathcal{P}$ of point symmetries, $4/mmm$; the site symmetry

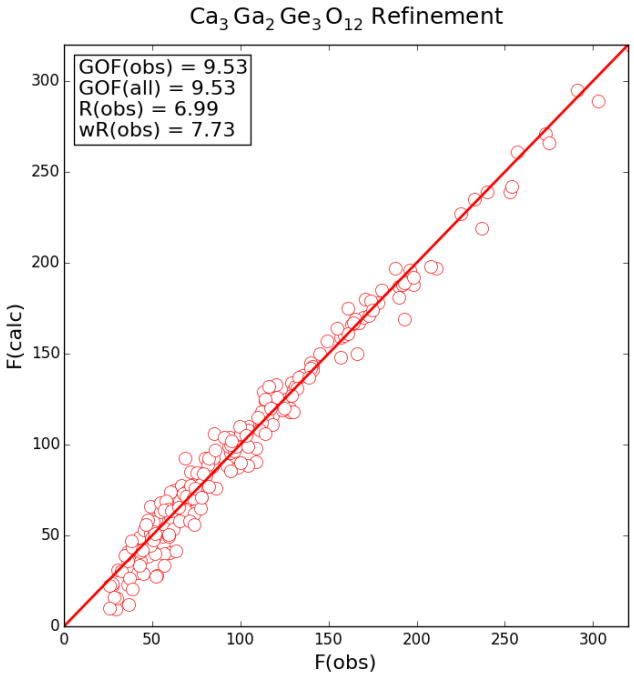

Figure 3.12: Refinement of the crystal structure in $Ca_3Ga_2Ge_3O_{12}$. The observed and calculated structure factors are compared, showing that the refinement converged with acceptable values for TOF scattering, namely below 10, thereby demonstrating a successful quantitative structural characterization from single-crystal in this material.

$\mathcal{S}_o < \mathcal{P}$ of the origin is mmm, through which a $2/m$ axis along the primary[14] direction and $2/m$ axis along the tertiary[15] direction intersect. High symmetry projections are along the $[1,0,0]$, $[1,1,0]$, and $[0,0,1]$ directions with

[14]The primary axis is along $\vec{c}$; this $2/m$ axis is equivalent to a 2-fold $\parallel \vec{c}^*$, and mirror plane $\perp \vec{c}^*$.

[15]The tertiary axis is along the diagonal of the plane $\perp \vec{c}$; this $2/m$ axis is equivalent to a 2-fold rotational element $\parallel (\pm\vec{a}^* \pm \vec{b}^*)$, and mirror plane $\perp (\pm\vec{a}^* \pm \vec{b}^*)$.

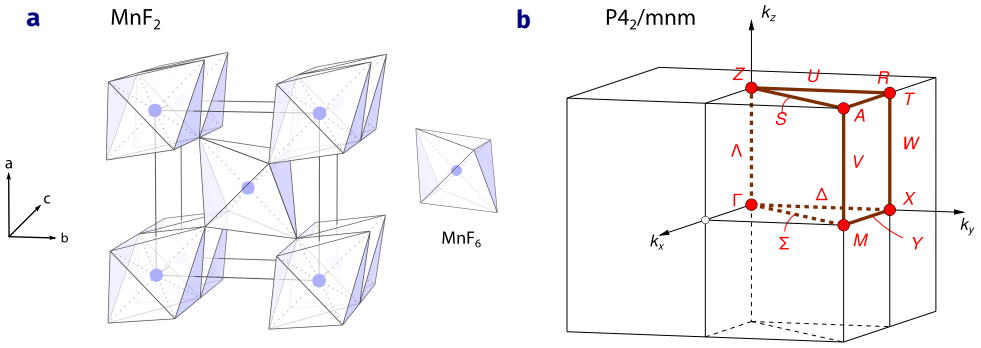

Figure 3.13: Crystal structure of MnF_2 (a), drawn using the `VESTA` program [150]. Brillouin-zone associated with Federov group $P4_2/mnm$ (b) drawn using the `KVEC` program of the Bilbao crystallographic server [151].

respective point symmetries $p4gm$, $c2mm$, and $p2mm$.

The symmetry elements of $\mathcal{G}$ are generated by the combination of the elements of $\mathcal{P}$ with the translation group $\mathcal{T}$. When the translation is non-primitive, systematic absences in the diffraction are manifest. In the primitive tetragonal basis with $\tau = (1/2,\ 1/2,\ 1/2)$, the symmetry elements of $\mathcal{G}$ can be expressed in Seitz notation [49] as follows:

$$\begin{array}{llll} \{1|0\}, & \{2_{001}|\tau\}, & \{4^{+}_{001}|\tau\}, & \{4^{-}_{001}|\tau\}, \\ \{2_{010}|\tau\}, & \{2_{100}|\tau\}, & \{2_{110}|0\}, & \{2_{1\bar{1}0}|0\}, \\ \{\bar{1}|0\}, & \{m_{001}|0\}, & \{\bar{4}^{+}_{001}|\tau\}, & \{\bar{4}^{-}_{001}|\tau\}, \\ \{m_{010}|\tau\}, & \{m_{100}|\tau\}, & \{m_{110}|0\}, & \{m_{1\bar{1}0}|0\}. \end{array} \tag{3.39}$$

The 4_2 screw-axis $\parallel \vec{c}^{*}$ generates an extinction condition along the $[0, 0, l]$ zone-

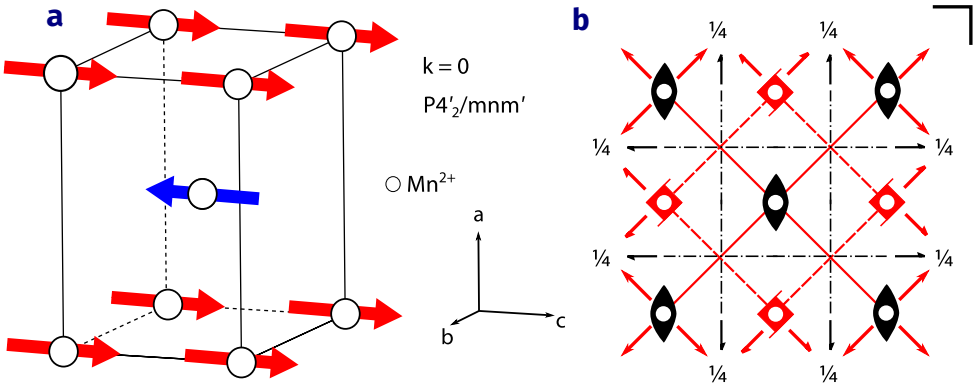

Figure 3.14: Magnetic structure of MnF_2 below T_N. The system orders under the antiferromagnetic propagation vector $\vec{k} = 0$ at the Brillouin zone center, with the symmetry of the type-III Shubnikov group $P4'_2/mnm'$. Point group symmetry shown following Ref. [154].

axis for reflections $l = 2n + 1$, while the 2_1 screw-axes $\parallel \vec{a}^*$ and $\vec{b}^*$ generate extinctions along $[h, 0, 0]$ and $[0, k, 0]$ for reflections $h = 2n + 1$ and $k = 2n + 1$ respectively. The n-glide $\perp \vec{c}^*$ generates extinctions of the $(h, k, 0)$ zone for reflections $h + k = 2n + 1$.

The two magnetic Mn^{2+} ions in the crystal basis occupy positions $X_1 = (0, 0, 0)$ and $X_2 = (1/2,\ 1/2,\ 1/2)$; their $\mathcal{G}$-orbits are identical and belong to the $2a$ Wyckoff position. These are octahedrally coordinated to six non-magnetic F^- ions which occupy the non-centrosymmetric $4f$ position. The crystal-field environment is defined by the resulting framework of corner and edge-sharing MnF_6 octahedra ($m\bar{3}m$ point group), subject to a small distortion with two shorter (2.14 Å) and four longer (2.17 Å) Mn–F bonds. The selection of the free-ion Mn^{2+} electronic ground state can be understood from

Hund's rules: each of the $3d^5$ electrons with spin quantum number $m_s = 1/2$ singly occupy the orbitals $m_l = (-2, -1, 0, +1, +2)$, minimizing their mutual Coulombic repulsion and stabilizing a high-spin $S = \sum m_s = 5/2$ state with $L = \sum m_l = 0$; since the d-band is half-filled, the total angular momentum is $J = |L - S| = 5/2$. The octahedral crystal-field environment splits the free-ion ground state among a low-lying orbital triplet t_{2g} and an excited orbital doublet e_g. Their energy-shifts with respect to the free-ion state are $-2\Delta/5$ and $3\Delta/5$ respectively, where $\Delta = 10Dq$ is the octahedral crystal-field splitting energy. Since these energy shifts (associated with the splitting of the d-band) are weak compared to the pairing energy of two electrons $m_s = \pm 1/2$ in the same orbital m_l (underpinned by the exclusion principle), the ion in the crystal-field remains in the high-spin $S = 5/2$ state for which there is no orbital contribution to the total angular momentum.

In the absence of spin-orbit coupling, the Bloch functions of the lattice $\psi_{\vec{k}}(\vec{r})$ are separable, and are composed from the product of spatial and spin wavefunctions, governed by Coulombic and exchange interactions respectively. Describing the eigenstates of electrons, the symmetry of these wavefunctions are restricted by the requirement that the overall Bloch function is antisymmetric under exchange in the position basis, on account of fermionic statistics. From inelastic neutron scattering [155], the nearest-neighbor Mn^{2+} ions are found to be coupled by ferromagnetic exchange $J_1 = 0.028$ meV along $\langle 0, 0, 1 \rangle$ directions, concomitant with a small single-ion anisotropy D arising from their long-range dipole-dipole interactions [156]. A strong antiferro-

magnetic superexchange $J_2 = SI{-}0.152$ is induced between next-nearest-neighbor Mn^{2+} ions along $\langle 1,1,1\rangle$ directions, mediated by the significant overlap of the Mn^{2+} and F^- electronic wavefunctions along $\langle 1,1,0\rangle$ directions, while higher-order exchange interactions[16] are negligible. With indices j,k running over the nearest and next-nearest neighbors of sites i, the magnetism can be summarily described in the absence of external applied fields by the Heisenberg Hamiltonian,

$$\hat{\mathcal{H}} = -\frac{1}{2}J_1 \sum_{ij} \vec{S}_i \cdot \vec{S}_j - \frac{1}{2}J_2 \sum_{ik} \vec{S}_i \cdot \vec{S}_k - D\sum_i (S_i^z)^2. \tag{3.40}$$

In the paramagnetic phase above $T_\mathrm{N} \approx 67\,\mathrm{K}$ [157, 158], the Mn atoms on each sublattice are equipped with a localized magnetic dipole moment; the directions of these pseudovectors[17] are uncorrelated as thermal fluctuations dominate and the time-average of the moment density is vanishing. The symmetry elements of $\mathcal{G}$ [see Eq. (3.39)] are a set of spatial unitary operators, and account fully for the non-magnetic symmetries of the crystal[18]. The random distribution of pseudovectors over the crystal volume in the paramagnetic phase admits a continuous degree of rotational freedom due to large $N \sim N_A$ statistics; consequently, the time-average crystal potential is invariant under

[16] For instance the contribution from $J_3 = -0.004\,\mathrm{meV}$ along $\langle 1,0,0\rangle$ directions.

[17] The term pseudovector is used interchangeably with axial vector to describe the distinct symmetry properties of the magnetic moment, distinct to the transformation properties of polar vectors: under the rotation element R, the pseudovector $\vec{v}$ transforms as $\vec{v}' = \det\mathsf{R}(\mathsf{R}\vec{v})$.

[18] Defined on a Hilbert space, unitary operators are linear and preserve the inner product $\langle \hat{U}f|\hat{U}g\rangle = \langle f|g\rangle$. They provide an isometric mapping that leaves distances in the image unchanged; in fact, the mapping is surjective and satisfies $\hat{U}^\dagger\hat{U} = \hat{U}\hat{U}^\dagger = E$.

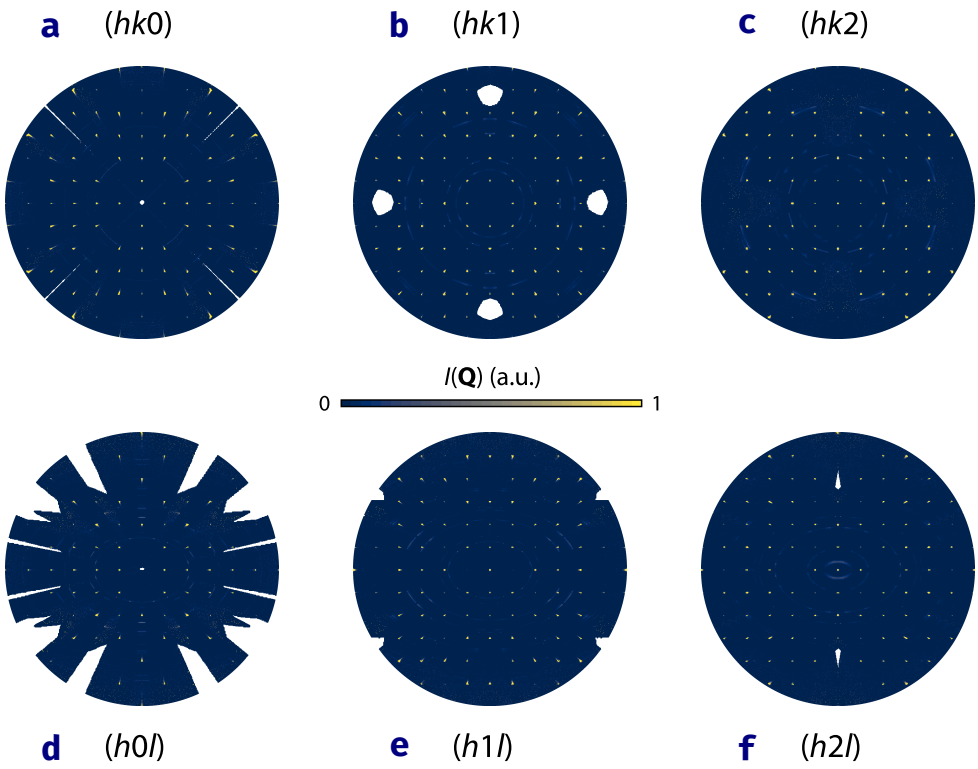

Figure 3.15: Normalized extracted planes, MnF_2 ($T = 4.7\,K$). Data normalized to incoherent scattering of absorption corrected Vanadium sphere. Symmetrization using the Laue group $(4/mmm)$ has been applied to six goniometer configurations representing a redundant volume of reciprocal space, combined using the method described in Ref. [2]. The ends of the detector tubes have been masked to reduce streaks at high $\vec{Q}$, and the data have been smoothed using a Gaussian profile function. Powder rings arising from the scattering sample environment components are visible, showing texturing from preferred orientation, as well as scattering from secondary crystallites.

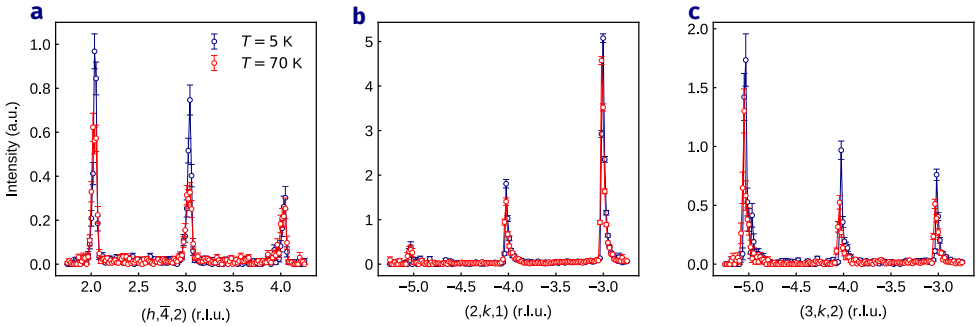

Figure 3.16: Linecuts along the $[h, \overline{4}, 2]$, $[2, k, 1]$, and $[3, k, 2]$ zone-axes in MnF_2 at $T = 5\,\mathrm{K}$ and $T = 70\,\mathrm{K}$, showing development of intensity at $\vec{k} = 0$ positions.

the antiunitary[19] time-reversal symmetry operator $\theta = 1'$, which expresses mapping $\theta : t \mapsto -t$. This can be understood by realizing that θ reverses the sense of electric current circulation $i = dq/dt$ associated with the magnetic dipole moment $|\mu| = \pi r^2 dq/d\mathrm{t}$, from which it follows that $\theta : \mu \mapsto -\mu$. We see that, in addition to the symmetries of the unitary group $\mathcal{G}$, the paramagnetic structure is additionally invariant under the antiunitary group $\theta\mathcal{G}$ of primed elements. The full group of symmetries $\mathcal{M}$ of the paramagnetic crystal potential can be expressed by the S^{II} (gray) group $P4_2/mnm\ 1'$, which is nonunitary and constructed by the direct sum $\mathcal{M} = \mathcal{G} \oplus \theta\mathcal{G} = \mathcal{G} \otimes \{E, \theta\}$.

At temperatures close to T_{N}, thermal fluctuations compete with short-range antiferromagnetic correlations; the equilibrium response is characterized by broad-in-momentum critical scattering in static structure factor, given

[19] Antiunitary operators have instead the property $\langle \hat{U} f | \hat{U} g \rangle = \langle f | g \rangle^* = \langle g | f \rangle$. These are self-adjoint, satisfying the relation $\hat{U}^\dagger \hat{U} = \hat{U}\hat{U}^\dagger = 1$, and used in the description of time-reversal and charge-conjugation symmetries.

by $S(\vec{Q}) \equiv \int S(\vec{Q},\omega)\,\mathrm{d}\omega$. As temperature is decreased below the second-order phase boundary, long-range antiferromagnetic order characterized by the magnetic propagation vector $\vec{k} = 0$ is stabilized; the order parameter in this state is the sublattice magnetization, and its square is coupled to the intensity of the magnetic scattering. The uniaxial anisotropy D is responsible for the collinear, mutually antiparallel alignment of the pseudovectors on each Mn-sublattice along $\langle 0,0,1\rangle$ directions with ordered moment 4.6(1) μ_{B}, as well as the gap in the magnon dispersion at the Γ-point of the BZ [155]. Since the metric of the unit cell is nominally unchanged under the action of $\vec{k}$, the BZ of the crystal and magnetic structures are coincident. However, since the continuous rotational symmetry of the pseudovectors in the paramagnetic phase is spontaneously broken, the ordered state has reduced symmetry and can be understood as a group-subgroup relation.

In the ordered phase, a subset of the unitary operators of group $\mathcal{G}$ leave the structure invariant,

$$\begin{array}{llll} \{1|0\}, & \{2_{001}|\tau\}, & \{2_{010}|\tau\}, & \{2_{100}|\tau\}, \\ \{\bar{1}|0\}, & \{m_{001}|0\}, & \{m_{010}|\tau\}, & \{m_{010}|\tau\}. \end{array} \tag{3.41}$$

These symmetry operations define a unitary subgroup $\mathcal{H}$ of index $[\mathcal{H}:\mathcal{G}] = 2$. The symmetry elements of $\mathcal{H}$ are those of the Federov group $Pnnm$ in its standard setting. The symmetry of the ordered phase is that of the Shubnikov S^{III} (translationgleiche) group $P4'_2/mnm'$ (point group $4'/mm'm$). These S^{III} groups are constructed by the relation $\mathcal{H} \oplus \theta(\mathcal{G} - \mathcal{H})$. The representa-

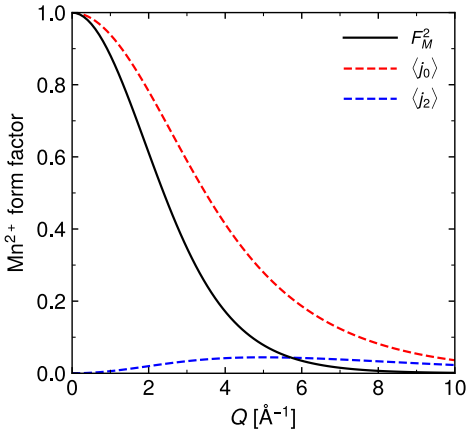

Figure 3.17: Magnetic form factor for MnF_2 ($g \approx 2$) showing the fall-off at high momentum transfer $\vec{Q}$.

tion of the gray group under the propagation wavevector $\vec{k} = 0$ at the $2a$ position can be decomposed as the direct sum of the irreducible representations $\Gamma_2^+ \oplus \Gamma_3^+ \oplus 2\Gamma_5^+$, where the representations Γ_2^{2+} and Γ_3^+ are one-dimensional, and the representation Γ_5^+ is two-dimensional. The $\vec{k}$-vector type is Γ, the coordinates of the vectors of the star of $\vec{k}$ are $(0, 0, 0)$. For the unitary subgroup, the $\vec{k}$-vector type is Γ, the coordinates of the vectors of the star are $(0, 0, 0)$, and the unitary little co-group is mmm. In this case, there is no structural distortion associated with the reduced symmetry of the ordered phase. This is in contrast to the case of rutile-type NiF_2, which undergoes an orthorhombic distortion below T_N [159]. However, the c-axis has been found to experience magnetorestriction in MnF_2 with decreasing temperature; below T_N, the elastic strain Δc is coupled linearly to the square of the

Table 3.3: Crystal structure parameters for MnF_2 at $T = 4.7\,\mathrm{K}$ obtained from a refinement of neutron single-crystal diffraction data taken on the WISH instrument, ISIS. Data processing was achieved using the `MantidPlot` framework [38]. Integrated reflections were combined in the refinement of the nuclear structure using `Jana2006` [143], with reflections with $I/\sigma > 3$ discarded. For each atom type, the Wyckoff position (WP) and site symmetry are given, along with its fractional coordinates $(x/a, y/b, z/c)$, isotropic displacement factor (B_{iso}), and site occupation factor (SOF).

Atom	x	y	z	B_{iso}	SOF	WP	Site symmetry
Mn	0.00000	0.00000	0.00000	0.051	1.00	$2a$	$m.m'm'$
F	−0.30362	−0.30362	0.00000	0.051	1.00	$4f$	$m.2'm'$

$G = P4'_2/mnm'$ (BNS 136.499), $a = 4.95750$ Å, $c = 3.35530$ Å, $V = 82.462556$ Å^3, GOF = 7.25 %, R_{p}(nuc) = 11.74 %, R_{wp}(nuc) = 12.22 % R_{p}(mag) = 11.27 %, R_{wp}(mag) = 11.67 %, ordered moment = 4.151(3) μ_{B}

antiferromagnetic order parameter [160]. The magnetic structure is shown in Fig. 3.14.

The symmetry operations of the magnetic structure are

$$\begin{array}{llll} \{1|0\}, & \{2_{001}|\tau\}, & \{4^{\prime+}_{001}|\tau\}, & \{4^{\prime-}_{001}|\tau\}, \\ \{2_{010}|\tau\}, & \{2_{100}|\tau\}, & \{2'_{110}|0\}, & \{2'_{1\bar{1}0}|0\}, \\ \{\bar{1}|0\}, & \{m_{001}|0\}, & \{\bar{4}^{\prime+}_{001}|\tau\}, & \{\bar{4}^{\prime-}_{001}|\tau\}, \\ \{m_{010}|\tau\}, & \{m_{100}|\tau\}, & \{m'_{110}|0\}, & \{m'_{1\bar{1}0}|0\}. \end{array} \tag{3.42}$$

In addition to the general rule, along the $[h, 0, 0]$ and $[0, k, 0]$ zone-axes, magnetic reflections are systematically extinct for reflections $h = 2n$ and $k = 2n$; along the $[0, 0, l]$ zone axis, magnetic reflections are systematically extinct $\forall l$.

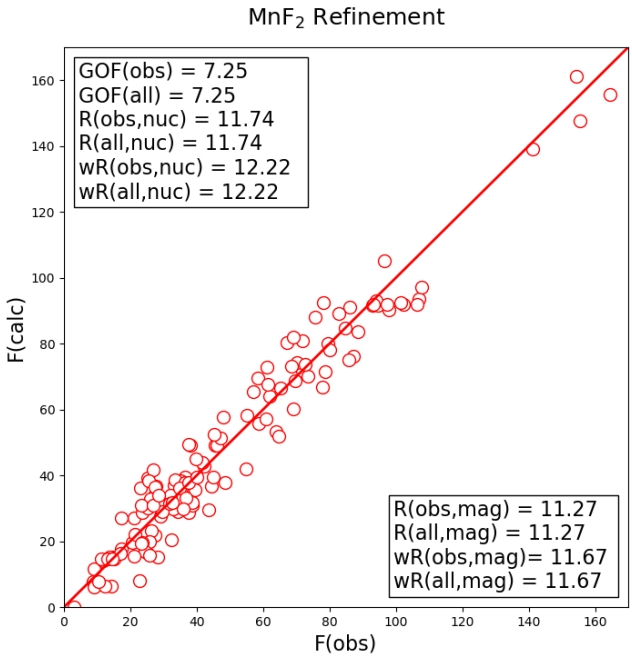

Figure 3.18: Refinement of the crystal and magnetic structures in MnF_2. The observed and calculated structure factors are compared, showing that the refinement converged with acceptable values for TOF scattering, namely below 10, thereby demonstrating a successful quantitative structural characterization from single-crystal in this material.

A high-quality single-crystal was provided by the WISH team; single crystal neutron diffraction data were collected across several goniometer configurations covering the asymmetric unit of the BZ, as determined using the `CrystalPlan` program to optimize angular settings for maximum coverage in the minimal number of runs. This is the second sample that was tested with the fully motorized, low temperature goniometer, and the first mag-

netic structure refined from single-crystal on WISH. Data were normalized to the incoherent scattering of V/Nb using the `mantid` program; using the `LinkedUBs` algorithm, a full set of consistent UB matrices were refined. Their quality is demonstrated by the joining of datasets to present the reciprocal lattice planes through the normalized volume of combined data given in Fig. 3.15. Having taken into account the fall-off of the magnetic form-factor presented in Fig. 3.17, spherical integration of reflections was carried out in reciprocal space and subsequently combined using `mantid`. The combined integrated intensities were used in the refinement of the crystal structure in `Jana2006` with a type-I extinction correction applied in finding the corrected structure, filtering reflections with $I/\sigma > 3$. The results of the refinement are presented in Table 3.3 and compare favorably with the values presented in the literature [153]. The observed and calculated structure factors are compared in Fig. 3.18. The refinement converged with acceptable values for TOF scattering, namely below 10, thereby demonstrating a successful quantitative magnetic structure characterization from single-crystal in this material.

3.5.3 Short-range magnetic order in spinel $GeNi_2O_4$

The 1-2-4 germanate garnet $GeNi_2O_4$ is a spinel material, with general stoichiometry AB_2X_4 (X = O, S, Se, Te). LiV_2O_4 is a famous member of the spinel family, which shows heavy-fermion behavior without having any f-electron states. Spinels are a well studied class of materials, with the structure of Magnetite — also known as lodestone in ancient times — first charac-

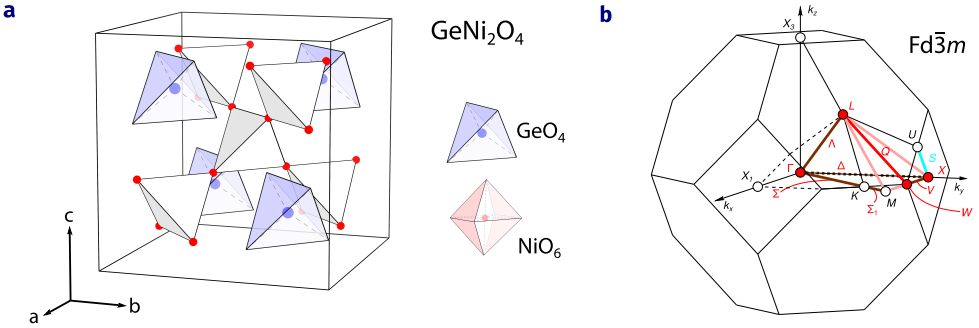

Figure 3.19: Crystal structure of $GeNi_2O_4$ (a), drawn using the `VESTA` program [150]. Brillouin-zone associated with the Federov group $Fd\bar{3}m$ (b) drawn using the `KVEC` program of the Bilbao crystallographic server [151].

terized by Bragg in 1915. In normal spinel materials such as MgV_2O_4, the tetrahedral site is the A-site and the octahedral site is the B-site, while in inverse spinels — such as Mangenite $Fe^{3+}Fe^{2.5+}O_4$ — the tetrahedral site is the B-site and the octahedral site is the A-site. These centrosymmetric oxides have the symmetry nonsymmorphic Federov group $\mathcal{G} = Fd\bar{3}m$ with $Z = 8$, the non-magnetic B-site occupied by octahedrally coordinated Ge^{4+} cations which form a diamond sublattice [161].

The A-site supports tetrahedrally coordinated magnetic Ni^{2+} cations ($3d^8$, $S = 1$, $g = 2.34$) which form an edge-sharing pyrochlore sublattice. Two distinct Néel phases exist below with transition temperatures $T_{N1} = 12.1\,\mathrm{K}$ and $T_{N2} = 11.4\,\mathrm{K}$, with no evidence found to suggest that they are associated with a structural transition. In these spinels, due to the octahedral oxygen crystal field, the degeneracy of the five d orbitals is lifted with three t_{2g} or-

bitals with smaller energy and two e_g orbitals with higher energy. The orbital occupation for the Ni^{2+} ions differ by a hole in the t_{2g} orbitals, which substantially changes the first neighbor interaction. The magnetic structure has been well studied [162–164]. A collinear structure with propagation wavevector $\vec{k} = (\frac{1}{2}, \frac{1}{2}, \frac{1}{2})$ was proposed in Ref. [162]. The two antiferromagnetic structures were found in Ref. [163] and frustration investigated in Ref. [164]. Three of the four Ni^{2+} ions on each tetrahedron belong to a Kagomé plane, while the fourth belongs to a triangular plane. Spins with the Kagomé planes are ferromagnetically coupled, while spins between the adjacent triangular planes are antiferromagnetically coupled.

The crystal structure and first BZ of $GeNi_2O_4$ is shown in Fig. 3.19. A high-quality single-crystal was provided by the WISH team; single crystal neutron diffraction data were collected across several goniometer configurations covering the asymmetric unit of the BZ, as determined using the `CrystalPlan` program to optimize angular settings for maximum coverage in the minimal number of runs. This is the first diffuse scattering dataset that was collected with the fully motorized, low temperature goniometer. Data were normalized to the incoherent scattering of V/Nb using the `mantid` program; using the `LinkedUBs` algorithm, a full set of consistent UB matrices were refined. The joining of datasets was achieved using the procedure in [2]; the combined reciprocal lattice planes showing the diffuse scattering at $T = 4.7\,\mathrm{K}$ are presented in Fig. 3.20. A high temperature run has been subtracted from the low temperature data to reveal the diffuse scattering. The low temperature data

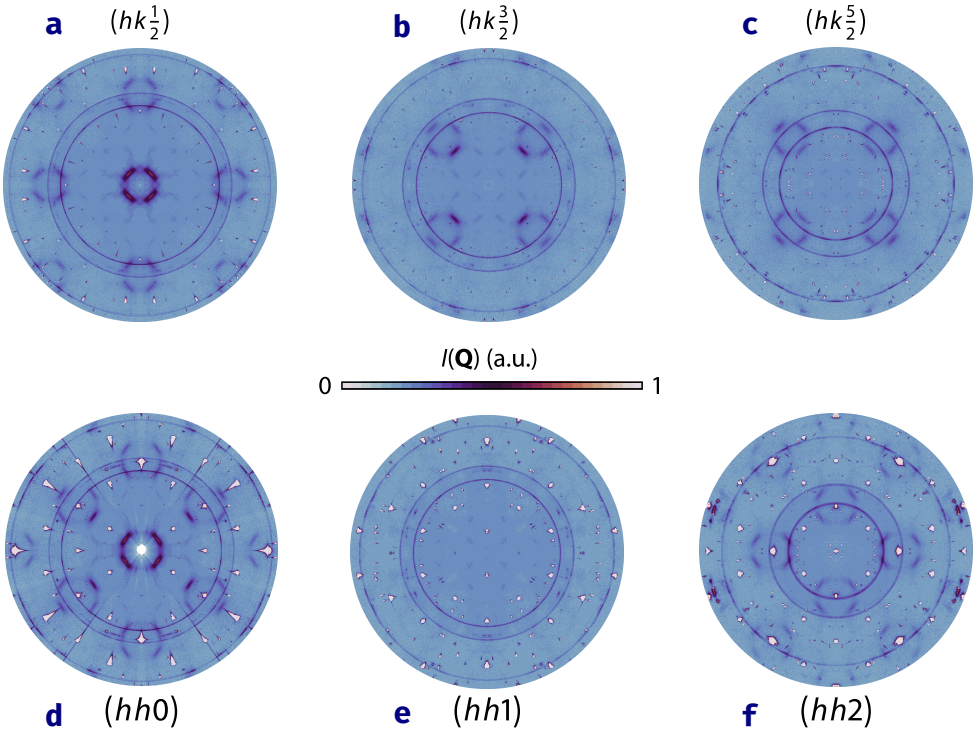

Figure 3.20: Short-range magnetic correlations in the Néel phase of spinel $GeNi_2O_4$ at $T = 4.7\,\mathrm{K} < T_N$. Broad in $\vec{Q}$ scattering is manifest in the (h, k, n) zone shown in (a-c) for $n = l/2$ and in the (h, h, n) zone shown in (d-f) for $l = 2n$ with $n \in \mathbb{Z}$).

and high temperature data are taken at different stick heights, evidenced from the offset of the $(0, 0, l)$ reflections at nominally $(\omega, \phi) = (0, 0)$ positions at low and high temperatures.

In general, the intensity integrated over all wavevectors $\vec{Q}$ and energies ω is constant as external variables (temperature, pressure, magnetic field, *etc.*) are changed; the intensity is, however, redistributed in reciprocal space and is summarized by the total moment sum rule

$$\frac{1}{\mathrm{d}^3\vec{Q}} \sum_{\alpha} \int \mathrm{d}^3\vec{Q} \int \hbar \mathrm{d}\omega S^{\alpha\alpha}(\vec{Q}, \omega) = \langle \vec{S}(0) \cdot \vec{S}(0) \rangle = S(S+1). \qquad (3.43)$$

In $GeNi_2O_4$, strong paramagnetic diffuse scattering is manifest above T_N. Unlike its counterpart below T_N giving δ-function (convolved with instrument resolution function) Bragg reflections, the scattering intensity $I(\vec{Q})$ in the paramagnetic phase is characterized by continuous variation with wavevector. Below T_N, magnetic intensity is increasingly redistributed among positions of the $\vec{k}$-active in Bragg channel with decreasing temperature as long-range order evolves below the transition. Magnetic diffuse scattering can give rise to a myriad of shapes in reciprocal space including half-moons, pinch-points, and Kagomé type correlations [165] — all of which are indicative of frustrated magnetic interactions and short-range order. The diffuse scattering observed in Fig. 3.20 indicates the presence of non-trivial spin correlations, for which a more detailed study would be worthwhile. These data are useful for Monte Carlo simulations in so far as accessing the reciprocal space volumes presented

herein can help to constrain the problem. These results demonstrate that in addition to quantitative structural refinements, the `LinkedUBs` algorithm facilitates the analysis of diffuse scattering data in single-crystals, thereby further expanding the scope of the single-crystal capability of WISH.

3.6 Conclusions

We have developed a novel algorithm for the `mantid` neutron scattering analysis framework — `LinkedUBs` — which allows for the creation of a set of consistent UB matrices for a single-crystal dataset comprising a number of runs. Respecting the continuity of reciprocal space, these enable quantitative structural characterizations to be carried out routinely on the instrument, thereby expanding the scope of its scientific program. Noting the importance of extinction correction, we apply this algorithm to a number of single-crystal datasets, demonstrating the data collection and analysis methodology, noting the importance of extinction corrections to be applied to the integrated reflections for successful refinements. We first characterized the crystal structure of the garnet $Ca_3Ga_2Ge_3O_{12}$ material (Sec. 3.5.1), then went on to characterize the magnetic structure of rutile type MnF_2 (Sec. 3.5.2). We also applied the algorithm in the visualization of reciprocal space planes, producing sets of planes for all materials considered. With successful structural characterizations achieved in these materials — evaluated by noting the acceptable nature of the R-factors achieved from the associated structural refinements

in `Jana2006` — we went on to investigate magnetic diffuse scattering in the spinel material $GeNi_2O_4$ (Sec. 3.5.3). Our results indicate the presence of strong magnetic diffuse scattering below the Néel temperature, which indicates the presence of non-trivial spin correlations that would be worthwhile studying in greater detail in future measurements.

Chapter 4

Short-range order and topology in Ising α-CoV_2O_6

4.1 Chapter summary

Belonging to the 2D Ising universality class, the insulating $j_{\text{eff}} = \frac{1}{2}$ spin-chain material α-CoV_2O_6 supports a global $U(1)$ symmetric Néel state and distinct periodic magnetic structures induced by applied fields. These are based upon collinear arrangements of localized Co^{2+} moments, occupying the sites of an anisotropic triangular sublattice. Hysteretic and cascading magnetization plateaus are manifest below T_{N}, for which the total $S^z_{\text{tot}} = \sum_i S^z_i$ does not change in response to an increasing applied field [166]. This suggests the presence of an energy gap and exponentially decaying spatial correlations. In this chapter, we present results from neutron diffraction and low-temperature magnetization, in search of resolution to this apparent departure from Haldane's theorem (discussed in Sec. 4.3.2).

At dilution temperatures, no long-range translational symmetry breaking occurs in the neighborhood of the plateaus below the ferromagnetic phase which occurs at a saturation field of $\sim 4\,\mathrm{T}$; instead, broad in $\vec{Q}$ scattering arising from short-range ordered states is observed in the static structure factor $S(\vec{Q}) \equiv \int S(\vec{Q},\omega)\,\mathrm{d}\omega$. Antiphase domains, as evidenced from the nature of the diffuse scattering, confer q-fold degenerate local periodicities $\hat{T}^q$ and characterize the ratios M/M_s of the observed plateaus. This correspondence is identified as the signature of an emergent gauge structure, consistent with an extension of the Lieb-Schultz-Mattis theorem (discussed in Sec. 4.3.3), in which the magnetization per site $m = \frac{1}{L}\sum_i^L \hat{S}_i^z$ is understood to be topologically quantized as $(S - m)$. Echoing the hidden symmetry breaking in Fractional Quantum Hall systems, we demonstrate a correspondence between local translational symmetry breaking with the stabilization of magnetization plateaus in an Ising magnet. The results presented in this chapter have been published in Ref. [167].

The contributions to this chapter are as follows. Magnetization measurements were carried out by Sean Giblin (Cardiff), Carley Paulsen (CNRS), Lewis Edwards (Cardiff), and Gavin Stenning (ISIS). Single-crystal neutron diffraction experiments in magnetic field on the WISH instrument were carried out by Chris Stock (Edinburgh), Sean Giblin (Cardiff), and Pascal Manuel (ISIS). Single-crystal diffraction experiments in magnetic field on the RITA instrument were carried out by Chris Stock (Edinburgh), Manila Songvilay (Edinburgh), and Christof Niedermayer (PSI). Single-crystal diffrac-

tion measurements in zero magnetic field were carried out on the MORPHEUS instrument by Chris Stock (Edinburgh) and Manila Songvilay (Edinburgh). Neutron powder diffraction experiments in magnetic field were carried on the TASP instrument by Lewis Edwards (Cardiff), Sean Giblin (Cardiff), Chris Stock (Edinburgh), Manila Songvilay (Edinburgh), and Greg Tucker (PSI). Single-crystal and powder neutron diffraction experiments were carried out in zero magnetic field using the WISH instrument were carried out by Lewis Edwards (Cardiff), Sean Giblin (Cardiff), Chris Stock (Edinburgh), Manila Songvilay (Edinburgh), Pascal Manuel (ISIS). Analysis of data was carried out by Lewis Edwards (Cardiff) and theoretical support was provided by Harry Lane (Edinburgh).

4.2 Introduction

The Quantum Hall effect (QHE) [168] is defined by the non-uniform variation of the electrical Hall conductivity under the effect of varying applied field; this is in contrast to the response expected from conventional electrostatics where a continuous change is manifest. The plateaus realized in the Hall resistivity in the case of the QHE have been the focus of intense interest and have been attributed to topological edge states [169]. Meanwhile, analogies resulting from bulk Bloch states are rare, and particularly magnetic analogues displaying steps in the magnetization.

Neutron scattering provides a means of probing the underlying symmetry

of magnetic correlations in condensed matter systems through the dynamical structure factor $S(\vec{Q},\omega)$. A notable accomplishment of the technique is the differentiation of the dynamics of chains of integer and half-integer spins [170]; Indeed, Haldane was jointly awarded the 2016 Nobel prize, along with co-recipients Thouless and Kosterlitz, for his work on the problem [10, 11, 171]. The spectrum of magnetic excitations in half-integer spins has been found to be gapless [172, 173], while integer spins display a gapped magnon spectrum consistent with the Haldane conjecture [10, 11, 174, 175]. In the absence of inter-chain interactions, neither class of spin chain shows spontaneous symmetry breaking; no change to the equilibrium structure factor $S(\vec{Q})$ is observed associated with the development of long-range order.

By Haldane's conjecture (Sec. 4.3.2), the theoretical predictions for the spectrum of magnetic excitations in integer and half-integer spins are at odds; an extension [12, 176] of the Lieb-Schultz-Mattis theorem (Sec. 4.3.3), however, provides resolution. Arguing on topological grounds [176], the existence of analogous Haldane gapped phases in half-integer spins have been demonstrated to exist in principle, concomitant with plateaus of the magnetization for which the total S^z_{tot} is robust to varying applied fields. The energetics of these gapped phases resemble those of spin-Peierls dimerized states [177, 178], and indeed, those of Haldane gapped phases observed in integer spin chains.

Plateaus of the magnetization have been reported in a number of insulating triangular lattice materials [179–190] and also in materials with a continuous symmetry [191–194] where complex field-induced magnetic transitions are

observed. In these materials, the energetics are complicated by far-reaching exchange interactions between the constituent magnetic ions, which determine the in-field phase diagram. Despite the presence of multiple competing interactions, the realization of fractional steps of the magnetization — akin to the plateaus of the resistivity observed in fractional quantum Hall systems — is rare in the truly Ising limit.

Assuming an axially symmetric Hamiltonian $\mathcal{H}$, discrete steps in the magnetization can be understood to originate from the underlying translational symmetry, placing restrictions on the values of the complex geometric phase acquired upon rotating the spins around the axis of symmetry. Akin to that gained by a Foucault pendulum as it undergoes a unitary transformation about the Earth's axis, for a Hamiltonian invariant under a site translation $\hat{\mathcal{H}} \rightarrow \hat{T}\hat{\mathcal{H}}\hat{T}^{-1}$, a norm preserving unitary rotation of the spins generates a geometric phase under the following large gauge transformation (see Sec. 4.3.3)

$$\hat{T}\hat{U}\hat{T}^{-1} = \hat{U}\ \exp[2\pi i\,(S-m)]. \tag{4.1}$$

For $(S-m) \notin \mathbb{Z}$, the rotated state must be orthogonal to the ground state, representing an excited state with an infinitesimally larger energy $\sim O(\frac{1}{L})$ in the thermodynamic limit [176]. These states give rise to a gapless continuum consistent with Haldane's conjecture [10, 11].

In the case of integral values, the states are gapped and cannot be smoothly transformed through low-lying orthogonal states with applied field; this gives

rise to emergent magnetization plateaus and a Bloch state analog of the quantum Hall effect. Plateaus of the magnetization can also be realized for fractional values of the topological index, supported by an emergent higher order periodicity through the spontaneous breaking of the Hamiltonian's symmetry, by further analogy with the quantum Hall effect. The establishment of this magnetization-induced symmetry can give rise to the emergence of new, modulated ground states, though the stability of such states is ultimately determined by the interaction terms present in the microscopic Hamiltonian. In this chapter, we report the emergence of such symmetries in the Ising magnet α-CoV_2O_6 [195], which displays magnetization plateaus [4–9], using neutron diffraction and low temperature magnetization.

Centrosymmetric, and with a monoclinic Bravais lattice Λ, the insulating Vanadate α-CoV_2O_6 is invariant under the spatial isometries of the symmorphic Federov group $G = C2/m$ [3, 5, 195–197]. This particular allotrope of CoV_2O_6 is distinct from the triclinic γ-polymorph with $P\bar{1}$ symmetry [4, 8, 198, 199], which will not be discussed here. Results from x-ray Laue characterization measurements, conducted at the Materials Characterization Lab (ISIS, UK), are presented in Fig. 4.1; the $(h, 0, 0)$ and $(0, 0, l)$ zone centers of the reciprocal lattice are shown, albeit with some misalignment of the crystal. Using the unique b-axis setting of the crystal space group, the metric tensor of the lattice is defined by the unit cell parameters $a = 9.2283(1)$, $b = 3.50167(5)$, $c = 6.5983(1)$ Å, and a monoclinic angle $\beta = 112.0461(7)°$. The crystal structure is shown in Fig. 4.2(a), illustrating the neighboring

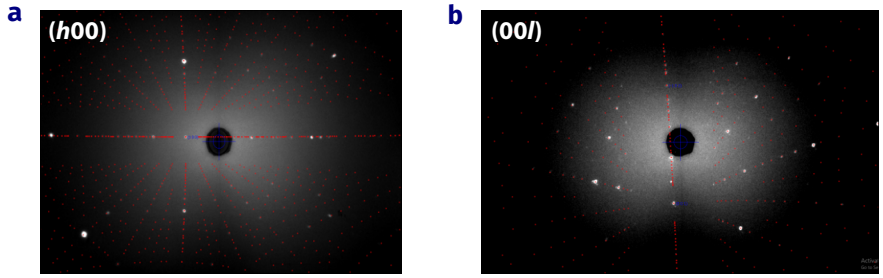

Figure 4.1: Results from x-ray Laue characterization of α-CoV_2O_6 obtained at the Materials Characterization Lab (ISIS, UK). (a) shows the diffraction from the crystal aligned roughly along the $[h, 0, 0]$ zone axis, while (b) shows the diffraction from the crystal aligned roughly along the $[0, 0, l]$ zone axis.

chains of Co atoms along the b-axis; alongside this, the first Brillouin zone (BZ) is shown in Fig. 4.2(b), with the asymmetric unit indicated[1].

Magnetic Co^{2+} ions ($L = 2, S = \frac{3}{2}$) are located on the G-orbits of the $2c$ Wyckoff position, associated with a $2/m$ point group symmetry. Chains of distorted CoO_6 octahedra span the b-axis and are interspersed by VO_5 square pyramids. Neighboring chains are offset by $\pm\frac{1}{2}b$ and define an exchange network based upon an anisotropic motif out of the ac-plane [201–205]. In Fig. 4.2(c), the typical morphological features of single-crystals are shown; prominent crystal faces have been annotated with corresponding principal directions of the reciprocal lattice. Belonging to the Brannerite class characterized by the UTi_2O_6 structure [200], single crystals form with a prismatic habit and well defined faces on opposite sides of the crystal, convenient for

[1]The asymmetric unit is defined by the set $\{(x, y, z) \,|\, x \in [0, 0.5], y \in [0, 0.25], z \in [0, 1]\}$.

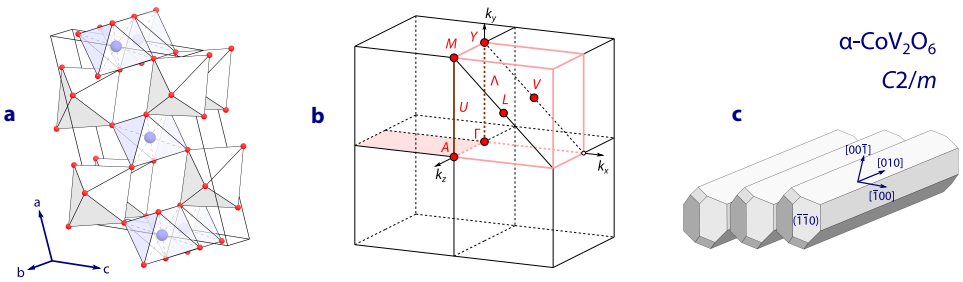

Figure 4.2: (a) shows the crystal structure of α-CoV_2O_6 , drawn using the `VESTA` program [150]. Co atoms (blue) occupy the $2c$ Wyckoff position, with $2/m$ PG symmetry, coordinated by oxygen (red) in CoO_6 octahedra, with distortion modes active along the octahedral axis and within the octahedral plane. Chains of distorted CoO_6 octahedra span the b-axis and are interspersed by VO_5 square pyramids (white), while neighboring chains offset by $\pm\frac{1}{2}b$ define an anisotropic exchange motif out of the ac-plane. (b) shows the first BZ of $G = C2/m$, drawn using the `KVEC` program of the `Bilbao crystallographic server` [151], with the asymmetric unit indicated. (c) shows the Brannerite morphology [200] of single-crystals with the principal directions of the reciprocal lattice indicated.

the purposes of co-alignment.

The d-orbital states of Co^{2+} in a cubic crystalline-electric field (CEF) are split among a low-lying triply degenerate ground $|t_{2g}\rangle$ state and an excited $|e_g\rangle$ state. Depending on the relative strength of the Hund's coupling, as compared to the energy splitting $10Dq$, both high $S = \frac{3}{2}$ and low $S = \frac{1}{2}$ complexes can be realized, with the former state manifest in the case of weak Coulombic interactions. Further splittings of the CEF are induced by the effects of spin-orbit coupling (SOC), giving rise to a ground $j_{\text{eff}} = \frac{1}{2}$ state lying below $j_{\text{eff}} = \frac{3}{2}$ and $j_{\text{eff}} = \frac{5}{2}$ multiplets, for which the energy separations are fixed by the Landé interval rule [206, 207]. Octahedral O_h coordination of the Co^{2+} Kramers ion on the $2c$ site is forbidden by the $2/m$ site symmetry; distortion modes both within and perpendicular to the octahedral plane are thus active, giving rise to degenerate splittings of the CEF by Kramers theorem.

For lattice translations $\tau_j \in \Lambda$ with $j = 1, 2, 3$, the spatial isometries of G, written in Seitz notation, take the form

$$\begin{aligned} &\{1|0\}, \quad \{2_{010}|0\}, \quad \{\bar{1}|\tau_1\}, \quad \{m_{010}|\tau_1\}, \\ &\{1|\tau_3\}, \quad \{2_{010}|\tau_3\}, \quad \{\bar{1}|\tau_2\}, \quad \{m_{010}|\tau_2\}, \end{aligned} \tag{4.2}$$

where $\tau_1 = (0, 0, \frac{1}{2}), \tau_2 = (\frac{1}{2}, \frac{1}{2}, 0)$, and $\tau_3 = (\frac{1}{2}, \frac{1}{2}, \frac{1}{2})$. Despite the presence of symmetry elements g combining non-primitive lattice translations with point symmetry operations, the structure is symmorphic since all isometries

$g \in G$ leave a single point fixed. The paramagnetic phase for $T > T_{\mathrm{N}}$ has additional non-unitary symmetries since the localized Co^{2+} moments possess full SU(2) rotational freedom. This implies an invariance of spins under time reversal $\hat{T} : t \to -t$, with states transforming according to the relation $\hat{U}_{\theta}^{(\alpha)} |\psi\rangle = |\psi\rangle$ for any $\theta \in \mathbb{R}$ and $\alpha = 1, 2, 3$. Accordingly, the full symmetry group M of the disordered high temperature phase is antiunitary, given the presence of nonunitary symmetries, and is constructed by direct sum with the primed group θG. Described by a type-II Shubnikov (gray) group $M = G \oplus \theta G = G \otimes \{E, \theta\}$, the paramagnetic phase has $C2/m1'$ (BNS 12.59) symmetry. The complete set of isometries include primed elements of the form

$$\begin{aligned} &\{1'|\tau_1\}, \quad \{2'_{010}|\tau_1\}, \quad \{\bar{1}'|0\}, \quad \{m'_{010}|0\}, \\ &\{1'|\tau_2\}, \quad \{2'_{010}|\tau_2\}, \quad \{\bar{1}'|\tau_3\}, \quad \{m'_{010}|\tau_3\}. \end{aligned} \tag{4.3}$$

A sharp peak in the magnetic susceptibility $\chi(T)$ is manifest below 15 K, for an excitation field of $\mu_0 \mathrm{H} = 0.1$ T along the crystallographic c-axis. This evidences a transition from the paramagnetic phase [208]. Dominant antiferromagnetic interactions are suggested[2] by a negative Weiss temperature $\theta = -9.2\,\mathrm{K}$, obtained from a fit of the inverse susceptibility $\chi^{-1}(T)$ to a Curie–Weiss law $\chi(T) = N\mu_{\mathrm{eff}}^2 / 3k_{\mathrm{B}}(T - \theta)$ in Ref. [208]. Antiferromagnetic order is further corroborated by a λ-type anomaly in the specific heat $C_{\mathrm{p}}(T)$, shown in Fig. 4.3(a) from Ref. [208], and has been confirmed by neutron powder

[2] Note the contextual usage of the θ parameter here to describe the Weiss temperature, and not the time reversal operator, as used previously in the context of magnetic symmetry.

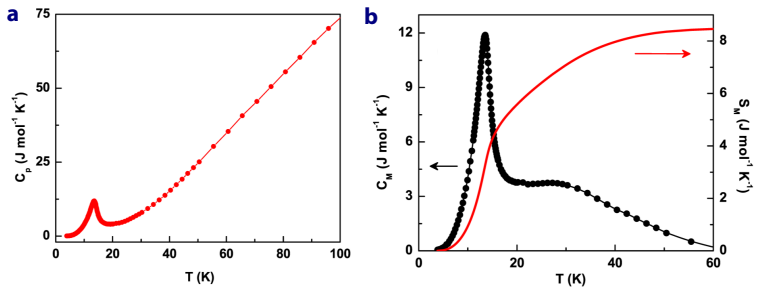

Figure 4.3: (a) shows the temperature dependence of specific heat $C_{\mathrm{p}}(T)$ in zero applied field, displaying a λ-type anomaly close to T_{N}. (b) shows an estimation of the magnetic contribution to the specific heat, $C_{\mathrm{M}}(T)$, calculated by subtraction of the lattice contribution, estimated by a fit to the Einstein model for temperatures $50-222\,\mathrm{K}$. The entropy removal is then calculated by integration $S_{\mathrm{M}}(T) = \int C_{\mathrm{M}}(T)/T\,\mathrm{d}T$ and appears consistent with Co^{2+} ions in a low spin $S = \frac{1}{2}$ state. Adapted from Ref. [208].

diffraction, which finds Néel type ordering of localized Co^{2+} moments with propagation wavevector $\vec{k} = (1, 0, \frac{1}{2})$ [4, 209]. The ground state is discussed in more detail in Secs. 4.5.1 and 4.5.2, where neutron single crystal and powder diffraction results from the WISH and RITA-II instruments are presented.

The estimated $S_{\mathrm{M}}(T)$ at 20 K is shown in Fig. 4.3(b) from Ref. [208], and is smaller than is expected to result from $S = \frac{3}{2}$ Ising moments — instead, a limiting value of $S_{\mathrm{M}} = R\ln 2$ is instead observed, consistent with $S = \frac{1}{2}$ [208]. Moreover, a release of entropy below 20 K suggests the intra-chain degree of freedom is frozen out, resulting in the formation of a 1D chain configuration with strong in-chain coupling and weak inter-chain coupling [208]. This is supported by results from inelastic neutron scattering (INS) [207]. The

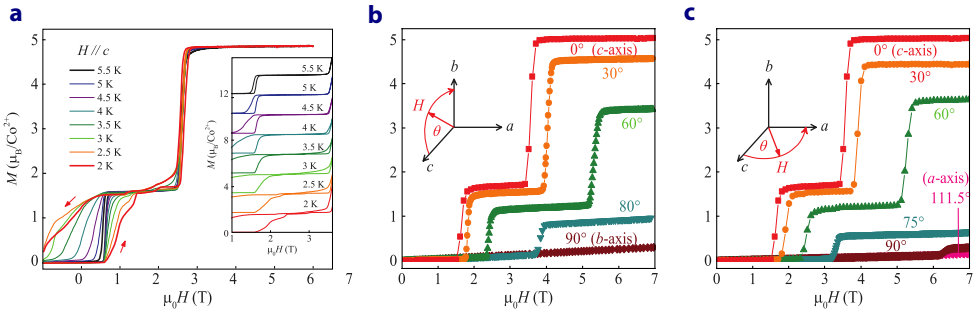

Figure 4.4: (a) shows the T dependence of magnetization plateaus below T_{N}, showing an increase in hysteresis and fine structure of with decreasing temperature, along with an evolution of the critical fields. (b-c) shows the directional dependence of the magnetization for field in the *bc*- and *ac*-plane respectively. Adapted from Ref. [9].

susceptibility response and decay rate for field μ_0H applied along the a and b-axes is far smaller [3]. This suggests an easy axis perpendicular to the chain direction — that is, along the c-axis. Meanwhile[3], a modest linear response is observed in the magnetization M for μ_0H applied along the a and b-axes below T_{N}, thereby providing additional evidence for a uniaxial anisotropy [208].

Of particular interest, a hysteric and cascading series of magnetization plateaus are manifest for $T < T_{\mathrm{N}}$, in which the total quantity $S^z_{\mathrm{tot}} = \sum_i S^z_i$ is robust to varying applied fields [4–9]. For μ_0H along the c-axis, an $M/M_{\mathrm{s}} = \frac{1}{3}$ plateau[4] is stabilized, with additional steps observed upon decreasing temperature [4]. This is accompanied by enhanced hysteresis at lower temperatures [4]. The magnetization as a function of temperature below T_{N} is shown

[3]Note the contextual usage of the M parameter here to describe the magnetization, and not the magnetic space group, as used previously in the context of symmetry.
[4]We use M_{s} to represent the saturation magnetization.

in Fig. 4.4(a) from Ref. [9]. The total moment in the plateau estimated as $\sim 4.6\mu_{\mathrm{B}}/\mathrm{Co}^{2+}$, far greater than is expected for a spin-only complex — this discrepancy therefore suggests a significant orbital contribution [4–9]. Rich hysteretic phenomena are manifest below 5 K, as shown in Fig. 4.4(a), along with a shifting of the critical fields as temperature is varied. Moreover, Figs. 4.4(b−c) demonstrate the fragility of the plateau state and critical transition fields to the direction of applied field. Initially suggested in Ref. [3] from magnetization measurements, this was later confirmed by x-ray magnetic circular dichroism [210], which also supports strong compression of the CoO_6 octahedra — consistent with the $2/m$ symmetry of the Co $2c$ site [210].

Neutron powder diffraction found that in the vicinity of the $M/M_{\mathrm{s}} = \frac{1}{3}$ plateau, the magnetic propagation vector shifts to $\vec{k} = (-\frac{1}{3}, 1, \frac{1}{3})$. This breaking of symmetry is associated with a group-subgroup relation, marking a change of phase as a long-range ferrimagnetic structure is stabilized [211, 212]. Meanwhile, INS on powdered samples found spin-orbit transitions between the ground $j_{\mathrm{eff}} = \frac{1}{2}$ doublet and the $j_{\mathrm{eff}} = \frac{3}{2}$ and $j_{\mathrm{eff}} = \frac{5}{2}$ multiplets. An appreciable energy separation between the $j_{\mathrm{eff}} = \frac{3}{2}$ spin-orbit levels and $j_{\mathrm{eff}} = \frac{1}{2}$ ground state results from the combination of the local octahedral crystal field and SOC, while the small exchange coupling between the spins relative to the anisotropy energy is suggestive of an underlying uniaxial Ising symmetry [207]. The ground state of Co^{2+} can be projected onto a $j_{\mathrm{eff}} = \frac{1}{2}$ state [208, 213], and is well separated in energy from the $j_{\mathrm{eff}} = \frac{3}{2}$ spin-orbit levels [207], differing from rocksalt CoO, in which strong mixing between the

j_{eff} spin-orbit levels is induced by a large exchange constant [213–215].

Low energy magnetic excitations are found deep within the Néel state, taking the form of either two distinct modes or a single dispersing band as shown in Fig. 4.5 from Ref. [207]; in either case, these data suggest a gap in the magnetic dynamics[5]. Local distortions of the crystalline electric field further support an Ising anisotropy [210, 217] — this is evidenced by the gap in the magnetic dynamics, along with the magnetic critical scattering discussed in Sec. 4.5.3. Closer examination of the magnetization curve below 5 K presented in Fig. 4.4(a) from Ref. [9] (as well as at dilution temperatures in Secs. 4.5.3 and 4.5.4) reveals fine structure beyond that of the well-studied $M/M_{\text{s}} = \frac{1}{3}$ plateau found to be associated with a long-range ferrimagnetic transition of the magnetic structure [211, 212]. The satisfactory explanation of the stabilization of these states has proven difficult to tackle and has, as such, remained an open question in the literature.

4.3 Theoretical considerations

It is natural to ask whether the emergence of such fractional plateaus coincides with the onset of distinct magnetic correlations. In the following exposition, we address this question and discuss two predictive models, exploiting different features of the crystal and magnetic symmetry.

[5] To elucidate the exact nature of these low temperature modes, single-crystal INS is necessary to determine their $\vec{Q}$-dependence. We had prepared to conduct this experiment on the IN5 beamline [216] (ILL, France), but unfortunately, both of our beamtime applications were unsuccessful.

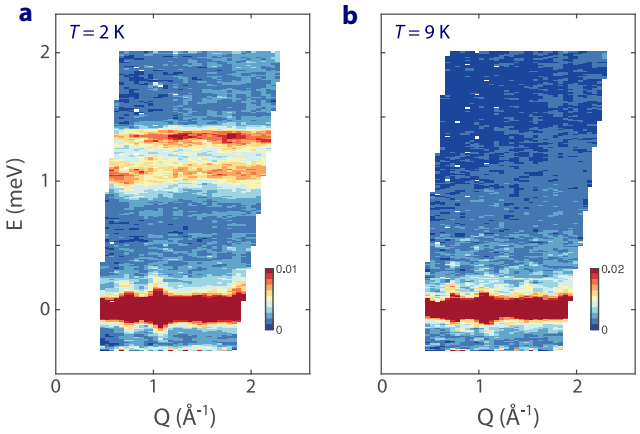

Figure 4.5: Low energy magnetic excitations within the Néel state observed from INS on powder samples in α-CoV_2O_6 . Either two separate excitations or a broad band of excitations are present, suggesting the possibility of a gapped spectrum of states. Adapted from Ref. [207].

4.3.1 TLA and ANNNI models

Somewhat subtle, yet nonetheless striking, is the anisotropic triangular motif that defines a network of magnetic exchange out of the *ac*-plane; with this in mind, the role of competing interactions and magnetic frustration is called into question. We note a resemblance of this structural feature to the geometrically frustrated triangular lattice antiferromagnet (TLA), for which field-induced phases have predicted in Ref. [194] as a function of anisotropy D and nearest-neighbor exchange coupling J_1. This model was originally developed to explain the noncollinear incommensurate phase observed in ferroelectric $CuFe_2O_4$ [191, 192, 194, 218]. The phase diagram of the model, which considers the couplings between magnetic and ferroelectric moments,

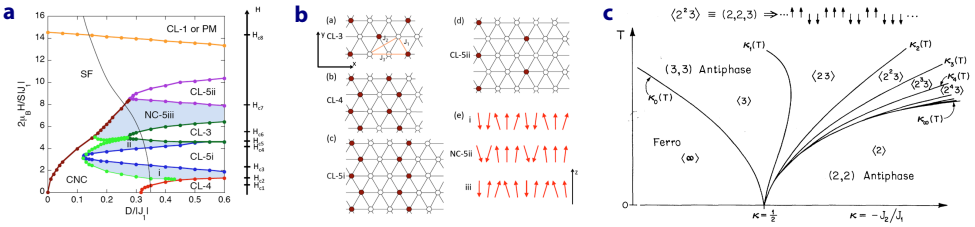

Figure 4.6: (a) shows the phase diagram of $CuFe_2O_2$, displaying an array of possible collinear phases as a function of anisotropy D, and exchange J_1, with the schematic representations of the collinear phases shown in (b) with three, four, or five sublattices, where white and red circles denote magnetic sites of opposite spin direction. From Ref. [194]. (c) shows an infinity of commensurate phases based upon antiphase boundaries in the anisotropic next-nearest-neighbor Ising (ANNNI) chain, springing from a multiphase point at zero temperature, as a function of relative exchange, $-J_2/J_1$. Adapted from Ref. [219].

is shown as a function of $D/|J_1|$ in Fig. 4.6(a) from Ref. [194]. Along with the emergence of equilibrium magnetization plateaus, the model predicts the realization of numerous collinear and noncollinear ordered states, which stabilize depending on the ratio $D/|J_1|$. A subset of these, with varying numbers of sublattices, are shown in Fig. 4.6(b) from Ref. [194]. A central prediction of the model is the instability of collinear phases to noncollinear order with decreasing anisotropy. Given its large anisotropy, α-CoV_2O_6 may present an interesting case where a suitable balance of interactions facilitate the stabilization of collinear phases that may be observed in diffraction experiments.

Equipped with a strong uniaxial anisotropy, ferromagnetically coupled chains of localized Co^{2+} moments imbue the crystal structure and define

a second key structural feature. Casting the problem in this light provides the opportunity, by course-graining, to reduce the complexity of the interaction problem. In Fig. 4.6(c), the phase diagram of an anisotropic next-nearest-neighbor Ising model (ANNNI) as a function of the ratio $\kappa = -J_2/J_1$ is presented from Ref. [219]. Central to the model is the stipulation of an on-site $\mathbb{Z}_2$ symmetry about a global axial direction, with nearest-neighbor exchange interactions $J_0, J_1 > 0$ within $S = \frac{1}{2}$ layers and competing next-nearest-neighbor couplings $J_2 = -\kappa J_1$ between layers. Unlike the TLA model discussed previously, the ANNNI model is restricted to the consideration of commensurable collinear phases, emerging at low temperatures.

The resulting phase space is no less rich, however, with an infinity of distinct, spatially modulated phases predicted to spring from a multiphase point, based upon antiphase boundaries with wavevectors $q_j = \pi j/[(2j+1)a]$ for $j \in \mathbb{N}_0$ [219]. These states are notated by $\langle 2^{j-1}3\rangle$; referring to the axial symmetry, the states comprise $j-1$ pairs of lattice layers pointing two-up, two-down, followed by three layers all pointing up. For instance, the state $\langle 2^3 3\rangle \equiv (2,2,3)$ takes the form $\ldots \uparrow\uparrow\downarrow\downarrow\uparrow\uparrow\uparrow\downarrow\downarrow\uparrow\uparrow \ldots$, with the antiphase boundary about the center clear. For $\kappa > \frac{1}{2}$, the ground state is the four-fold degenerate antiphase $\langle 2\rangle$ phase with wavevector $q = q_{\text{inf}} = 2\pi/4a$ [219]. Experimentally, the formation of antiphase states would manifest a response in $S(\vec{Q})$ resembling the characteristic signature of stacking fault defects, with magnetic spectral weight in reciprocal space redistributed among short-range correlations.

4.3.2 Haldane's conjecture

Exotic in nature, 1-dimensional (1D) antiferromagnets are chiefly characterized by the stabilization of disordered ground states [220]. Referring to Ref. [221], we consider the antiferromagnetic Heisenberg model with spin $S = \frac{1}{2}, 1, \frac{3}{2}, \ldots$ on the 1D lattice $\Lambda_L = \{1, 2, \ldots, L\}$, where L is even. Haldane argued in 1983 that an excitation gap is manifest for chains of integer spins, but is absent in the case of half-integer spins [10, 11]. In the following exposition, we present arguments from Ref. [221] to support the manifestation of this behavior.

Spin operators act on a $(2S + 1)$ dimensional Hilbert space, denoted by $\mathfrak{h}_0$. A spin is present on each lattice site $x \in \Lambda$, and is associated with a Hilbert space $\mathfrak{h}_x$ identical to that of $\mathfrak{h}_0$. The basis state of $\mathfrak{h}_x$ corresponding to $|\psi^\sigma\rangle \in \mathfrak{h}_0$ is denoted by $|\psi^\sigma_x\rangle$, while spin configurations are determined by the multi-index $\sigma = (\sigma_x)_{x\in\Lambda}$, with $\sigma_x = -S, \ldots, S-1, S$. The Hilbert space of the spin system on the lattice Λ is given by $H = \bigotimes_{x\in\Lambda} \mathfrak{h}_x$, and has dimension $(2S+1)^{|\Lambda|}$. These definitions facilitate the definition of a standard basis, as given by the expression

$$|\psi^\sigma\rangle = \bigotimes_{x\in\Lambda} |\psi^{\sigma_x}_x\rangle \,. \tag{4.4}$$

Invoking periodic boundary conditions, we identify $\hat{S}_{L+1}$ with $\hat{S}_1$ and finally

define the spin Hamiltonian for our system by

$$\hat{\mathcal{H}} = \sum_{x=1}^{L} \hat{S}_x \cdot \hat{S}_{x+1}. \tag{4.5}$$

Assuming that our antiferromagnetic spin system occupies a connected bipartite lattice, with sublattices $|A| = |B|$, the Marshall-Lieb-Mattis theorem [222, 223] is valid and states that the ground state can be expanded in the standard basis [Eq. (4.4)]

$$|\Phi_{\mathrm{GS}}\rangle \sum_{\substack{\sigma \\ (\overline{\sigma}=0)}} \left\{ \prod_{x\in B} (-1)^{\sigma,-S} \right\} c_\sigma \, |\psi^\sigma\rangle \,, \tag{4.6}$$

with coefficients satisfying $c_\sigma > 0$ for any σ with $\overline{\sigma} = 0$. In Eq. (4.6), we have also used the definition $\overline{\sigma} = \sum_{x\in\Lambda} \sigma_x$. This theorem guarantees that the ground state $|\Phi_{\mathrm{GS}}\rangle$ is unique and has $S_{\mathrm{tot}} = 0$; this implies $(\hat{S}_{\mathrm{tot}})^2 \, |\Phi_{\mathrm{GS}}\rangle = 0$, and furthermore that $\hat{S}^{(\alpha)} \, |\Phi_{\mathrm{GS}}\rangle = 0$, for $\alpha = 1, 2, 3$. The rotation operator is defined by

$$\hat{U}_\theta^{(\alpha)} = \exp\Big[-i\theta \hat{S}_{\mathrm{tot}}^{(\alpha)}\Big] = \prod_{x\in\Lambda} \exp\Big[-i\theta \hat{S}_x^{(\alpha)}\Big], \tag{4.7}$$

and from this, we can see the ground state is $SU(2)$ invariant for any $\theta \in \mathbb{R}$, since we have $\hat{U}_\theta^{(\alpha)} \, |\Phi_{\mathrm{GS}}\rangle = |\Phi_{\mathrm{GS}}\rangle$ for $\alpha = 1, 2, 3$.

The $S = \frac{1}{2}$ antiferromagnetic Heisenberg chain is among the most well-studied problems in many-body physics; it is known to be 'exactly solvable',

thereby allowing physical quantities to be calculated under a set of plausible assumptions. The first exact solution was obtained by Bethe in 1931 [224] using an ansatz method which allowed for the computation of energy eigenstates as well as their eigenenergies. Based on exact computations such as these, the ground state and low-energy excitations of the model are generally believed to satisfy the following conditions, namely (a) the ground state is unique for both finite and infinite L, (b) there is no energy gap above the ground state energy, and finally (c) the ground state correlation function decays slowly following a power law. The Marshall-Lieb-Mattis theorem [Eq. (4.6)] guarantees the uniqueness of the ground state, as stated in (a) for finite L. In the case of $L \to \infty$, uniqueness implies an absence of long-range order, or equivalently, an absence of spontaneous symmetry breaking (c.f. Shastry's theorem [225, 226]). In 1D, the stabilization of antiferromagnetic order in the ground state order is inhibited by strong 'quantum fluctuations'.

When we refer to an absence of a gap, there is in fact a state with an infinitesimally higher energy than the ground state; this scales according to $\mathcal{O}(\frac{1}{L})$, and as L grows, a gapless continuum is manifest in the $L \to \infty$ limit. In terms of (c) above, it is believed that the two-point correlation function in the ground state has asymptotic behavior, with the functional form

$$\langle \Phi_{\mathrm{GS}} | \, \hat{S}_x \cdot \hat{S}_y \, | \Phi_{\mathrm{GS}} \rangle \sim (-1)^{x-y} \frac{\sqrt{\log |x-y|}}{|x-y|}, \tag{4.8}$$

valid for $1 \ll |x-y| \ll L$. Leading order behavior is manifest due to the

$(-1)^{x-y}/|x-y\,|$ term and gives rise to a slow decay, while by the logarithmic term provides a subtle correction [227–229]. We see that the sign factor is consistent with the expression $\langle \Phi_{\rm GS}|\, \hat{S}_x \cdot \hat{S}_y\, |\Phi_{\rm GS}\rangle > 0$ when $x, y \in A$ or $x, y \in B$ and $\langle \Phi_{\rm GS}|\, \hat{S}_x \cdot \hat{S}_y\, |\Phi_{\rm GS}\rangle < 0$ when $x \in A, y \in B$ or $x \in B, y \in A$. These inequalities follow from the Marshall-Lieb-Mattis theorem, with the sets A and B referring to each sublattice of the bipartite lattice. The functional form of the correlation function bears resemblance to that of the power law decay manifest in the classical D ≥ 2 Ising model [230, 231]; this is generally associated with critical phenomena, and indeed, a quantum critical point is well known to manifest in the $S = \frac{1}{2}$ antiferromagnetic Heisenberg chain.

In the parlance of field theory, the generally accepted assumptions about the model are consistent with a description of the low energy properties in terms of a massless field theory, without the presence of spontaneous symmetry breaking. In this case, gapless behavior is manifest corresponding to the creation of massless particles from the vacuum with infinitesimally small energy cost; such particles are mediated by a long-ranged force, decaying with a power law as in Eq. (4.8).

While it is only possible to obtain exact solutions in the case of $S = \frac{1}{2}$, it was argued by Haldane in two 1983 papers that qualitative differences can be discerned between the low energy properties of the model, depending on whether the value of S is a half-odd integer or a whole integer [10, 11]. While both half-odd and whole integer spin chains share the property of a unique ground state for both finite and infinite L, quantum fluctuations are

much stronger in the latter case. In the case of half-odd integer S, Haldane argued that the low-energy properties are characterized additionally by (a) the lack of an energy gap above the ground state, and (b) the slow decay of the ground state correlation function, following a power law; for these reasons, the ground state is critical in the parlance of statistical mechanics, and massless in the parlance of quantum field theory. These properties are in contrast to the case of integer S, which Haldane argued is characterized by (a) the existence of a nonvanishing energy gap above the ground state energy, and (b) the exponential decay of the ground state correlation function.

The existence of a gap for integer S, as stated in (a) above, implies that there exists a strictly positive difference between the ground state energy and the first excitation energy — which is nearly independent of the system size L — with the energy difference Δ_{H} known as the Haldane gap. Haldane argued, with a field theoretic analysis [10, 220, 232], that the gap energy varies according to $\Delta E \simeq 2S\exp(-\pi S)$ for $S \gg 1$. As discussed in (b) above, the ground state correlation function decays exponentially, implying that asymptotic behavior is manifest; the functional form varies according to

$$\langle \Phi_{\mathrm{GS}} | \, \hat{S}_x \cdot \hat{S}_y \, | \Phi_{\mathrm{GS}} \rangle \sim \frac{(-1)^{x-y}}{|x-y\,|^{1/2}} \exp\left[-\frac{|x-y\,|}{\xi} \right], \tag{4.9}$$

and is valid for x and y such that $\xi \ll |x-y\,| \ll L$. Here, ξ is the correlation length with $0 < \xi < \infty$, with the main term given by $(-1)^{x-y}\exp[-|x-y\,|/\xi]$. A power law correction, given by $|x-y\,|^{-1/2}$, is present as a generic feature of

the disordered ground state in 1D quantum systems and in equilibrium states of 2D classical systems. The asymptotic behavior is essentially the same as the Ornstein-Zernike form, manifest in 2D Ising model at $T > T_c$, with the addition of an oscillating sign factor on account of the antiferromagnetism. Disorder is expected in the ground state of integer S chains at low temperatures akin to that manifest generally at higher temperatures where strong thermal fluctuations dominate; the origin of this disorder is instead thought to originate from strong quantum fluctuations.

4.3.3 Lieb-Schultz-Mattis theorem

By Haldane's conjecture, we do not expect an energy gap to manifest in the spectrum of the half-integer S chain; on account of this, we therefore do not expect the presence of magnetization plateaus in this system based on energetics alone. In the case of dimerized $S = \frac{1}{2}$ magnets, however, a gap in the energy spectrum is manifest [177, 178], and thereby allows the system to support the emergence of magnetization plateaus [233]. Half-integer S chains have been proposed to host analogous Haldane gapped phases [176], and hence, plateaus of the magnetization based on general reasoning and the Lieb-Schultz-Mattis (LSM) theorem [12]. Following from this realization, spatially short ranged dilute-dimerized phases have been predicted to exist in half-integer spins [234].

Alternative explanations for the presence of magnetization plateaus in half-integer S chains include, for instance, the order by disorder mecha-

nism in which a ground state is stabilized on account of quantum fluctuations [235–237]. However, the LSM theorem states that it is possible for a spin chain to have an energy gap without breaking long-range translational symmetry in the case where the magnetization per spin satisfies the condition $(S - m) \in \mathbb{Z}$. In the case that $(S - m) = p/q$ where p and q are coprime [i.e. $\gcd(p, q) = 1$], a short-range ordered state can be stabilized preserving gauge-invariance with a periodicity of $\hat{T}^q$. In the case where magnetization plateaus are manifest, one can assign to each plateau a value of p/q and hence extract the translational symmetry of the ground state, using the general arguments outlined previously. Such periodicities represent a state magnetization induced symmetry; they are associated with modulated ground states, although their stability is dependent on the interaction terms present microscopic Hamiltonian.

Referring to Refs. [12, 176, 234], we consider a Hamiltonian $\hat{\mathcal{H}}$ that is invariant under rotations about the z-axis. We define a unitary transformation, according to

$$\hat{U} = \exp\left[-i \sum_{j=1}^{L} \left(\frac{2\pi j}{L}\right) \hat{S}_j^z\right], \tag{4.10}$$

where L specifies the size of the system. Considering a state $|\psi\rangle$ with energy ϵ, we perform a unitary rotation about the z-axis to acquire a new, rotated state with an energy ϵ'

$$\hat{\mathcal{H}}(\hat{U}\,|\psi\rangle) = \epsilon'(\hat{U}\,|\psi\rangle). \tag{4.11}$$

This leads, after algebraic manipulation, to the relation

$$\langle\psi|\,(\hat{U}^{\dagger}\hat{\mathcal{H}}\hat{U})\,|\psi\rangle = \epsilon' - \epsilon = \delta, \tag{4.12}$$

where we have defined $\delta = \epsilon' - \epsilon$; subsequent expansion of the unitary rotation operator then yields

$$\langle\psi|\,\{[1+\mathcal{O}(\tfrac{1}{L})]\hat{\mathcal{H}}[1+\mathcal{O}(\tfrac{1}{L})] - \hat{\mathcal{H}}\}\,|\psi\rangle = \delta, \tag{4.13}$$

therefore implying that $\delta \sim \mathcal{O}(\frac{1}{L})$. From this, we can infer that there exists an excited state with an energy $\mathcal{O}(\frac{1}{L})$, unless $\hat{U}\,|\psi\rangle$ and $|\psi\rangle$ are not mutually orthogonal, in which case, we instead have $\epsilon = \epsilon'$. We can demonstrate this through consideration of two eigenstates of the Hamiltonian, namely $|\psi_1\rangle$ and $|\psi_2\rangle$, having energies ϵ_1 and ϵ_2 respectively. By premultiplication of each state's Schrödinger equation with the other state, we obtain the relations

$$\langle\psi_2|\,\hat{\mathcal{H}}\,|\psi_1\rangle = \epsilon_1\,\langle\psi_2|\psi_1\rangle\,, \tag{4.14}$$

$$\langle\psi_1|\,\hat{\mathcal{H}}\,|\psi_2\rangle = \epsilon_2\,\langle\psi_1|\psi_2\rangle\,. \tag{4.15}$$

The Hermitian conjugate of Eq. (4.15) can be equated with the LHS of Eq. (4.14), from which it is clear that the equality

$$\epsilon_2\,\langle\psi_2|\psi_1\rangle = \epsilon_1\,\langle\psi_1|\psi_2\rangle \tag{4.16}$$

holds only if $\epsilon_1 = \epsilon_2$ or $\langle\psi_2|\psi_1\rangle = 0$. In other words, in the case where differing eigenvalues $|\psi_1\rangle$ and $|\psi_2\rangle$ are manifest, it must be the case that they are orthogonal. Therefore, if there is a low-lying state with a different energy to the ground state, then $|\psi\rangle$ and $\hat{U}|\psi\rangle$ are necessarily orthogonal.

We suppose now that $\hat{\mathcal{H}}$ is invariant under lattice translations, as encoded by the operator $\hat{T}$; this symmetry of the system provides the mapping

$$\hat{U} \to \hat{T}\hat{U}\hat{T}, \tag{4.17}$$

and by inserting our definition of the unitary operator [Eq. (4.10)], we find

$$\begin{aligned}\hat{T}\hat{U}\hat{T} &= \exp\left[-i\sum_{j=1}^{L}\left(\frac{2\pi j}{L}\right)\hat{S}^z_{j+1}\right] \\ &= \exp\left[-i\sum_{j=1}^{L}\left(\frac{2\pi j}{L}\right)\hat{S}^z_{j}\right]\exp\left[-i\left(\frac{2\pi}{L}\right)\sum_{j=1}^{L}\hat{S}^z_{j}\right]\exp\left(2\pi\hat{S}^z_1\right).\end{aligned} \tag{4.18}$$

This leads us to the equality

$$\begin{aligned}\hat{T}\hat{U}\hat{T} &= \hat{U}\exp\left[2\pi i\hat{S}^z_1 - i\left(\frac{2\pi}{L}\right)\sum_{j=1}^{L}\hat{S}^z_j\right] \\ &= \hat{U}\exp\left[2\pi i\left(S-m\right)\right],\end{aligned} \tag{4.19}$$

where we have used periodic boundary conditions in simplifying the expression, and further identified the magnetization per site as $m = \frac{1}{L}\sum_{j=1}^{L}\hat{S}^z_j$. We

find, therefore, that the effect of the translation operator is to introduce a phase factor, akin to a Berry phase, with the topological index $C = (S - m)$.

We revisit the considerations of orthogonality of $|\psi\rangle$ and $\hat{U}|\psi\rangle$, and apply the mapping of $\hat{U}$, as provided by Eq. (4.17). If these two states are to be orthogonal, then we require that

$$\langle\psi|\hat{U}|\psi\rangle = \langle\psi|\hat{U}|\psi\rangle \exp\left[2\pi i(S-m)\right]. \tag{4.20}$$

It is clear that for this to hold true, we require (a) that the initial and rotated states are orthogonal, and (b) $(S-m) \in \mathbb{Z}$. In the case that $(S-m) \notin \mathbb{Z}$, there exists a low lying state with energy $\mathcal{O}(\frac{1}{L})$. As $L \to \infty$ we therefore expect a continuum of such states, and hence gapless excitations. By contrast, if $(S-m) \in \mathbb{Z}$ there is no low-lying state with energy $\mathcal{O}(\frac{1}{L})$; a gap to the first excited state is therefore manifest. When a gap to the first excited state is present, a slowly ramping applied magnetic field will not give rise to a deformation of the ground state to another eigenstate. Consequently, a magnetization plateau can be realized; this argument can also be applied in these cases of higher order $\hat{T}^q$ symmetries, with the quantization condition given by $n(S-m) \in \mathbb{Z}$.

An analogy with the fractional quantum Hall effect (FQHE) can be made if we consider cases where the quantization is not met. For instance, consider the case where $(S-m) = \frac{1}{4}$; from Eq. (4.18), we know that the unitary rotation $\hat{U}$ has the effect of changing the eigenvalue of $\hat{T}$ by a phase factor

$\exp[2\pi i(S-m)]$. In this case, repeated application of the $\hat{U}$ operator three times results in three distinct $\hat{T}$ eigenvalues, with the fourth application of $\hat{U}$ resulting in the same eigenvalue as $|\psi\rangle$. Since the three orthogonal rotated states have low energy $\sim \mathcal{O}(\frac{1}{L})$, in the limit $L \to \infty$ the un-rotated state and its three rotated states form a four-fold degenerate subspace. These four states all have different eigenvalues of $\hat{T}$, however; consequently, the $(S-m) = \frac{1}{4}$ state is endowed with a $\hat{T}^4$ symmetry. We should therefore expect a gap in this four-site translation-invariant state, as it is not possible for it to be rotated by $\hat{U}$ to an orthogonal state with an energy $\mathcal{O}(\frac{1}{L})$.

If the energies can be accessed, in theory other $\hat{T}^q$ states can be probed. Some of these may be unstable, however, and a more detailed examination of the interaction terms in Hamiltonian via a bosonization procedure could impart a more rigorous understanding of plateau selection rules. Alternatively, based on an intuition for the ground states of chain-like systems, we may hypothesize that from classical point of view, possible ground states may manifest in the form of (a) the $\hat{T}^2$ state with $(S-m) = \frac{1}{2}$ given by $\ldots\uparrow\downarrow\uparrow\downarrow\ldots$, or (b) the $\hat{T}^4$ state with $(S-m) = \frac{1}{4}$ given by $\ldots\uparrow\uparrow\downarrow\downarrow\uparrow\uparrow\downarrow\downarrow\ldots$. Other possible ground states could be stabilized such as VBS-like states, or 'dimer density waves' type states; in the case of integer values, however, states are gapped and cannot be smoothly transformed with the application of field, leading to the emergence of magnetization plateaus and a Bloch state analogue of QHE [168, 169, 176].

4.4 Experimental details

Before embarking on an investigation of the field induced plateau states, as described in Sec. 4.5.3, a concrete understanding of the virgin state is required. In general, the long wavelength properties of correlated d-electron systems are complicated by an active orbital degree of freedom. For instance, orbital ordering has been found to drive multiferroicity and magnetoelectric coupling in GeV_4S_8 [238], while in the related ferroelectric Vanadate system $Co_2V_2O_7$, a noncollinear magnetic ground state has been reported in concert with magnetoelastic coupling [239]. After developing a more complete understanding of the ground state, we investigate field-induced magnetic correlations in the vicinity of the plateaus in Sec. 4.5.3 and the stability of these states in Sec. 4.5.4.

Single crystal [3] and powder [209] samples of α-CoV_2O_6 used in the experiments described in this chapter were prepared using the flux method by colleagues Chris Stock and Manila Songvilay at the University of Edinburgh. Our samples were characteristically small with typical masses in the range $m = 0.6 - 4\,\mathrm{mg}$, and spatial dimensions typified by the following ranges of length $l = 2 - 4\,\mathrm{mm}$, width $w = 0.6 - 2\,\mathrm{mm}$, and thickness $t = 0.3 - 0.7\,\mathrm{mm}$. The morphological characteristics of our single crystal samples were investigated by XRD, carried out on a number of a number of samples using a Laue diffractometer at the materials characterization lab (ISIS, UK). Our samples were found to reliably conform to the features expected from crystals of the

Brannerite series; these synthetic Vanadates form with a prismatic habit and commonly display an orthogonal prism zone, as illustrated in Fig. 4.2(a). This morphological feature is useful for coalignment since prominent $(\overline{h}, 0, l)$ and $(h, 0, \bar{l})$ faces manifest on opposite sides of the crystal, thereby allowing for the convenient assembly of large crystal volumes with minimal mosaic — albeit at the cost of introducing an inconsequential π-domain.

4.4.1 Ground state magnetism

The WISH diffractometer (ISIS, UK) was used to characterize the temperature dependence of single crystals and powders in zero applied magnetic field; the results of these investigations are presented in Secs. 4.5.1 and 4.5.2 respectively. A 4.36 g powdered sample was sealed within a 6 mm Vanadium can to achieve a low degree of background contamination. Data were collected in increments of 0.5 K from 1.4 K before decrementing to increments of 0.25 K near T_N for enhanced detail in the vicinity of the critical region around the antiferromagnetic transition.

For this experiment, the piezoelectric jaws in the last few meters of the instrument were configured to deliver a beam divergence of 0.2°, while the counter-rotating Fermi choppers along the primary flight path of the beamline were phased to provide measurements in a single time-of-flight frame, thereby reducing the degree of frame overlap. This facilitates measurements with a spatial resolution of $\Delta Q/Q = 0.03\,\%$, as defined in Chap. 3, necessary for accurate Le Bail refinements to track the evolution of unit cell parameters.

Good counting statistics were required in this investigation of the coupling between spin and lattice systems for the sufficiently accurate determination of bond lengths and their evolution with temperature. Accordingly, data was collected continuously until a beam current of 33 µA was obtained at 16 K to facilitate an accurate refinement of paramagnetic structure, while in the ordered phase at 1.5 K an incident beam current of 10 µA was recorded. At intermediate temperatures, an incident beam current of 5 µA was recorded to facilitate a cyclic refinement of the structure with changing temperature. Data was normalized to the incoherent scattering of Vanadium and grouped into two sets of five banks, sharing an average 2θ value, using the `MantidPlot` program [38]. Structural refinements[6] were carried out using the `Jana2006` program [143], with a separate instrument resolution function used for each set of angle-grouped banks.

The temperature dependence of nuclear and magnetic reflections was studied on a single crystal sample aligned with $(h, 0, l)$ in the horizontal scattering plane, mounted upon a small Aluminum goniometer, secured in Aluminum foil, and tied off with Cadmium wire. The segments of the mount exposed to the beam shielded were with Cadmium for a minimal and predictable background signal, and further improved through use of a dedicated low-

[6] We note that the neutron refinements would have benefited from the refinement of the Vanadium position and anisotropic displacement factors (ADPs) from XRD data (as defined in Chap. 3), on account of the small coherent neutron scattering length for Vanadium. Due to technical difficulties with the low temperature x-ray diffractometer available to us at the Centre national de la recherche scientifique (CNRS), however, this was unfortunately not possible.

background Oxford Instruments Variox cryostat. The Fermi choppers along the primary flightpath were phased to deliver a double frame for maximum flux at the sample position. Characterization on the RITA instrument, as described in Sec. 4.4.2, found an enhancement of intensity of the nuclear $\vec{Q} = (0, 0, 2)$ reflection below T_{N}. To investigate the possibility of a potentially weak incommensuration — that is, an additional $\vec{k} = 0$ component — the equivalent $\vec{Q} = (0, 0, \overline{2})$ reflection was oriented and measured at 90°, where diffracted flux is at its highest for comparison to the RITA data. This reflection is appropriate since it occurs at low Q and therefore suffers minimal dampening from the effects of the magnetic form factor $f(Q)$.

For this experiment, the piezoelectric jaws were configured to deliver a beam divergence of 0.4°, with the beam-scraper configured to shape the exit profile of the beam to 20×40 mm. Data were collected between the cryostat base temperature 1.43 K and 15.5 K, with counting statistics defined by the requirement of 10 µA beam current per run. Temperature increments between runs were decremented to steps of 0.125 K between 12 and 15.5 K for detail around the transition, with the final run at 16 K in the paramagnetic phase having counting statistics defined by a collected beam current of 15 µA to enable robust comparisons. In addition to the primary crystallite, intensity from a smaller, secondary crystallite is present; these contact twins are related by an Albite twin law, characterized by the twin-plane $\{h, 0, 0\}$. Separate UB matrices were refined for each crystallite, used in the conversion between the lab frame and reciprocal lattice frames. These were maintained throughout

subsequent analysis of reflections. Raw data was normalized to incident beam current (μA) and to incident monitor counts after being cropped between the resolution limits $6 \times 10^3 - 99 \times 10^3$ μs of time-of-flight. Both panel and monitor data were normalized to the incoherent scattering of an absorption corrected $V_{0.95}/Nb_{0.05}$ sphere dataset with excellent statistics.

4.4.2 Field-induced magnetism

Exploratory magnetization experiments below 0.1 K were carried out by colleagues at the Institut Néel in Grenoble on a single crystal sample, with field oriented approximately along the *c*-axis, using a low temperature SQUID magnetometer [240] and a Physical Properties Measurement System (PPMS). The results of these measurements are presented alongside in-field neutron diffraction data in Sec. 4.5.3.

Further magnetization measurements were carried out using a coaligned array of single-crystals of total mass 6 mg, mounted by GE varnish to a copper plate with dimensions 4 mm × 4 mm × 0.1 mm. Measurements at $T = 2.5$ K were carried out in a PPMS, equipped with vibrating sample magnetometer (VSM) at Cardiff University. Additional magnetization measurements at $T = 0.4$ K were performed in a Magnetic Properties Measurement System (MPMS3) equipped with a sub-2 K *i*Helium3 dilution system at the materials characterization lab, ISIS, UK. In both cases, the coaligned sample array was secured in a standard-issue Quantum Design straw mount. The degeneracy of the states underlying the magnetic transitions were investigated by

examining the hysteresis effects associated with minor field-loops, along with the dynamical properties of the plateaus, as described in Sec. 4.5.4; these were investigated by considering the effects of varying field-sweep rates, as well as the magnetic relaxation resulting from interrupted field sweeps. The coaligned sample array was aligned such that the vertical magnetic field was orientated principally along the easy c-axis, but with a small component out of the ac-plane. Despite best efforts to mount the sample array robustly, comparison against directionally dependent magnetization data in Ref. [9] suggests that some slip or reorientation occurred in applied fields, and was most severe at low temperatures. It is possible that this was caused by shear forces on the corners of the copper plate — initially installed biting into the internal walls of the straw — induced by thermal contraction during cooling.

Neutron diffraction experiments under applied magnetic fields were carried out on the WISH diffractometer (ISIS, UK). Due to kinematic constraints of the vertical magnetic field layout, access to magnetic Bragg peaks given the reduced detector coverage required an appreciable component of the magnetic field out of the ac-plane. Refined from a single nuclear and single magnetic Bragg reflection, the sample orientation was defined by a UB matrix with components of 2.1°, 15.2°, and 85.3° along the a, b, and c axes respectively. Single crystals were studied between $T = 0.1 - 4.5\,\mathrm{K}$ over the course of two beamtime cycles, with great care taken to ensure that the sample orientation was the same each time; the results obtained from these experiments are

presented in Sec. 4.5.3. Data were collected between absolute field limits[7] of $\mu_0 \mathrm{H} = 0.015 - 6\,\mathrm{T}$ in all four quadrants of the magnetization curve. This provided information on the hysteretic nature of the magnetic correlations, with counting statistics of 30 µA recorded at each field step. Raw data was normalized to incident beam current (µA) and to incident monitor counts after being cropped between the resolution limits $6 \times 10^3 - 99 \times 10^3\,\mu\mathrm{s}$ of time-of-flight. Both panel and monitor data were normalized to the incoherent scattering of an absorption corrected $\mathrm{V}_{0.95}/\mathrm{Nb}_{0.05}$ sphere dataset with excellent statistics. The intensity of magnetic reflections was obtained by spherical integration in reciprocal space, while linecuts through the diffuse scatter were calculated by binning along, and perpendicular to, the direction of the antiferromagnetic propagation wavevector, $\vec{k} = (1, 0, \frac{1}{2})$. The $\mu_0 \mathrm{H} = 6\,\mathrm{T}$ and $-6\,\mathrm{T}$ runs, at which the magnetic structure is fully polarized in the ferromagnetic phase, are used for background subtraction — the corresponding background subtraction for each run was dependent upon whether the given value of applied field was within the first two or last two quadrants respectively.

The MORPHEUS instrument was used to align a single crystal sample with $(h, 0, l)$ in the horizontal scattering plane ahead of a diffraction experiment in horizontal magnetic field using the RITA triple-axis spectrometer (both at PSI, Switzerland), to explore the directional dependence of applied field on the magnetic correlations manifest at low temperatures. An initial character-

[7] A small field of $\mu_0 \mathrm{H} = 0.015\,\mathrm{T}$ was used as an effective 'zero' since the Aluminum components of the sample environment are superconducting at this temperature in the absence of a magnetic field.

ization was carried out in an Orange cryostat in zero applied magnetic field, and the magnetic order parameter was measured in the Néel state over the range $T = 1.8 - 16\,\mathrm{K}$. Interestingly, the nuclear $\vec{Q} = (0, 0, 2)$ reflection was found to display a temperature dependence resembling that which would be expected from a second-order magnetic transition. This observation partly motivated a reinvestigation of the magnetic ground state — as described in Secs. 4.5.1 and 4.5.2 — specifically aiming to harvest more reflections since the detector coverage of RITA is limited, and to track their temperature dependence in order to determine whether this observation was the signature of an incommensuration of the magnetic ground state previously overlooked, or perhaps resulting from magnetoelastic coupling. Measurements in applied magnetic field were carried out using a dilution refrigerator insert to study the field dependence of the magnetic correlations in the vicinity of the magnetization plateaus at $T = 0.1\,\mathrm{K}$, with the horizontal magnetic field oriented along the c-axis, and with fixed a $E_i \equiv E_f = 5\,\mathrm{meV}$. Data were collected at fields up to $\mu_0\mathrm{H} = 6\,\mathrm{T}$, normalized to incident monitor count rate, and placed on an absolute scale by normalization to the incoherent scattering of a standard Vanadium dataset with good counting statistics. Given the reasonably low background achieved in the experiment, no subtraction was applied to the data, as presented in Sec. 4.5.3.

To reconcile the results obtained from differing field geometries on the WISH and RITA instruments — having nonzero and zero components of field along the b-axis respectively — neutron powder diffraction was carried out at

$T = 0.1\,\mathrm{K}$ using a dilution refrigerator insert, and additionally at $T = 1.5\,\mathrm{K}$ on the TASP triple-axis spectrometer (PSI, Switzerland). Both a monochromator and analyzer were employed, with a fixed $\mathrm{E}_i = 3\,\mathrm{meV}$ selected to achieve a low degree of background contamination of the diffraction signal. A 6 g powdered sample was pressed into a polycrystalline pellet to prevent the reorientation of grains in applied field and mounted in an Aluminum can; given the statistically random distribution of grains in powder, the applied field acted isotropically upon the sample. Cooling was enhanced by supplementary Helium exchange gas pressurized to 10 mbar, and connected to the mixing chamber of the dilution refrigerator via a weak link, which served as an additional pathway of heat transfer away from the sample. Beam shaping was achieved using a Beryllium filter, with $80'$ collimation on the scattering side. The results obtained from these experiments are presented in Sec. 4.5.3, with data normalized to incident monitor count rate for relative comparisons of the distribution of intensity throughout reciprocal space.

4.5 Results and discussion

We first discuss the characterization of the magnetic ground state by single crystal and powder neutron diffraction on the WISH instrument (ISIS, UK). Motivated by the observation of a second-order type development of intensity on the $\vec{Q} = (0, 0, 2)$ position from zero-field measurements on the RITA-II instrument (PSI, Switzerland) below T_N — kshown in Fig. 4.7 — we consider

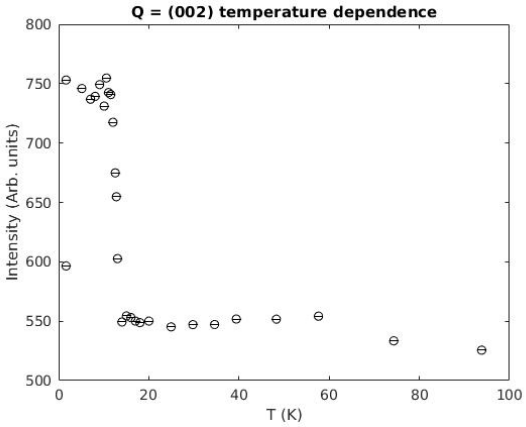

Figure 4.7: Temperature dependence of the $Q = (0, 0, 2)$ reflection observed on the RITA-II instrument in zero applied magnetic field. The enhancement of intensity below T_{N} is anomalous and suggests either the presence of an antiferromagnetic $\vec{k} = 0$ component, or strain arising from magnetoelastic coupling. This observation motivates a reinvestigation of the nature of the magnetic ground state, discussed in Secs. 4.5.1 and 4.5.2.

the possibility of an incommensuration of the Néel state. Since no opening of the magnetization curve is observed in this temperature region, any manifesting $\vec{k} = 0$ component would be associated with an antiferromagnetic-type distortion. The intensity variation appears to track that of the magnetic order parameter, so we note the possibility that multiple scattering is responsible, as well as the possibility of the coincidence of a twin satellite reflection on the $\vec{Q} = (0, 0, 2)$ position. To investigate this, we carried out single-crystal neutron diffraction on WISH to follow the temperature dependence of a number of magnetic reflections in the $(h, 0, l)$.

On the other hand, the intensity enhancement below T_{N} may be the signature of a magnetoelastic distortion giving rise to strain as a result of spin-phonon coupling, with a concomitant release of extinction. We carried out neutron powder diffraction on WISH to investigate any change to the structure, comparing refinements at each temperature step below T_{N}. We seek clarification of this question in the following sections Secs. 4.5.1 and 4.5.2, and aim to explain the result obtained on RITA-II before proceeding to investigate the field-induced correlations in the vicinity of the observed magnetization plateaus.

4.5.1 Néel state robust to incommensuration

In the ordered phase, the magnetic structure is defined by the Néel wavevector $\vec{k} = (1, 0, \frac{1}{2})$ which corresponds to an $(a, b, 2c; 0, 0, 0)$ supercell, characterizing the magnetic lattice Λ_k [209, 212]. Diagonal stripe-like order is manifest on account of the centering of $\vec{k}$, while the modulation of the crystal potential can be can be identified with a distortion at the M-point of the BZ. This provides insight into the nature of the irreducible representations (irreps) involved in the stabilization of the ordered state. Considering the Néel wavevector, the little co-group of unitary symmetries is $G_k = 2/m$, with elements

$$\{1|0\}, \quad \{2_{010}|0\}, \quad \{\bar{1}|0\}, \quad \{m_{010}|0\},$$

Table 4.1: The characters of the irreducible representations of the unitary little co-group $\chi_D(g) = \mathrm{Tr}\, D(g)$ for matrix representations D of the elements $g \in G_k = 2/m$. The decomposition with respect to the M point $(1, 0, \frac{1}{2})$ of the BZ, associated with the magnetic ordering of Co^{2+} moments occupying the $4c$ Wyckoff position, results in the sum of irreducible representations $\Gamma = 2mM_1^- \oplus mM_2^- = 2\Gamma_2 + \Gamma_1$.

Irrep	Basis vector	$\mathrm{Tr}\, D(g)$ for $g \in G_k$			
		$\{1\|0\}$	$\{2_{010}\|0\}$	$\{\bar{1}\|0\}$	$\{m_{010}\|0\}$
$\Gamma_1 = mM_1^+$	–	1	1	1	1
$\Gamma_2 = mM_1^-$	$\psi_1 = (100)$ $\psi_2 = (001)$	1	1	−1	−1
$\Gamma_3 = mM_2^+$	–	1	−1	1	−1
$\Gamma_4 = mM_2^-$	$\psi_3 = (010)$	1	−1	−1	1

while the magnetic little co-little group, M_k, is the antiunitary group $2/m1'$ of primed elements.

The magnetic representation for a given point in the BZ can be decomposed into contributions from the irreps of the little co-group $G_k = 2/m$ via the relation $\Gamma = \sum_\nu n_\nu \Gamma_\nu$, where n_ν is the multiplicity of the irrep Γ_ν calculated by the relation $n_\nu = [n(G_k)]^{-1} \sum_{h \in G_k} \chi_{\Gamma_\nu}(h) \chi_{\Gamma_\nu^*}(h)$. The Néel wavevector alone completes the star of $\vec{k}$ with degenerate forms related by lattice translations $\{1|\vec{t}\} \in \Lambda$. By considering magnetic distortions about the Co $4c$ Wyckoff site, the possible irreps of the magnetic phase can be elucidated. In line with expectations from Landau theory, a single $\vec{k}$-active defines the transition. The only irrep compatible with the manifesting magnetic order is the mM_1^- mode. Its action on elements of the little co-group

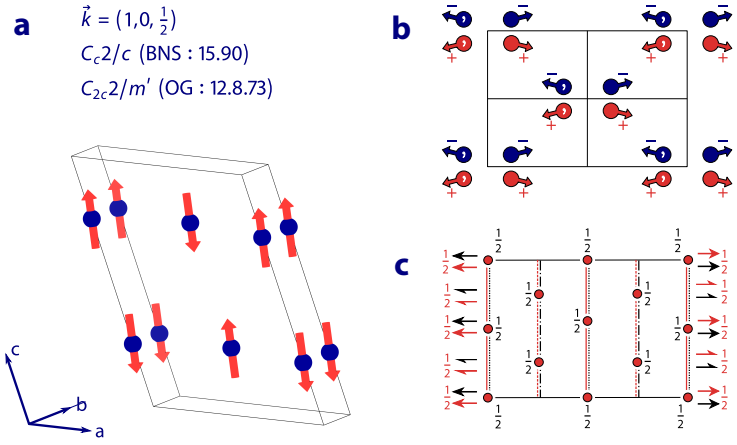

Figure 4.8: (a) shows the magnetic structure of the Néel state, with origin at the central $2/m'$ position. The stabilization of the long-range ordered phase below T_{N} is associated with a reduction of symmetry consistent with the group–subgroup relation $C2/m'$ (BNS 12.59) $\rightarrow C_c2/c$ (BNS 15.90). (b-c) shows the symmetries of the magnetic structure. See Refs. [54, 154] for notation.

$g \in G_k$, along with the basis vectors of the representations $\Gamma_m(4c)$ of G_k, are tabulated in Table 4.1.

The ordered phase is characterized by the magnetic space group C_c2/c (BNS 15.90) [209, 212], and is shown in Fig. 4.8(a) along with the magnetic symmetries in Fig. 4.8(b-c). We confirm the nuclear and magnetic structures by the refinement of neutron powder diffraction data obtained from the WISH diffractometer (ISIS, UK) at $T = 16\,\mathrm{K}$ and $T = 1.4\,\mathrm{K}$ respectively. Data was processed and grouped by bank in the `MantidPlot` program, and Rietveld refinements were carried out using the `Jana2006` program. Data from the $2\theta = 90°$ detector banks was refined above transition to obtain the nuclear

Table 4.2: Crystal structure parameters for α-CoV_2O_6 at $T = 16\,\mathrm{K} > T_\mathrm{N}$, obtained from a refinement of neutron powder diffraction data taken on the WISH instrument, ISIS. Data processing and grouping of banks by average 2θ was achieved using the `MantidPlot` framework [38]. The whole reduced dataset was used in a refinement of the nuclear structure using `Jana2006` [143], with separate instrument resolution functions for each set of grouped banks. For each atom type, the Wyckoff position (WP) and site symmetry are given, along with its fractional coordinates $(x/a, y/b, z/c)$, isotropic displacement factor (B_iso), and site occupation factor (SOF).

Atom	x	y	z	B_iso	SOF	WP	Site symmetry
Co	0.0000	0.0000	0.5000	0.0067(12)	1.00	$2c$	$2/m$
V	0.188(3)	0.0000	0.129(4)	0.027(5)	1.00	$4i$	m
O1	0.0348(2)	0.0000	0.2239(3)	0.0028(5)	1.00	$4i$	m
O2	0.3476(2)	0.0000	0.3911(3)	0.0033(4)	1.00	$4i$	m
O3	0.6916(2)	0.0000	0.0623(3)	0.0015(4)	1.00	$4i$	m

$G = C2/m$, $a = 9.2305(2)$ Å, $b = 3.50243(8)$ Å, $c = 6.59994(16)$ Å, $\beta = 112.0457(14)^\circ$
GOF = 8.78 %, $R_\mathrm{p} = 3.67\,\%$, $R_\mathrm{wp} = 4.85\,\%$

structure, while data from the $2\theta = 122^\circ$ detector banks was refined below the Néel transition to obtain the magnetic structure at both base temperature and intermediate temperatures. The fitted profiles are shown shown in Fig. 4.9(a) above the transition and Fig. 4.9(b) at base temperature respectively. The comparison between observed and calculated structure factors are shown in the insets, summarizing the quality of the refinements.

The refinement of the paramagnetic phase above the transition at $T = 16\,\mathrm{K}$ was terminated with figures of merit given by GOF = 8.78 %, $R_\mathrm{p} = 3.67\,\%$, and $R_\mathrm{wp} = 4.85\,\%$. The atomic positions and isotropic displacement factors obtained from this refinement are given in Table 4.2. We note that a more

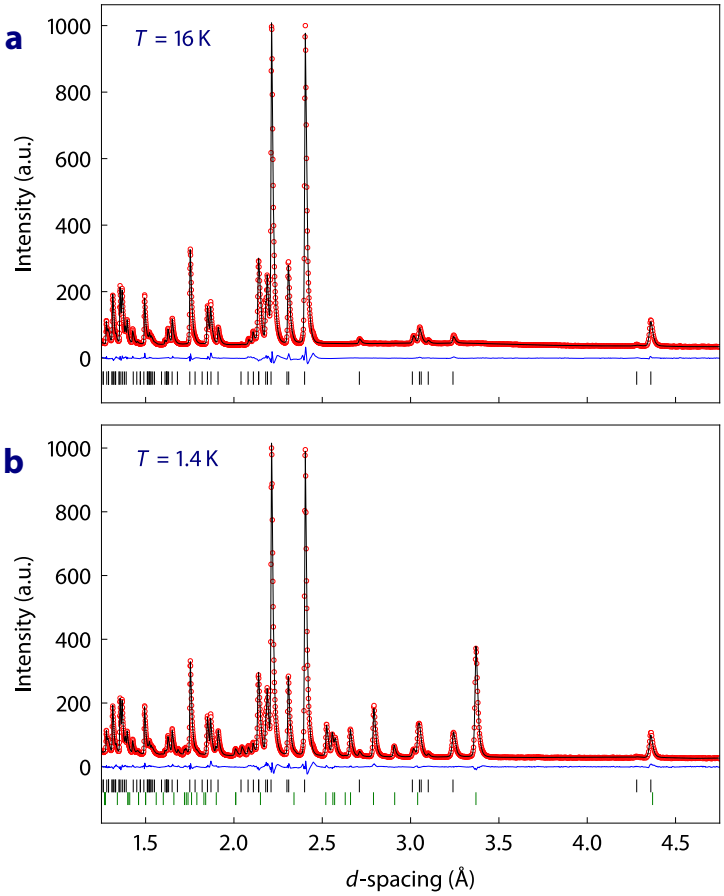

Figure 4.9: Neutron powder diffraction results obtained on the WISH diffractometer in zero applied field, at (a) $T = 16\,\mathrm{K}$ and (*b*) $T = 1.4\,\mathrm{K} < T_\mathrm{N}$. Rietveld refinements of the nuclear [panel (a)] and magnetic [panel (b)] phases are shown, with reflection positions indicated. Below T_N, the intensity profile of the diffraction is marked by enhanced spectral weight at reflection positions consistent with the propagation wavevector $\vec{k} = (1, 0, \frac{1}{2})$ at the M point of the BZ. The relationship between observed and calculated structure factors $F_\mathrm{calc}/F_\mathrm{obs}$ for the refined models are shown in the insets. The refinement above T_N, at 16 K, was terminated with GOF = 8.78 %, $R_\mathrm{p} = 3.67\,\%$, and $R_\mathrm{wp} = 4.85\,\%$. Meanwhile, deep within the Néel state at cryostat base temperature, $T = 1.4\,\mathrm{K}$, the profile was refined with overall figures of merit GOF = 5.40 %, $R_\mathrm{p} = 4.20\,\%$, and $R_\mathrm{wp} = 5.32\,\%$. The refined moment at base temperature was found to have components $m_a = 0.951(64), m_b = 0.000(0)$, and $m_z = 5.394(79)$, with a total moment of $m_\mathrm{tot} = 4.721(79)$ consistent with the ranges reported in previous reports [209, 212].

accurate refinement could have been obtained if XRD was carried out at the same temperature to refine the Vanadium position and isotropic displacement factor, subsequently fixing these parameters in the neutron refinement, since the coherent neutron scattering length of Vanadium is small. The diffractometer available to us at the CNRS was experiencing technical difficulties, however, so this could not be done. Despite this, considering the figures of merit obtained and the linear relationship between observed and calculated structure factors with few outliers, the fit quality is acceptable.

Meanwhile, the refinement of the ordered phase at $T = 1.4\,\mathrm{K}$ was terminated with figures of merit given by GOF $= 5.40\,\%$, $R_\mathrm{p} = 4.20\,\%$, and $R_\mathrm{wp} = 5.32\,\%$. A similar relationship between observed and calculated structure factors was obtained, characterizing an acceptable refinement. The refined moment in the Néel phase had components $m_a = 0.951(64), m_b = 0.000(0)$, and $m_z = 5.394(79)$, with a total moment of $m_\mathrm{tot} = 4.721(79)$ consistent with previous reports [209, 212]. No spectral weight was found to distribute among incommensurations of the Néel state, with no addition satellite peaks characterizing the presence of a second propagation vector manifest.

We show in Fig. 4.10 variation of the integrated intensity of the $\vec{Q} = (3, 0, \frac{1}{2})$ and $\vec{Q} = (0, 0, \overline{2})$ reflections obtained from single crystal on WISH, along with the variation of integrated intensity of the $\vec{Q} = (\overline{1}, 0, \frac{1}{2})$ obtained from single crystal on RITA-II. The intensity variation of the magnetic peaks characterize the magnetic order parameter $|M|^2 \propto |T - T_\mathrm{N}|^{2\beta}$ and are in broad agreement across instruments, corroborating the underlying Ising nature of

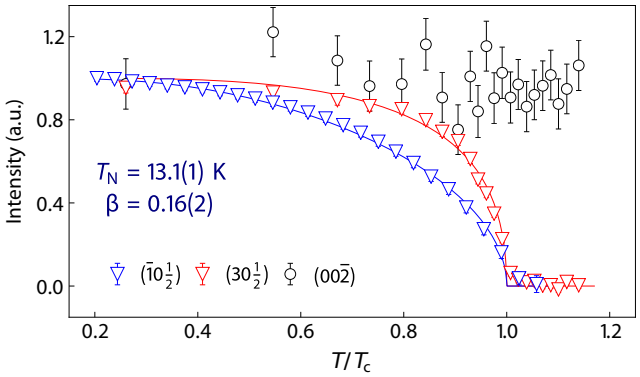

Figure 4.10: Magnetic order parameter $|M|^2 \propto |T - T_N|^{2\beta}$. Shown is the temperature dependence of the $(\bar{1}, 0, \frac{1}{2})$ reflection measured on RITA-II, along with the $(3, 0, \frac{1}{2})$ and nuclear $(0, 0, \bar{2})$ reflections measured on WISH. No additional satellite peaks were observed at the temperatures studied, while the variation of the nuclear $(0, 0, \bar{2})$ is centered on a constant value, within errorbar, indicating no magnetic $\vec{k} = 0$ contribution at the BZ center.

the material. The fit from WISH reveals $\beta = 0.16(2)$ consistent with the 2D-Ising universality class [241].

Our WISH data shows no evidence of the enhancement of intensity found for the $\vec{Q} = (0, 0, 2)$ reflection on the RITA-II instrument, with the equivalent $\vec{Q} = (0, 0, \bar{2})$ reflection effectively constant with decreasing temperature below T_N. Indeed, no other nuclear reflections were found to display anomalous temperature dependence, suggesting that there is in fact no additional $\vec{k} = 0$ contribution, and purely magnetic incommensuration of the ground state. These data suggest that the magnetic transition is driven by a single active irreducible representation, with agreement between WISH and RITA-

II, except with regard to the temperature variation of the $\vec{Q} = (0, 0, 2)$ type reflection. This observation lends weight to the possibility that multiple scattering, or perhaps the coincidence of a magnetic satellite from a twin crystallite with the $\vec{Q} = (0, 0, 2)$ position, explains the anomalous temperature dependence observed on RITA-II.

4.5.2 Néel state robust to magnetoelastic distortions

The temperature dependence of the lattice parameters was obtained from the refinement of our neutron powder diffraction data collected on the WISH instrument. These results are shown in Fig. 4.11, with the Q-resolution of WISH indicated. After the initial refinements of the nuclear structure at $T = 16\,\mathrm{K}$ and magnetic structure at base temperature $T = 1.4\,\mathrm{K}$, a cyclic refinement was carried out to refine the magnetic structure at intermediate temperatures using the `Jana2006` program. The refinement was run twice—once starting from base temperature and running up to $T = 15.5\,\mathrm{K}$, and then additionally in reverse order to check thata the refinement did not terminate along the way in local minima. The results from both sets of cyclic refinements were consistent, and demonstrate that the lattice parameters do not vary beyond experimental Q-resolution. For these measurements, WISH was run in high-resolution mode with $\Delta Q/Q = 0.03\,\%$.

Similarly, no variation to the bond lengths defining the oxygen coordination environments was found, suggesting no active distortion modes coupling the magnetic and structural subsystems, as would be observed for the case of

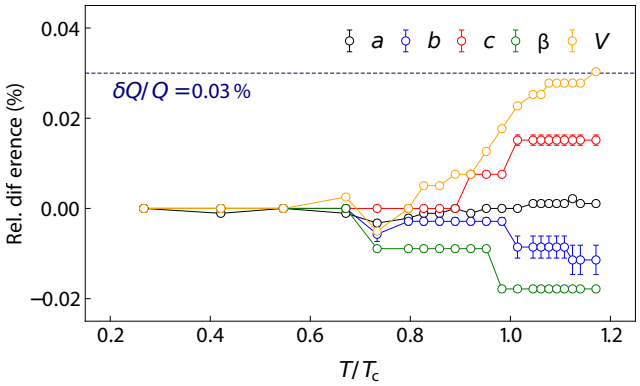

Figure 4.11: Temperature dependence of unit cell metrics. Within resolution $\Delta Q/Q = 0.03$, there is no significant change to the lattice parameters, and therefore based on this there is no measured magnetoelastic effect in the virgin state.

Jahn-Teller or Spin-Peierls distortions. We conclude this section by suggesting that the anomalous temperature dependence of the $\vec{Q} = (0, 0, 2)$ reflection observed on RITA-II was most likely an artifact resulting from either multiple scattering, or from the coincidence of a magnetic satellite from a twin crystallite with the position of the nuclear $\vec{Q} = (0, 0, 2)$ reflection in reciprocal space. Having now achieved a satisfactory understanding of the nature of the magnetic ground state, we continue to investigate the more complex phenomena observed in applied magnetic fields.

4.5.3 Commensurable SRO induced by applied fields

In this section, we combine low temperature magnetization with neutron diffraction measurements, to develop an understanding of the magnetic cor-

relations in states induced by applied fields. We first consider the results of single crystal neutron diffraction carried out on the WISH instrument (ISIS, UK). As discussed in Sec. 4.4, the sample was aligned in the $(h, 0, l)$ plane and mounted in the vertical magnet. The detector coverage is limited in this reduced geometry configuration, so while it was possible to align the easy c-axis approximately parallel to the vertical direction of applied field, it was necessary to impose a slight misorientation of the sample to provide access to the required magnetic reflections. The resulting sample orientation was such that the vertical magnetic field had components of 2.1, 15.2, and 85.3° along the a, b and c axes respectively. A summary of results obtained at $T = 0.1\,\mathrm{K}$ after zero-field cooling are shown in Fig. 4.12. Linecuts parallel to the direction of the antiferromagnetic propagation vector $[h, 0, \frac{1}{2}h]$ are shown alongside the corresponding $(h, 0, l)$ plane for magnetic fields increasing and decreasing about saturation at $\mu_0\mathrm{H} = 6\,\mathrm{T}$ where the magnetic structure is fully polarized in the $\vec{k} = 0$ ferromagnetic phase. As described in Sec. 4.4, this run at $\mu_0\mathrm{H} = 6\,\mathrm{T}$ has been used as a measure of the background signal, and has thus been subtracted from the data presented.

The $\vec{Q} = (1, 0, \frac{1}{2})$ peak observed at[8] $\mu_0\mathrm{H} = 0.015\,\mathrm{T}$ is shown in Fig. 4.12(a) and is representative of long-range magnetic order, consistent with the virgin antiferromagnetic propagation wavevector, corresponding to the $(a, b, 2c; 0, 0, 0)$

[8] We note that instead of a starting measurement at zero applied field exactly, a small applied field (namely $\mu_0\mathrm{H} = 0.015\,\mathrm{T}$) was necessary to inhibit a superconducting response in Al components of the sample environment that would contribute to an increased background in the scattering response.

supercell described in Secs. 4.5.1 and 4.5.2. No other magnetic peaks were observed at this temperature and field, which confirms the stability of the magnetic ground state down to $T = 0.1\,\mathrm{K}$; in terms of the magnetic symmetry, we can ascribe the periodicity $\langle\hat{T}^2\rangle = \uparrow\downarrow$ to this state. Upon increasing the applied field to $\mu_0\mathrm{H} = 3.25\,\mathrm{T}$ [shown in Fig. 4.12(b)], magnetic spectral weight in reciprocal space is redistributed from the long range $\langle\hat{T}^2\rangle = \uparrow\downarrow$ peak at $\vec{Q} = (1, 0, \frac{1}{2})$ among new momentum broadened magnetic peaks at positions consistent with the propagation wavevector $\vec{k} = (\frac{1}{2}, 0, \frac{1}{4})$. These peaks are characteristic of spatially short-range magnetic correlations with a translational periodicity of either a $\langle\hat{T}^4\rangle = \uparrow\uparrow\downarrow\downarrow$ state, or a $\uparrow\uparrow\uparrow\downarrow$ state. We note that while there is an inherent ambiguity of the relative arrangement of spins for $\langle\hat{T}^4\rangle$ magnetism from the momentum dependence alone, both of the possible states exhibit antiphase boundaries.

Upon cycling through to saturation at $\mu_0\mathrm{H} = 6$ and subsequently decreasing the magnetic field, new momentum broadened magnetic peaks are manifest at positions consistent with the commensurate propagation wavevector $\vec{k} = (\frac{2}{3}, 0, \frac{1}{3})$, and with a state of $\langle\hat{T}^3\rangle$ periodicity. These are shown at $\mu_0\mathrm{H} = 2.25\,\mathrm{T}$ in Fig. 4.12(c) and marked by clear extinction at the $\vec{Q} = (1, 0, \frac{1}{2})$ position, indicating a lack of contribution from the $\langle\hat{T}^2\rangle$ state, contrasting that observed on the upwards field sweep. Occurring in concert with a $M/M_s = \frac{1}{3}$ of the bulk magnetization [shown later in Fig. 4.17(a)], the $\langle\hat{T}^3\rangle$ periodicity is expected based on previous powder diffraction and reports of plateaus of the saturated magnetism [4–9]. Upon returning to

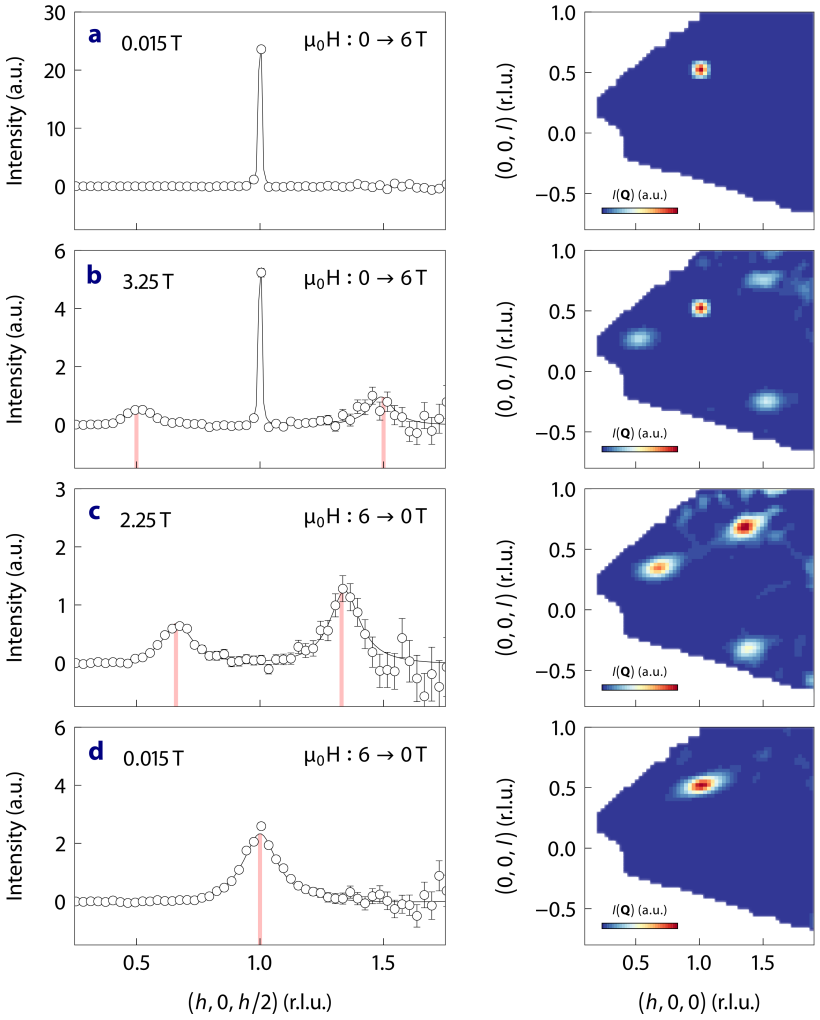

Figure 4.12: WISH SX, $T = 0.1\,\mathrm{K}$ with $\mu_0 \mathrm{H}_b \neq 0$. A 6 T background run has been subtracted from the data. In panel (a), long range magnetic order is seen at 0.015 T, with this small field used to kill the superconductivity in the Aluminum sample environment at these low temperatures of 0.1 K. In panel (b), intensity from the long range Néel wavevector $\vec{k} = (1, 0, \frac{1}{2})$ is redistributed among short-range magnetic correlations with $\vec{k} = (\frac{1}{2}, 0, \frac{1}{4})$ below the ferromagnetic phase boundary above 4 T. In panel (c), the wavevector has shifted from $\vec{k} = (\frac{1}{2}, 0, \frac{1}{4})$ to $\vec{k} = (\frac{2}{3}, 0, \frac{1}{3})$, and the long range Néel wavevector is absent. Upon return to $\mu_0 \mathrm{H} = 0.015\,\mathrm{T}$, the Néel phase is disordered, showing the hysteresis effect. Lineshapes have been fit with a lattice Lorentzian given in Eq. (4.21).

μ_0H = 0.015 T [shown in Fig. 4.12(d)], the long-range ordered $\vec{k} = (1, 0, \frac{1}{2})$ state is not fully recovered; it displays, instead, spatially short-range correlations based on the broadening of the $\vec{Q} = (1, 0, \frac{1}{2})$ reflection in momentum. This observation is indicative of a hysteretic response, with different $\langle \hat{T}^q \rangle$ correlations manifest based on field-history.

A Lorentzian lineshape is traditionally used in scattering experiments to fit the $\vec{Q}$-dependence of the magnetic reflections and subsequently extract a correlation length. The use of this functional form can be problematic, however, since the integral does not converge for dimension, D > 1. As discussed in Refs. [242, 243], resolution to this problem can be sought through the use of lattice-Lorentzians, for which the $\vec{Q}$-dependence of the scattered intensity is given by the relation

$$I(\vec{Q}) \propto \frac{\sinh(a_\alpha \xi_\alpha^{-1})}{\cosh(a_\alpha \xi_\alpha^{-1}) - \cos(\vec{Q} \cdot \vec{a}_\alpha)}, \tag{4.21}$$

where the correlation length along a particular direction $\vec{a}_\alpha$ is given by ξ_α. We note that the diffraction experiments on WISH are energy integrating, providing a measure of $S(\vec{Q}) \equiv \int S(\vec{Q}, \omega)\, \mathrm{d}\omega$. The correlation lengths are therefore the instantaneous values [70]. Eq. (4.21) is the functional form of the lineshape used to extract the correlation lengths, with fits of the extracted cuts along the $[h, 0, \frac{1}{2}h]$ direction shown in Fig. 4.12.

The shift of the propagation wavevector for field cycled up/down about saturation in the ferromagnetic phase at μ_0H = 6 T is clearly seen in Fig. 4.13. In

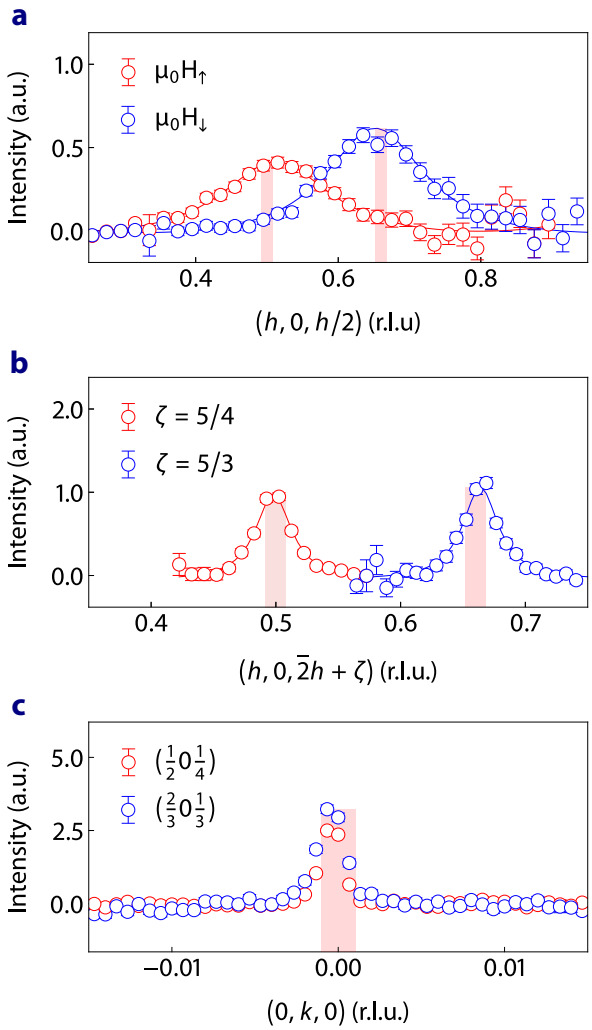

Figure 4.13: Lineshapes of the diffuse scattering observed on the WISH diffractometer in applied fields along the $[h, 0, \frac{1}{2}h]$ direction are shown in panel (a), and along the $[h, 0, \bar{2}h + \zeta]$ direction, perpendicular to the Néel wavevector, in panel (b). The lineshapes out of the $(h, 0, l)$ plane along the $[0, k, 0]$ direction are shown in panel (c). A hierarchy of length scales are clearly observed, with very short-range magnetic correlations along the direction of the Néel wavevector, shorter than those observed in the perpendicular direction. Out of plane, correlations are comparatively long-range, consistent with the 2D nature of the short-range order. Lineshapes have been fit with a lattice Lorentzian given in Eq. (4.21).

addition to the changing localization of the short-range magnetic correlations in reciprocal space, we observe a marked difference in the correlation lengths parallel [Fig. 4.13(a)] and perpendicular [Fig. 4.13(b)] to the direction of the antiferromagnetic propagation wavevector. This anisotropic broadening gives insight into the nature of the magnetic structure and suggests enhanced disorder along the $[h, 0, \frac{1}{2}h]$ direction. In Fig. 4.13(c), we see that magnetic correlations out of the $(h, 0, l)$ plane are long-range, which suggests that the ferromagnetic nature of the spin-chains along the $[0, k, 0]$ direction is not compromised. These observations suggest the possibility of ferromagnetic spin-planes stacked in antiferromagnetic antiphase arrangements along the direction of the antiferromagnetic propagation wavevector. Based on this idea, the proposed magnetic structures of the $\langle\hat{T}^2\rangle$, $\langle\hat{T}^3\rangle$, and $\langle\hat{T}^4\rangle$ states observed on WISH are shown in Fig. 4.14.

In Figs. 4.15 and 4.16, we compare the influence of temperature on the manifesting magnetic correlations for up and down field cycles about saturation at $\mu_0\mathrm{H} = 6\,\mathrm{T}$ respectively. Three sets of neutron data at different temperatures were collected over the course of two beamtime cycles. As discussed in Sec. 4.4, the low temperature data at $T = 0.1\,\mathrm{K}$ was collected separately to the data at $T = 1.6\,\mathrm{K}$ and $T = 4.5\,\mathrm{K}$ in the following cycle, with great care taken to ensure that the alignment of the sample was consistent for both experiments. At the start of each cycle, a long Vanadium dataset is collected on WISH for the purposes of normalization to the incoherent scattering; the data presented here were normalized with the appropriate

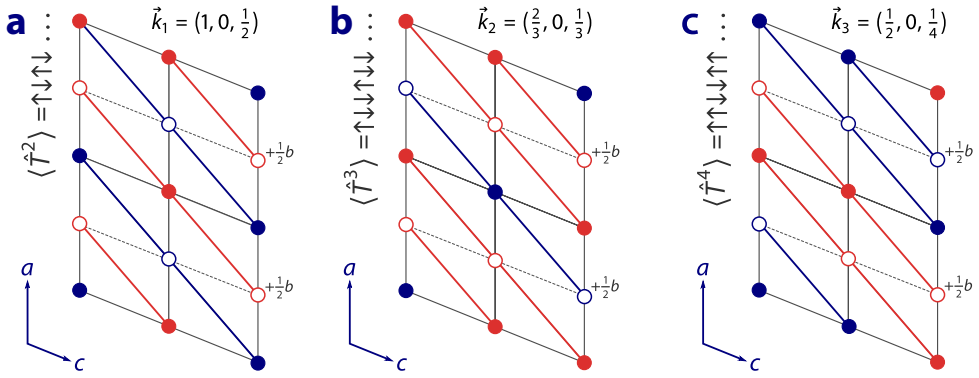

Figure 4.14: Magnetic structures projected in the *ac*-plane based on antiphase boundaries showing the long-range Néel state with $\langle\hat{T}^2\rangle$ symmetry in panel (a), and short-range structures with $\langle\hat{T}^3\rangle$ and $\langle\hat{T}^4\rangle$ periodicities in panels (b) and (c) respectively. Red (blue) circles represent chains of up (down) spins along the crystallographic *b*-axis.

absorption corrected Vanadium run for their respective beamtime cycle.

In Figs. 4.15(a-c), the temperature dependence zero-field cooled states are shown for the field-cycling sequence μ_0H : $0 \rightarrow 6\,$T at $T = 0.1\,$K. Intensity from the long range $\vec{k} = (1, 0, \frac{1}{2})$ is increasingly redistributed among short-range correlations at positions consistent with the magnetic propagation wavevector $\vec{k} = (\frac{1}{2}, 0, \frac{1}{4})$ with increasing field, before saturation in the $\vec{k} = 0$ ferromagnetic phase above μ_0H $= 4\,$T. In Figs. 4.15(d-f), at $T = 1.6\,$K, a coexistence of $\langle\hat{T}^3\rangle$ and $\langle\hat{T}^2\rangle$ orders is observed, before subsequently yielding to a state of pure $\langle\hat{T}^3\rangle$ order with magnetic propagation wavevector $\vec{k} = (\frac{2}{3}, 0, \frac{1}{3})$ as field is increased. Meanwhile, in Figs. 4.15(g-i), at $T = 4.5\,$K, very weak $\langle\hat{T}^3\rangle$ order can be seen to coexist with the $\langle\hat{T}^2\rangle$ phase, before again yielding to the $\langle\hat{T}^3\rangle$ phase at higher fields. The spectral

weight distributed among short-range correlations is increasingly suppressed with increasing temperature, which suggests that the short-range antiphase states are fragile to increasing temperature.

In Figs. 4.16(a-c), the temperature dependence zero-field cooled states are shown for the downward field cycling from saturation in the $\vec{k} = 0$ ferromagnetic phase, according to the sequence $\mu_0 \mathrm{H} : 6 \rightarrow 0\,\mathrm{T}$ at $T = 0.1\,\mathrm{K}$. There is a marked absence of magnetic correlations consistent with the wavevector $\vec{k} = (\frac{1}{2}, 0, \frac{1}{4})$, with broad diffuse scattering distributed among $\langle \hat{T}^3 \rangle$ correlations instead. In addition, a background of paramagnetic diffuse scattering is manifest, indicating enhanced disorder. The $\langle \hat{T}^2 \rangle$ state does not make full recovery upon returning to $\mu_0 \mathrm{H} = 0.015\,\mathrm{T}$ and maintains short-range correlations after field cycling, as evidenced by its broad $\vec{Q}$-dependence.

The evolution of magnetic correlations at higher temperatures follow a similar pattern with the response at $T = 1.6\,\mathrm{K}$ [shown in Figs. 4.16(d-f)] and at $T = 4.5\,\mathrm{K}$ [shown in Figs. 4.16(g-i)], both characterized by the coexistence of $\langle \hat{T}^3 \rangle$ and $\langle \hat{T}^2 \rangle$ orders. We find, therefore, that the spatially short-range $\langle \hat{T}^4 \rangle$ periodicity is only stabilized in field at low temperatures, while the stabilization of the long-range $\langle \hat{T}^3 \rangle$ state at higher temperatures is consistent with the results of previously published in-field neutron powder diffraction [199, 211]. Finally, these results show that the suppression of long-range order is negatively correlated with increasing temperature, with the long-range $\langle \hat{T}^2 \rangle$ state almost fully recovered on return to $\mu_0 \mathrm{H} = 0\,\mathrm{T}$ at $T = 4.5\,\mathrm{K}$.

In Fig. 4.17, the low temperature magnetization — measured at $T = 0.085\,\mathrm{K}$ —

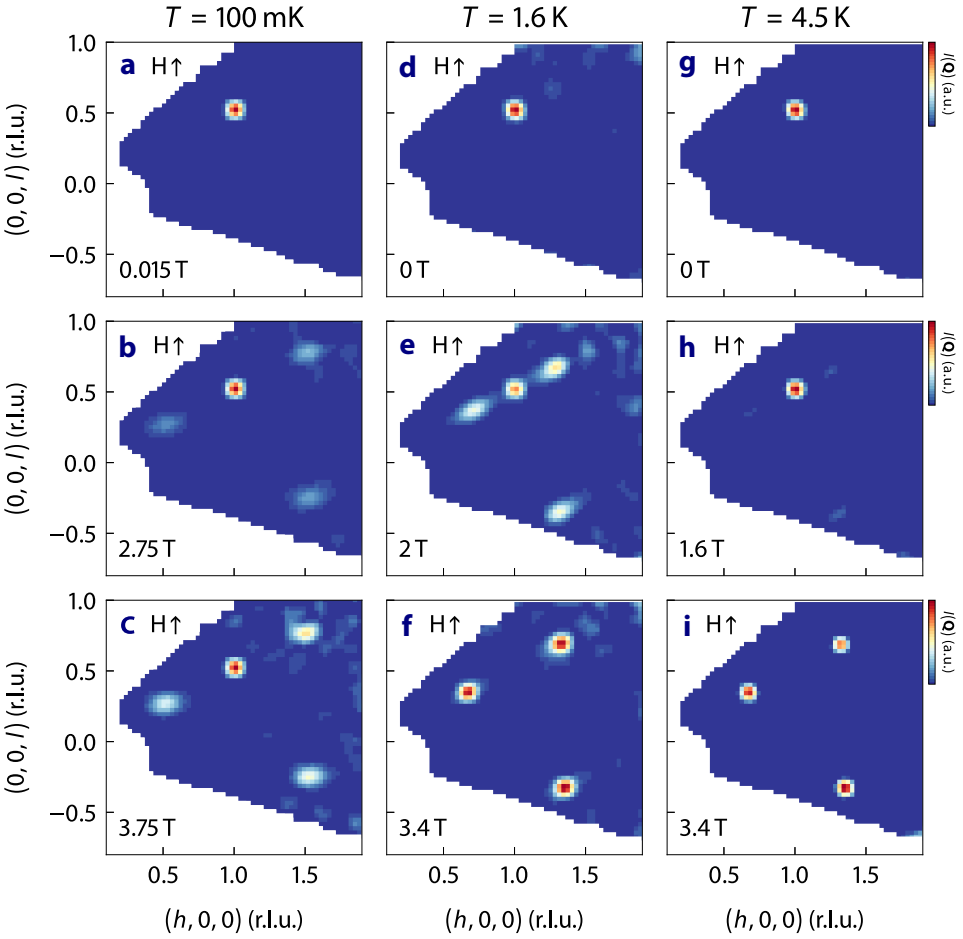

Figure 4.15: The temperature dependence of short-range magnetic correlations observed for field cycling from a zero-field cooled state is shown for the sequence $\mu_0 H : 0 \rightarrow 6\,T$. Results at $T = 0.1\,K$ are shown in panels (a-c) for increasing field, and demonstrate a coexistence of $\langle \hat{T}^2 \rangle$ and $\langle \hat{T}^4 \rangle$ periodicities. In panels (d-f), results obtained for increasing field at $T = 1.6\,K$ are shown, with coexisting $\langle \hat{T}^2 \rangle$ and $\langle \hat{T}^3 \rangle$ orders manifest. Finally, results obtained at $T = 4.5\,K$ are shown in panels (g-i), with very weak $\langle \hat{T}^3 \rangle$ order seen to coexist with the $\langle \hat{T}^2 \rangle$ phase before the onset of long-range $\langle \hat{T}^3 \rangle$ order at higher field, suggesting a fragility of the antiphase order to increasing temperature.

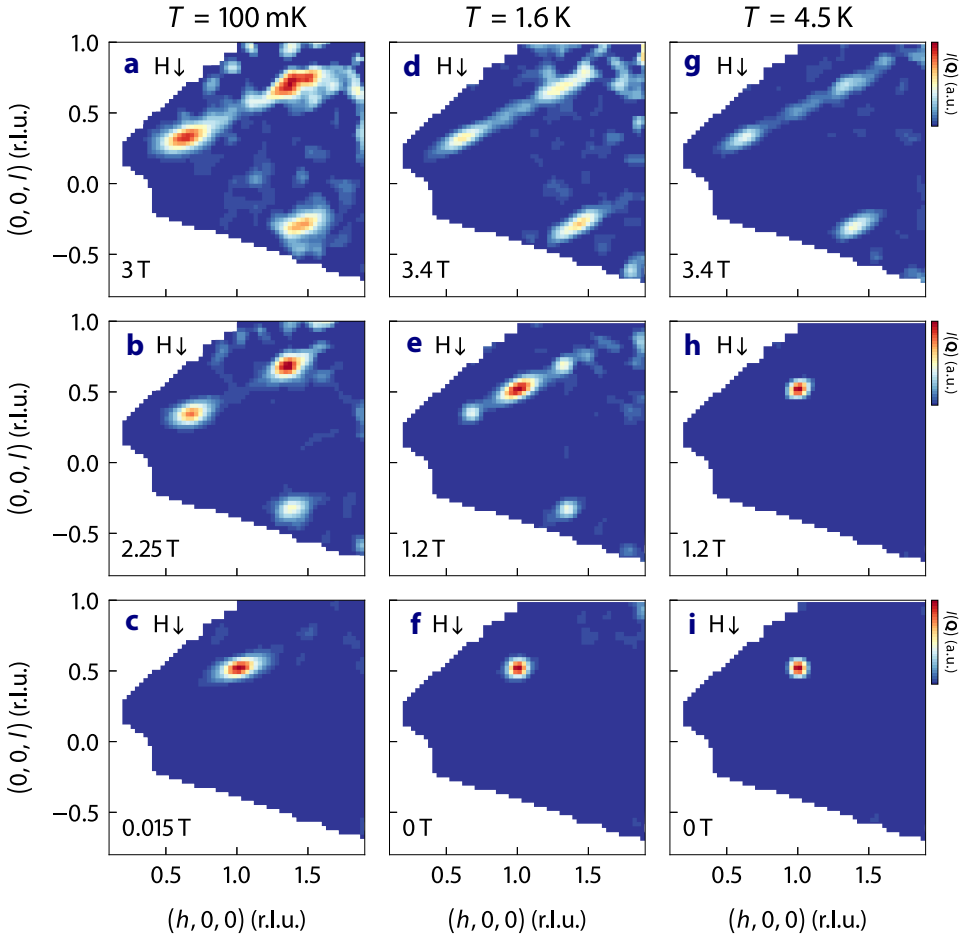

Figure 4.16: The temperature dependence of short-range magnetic correlations observed for the field sequence $\mu_0 \mathrm{H} : 6 \rightarrow 0\,\mathrm{T}$. Results at $T = 0.1\,\mathrm{K}$ are shown in panels (a-c) for decreasing field and demonstrate short-range $\langle \hat{T}^3 \rangle$ order before above $\langle \hat{T}^2 \rangle$ at $\mu_0 \mathrm{H} = 0.015\,\mathrm{T}$, with reduced correlation length. Paramagnetic background scattering is enhanced, suggesting increased disorder. In panels (d-f), results obtained for decreasing field at $T = 1.6\,\mathrm{K}$ are shown. Coexisting $\langle \hat{T}^2 \rangle$ and $\langle \hat{T}^3 \rangle$ orders are manifest above the $\langle \hat{T}^2 \rangle$ phase, with reduced correlation length. Finally, results obtained at $T = 4.5\,\mathrm{K}$ are shown in panels (g-i), with a similar pattern of spin orders emerging, characterized by the coexistence of $\langle \hat{T}^3 \rangle$ and $\langle \hat{T}^2 \rangle$ periodicities. In contrast to the results obtained at lower temperatures, the $\langle \hat{T}^2 \rangle$ phase makes full recovery.

is shown alongside the integrated intensities and correlation lengths of the magnetic reflections observed on WISH at $T = 0.1\,\mathrm{K}$. The correlation lengths parallel ($\xi_\parallel$) and perpendicular ($\xi_\perp$) to the direction of the antiferromagnetic propagation wavevector, along which the peaks broaden, was extracted from fits to Eq. (4.21). With field increasing from zero, intensity is redistributed from the $\vec{Q} = (1, 0, \frac{1}{2})$ among short-range $\langle\hat{T}^4\rangle$ correlations and the $\vec{k} = 0$ component. With further increasing field, the $\langle\hat{T}^4\rangle$ peaks give up intensity to the nuclear $\vec{Q} = (0, 0, 2)$ peak which captures nearly all spectral weight by saturation. With decreasing field from saturation, the intensity from the nuclear $\vec{Q} = (0, 0, 2)$ is redistributed among $\langle\hat{T}^3\rangle$ correlations, before finally feeding into the $\vec{Q} = (1, 0, \frac{1}{2})$ peak characterizing short-range $\langle\hat{T}^2\rangle$ order. The anisotropy of the magnetic correlations is clearly shown in Figs. 4.17(c-d), where the correlation length parallel to the broadening direction is bound by a maximal value of just a few unit cells which is much smaller than that observed perpendicular to the broadening direction.

To further investigate the effect of applied field direction on the stabilization of spin orders, we conducted a single-crystal neutron diffraction experiment on the RITA-II triple-axis spectrometer (PSI, Switzerland) in horizontal magnetic field, where the kinematic restrictions manifest on WISH did not pose an issue. The results of this experiment are shown in Fig. 4.18 overleaf, with field parallel to the crystallographic c-axis and minimal components along the crystallographic a- and b-axes. Linecuts parallel to the antiferromagnetic propagation vector along the $[h, 0, \frac{1}{2}h + 1]$ direction are shown

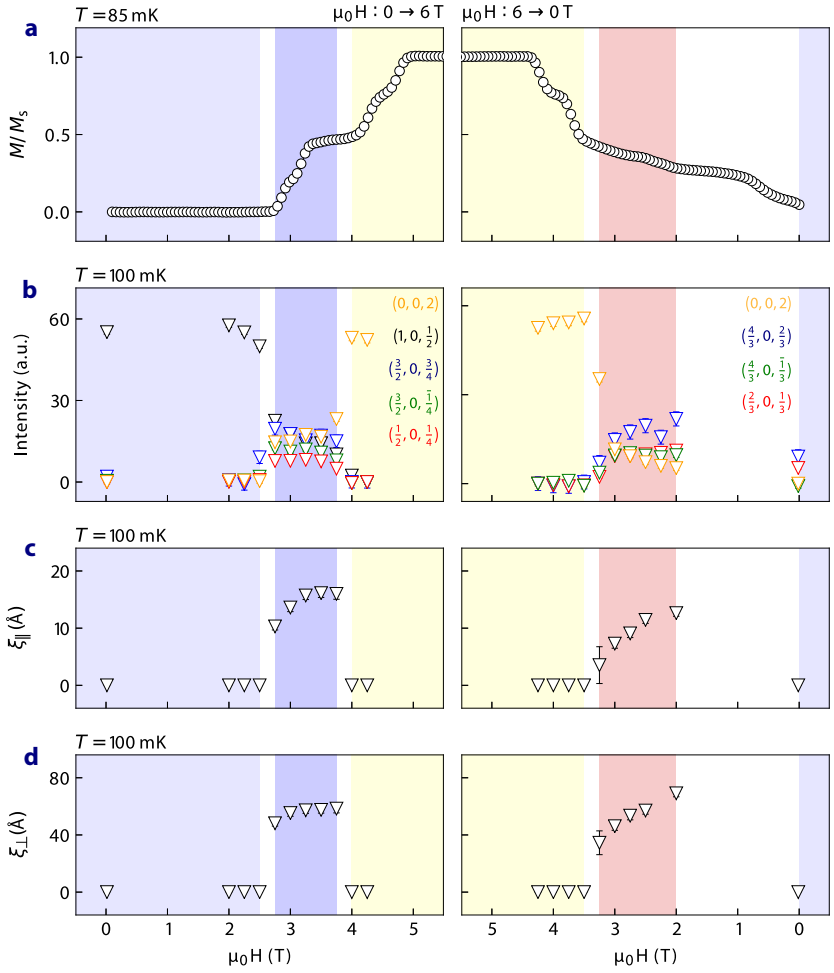

Figure 4.17: Low temperature magnetization at $T = 0.085\,\mathrm{K}$ is shown in panel (a) along with integrated intensities (panel b), and correlation lengths parallel (panel c) and perpendicular (panel d) to the direction of the antiferromagnetic propagation wavevector, extracted from single-crystal neutron diffraction on WISH at $T = 0.1\,\mathrm{K}$. On increasing field, intensity from the antiferromagnetic $\vec{Q} = (1, 0, \frac{1}{2})$ is redistributed among $\langle \hat{T}^4 \rangle$ correlations, which finally are directed into the $\vec{k} = 0$ channel as the structure saturates in the ferromagnetic phase. With decreasing temperature, the ferromagnetic $\vec{k} = 0$ phase gives up spectral weight to $\langle \hat{T}^3 \rangle$ correlations, with magnetic spectral weight recovered by the short-range $\langle \hat{T}^2 \rangle$ phase on return to zero field. Very short-range correlations of just a few unit cells are manifest along the stacking direction, with longer correlation lengths in the perpendicular direction characterizing the anisotropy of the correlations.

alongside the corresponding $(h, 0, l)$ planes.

In Figs. 4.18(a-b), the results obtained for the field cycling sequence μ_0H : $0 \rightarrow 4.5\,\mathrm{T}$ at $T = 0.1\,\mathrm{K}$ are shown, starting from an initial zero-field cooled state. Long-range resolution limited $\langle \hat{T}^2 \rangle$ order is manifest at $\mu_0\mathrm{H} = 2\,\mathrm{T}$, and is evidenced by a sharp peak at the $\vec{Q} = (1, 0, \frac{3}{2})$ position [shown in Fig. 4.18(a)]. With increasing applied field, a shift of the propagation wavevector from $\vec{k} = (1, 0, \frac{1}{2})$ to $\vec{k} = (\frac{2}{3}, 0, \frac{1}{3})$ occurs, with long-range resolution limited $\langle \hat{T}^3 \rangle$ order evidenced by a peak at the $\vec{Q} = (\frac{2}{3}, 0, \frac{4}{3})$ position for $\mu_0\mathrm{H} = 3\,\mathrm{T}$ [shown in Fig. 4.18(b)]. Upon decreasing field from saturation in the ferromagnetic phase at $\mu_0\mathrm{H} = 4.5\,\mathrm{T}$, no shift of the propagation wavevector is observed, in contrast to that observed on WISH. The $\langle \hat{T}^3 \rangle$ phase is consequently robust to the cycling of field about the ferromagnetic phase when field is applied strictly along the crystallographic c-axis. This is demonstrated at $\mu_0\mathrm{H} = 3.25\,\mathrm{T}$ and $1.5\,\mathrm{T}$ in Figs. 4.18(c-d) respectively, which show the development of a long-range, resolution limited Bragg peak at the $\vec{Q} = (\frac{2}{3}, 0, \frac{4}{3})$ position.

As compared to the results obtained on WISH, we observe fewer instabilities on changing magnetic field at low temperatures below on the onset of Néel order, as well as a lack of hysteresis. On WISH, we observed that local antiphase boundaries form when the field is rotated away from the c-axis, allowing spin orders with $\langle \hat{T}^4 \rangle$ periodicity to emerge. These, we note, can be

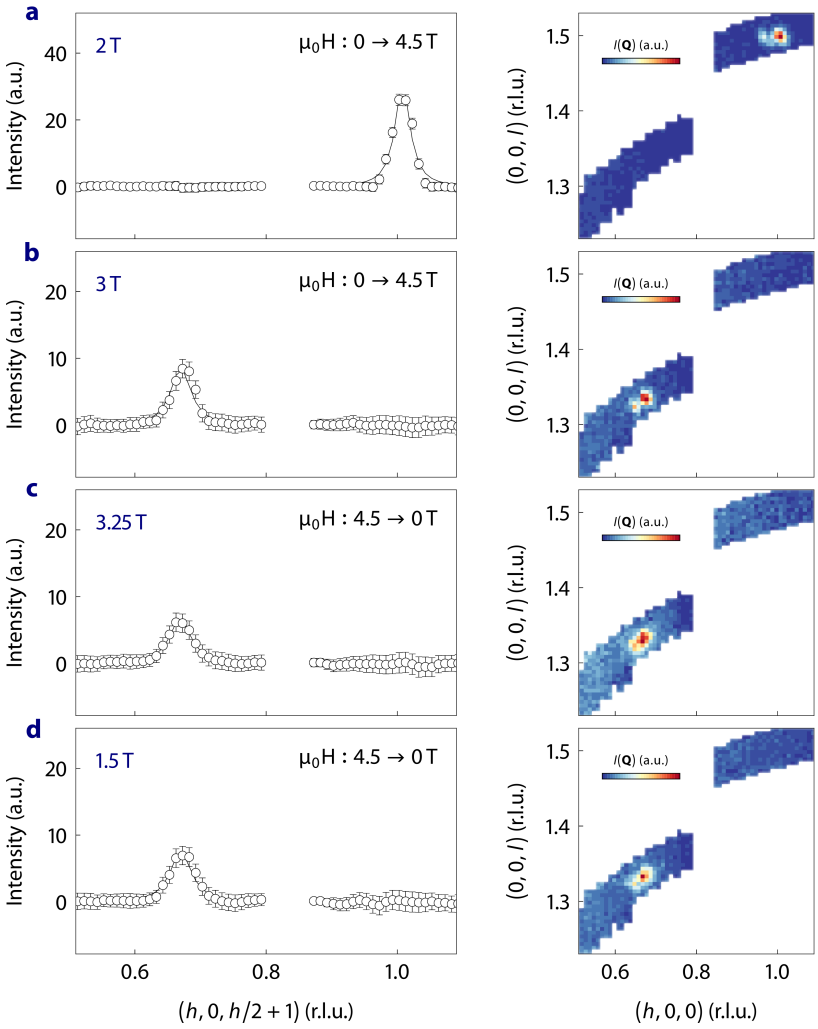

Figure 4.18: The field dependence of magnetic correlations observed on the RITA-II instrument, with horizontal magnetic field parallel to the crystallographic c-axis at $T = 0.1\,\mathrm{K}$. Linecuts along the $[h, 0, \frac{1}{2}h + 1]$ direction, parallel to the antiferromagnetic propagation vector, are shown alongside the corresponding $(h, 0, l)$ for field cycles about saturation in the ferromagnetic phase at $\mu_0\mathrm{H} = 4.5\,\mathrm{T}$, starting from a zero-field cooled state. In contrast to the results obtained on WISH, no $\langle\hat{T}^4\rangle$ order was observed, suggesting this phase is unstable to applied field direction, manifesting only when field is rotated away from the crystallographic c-axis.

constructed[9] as $\langle\hat{T}^4\rangle = \uparrow\uparrow\downarrow\downarrow$ or $\uparrow\uparrow\uparrow\downarrow$, consequently manifesting as $\langle\hat{T}^3\rangle$ order with antiphase boundaries [244]. We conclude that based on the absence of these effects in the RITA-II data, where field was applied strictly along the crystallographic c-axis (made possible by favorable kinematics of the horizontal magnet geometry, in contrast to the limited out-of-plane coverage in the vertical magnet on WISH), that the switching of the propagation wavevector and strong hysteresis observed on WISH are instabilities that depend sensitively on the direction of applied field.

We emphasize that the spatially short-range ordered states observed on WISH are not compatible with an interpretation based on magnetic field induced phase transitions, since there is no breaking of long-range translational symmetry. Since the spin orders have finite correlation length, long-range translational symmetry is not broken, and there is no change to either the dimension of the irrep or the little co-group G_k; consequently, the symmetry of the BZ remains unchanged in these short-range ordered states. Demonstrated in Fig. 4.17 is the clear manifestation of a hysteresis effect when cycling the field through to saturation in the ferromagnetic phase and returning back to zero applied field. Short-range antiphase order with $\langle\hat{T}^4\rangle$ periodicity is stabilized on increasing applied field, while short-range $\langle\hat{T}^3\rangle$ order, followed finally by $\langle\hat{T}^2\rangle$ order is stabilized on decreasing field from saturation. With reference

[9]Consider, for instance, a $\langle\hat{T}^{3+}\rangle = \uparrow\uparrow\downarrow$ state and a $\langle\hat{T}^{3-}\rangle = \downarrow\downarrow\uparrow$ state. We note the following equivalence of antiphase states, $\langle\hat{T}^{3+}\hat{T}^{3+}\hat{T}^{3-}\hat{T}^{3-}\rangle = \uparrow\uparrow\downarrow\uparrow\uparrow\downarrow\downarrow\uparrow\downarrow\downarrow\uparrow \equiv \langle\hat{T}^{3+}\hat{T}^{4}\hat{T}^{2}\hat{T}^{3-}\rangle$, which therefore implies that coexisting $\langle\hat{T}^{2,3,4}\rangle$ can be created with $\langle\hat{T}^3\rangle$ order with antiphase boundaries.

to the hysteresis reported in Fig. 4.17, given the insulating nature [245] and the requirement of gauge invariance, we note that the observed change in the ground state — despite having completed a closed loop of abelian unitary transformations — may be indicative of an non-trivial, underlying topological structure.

Based on the large gap to magnetic excitations ($\sim 1\,\mathrm{meV}$) in comparison to the applied fields ($1\,\mathrm{T} \sim 0.1\,\mathrm{meV}$), we do not expect a violation of the adiabatic theorem. However, a highly degenerate ground state is expected for Ising spins on a triangular motif [246], and we note reports of hysteresis effects in fractional quantum Hall systems [247, 248]. The local $\langle \hat{T}^4 \rangle$ order stabilized in α-CoV_2O_6 at low temperatures with a field component along the crystallographic b-axis has a correlation length of only a few unit cells along the stacking direction, and coexists with other periodicities. These states are analogous to the 'dilute' dimer phases proposed for alternating $S = \frac{1}{2}$ chains in the presence of next-nearest-neighbor interactions [234]. Together, these results support the prediction of an infinite number of collinear, commensurate magnetic phases in anisotropic next-nearest-neighbor Ising (ANNNI) systems with $-J_2/J_1 > 1/2$ as $T \to 0\,\mathrm{K}$ [219].

The presence of plateaus in the magnetization implies an energetic gap; we seek resolution by appeal to an extension [176] of the Lieb–Schultz–Mattis theorem [12] which, as described in Sec. 4.3.3, supposes that an energetic gap can occur without breaking translational symmetry if the magnetization per spin $m = \frac{1}{L}\sum_{i=1}^{L} S_i^z$ satisfies $(S - m) = p/q$, where p and q are coprime

Table 4.3: Values of $(S-m)=p/q$ for each of the magnetization plateaus observed in Fig. 4.17, with $m=\frac{1}{L}\sum_{i=1}^{L}S_i^z$ characterizing the observed periodicities.

$(S-m)=p/q$	$M/M_{\rm s}$	$\langle\hat{T}^q\rangle$
$\frac{1}{2}-\frac{1}{2}=0$	1	$\langle\hat{T}^1\rangle=\uparrow\uparrow$
$\frac{1}{2}-0=\frac{1}{2}$	0	$\langle\hat{T}^2\rangle=\uparrow\downarrow$
$\frac{1}{2}-\frac{1}{6}=\frac{1}{3}$	$\frac{1}{3}$	$\langle\hat{T}^3\rangle=\uparrow\uparrow\downarrow$
$\frac{1}{2}-\frac{1}{4}=\frac{1}{4}$	$\frac{1}{2}$	$\langle\hat{T}^4\rangle=\uparrow\uparrow\downarrow\downarrow,\uparrow\uparrow\uparrow\downarrow$

$p,q\in\mathbb{Z}$ satisfy $\gcd(p,q)=1$

[such that $\gcd(p,q)=1$], since the ensuing $\langle\hat{T}^q\rangle$ symmetry is gauge invariant. In the presence of this gauge symmetry, the Hamiltonian $\mathcal{H}$ is invariant under the slow unitary rotation of localized magnetic moments, according to $\langle\psi|\,U^\dagger\mathcal{H}U-\mathcal{H}\,|\psi\rangle=\mathcal{O}(1/L)$, with a concomitant increase in magnetization if the rotated state $U\,|\psi\rangle\perp|\psi\rangle$. In Table 4.3 we show the prescription of a value p/q to each of the magnetization plateaus and hence extract the translational symmetry of the ordered phase.

To reconcile our results from the WISH and RITA instruments, we performed a neutron powder diffraction experiment on the TASP triple-axis spectrometer (PSI, Switzerland), with results shown in Fig. 4.19. In this experiment, due to the nature of powder containing a random distribution of grain orientations, the applied field was isotropic among grains. In order to prevent the reorientation of grains in field and to preserve the isotropic nature

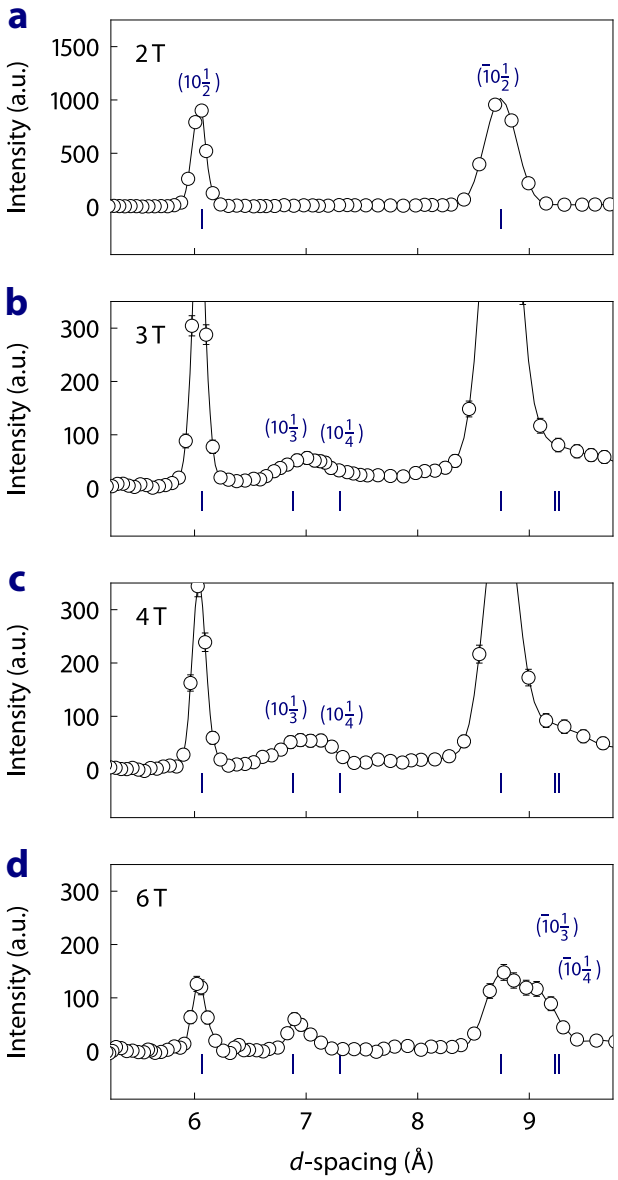

Figure 4.19: Results from neutron powder diffraction on the TASP instrument showing the presence of both $\langle \hat{T}^3 \rangle$ and $\langle \hat{T}^4 \rangle$ periodicities at $T = 0.1\,\mathrm{K}$. The powder sample was pressed into a pellet to prevent reorientation in field, placed in an Aluminum can and supplemented with ^{3}He exchange gas to enhance cooling. Note the coexistence of multiple orders due to the isotropic nature of the applied field on the powder sample, with distribution of orientations.

of applied field, we used a pressed polycrystalline pellet in our measurements at $T = 0.1\,\mathrm{K}$. The resulting diffraction pattern on the zero-field cooled sample at an applied field of $\mu_0\mathrm{H} = 2\,\mathrm{T}$ is shown in Fig. 4.19(a). Long-range magnetic order is evidenced by the emergence of resolution limited magnetic Bragg peaks; these satellite reflections occur at d-spacings consistent with the propagation wavevector $\vec{k} = (1, 0, \frac{1}{2})$, and also with our results from WISH and RITA-II.

With increasing applied magnetic field, a complex series of peaks at d-spacings consistent with simultaneous emergence of spin orders based on $\langle\hat{T}^3\rangle$ and $\langle\hat{T}^4\rangle$ periodicities, coexisting with $\langle\hat{T}^2\rangle$ order, is shown in Figs. 4.19(b-d). The distribution of spectral weight is modulated with increasing applied field, demonstrating that the stabilization of different $\langle\hat{T}^q\rangle$ correlations is dependent on the strength and direction of applied field, therefore accounting for the discrepancies obtained in the results of our experiments on the WISH and RITA-II instruments.

4.5.4 Stability of field-induced magnetization plateaus

We consider, finally, the stability of the field induced magnetization plateaus at low temperatures, and investigate the magnetic dynamics through measurements of the bulk magnetization at various sweep rates, $\mathrm{dH}(t)/\mathrm{d}t$. Based on single-crystal x-ray Laue diffraction measurements on a number of samples from our batch of single-crystals, the morphological features of α-$\mathrm{CoV_2O_6}$ were deduced. The reciprocal lattice directions and their corresponding crys-

tal faces were deduced from these measurements and are illustrated along with the crystal structure and BZ in Fig. 4.2. These crystal features were used to construct a coaligned array of single-crystals of total mass of 6 mg. This was attached to a 4 mm × 4 mm × 0.1 mm copper plate by GE varnish suitable for measurements at dilution temperatures with favorable thermal transport properties, and subsequently secured in a standard PPMS/MPMS3 straw mounting system. As described in Sec. 4.4, the magnetization was measured at $T = 0.4\,\mathrm{K}$ in an MPMS3 with with a sub-2 K *i*Helium3 dilution system, and also at $T = 2.5$ K in a PPMS with VSM insert. The results for a number of different sweep rates are shown in Fig. 4.20.

The results obtained from cycling the magnetic field between $\mu_0\mathrm{H} = 0-6\,\mathrm{T}$ on a zero-field cooled state are shown for sweep rates of $\mathrm{dH}(t)/\mathrm{d}t = 2.5$ and 100 Oe/s at $T = 0.4\,\mathrm{K}$ in Fig. 4.20(a). Since the saturated moment is lower than expected [4–9], it is possible that the orientation of the sample mounted in the straw was compromised upon cooling to dilution temperatures, caused by the changing shear forces acting upon the edges of the copper plate housing the sample array, as the straw is subject to thermal contraction with decreasing temperature, combined with subsequent misalignment of the sample array in applied field. Moreover, the difference in magnetization at small fields observed between the major and minor loops is likely the result of the stabilization of different modulated magnetic states. This difference was observed when investigating minor loops in the magnetization; in order to remove this difference, a careful sequence of field de-training on the downward

sweep would have been required, but was not possible due to the limited time available to us on the MPMS3 at the materials characterization lab (ISIS, UK) during COVID-19.

In Fig. 4.20(b), for magnetic field sweep rates $\mathrm{dH}(t)/\mathrm{d}t = 0.5$ Oe/s, 20 Oe/s, and 100 Oe/s at $T = 2.5\,\mathrm{K}$, we observe shifting of the critical fields and additional fine structure below the $M/M_\mathrm{s} = \frac{1}{3}$ plateau consistent with previous reports [9]. The series of plateaus observed $T = 0.4\,\mathrm{K}$, shown in Fig. 4.20(a), are distinctly different, however, manifesting at multiples of $\frac{1}{12}$ and presenting plateaus at $M/M_s = \frac{1}{4}$, $\frac{1}{3}$, $\frac{1}{2}$, $\frac{3}{4}$, although distorted slightly by the effects of demagnetization, which have not been corrected for. These observations are consistent with the short-range commensurate spin orders described in Sec. 4.5.3, and are deeply related to the stabilized magnetization plateaus through the symmetry of the underlying magnetic correlations.

The magnetic relaxation was measured at $T = 0.4\,\mathrm{K}$ from the $M/M_\mathrm{s} = \frac{1}{2}$ plateau state, accessed by ramping the applied field to $\mu_0\mathrm{H} = 3.5\,\mathrm{T}$ at rates of $\mathrm{dH}(t)/\mathrm{d}t = 20$ Oe/s, 100 Oe/s, and 500 Oe/s, before abrupt removal of the field. The relaxation from this prepared state initially decreased very quickly, with the evolution of the long-timescale component of the relaxation, after this initial drop shown in Fig. 4.21(a). The timescales of magnetic relaxation characterized as a function of field ramping rate with a phenomenological stretched exponential model of the form $M(t) = M_0 \pm M_1 \exp\{[-(t/\tau)^\beta]\}$, as shown in Fig. 4.21(b). Fits to this component of the relaxation reveal a slow timescale, on the order of 2000 s, which supports suggestions of the

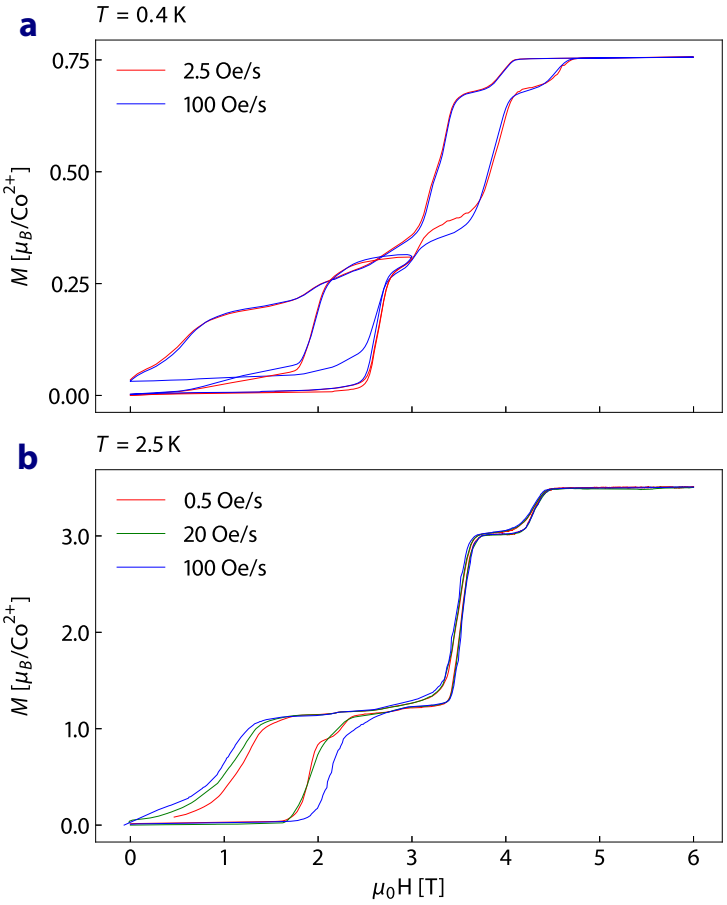

Figure 4.20: Major and minor hysteresis loops observed for a number of rates of magnetic field sweep $\mathrm{dH}(t)/\mathrm{d}t$ on a zero-field cooled state at temperatures $T = 0.4\,\mathrm{K}$ and $T = 2.5\,\mathrm{K}$ obtained using a PPMS with VSM insert and in an MPMS3 with sub-2 K *i*Helium3 dilution system respectively.

metastability of the plateaus [4–9].

The magnetic relaxation was additionally measured at $T = 2.5\,\mathrm{K}$ in two modalities, as shown in Fig. 4.22. In Fig. 4.22(a), the magnetic field was held

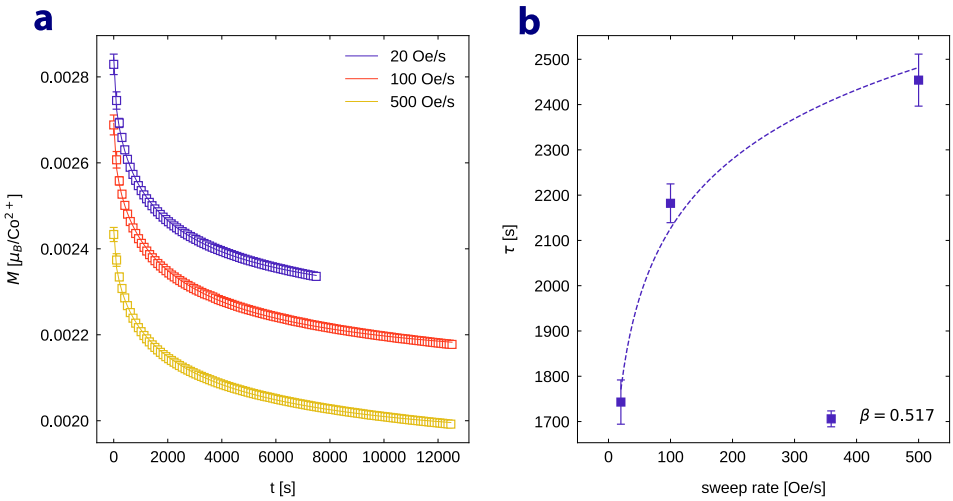

Figure 4.21: Interrupted field-sweeps at $T = 0.4$ K. The relaxation of the magnetization for a field ramping rates of 20, 100 and 500 Oe/s is shown in (a) with fits to a stretched exponential mode. Fits to a phenomenological stretched exponential model yield an exponent $\beta = 0.491$, with (b) showing the sweep-rate dependence of the extracted timescales, in which the broken line a guide to the eye.

constant in the vicinity of the M/M_s plateau at $\mu_0 H = 2.2\,T$ and the evolution of the magnetization $M(t)/M(0)$ tracked with time. Fits to a stretched exponential model reveal different timescales of the dynamical evolution of the magnetization when field was set to the target field with different sweep rates of 2 Oe/s and 20 Oe/s. The relaxation of the magnetization shown in Fig. 4.22(b) is much faster than that observed at $T = 0.4\,K$, which suggests a critical slowing down of the dynamics at lower temperatures.

While we do observe a clear difference in the magnetic dynamics at $T = 0.4\,K$ and $T = 2.5\,K$, more measurements are required to gain further in-

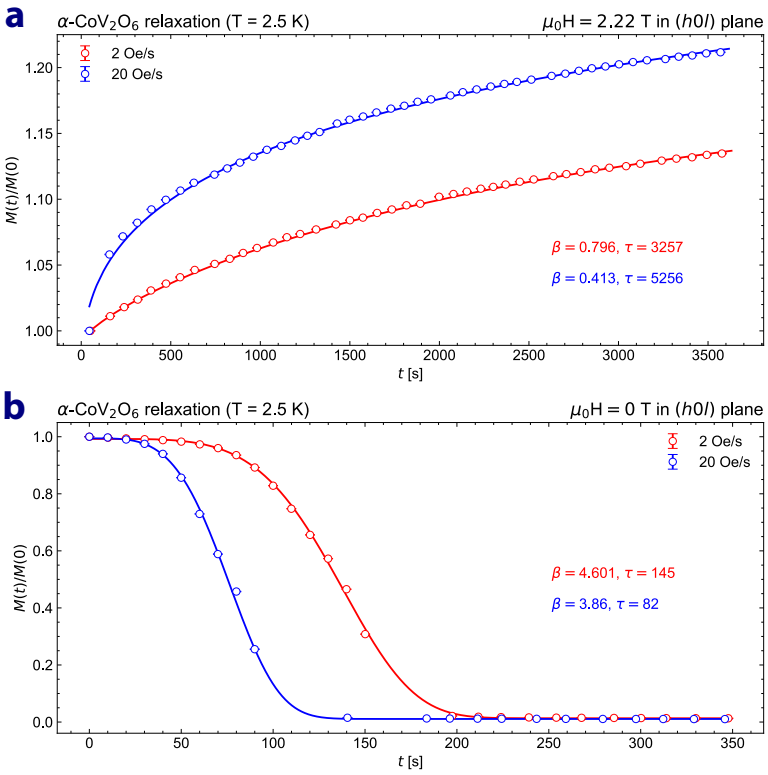

Figure 4.22: Magnetic dynamics observed at $T = 2.5\,\mathrm{K}$ for sweep rates $\mathrm{d}H(t)/\mathrm{d}t = 2$ Oe/s and 20 Oe/s for (a) field held at $\mu_0 H = 2.2\,\mathrm{T}$ in the vicinity of the $M/M_\mathrm{s} = \frac{1}{3}$ plateau and (b) for relaxation after the field is set to $\mu_0 H = 0\,\mathrm{T}$.

sight into the stability of the states. However, our results are not consistent with a violation of the adiabatic theorem, which supports the notation of an underlying non-trivial topological structure in α-CoV_2O_6 . More detailed measurements of minor hysteresis loops, for instance, would be particularly useful to further investigate the topological structure and learn more about

the stability of the field induced magnetic transitions pertaining to the nature of the magnetic Hamiltonian.

4.6 Conclusions

We have re-investigated the nature of the Néel state based on the observation of an enhancement of intensity of the nuclear $\vec{Q} = (0, 0, 2)$ reflection below T_{N} on the RITA-II instrument in zero applied magnetic field. Single-crystal neutron diffraction measurements in zero applied field on the WISH instrument did not find any nuclear peaks to display such a temperature dependence. The magnetic order parameter, measured as $|M|^2 \propto |T - T_{\mathrm{N}}|^{\beta}$, revealed a critical exponent of $\beta = 0.16(2)$ which suggests that α-$\mathrm{CoV_2O_6}$ belongs to the 2D Ising universality class [241].

We find additionally, by neutron powder diffraction on WISH, no evidence for magnetoelastic coupling that may have contributed strain and a concomitant release of extinction to explain the RITA-II result, with lattice parameters and bond lengths not found to vary beyond the $\Delta Q/Q = 0.03\,\%$ resolution of WISH. The fidelity of the ground state is therefore preserved, with the most likely explanations for the RITA-II result being the coincidence of a twin magnetic reflection with the nuclear $\vec{Q} = (0, 0, 2)$ reflection, or perhaps multiple scattering with multiple diffraction vectors adding up on the surface of a Laue sphere.

We have applied low temperature magnetization and neutron diffraction

to study the emergence of multiple field induced commensurate periodicities in an Ising $j_{\text{eff}} = \frac{1}{2}$ magnet. We find these to occur in concert with a series of metastable magnetization plateaus, with the nature and periodicity $\langle \hat{T}^q \rangle$ of the spin ordered states found to depend sensitively on the direction of applied field. When field is applied strictly along the crystallographic c-axis, long range resolution limited Bragg peaks, with $\langle \hat{T}^2 \rangle$ and $\langle \hat{T}^3 \rangle$ periodicities, define the response observed in the equilibrium structure factor $S(Q) \equiv \int S(Q, \omega) \mathrm{d}\omega$. When field is rotated away from the c-axis, we observe short-range ordered states of the same periodicities, states additionally based on $\langle \hat{T}^4 \rangle$ periodicity. The $\langle \hat{T}^4 \rangle$ state is only observed at low temperature, just as for the $M/M_{\text{s}} = \frac{1}{4}, \frac{1}{2}, \frac{3}{4}$ magnetization states, with the short-range ordered antiphase states and the resulting diffuse scattering found to be fragile to temperature, tending towards long-range ordering with increasing temperature supporting the results of previous neutron powder diffraction [199, 211].

Since the short-range ordered commensurable states observed on WISH do not break long-range translational symmetry, we interpret these states — based on antiphase boundaries — as a manifestation of an underlying topological structure, based on the Lieb–Schultz–Mattis theorem; in this framework, we prescribe a topological index to the magnetization plateau and find this to be deeply connected to the symmetry of the short-range field induced spin orders in its vicinity.

Chapter 5

Far-from-equilibrium correlations in $Dy_2Ti_2O_7$

5.1 Chapter summary

The spin ice material $Dy_2Ti_2O_7$ is a frustrated material where the magnetic spins on a tetrahedron can only point into or out of the $\langle 1, 1, 1 \rangle$ crystallographic axis due to the competition between the long range dipolar interaction and the local exchange interaction. Consequently, the ground state is degenerate, realizing a manifold of lowest energy states. Excitations out of this ground state make a 3-in, 1-out excitation which is shown to behave like a magnetic monopole. These monopoles are thermally created, and the density of the monopoles can be controlled by cooling through a transition. We have developed a new technique to do this, which we implement on the WISH instrument to study the microscopic evolution of the correlations as the monopole density is changed. In doing so, we demonstrate a novel technique

for the study of non-equilibrium studies using neutron scattering.

The contributions to this chapter are as follows. The design and testing of the avalanche quench methodology was carried out by Lewis Edwards (Cardiff) and Sean Giblin (Cardiff). Testing of the methodology in the E18 refridgerator at ISIS was carried out by Lewis Edwards (Cardiff), Sean Giblin (Cardiff), Chris Lawson (ISIS), and Pascal Manuel (ISIS). Single-crystal neutron scattering data was collected on WISH at ISIS by Lewis Edwards (Cardiff), Sean Giblin (Cardiff), and Pascal Manuel (ISIS). Analysis of data was carried out by Lewis Edwards (Cardiff).

5.2 Introduction

The rare-earth pyrochlore $Dy_2Ti_2O_7$ (DTO) is a classical spin ice material crystallizing in the cubic $Fd\bar{3}m$ pyrochlore structure, as shown in Fig. 5.1. The A and B sites of the lattice are populated by Dy^{3+} and Ti^{4+}ions respectively, forming a network of corner sharing tetrahedra with local D_{3d} point group symmetry. The localized magnetic moments are of Ising character and are constrained to point parallel or anti-parallel to their local $\langle 1,1,1\rangle$ directions due to the effects of the crystal electric field and strong single ion anisotropy. The spin ice state is termed thus due to the similarity of its magnetic ground state to the structure of water ice, wherein a 2-near, 2-far H^+ configuration — with respect to the pyrochlore lattice of covalent O^{2-} bonds — gives rise to a degenerate ground state and a finite entropy of

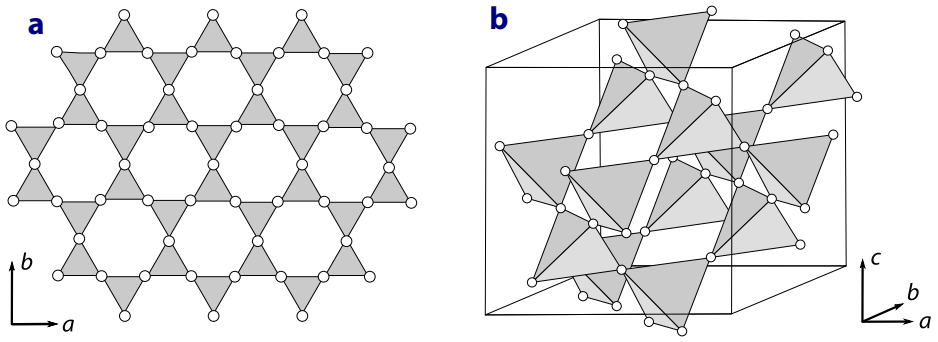

Figure 5.1: Geometry of the (a) Kagomé and (b) the pyrochlore lattice [250]. The Kagomé is in some sense the equivalent of the pyrochlore lattice in 2D, and is the most basic frustrated lattice. In the case of the canonical '227' spin ices with general composition $A_2B_2O_7$ and the symmetry of the $Fd\bar{3}m$ Federov group, magnetic A and B type ions establish a network of corner sharing network; the central points of the tetrahedra define a medial, or dual, diamond lattice.

$R\log(3/2)$, even at zero temperature. Experimental measurements of this effect in spin ice, often referred to as the Pauling entropy, are shown in Fig. 5.2, and is one of the defining features of the state. The multiplicity of the ground state is 2^{2N}, where N denotes the number of tetrahedra. Noting the geometric frustration and the so-called 'ice rules' that stipulate a 2-in, 2-out condition on each tetrahedron, a factor of $(6/16)^N$ contributes to the multiplicity, finally leading — via the Boltzmann entropy formula — to a residual entropy in spin ice of $R/2\log(3/2)$ per mole [249].

DTO has a large energy gap of 380 K between the ground and excited state [251], and a partially filled f-band. Interactions between the unpaired $4f$ electrons are responsible for the low energy properties and — by a hier-

archy of energy scales — the manifestation of the spin ice state in $A_2B_2O_7$ oxides [250]. For rare earth ions, a $^{2S+1}L_J$ ground state follows from Hund's rules and consists of $2J+1$ states, expressed as $|J, J_z\rangle$; Dy ions in particular have $J = 15/2$ with $L = 5$ and $S = 5/2$. The Stevens operators $O_l^m(\hat{J})$ allow for the expression of the crystal field interaction in terms of angular momentum operators by the Wigner Eckart theorem (see Ref. [45]), $\mathcal{H}_{\rm cf} = \sum_{l,m} B_l^m O_l^m(\hat{J})$. As discussed in Refs. [252, 253], the local D_{3d} point symmetry relevant to the A and B sites of the lattice allows the crystal field to be constrained, leading to an effective Hamiltonian [254] $\mathcal{H}_{\rm cf} = B_2^0 O_2^0 + B_4^0 O_4^0 + B_4^3 O_4^3 + B_6^0 O_6^0 + B_2^3 6_3^6 + B_2^6 O_6^6$. As noted in Ref. [253], the $B_2^0 O_2^0$ term is of particular relevance to the determination of the easy-axis anisotropy direction, where the operator is $O_2^0(\hat{J}) = 3\hat{J}_z^2 - J(J+1)$. When this term dominates, a negative B_2^0 will prefer an easy axis-ground state with $J_z = \pm J$. The oxygen environment is characterized by O(1) atoms external to the tetrahedra occupying the low symmetry $48f$ positions, and O(2) atoms internal to the tetrahedra occupying the $8b$ sites. These oxygen positions in the lattice define a cage surrounding rare-earth atoms; its geometry is that of a perfect cube for the free O(1) position, $x = 3/8$, and becomes increasingly distorted for greater deviations from this. In $Dy_2Ti_2O_7$, the cage is distorted along the local cubic $\langle 1, 1, 1\rangle$ direction.

The nearest neighbor exchange interaction is ferromagnetic, and is frustrated by the dipolar interaction [255]. With J the exchange coupling constant, D the dipolar coupling constant, and $r_{\rm nn}$ the nearest neighbor distance,

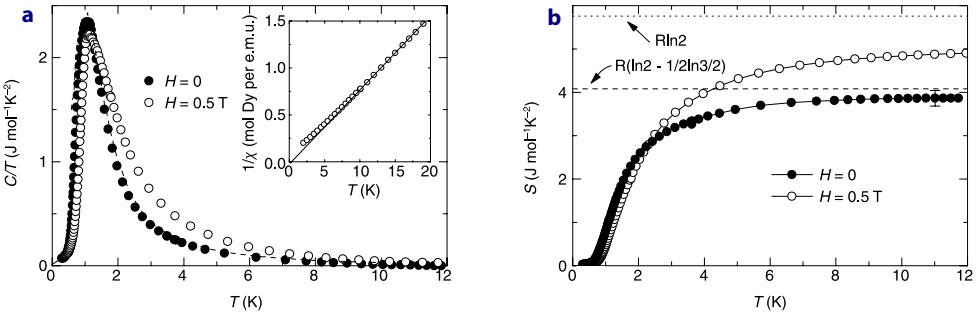

Figure 5.2: Specific heat and entropy in DTO spin ice. (a) shows the specific heat at $\mu_0\vec{H} = 0$ and $\mu_0\vec{H} = 0.5\,\mathrm{T}$, while (b) shows the entropy change $\Delta S = \int_{T_1}^{T_2} C(T)/T\,\mathrm{d}T$. From Ref. [249].

the spin ice Hamiltonian is [256]

$$\mathcal{H} = -J\sum_{\langle ij\rangle}\vec{S}_i\cdot\vec{S}_j + Dr_{\mathrm{nn}}^3\sum_{i>j}\left[\frac{\vec{S}_i\cdot\vec{S}_j}{|r_{ij}|^3} - \frac{3(\vec{S}_i\cdot\vec{r}_{ij})(\vec{S}_j\cdot\vec{r}_{ij})}{|r_{ij}|^5}\right]. \tag{5.1}$$

Local violation of the 'ice rule' by thermally activated spin flips to configurations with 3-in/1-out gives rise to a pair of deconfined, pointlike topological defects with magnetic charges $\pm Qm$ on adjacent sites, which can propagate via subsequent spin flips [257]. These defects are flux sources of an emergent gauge field $\vec{\nabla}\times\vec{A}$ governed by the Maxwell action $-1/4\int F_{\mu\nu}F^{\mu\nu}\mathrm{d}^4x$, and their presence modifies spin entropy, induces an entropic force, and gives rise to long-distance dipolar spin correlations with a temperature dependent Coulomb interaction between defects [258]. These defects are emergent quasiparticle excitations resulting from the fractionalization of the local dipolar interaction, and resemble magnetic monopoles.

The diffraction response in spin ice is shown in Fig. 5.3 in the (h, h, l) plane at $T = 20\,\mathrm{K}, 1.3\,\mathrm{K}$, and $0.3\,\mathrm{K}$. The scattering response features spectral weight concentrated at the zone boundaries, as well as pinch point singularities at BCC lattice points; these are a characteristic signature of long-range dipolar correlations in the magnetic structure factor $S^{\alpha\beta}(\vec{Q})$, with their width providing a measurement of the screening of fields at long distances [259]. While polarized neutron scattering has been used with great success in measuring the diffuse scattering from spin ice materials in separating spin flip and non-spin flip correlations, temperature subtractions have been successfully used in non-polarized diffraction to access the magnetic correlations, most recently in Ref. [115].

While spin ice is predicted to order at low temperatures, no experimental evidence has yet been put forth to substantiate this claim, although specific heat measurements showing an upturn at low temperatures over long timescales have claimed this to be a signature of the effect [261]. A neutron diffraction experiment on the WISH diffractometer during a facility shutdown following — and even extending — their 600 s waiting protocol, however, found no evidence of this insofar as the magnetic correlations are concerned [115]. Seeing that oxygen defects are reported in Ref. [262], sample quality is a potential explanation for the results obtained in Ref. [261]. In Ref. [115] where no ordering was found, the structural characterization of the neutron sample on the SXD instrument at ISIS found little disorder, revealing a high quality sample [115].

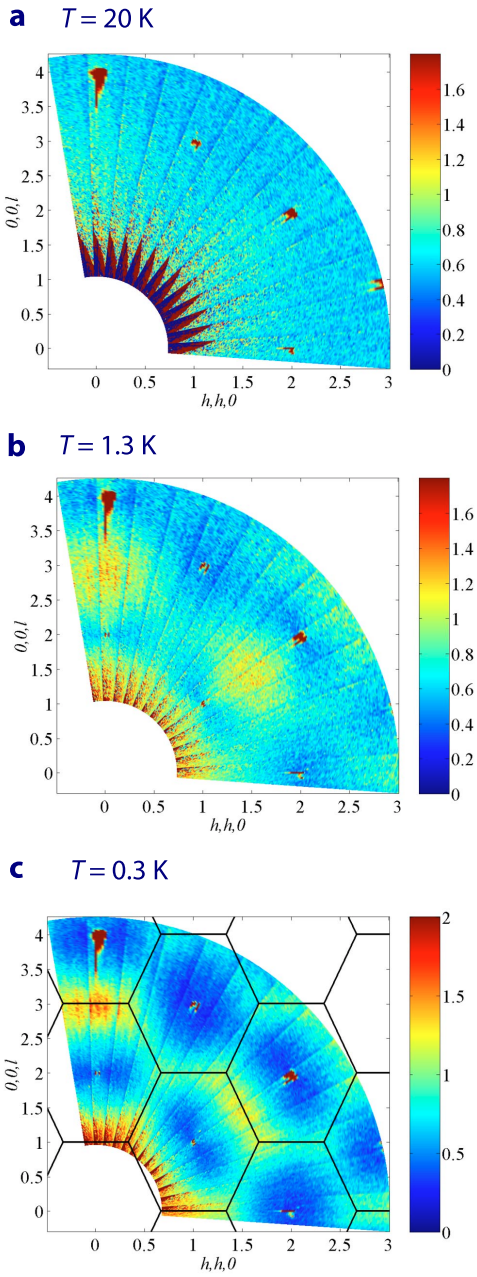

Figure 5.3: Diffuse scattering in spin ice at (a) $T = 20\,\mathrm{K}$, (b) $T = 1.3\,\mathrm{K}$, and (c) $T = 0.3\,\mathrm{K}$, showing the development of magnetic correlations with decreasing temperature. From Ref. [260].

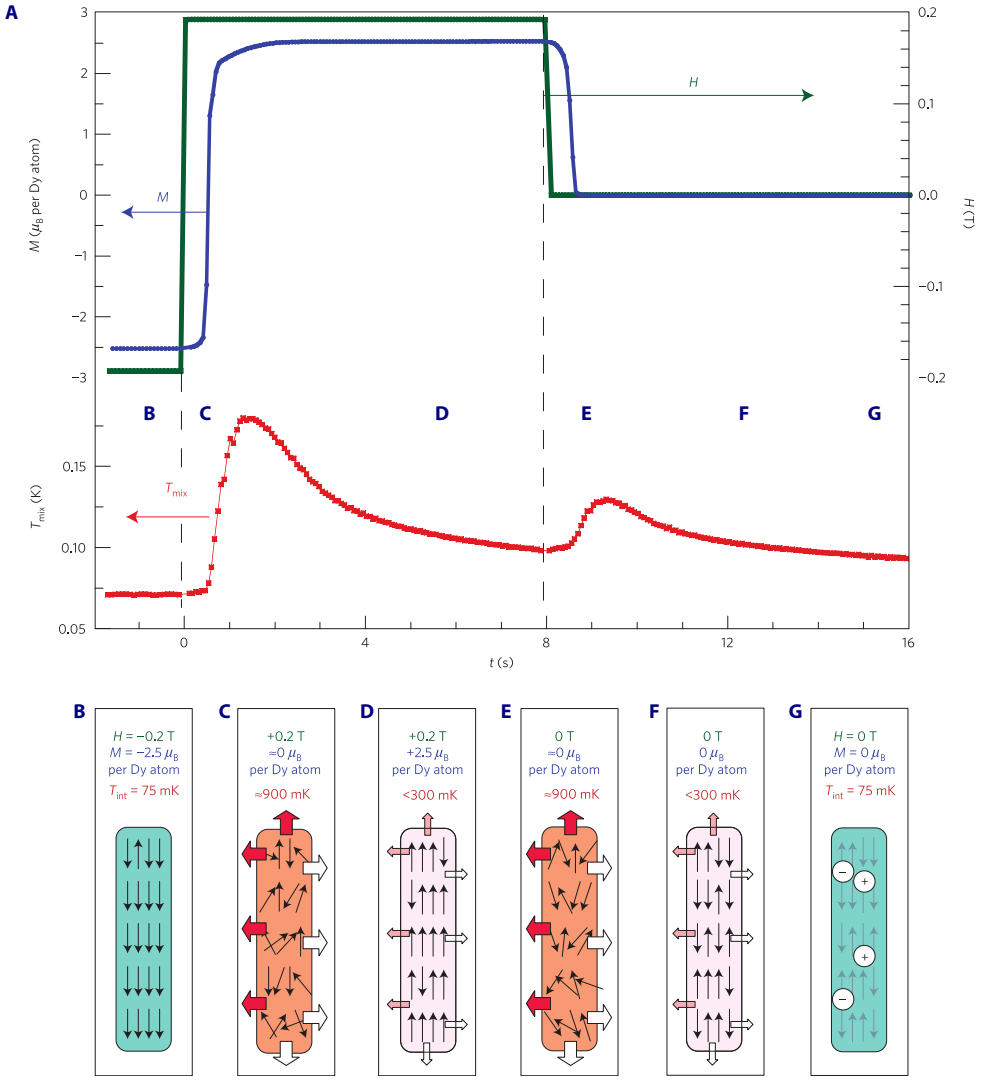

Figure 5.4: The avalanche quench method used to induce an out-of-equilibrium monopole population in DTO. The application of magnetic fields raises the sample temperature to 900 mK, before it is rapidly quenched through the spin ice freezing temperature, the dilution refrigerator mixing chamber temperature remaining under 200 mK throughout. Reproduced from Ref. [13].

Below a temperature of $T_f \sim 650\,\mathrm{mK}$, the spin ice state freezes, with the dynamics becoming much slower, thereby falling out of its equilibrium state with a small monopole population [263]. By providing a burst of thermal energy to the sample, an abundance of monopole/anti-monopole pairs can be created, with density quantified by the monopole current $\partial\vec{M}/\partial t$. This has been achieved using a method based upon the magnetothermal avalanche quench phenomenon at low temperatures in Ref. [13], illustrated in Fig. 5.4. At low temperatures where the population of occupied phonon modes is vanishing, the spin-spin channel dominates the dynamics and results in the slow relaxation of the equilibrium state. By cooling this thermally excited state rapidly through the spin ice freezing transition, a non-equilibrium monopole-rich state can be prepared [13]. Isotopically enriched ^{162}DTO has zero nuclear spin moment, so no relaxation can occur by assisted tunneling processes [14] — these states are metastable on the order of neutron scattering counting timescales, which provides an opportunity to investigate the spin correlations in this regime through the measurement of the magnetic neutron cross section, $\mathrm{d}\sigma/\mathrm{d}\Omega = A(\delta_{\alpha\beta} - \hat{Q}_\alpha\hat{Q}_\beta)S^{\alpha\beta}(\vec{Q})$.

5.3 Experimental details

As previously mentioned, spin ice undergoes a freezing transition at $T \sim 0.65\,\mathrm{K}$, during which it falls out of its equilibrium state with a small monopole population [263]. Careful bulk measurements on DTO by means of the novel

magnetothermal avalanche quench cooling protocol (AQP) [13] have found evidence for a magnetic analog of the Wien effect [264]. This places DTO in the regime of a weak magnetolyte. Other out-of-equilibrium phenomena have been observed during magnetic field sweeps — among which, magnetic avalanches — which were found to have a strong dependence on the thermal coupling of the sample to the heat reservoir: the mixing chamber plate of the dilution fridge.

The magnetothermal avalanche cooling method is reliant upon the conversion of magnetic work done to internal heat. At base temperature $\sim 100\,\mathrm{mK}$ in a dilution fridge, the application of a local magnetic field ($\sim 0.2\,\mathrm{T}$) induces an increase in the internal heat of a sample, which can occur up to $0.9\,\mathrm{K}$. The temperature is measured by mounting a thermometer directly to the sample during the AQP, and inferred from the increase in sample magnetization after the AQP to the equivalent isothermal magnetization at $0.9\,\mathrm{K}$. At its return to thermal equilibrium at $0.9\,\mathrm{K}$, the sample can cool quickly. Given that relatively little heat is transferred, the mixing chamber — the thermal reservoir — retains its cold temperature. Consequently, the sample cools rapidly; Fig. 5.4 reflects the cooling process, as well as the required field flips. This method facilitates a control over the cooling rate as the spin ice undergoes freezing transition.

The enabling of both rapid and slow cooling allows different densities of monopoles to be frozen in. The monopole population has previously been quantified through the monopole current $J = \mathrm{d}M/\mathrm{d}T$; this is reflected in

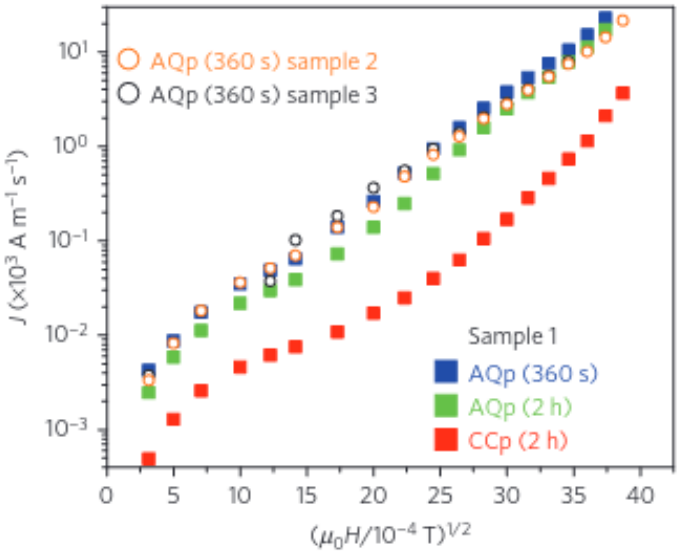

Figure 5.5: As compared to a conventional cooling protocol, the avalanche quench cooling method has been shown to result in the trapping of a reproducibly higher monopole population. From Ref. [264].

Fig. 5.5 alongside a bigger monopole current that is associated with a greater population. That the monopole current is larger than in the case of a conventional slow cooled sample is evidence that the avalanche quench protocol freezes in a greater population of monopoles. The potential for the creation of reproducible non-equilibrium states in spin ice was also demonstrated in previous experiments [13]. A large, high quality single crystal of ^{162}DTO — the same as that used in Ref. [115] — with mass 1.4 g was used in this experiment, and has previously been characterized using the SXD instrument, finding

very little structural disorder. We used this sample in our experiment since it has previously been very well characterized. The out-of-equilibrium states are metastable on the order of many days; here, we investigate the effect of the avalanche cooling protocol on the spin correlations as seen in the diffuse scattering, manifest in the equilibrium structure factor $S(\vec{Q}) \equiv \int S(\vec{Q}, \omega)\, \mathrm{d}\omega$.

Working closely with the ISIS technical staff, we prepared a simpler method to be used in the cryogen free E18 dilution refrigerator. Testing our method at Cardiff in a similar BlueFors dilution refrigerator, we were able to achieve cooling rates up to a maximum of $\sim 150\,\mathrm{mK\,s^{-1}}$ using a heater attached to the end of the sample, with a similar thermometer set up, as shown in panels (a) and (b) of Fig. 5.6. The cooling curve is shown in panel (c) of Fig. 5.6, which shows a much greater cooling rate than the $\sim 70\,\mathrm{mK\,s^{-1}}$ achieved previously in Ref. [13]. WISH was required due to the much-needed high resolution at low $\vec{Q}$, owing to the fall off of the magnetic form factor and low background required for discerning subtle diffuse features in the scattering. Measurement of the magnetization during the warming and cooling processes is perhaps the best case scenario; directly monitoring the sample temperature with a thermometer mounted to the bottom of the sample is, however, an equally effective method. The manipulation of monopole density by AQP supports the two key aims of this experiment: first, to develop experimental methods to probe non-equilibrium systems probed by neutrons, and second, to probe monopole rich states on the microscopic scale. The latter is of fundamental interest, given that monopoles may have some non-trivial types

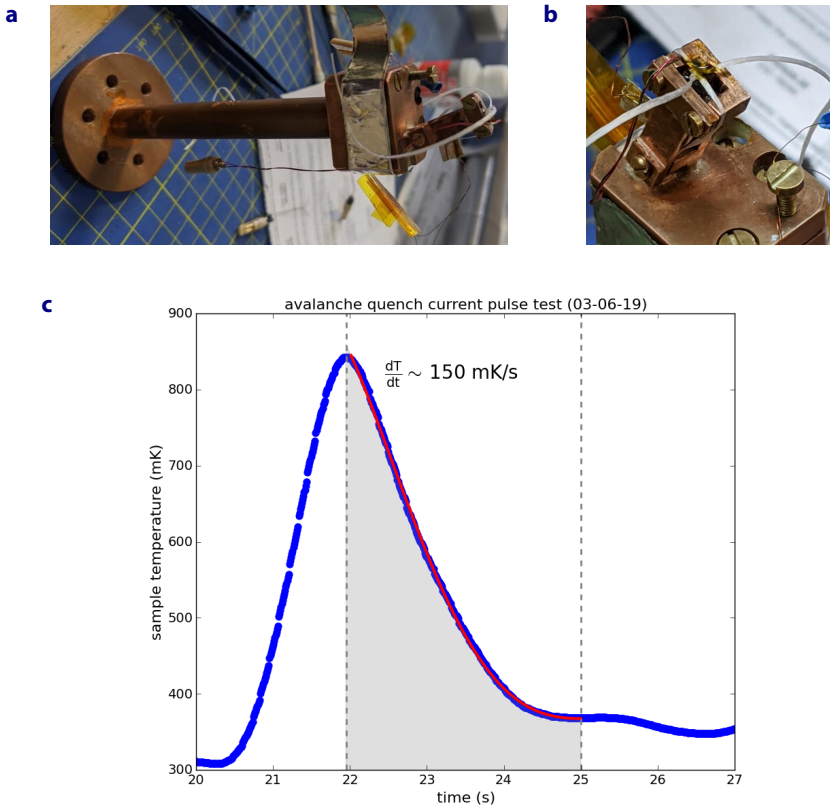

Figure 5.6: (a-b) Sample mount of $Dy_2Ti_2O_7$. (c) cooling curve achieved in the BlueFors dilution refrigerator at Cardiff using a pulse cooling method, with a resistive heater attached directly to the sample. This is more than double the cooling rate achieved in Ref. [13] of $\sim 70\,\mathrm{mK\,s^{-1}}$ so is likely to be sufficient when factors such as beam heating are taken into account.

of correlations. When the experiment was conducted, $Dy_2Ge_2O_7$ provided the only means of studying a state with more monopoles but was not available as a crystal.

Unfortunately, the E18 dilution refrigerator was damaged at ISIS in a

magnet quench during routine testing — a situation beyond our control — before we were able to test our pulse cooling method in the exact setup to be used on the beamline. As such, we were required to modify our setup as best as we could, and to work other standard equipment available to us. We had access to an Oxford instruments Kelvinox dilution insert (`NDRI-2`), to be used in conjunction with an Oxford Instruments Variox (OXF-09); it was therefore necessary to modify our experimental setup to accommodate the reduced cooling power.

Drawing from Refs. [265, 266], the heat transfer in solids by conduction follows the Fourier law

$$\vec{q} = -k(T)\vec{\nabla}T, \tag{5.2}$$

where q is the heat flux density, $k(T)$ the temperature dependent thermal conductivity, and T the temperature. In one dimension,

$$q = -k(T)\frac{\mathrm{d}T}{\mathrm{d}} \Rightarrow Q\int_0^L \frac{\mathrm{d}x}{A} = \int_{T_1}^{T_2} k(T)\mathrm{d}T, \tag{5.3}$$

where Q is the power, L the length along the x-axis, and A the cross section. For constants A and L, this simplifies to

$$\frac{Q}{A} = \frac{1}{L}\int_{T_1}^{T_2} k(T)\mathrm{d}T. \tag{5.4}$$

For most materials, $k(T)$ is strongly temperature dependent. For practical calculations, an average over the temperature region of interest is used, given

by the expression

$$\overline{k} = \frac{1}{T_2 - T_1} \int_{T_1}^{T_2} k(T) \mathrm{d}T. \tag{5.5}$$

Assuming perfect thermal contact with a heat bath and no internal dissipation, a steady-state thermal resistance can be defined from Eq. (5.4). For a rod with constant cross section A and length L, the thermal resistance takes the form

$$R_{\mathrm{th}} = \frac{T_2 - T_1}{Q} = \frac{L}{\overline{k}A}. \tag{5.6}$$

For transient conduction processes, energy conservation leads to a diffusion equation of the form

$$\rho C \frac{\partial T}{\partial t} = \vec{\nabla} \cdot [-k(T)\vec{\nabla}T] + Q, \tag{5.7}$$

where ρ is the density and C the specific heat capacity of the solid. The term on the left-hand side is identified with a thermal inertia. The first term on the right-hand side accounts for conduction and the second term represents a heat source. In 1D with constant thermal properties,

$$\frac{\partial T}{\partial t} = D \frac{\partial^2 T}{\partial x^2} + Q^{\star}, \tag{5.8}$$

where thermal diffusivity $D = k/\rho C$. From D, a characteristic diffusion time τ can be calculated, arising from the thermal perturbation, and is obtained by solving Eq. (5.8).

The cooling power of the Kelvinox `NDRI-2` dilution fridge insert used in test

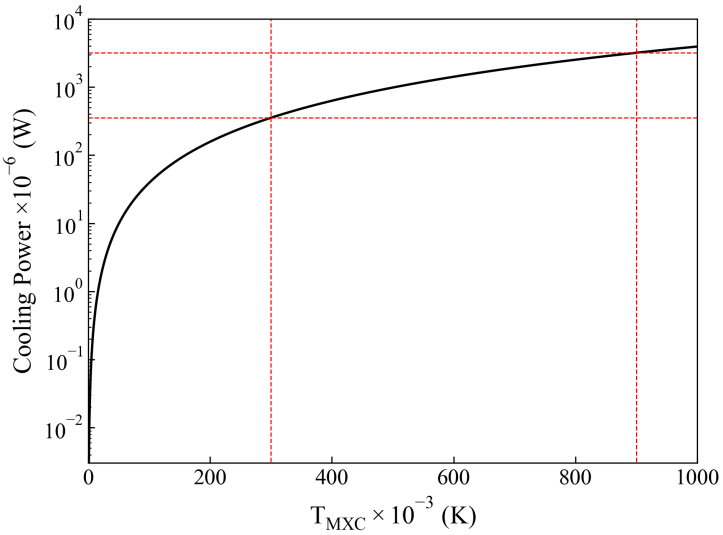

Figure 5.7: Kelvinox NDRI-2 dilution fridge insert cooling power curve. A fit to a function of the form $P(T) = aT^2$ was made using the data points $(T, P) = (15.75, 0)$ and $(25, 88)$ [mK, μW] from the manual. Extrapolation of this fit gives the cooling power at temperatures of interest, $(T, P) = (300, 353)$ and $(900, 3484)$ [mK, μW].

experiments is shown in Fig. 5.7. A fit to a function of the form $P(T) = aT^2$ was made using two data-points from the manual and extrapolated to higher temperatures, covering the temperature range of interest. At 300 mK the unit provides a cooling power of 353 µW, and at 900 mK, a cooling power of 3484 µW. The cooling power at 900 mK defines the upper limit of heat load that can be provided during the pulse heating protocol. The sample rig is essentially a spacer/adapter that allows the copper goniometer/sample mount to attach to the dipstick. On the dipstick end, the connection is M6 female and the goniometer/sample mount is M6 male. It is defined by the

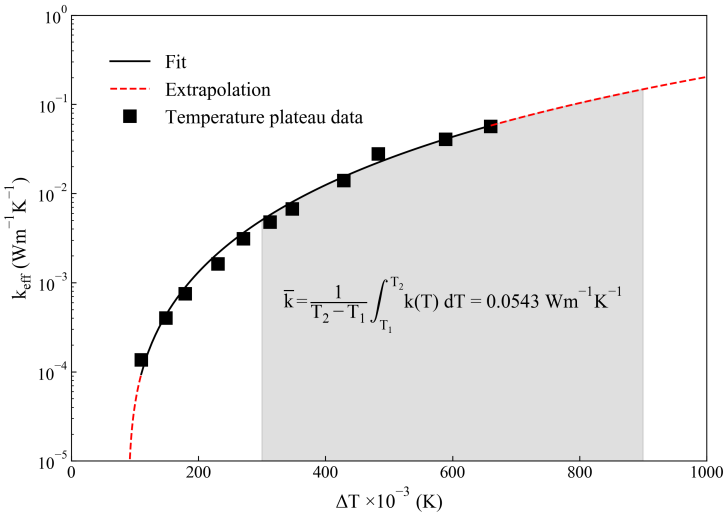

Figure 5.8: $Dy_2Ti_2O_7$ sample thermal conductivity measurement.

following dimensions

$$A = \pi r^2 = 103.87 \times 10^{-9}\ \mathrm{m}^2, \tag{5.9a}$$

$$L = 33 \times 10^{-3}\ \mathrm{m}. \tag{5.9b}$$

The sample is enclosed in a copper clamp which provides the thermal path through the adapter rig to the cold bath (mixing chamber). A 47 kΩ resistive heater glued directly to the sample on Rizla with GE varnish is used to heat the sample. A resistive thermometer is glued directly to the sample with GE varnish; this is not in direct contact with copper, and thus enables accurate measurement of sample temperature. An effective thermal conductivity at

each temperature can be calculated from

$$k_{\text{eff}} = \frac{QL}{A\,(T_2 - T_1)}, \tag{5.10}$$

with Q the heater power, T_1 the mixing chamber temperature, and T_2 the sample temperature. After the determination of the thermal conductivity at each of these temperatures, $\overline{k}$ can be calculated for temperatures between 300 and 900 mK.

Calculations on the optimization of the thermal link are shown in Fig. 5.9. From these calculations and from the perspective of achieving maximal heat transfer for the fastest cooling, the best course of action was to screw the Copper M6 goniometer directly to the mixing chamber (MXC) flange (without the shown copper cell) in order to maximize contact area of thermal pathway from sample to MXC. We used Gadolinium foil attached via Aluminum tape on the outer wall of the inner vacuum chamber (IVC) for collimation. The sample was enclosed firmly in copper cage to provide good thermal contact for heat transfer through goniometer to MXC stage, with a 2.096 kΩ resistive heater attached firmly to the extreme end of the sample, located furthest from MXC plate, on a flat portion of the crystal surface using thin nylon wire and GE varnish. The thermometer was clamped between the copper cage wall and in direct thermal contact with a large flat planar surface of the sample. We achieved 4-wire measurements of the thermometer voltage using a Stanford `SR850-DSP` lock-in amplifier while current was applied to a

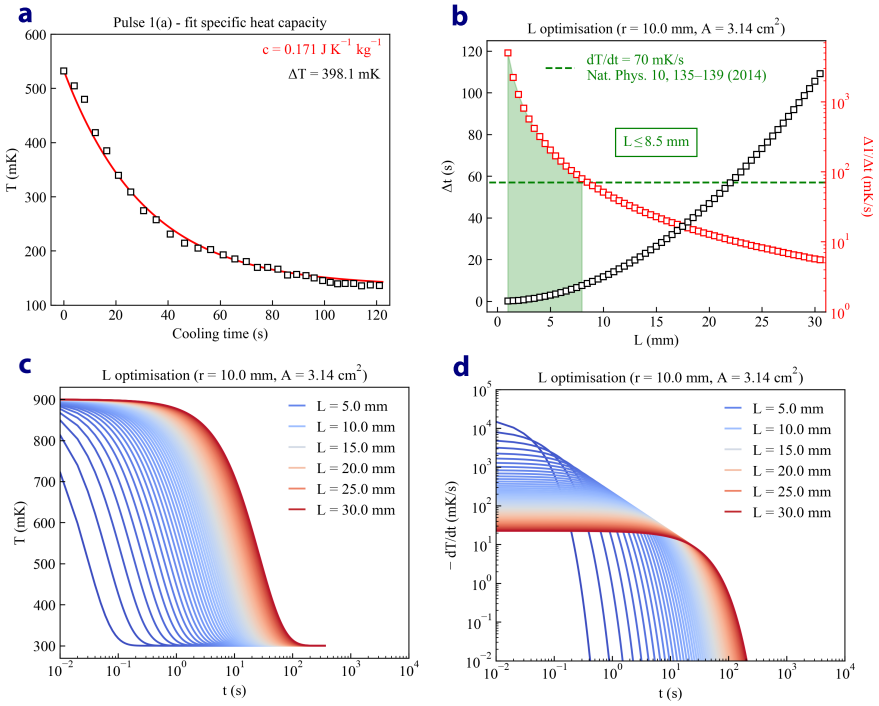

Figure 5.9: Optimization of the setup to be adapted for use in the less powerful Kelvinox dilution refrigerator insert, necessary since the cooling rate of $\sim 8.8\,\mathrm{mK\,s^{-1}}$ through the freezing transition to 300 mK is insufficient. From fits to the cooling curve we were able to extract a specific heat capacity and then investigate the effect of varying length and surface area. The best mount has the smallest thermal link distance and greatest surface area — for the best cooling rate, we simply screwed the goniometer directly into the MXC flange of the Kelvinox.

resistive heater with a `Keithley-220` power supply. Instrument control, data acquisition, and temperature conversion were achieved using `LabVIEW-2019`.

The beam-scraper was set to $20\,\mathrm{mm} \times 40\,\mathrm{mm}$, with beam divergence slits in medium resolution mode (0.4°), and choppers phased in double-frame mode.

The sample was aligned with (h, h, l) in the horizontal scattering plane and the rotation stage fine tuned such that the $(0, 0, 4)$ zone center was positioned close to 90° in detector bank 4, for the best statistics in this region of interest. Further, this matched initially the sample position in Ref. [115] for comparison, leaving 2 days for exploration after these initial measurements were obtained. Fast cooling protocol runs were carried out to probe spin correlations in non-equilibrium regime. Additionally, a slow cooling protocol run was carried out for comparison to fast cooled measurements. Finally, a high temperature run at 10 K was carried out for background subtraction to reveal the spin correlations, since polarization analysis was not available to us on WISH. Unfortunately, half way through the experiment, the facility had to shut down due to the COVID-19 pandemic, cutting our experiment short. Had the remainder of our beam-time been available to us, we would have adjusted the sample position to measure the $\vec{Q} = (0, 0, 2)$ position, where the Bragg peak is extinct and a pinch point manifest. As such, we present only an investigation of the zone boundary scattering around the $\vec{Q} = (0, 0, 3)$ position in reciprocal space, since the $\vec{Q} = (0, 0, 4)$ position is contaminated by nuclear Bragg contribution.

The data in detector space shows clear evidence for the existence of two crystallites; the dominant of these is hereafter referred to as 'main' and the weaker as 'secondary'. Main and secondary UB matrices have been optimized via an iterative process of manual peak indexation and refinement. Optimized lattice parameters are $a = b = c = 10.146(2)$ Å and $\alpha = \beta = \gamma = 90°$.

Observed reflections and systematic absences are consistent with an F centered unit cell, as expected for the space group. The main and secondary UBs are given by the matrices

$$\mathsf{U}_\mathrm{m} = \begin{pmatrix} -0.53724968 & -0.64230721 & 0.54662989 \\ 0.74125171 & -0.66877679 & -0.05730186 \\ 0.40237878 & 0.37440493 & 0.83541143 \end{pmatrix}, \tag{5.11}$$

$$\mathsf{U}_\mathrm{s} = \begin{pmatrix} -0.53348602 & -0.66060023 & 0.52820451 \\ 0.75269851 & -0.65564734 & -0.05976218 \\ 0.38579479 & 0.36569646 & 0.84701150 \end{pmatrix}. \tag{5.12}$$

Associated with these matrices are the angular values $\mathrm{tr}\,\mathsf{U}_\mathrm{m} = 1 + 2\cos\varphi_\mathrm{m} = -0.37061504$ (which gives $\varphi_\mathrm{m} = 133.3°$ for the main crystallite) and $\mathrm{tr}\,\mathsf{U}_\mathrm{s} = 1 + 2\cos\varphi_\mathrm{s} = -0.34212186$ (which gives $\varphi_\mathrm{s} = 132.1°$ for the secondary crystallite). The main and secondary sets of peaks predicted from these UB matrices are shown in Fig. 5.10. Based on these angles, the angular separation of the two crystallites can be calculated as $\delta\varphi = (\varphi_\mathrm{m} - \varphi_\mathrm{s}) = 1.2°$. In terms of the resultant diffuse scattering, such a small angular separation will not distort the response in any meaningful way.

The panel/monitor data was cropped between TOF $= 6000 - 99000\,\mu$s and normalized by proton charge. Panel data was then normalized to incident monitor data (`monitorID = 4`), and normalized to the incoherent scattering

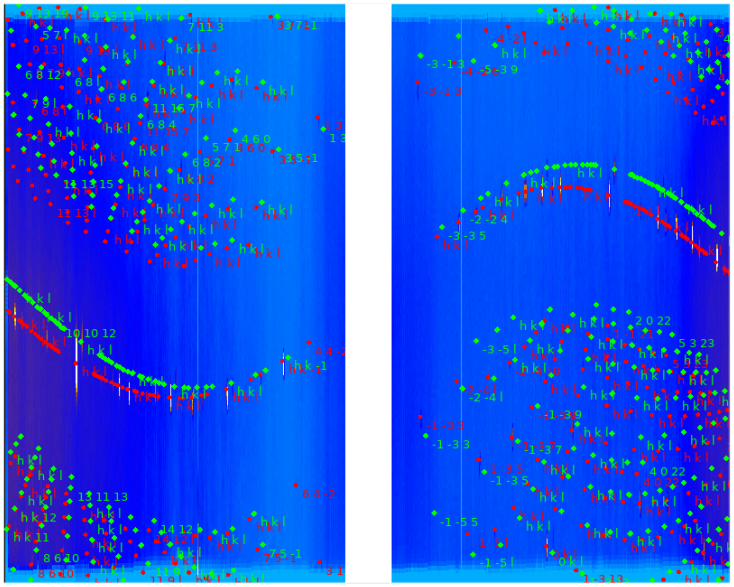

Figure 5.10: Indexation of Bragg peaks in detector space at $T = 0.35\,\mathrm{K}$. Predicted peaks calculated for the F-centered lattices of the main and secondary crystallites are shown in red and green respectively. These orientation matrices are used to transform the data to reciprocal space since sample orientation is fixed across runs.

of a standard absorption corrected Vanadium run. The normalized data was then treated with a Lorentz correction ($\lambda = 0.8 - 9.3\,\text{Å}$) and finally subject to a magnetic form factor correction for Dy^{3+} ions.

5.4 Results

The cooling rates achieved on the beamline are shown in Fig. 5.11. Given the limited cooling rate of the Kelvinox, as compared to the E18 cryogen free refrigerator, the cooling curves appear to plateau in the vicinity of the

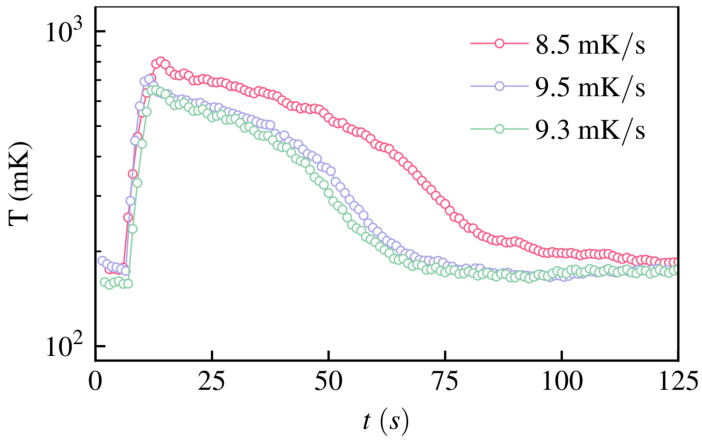

Figure 5.11: Cooling rates achieved on the beamline. In addition to a conventional slow cooling run, three attempts were made to achieve as fast a cooling rate as possible in the Kelvinox. All three fast runs were much slower than that of the $70\,\mathrm{mK\,s^{-1}}$ in Ref. [13].

freezing temperature, suggesting perhaps a degree of dynamical arrest thereby inhibiting the rapid cooling of the sample, as achieved on BlueFors at Cardiff. In panel (a) of Fig. 5.12 we show a high temperature subtraction from the slow cooled ($0.2\,\mathrm{mK\,s^{-1}}$) state at base temperature ($T = 0.3\,\mathrm{K}$) in the (h, h, l) reciprocal plane, confirming the usual pattern of diffuse scattering observed in previous experiments [260]. By comparison, in panel (b) we show the net scattering resulting from the fastest pulse cooling rate achieved ($9.5\,\mathrm{mK\,s^{-1}}$), with the slow cooled measurement shown in (a) subtracted from it. As can be seen, there is no significant change to the magnetic correlations manifest in the (h, h, l) plane for a fast cooling rate of ($9.5\,\mathrm{mK\,s^{-1}}$) as compared to ($0.2\,\mathrm{mK\,s^{-1}}$).

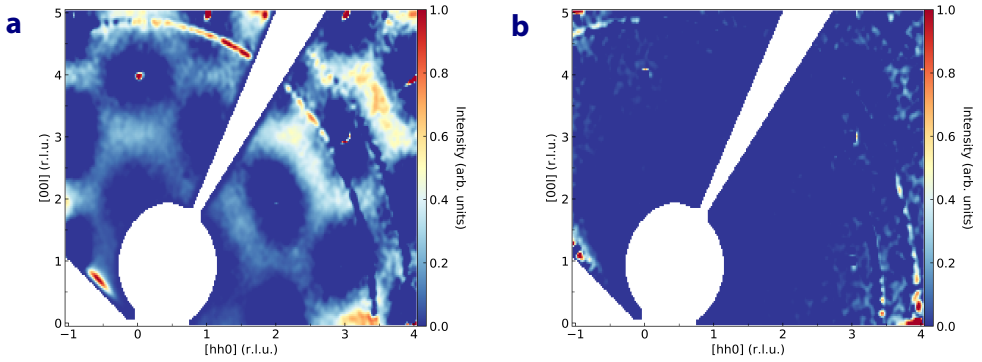

Figure 5.12: Diffuse scattering in (h, h, l) for slow and fast cooled states. Panel (a) shows the slow cooled ($0.2\,\mathrm{mK\,s^{-1}}$) state with a high temperature run at 10 K subtracted, showing the usual pattern of diffuse scattering observed in previous experiments [260].

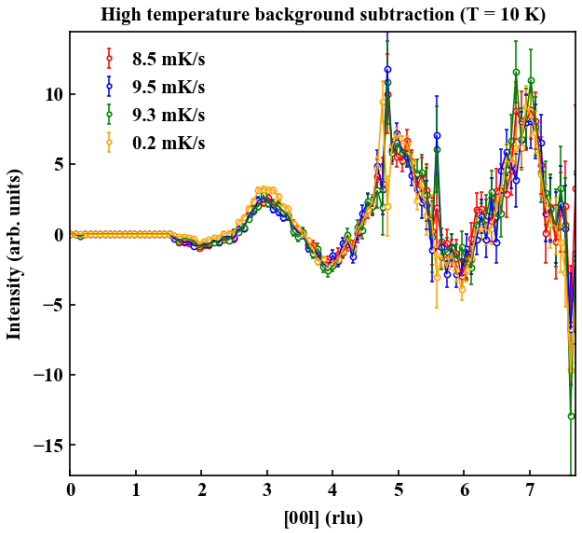

Figure 5.13: Linecut along the $(0, 0, l)$ direction for fast and slow cooling rates, showing no appreciable differences between cooling rates above the noise floor.

Linecuts along the $(0, 0, l)$ direction are given in Fig. 5.13 for both slow and fast cooling rates, and show no appreciable difference between the fast and slow cool measurements. Despite not having access to the $(0, 0, 2)$ position, in the vicinity of a pinch point feature, given that no differences in spectral weight along the rest of the zone axis were observed, it seems unlikely that such a difference would manifest here.

5.5 Conclusions

We have investigated the effect of cooling rate on the spin correlations at low temperature in the classical spin ice material $Dy_2Ti_2O_7$, and have shown that the rapid cooling rates achieved by the avalanche quench cooling protocol in Ref. [13] can be obtained more simply, and in a manner more amenable to beamline measurements, with a heat pulse protocol described in this chapter. Noting the reduced cooling rate of the Kelvinox dilution refrigerator as compared to that of E18 which we had planned to use, we can place an upper bound on the manifestation of non-trivial spin correlations resultant from quench cooling of $9.5\,\mathrm{mK\,s^{-1}}$ based on our measurements.

Chapter 6

Conclusion and outlook

In conclusion, this thesis has focused primarily on the application of single-crystal neutron diffraction techniques to the study of frustrated and correlated magnetic materials. The primary results obtained over the course of the experiments that form the basis to this thesis are summarized as follows.

In Chap. 3, we have presented the development of a new single-crystal algorithm, namely `LinkedUBs` which has been included in `mantid`, designed principally for the WISH diffractometer at the ISIS Pulsed Neutron and Muon Source, Didcot, UK. Foremost a powder instrument, WISH has limited out-of-plane coverage, thereby requiring multiple rotations of the sample in single-crystal experiments to achieve sufficient coverage in reciprocal space to facilitate quantitative structural characterizations. This novel algorithm is necessary to ensure that a continuous reciprocal space is maintained in the analysis of data, with initial direction choices made in the construction of the initial UB matrix maintained subsequently. Without the imposition of this constraint, spurious domain structure can appear manifest and thereby

inhibit the solution for space groups other than the highly symmetrical cubic family, where degeneracy of directions is manifest. We have also demonstrated the utility provided by the combined usage of `LinkedUBs` with an implementation of a method for the stitching together of runs with different statistical weightings in reciprocal space; the resulting reciprocal space volumes are especially useful in the analysis of diffuse scattering data and further extends the utility of the WISH instrument to deal routinely with single-crystal experiments and thereby enhance the science program of the instrument.

We have presented quantitative refinements of the crystal structure of the garnet material $Ca_3Ga_2Ge_3O_{12}$ and the crystal and magnetic structures of MnF_2 as proof of its utility. Given the ability of WISH to measure small magnetic moments and small sample volumes, the scope of the instrument is thereby broadened to allow for its strengths in this capacity to be expanded to the realm of single-crystal determination for complex magnetic structures. Moreover, the UB matrices produced by this algorithm can be used in the stitching together of runs to produce detailed reciprocal space planes, and we have demonstrated this utility by presenting magnetic diffuse scattering measurements in $GeNi_2O_4$, showing previously unseen magnetic correlations. This is a useful feature for diffuse scattering studies which are becoming increasingly common in the literature, and at higher demand by non-specialist neutron beam users.

In Chap. 4, we have applied single-crystal neutron diffraction and mag-

netization measurements in an applied magnetic field to study the multiple commensurate periodicities manifest in an Ising $j_{\text{eff}} = \frac{1}{2}$ magnet, published in Ref. [167]. From our single-crystal results on the WISH and RITA instruments, as well as our powder results from WISH and TASP, we have found a correspondence between short range ordered states and magnetization plateaus. Furthermore, we have found a co-existence of multiple short range symmetries when magnetic field is applied out of the easy plane. When magnetic field is applied strictly along the easy c-axis, only $\langle \hat{T}^3 \rangle$ symmetry is observed. This is in contrast to the case where field is applied out of the ac-plane, resulting in a component of field along the b-axis. In this case, as well as stabilizing multiple co-existing symmetries — including $\langle \hat{T}^4 \rangle$ periodicity — we observe a hysteresis effect and interpret our results based on the formation of magnetic antiphase boundaries. It would be worthwhile in the future to measure the $\vec{Q}$-dependence of magnetic excitations below T_{N} in an inelastic neutron scattering experiment, as we had intended to carry out. Further magnetization measurements in combination with single-crystal diffraction would be worthwhile in the search for new periodicities at low temperature, in particular, investigating the microscopic nature of states prepared by cycling field in minor loops.

In Chap. 5, we describe a new method of quench cooling to prepare out-of-equilibrium states in spin ice, achieving a maximum rate of $150\,\text{mK}\,\text{s}^{-1}$ in a BlueFors dilution refridgerator at Cardiff University. Due to complications relating to the maintenance of the E18 dilution refridgerator at ISIS, we were

unable to use this in our beamline experiment; instead, we adapted our cooling protocol to work with the lesser powered Kelvinox dilution refrigeration insert in conjunction with an Oxford Instruments Variox cryostat. Aiming to measure spin correlations in an out-of-equilibrium prepared monopole rich state, we implemented our cooling protocol on the beamline, as summarized by the rapid cooling of a heat pulse given to the sample through the spin ice freezing temperature, which thereby traps in an out-of-equilibrium population of monopoles. Our results did not indicate any change to the spin correlations in our fast cooled states up to a maximum of $9.5\,\mathrm{mK\,s^{-1}}$, as compared to conventional slow cool states. These results indicate a lower bound on the stabilization of non-equilibrium monopole populations amenable to changes in the spin correlation function and to the screening of the dipolar interaction at long distances, as evidenced by changes to the pinch points. It would be worthwhile to carry out the experiment we had set out to conduct using the same methodology in the more powerful E18 refrigerator. Our testing using a similar refrigerator at Cardiff indicated that the cooling through the spin ice freezing transition is sufficient to induce an enhanced monopole population, so if any change to the diffuse scattering — be they changes to the width of the pinch points, indicating a change to the screening of dipolar fields at long distances [259], or changes to the zone boundary scattering — they should be visible in a follow-up experiment when the E18 refrigerator is repaired.

References

[1] L. C. Chapon, P. Manuel, P. G. Radaelli, C. Benson, L. Perrott, *et al.*, Neutron News **22**, 22 (2011).

[2] T. M. Michels-Clark, A. T. Savici, V. E. Lynch, X. Wang, and C. M. Hoffmann, J. Appl. Crystallogr. **49**, 497 (2016).

[3] Z. He, J. I. Yamaura, Y. Ueda, and W. Cheng, J. Am. Chem. Soc. **131**, 7554 (2009).

[4] M. Lenertz, J. Alaria, D. Stoeffler, S. Colis, and A. Dinia, J. Phys. Chem. C **115**, 17190 (2011).

[5] K. Singh, A. Maignan, D. Pelloquin, O. Perez, and C. Simon, Journal of Materials Chemistry **22**, 6436 (2012).

[6] Y. Xiaoyan, J. Phys. Chem. A **116**, 2278 (2012).

[7] A. Saúl, D. Vodenicarevic, and G. Radtke, Phys. Rev. B **87**, 024403 (2013).

[8] Z. He and W. Cheng, J. Magn. Magn. Mater. **362**, 27 (2014).

[9] C. B. Liu, Z. Z. He, S. L. Wang, M. Yang, Y. Liu, *et al.*, J. Phys.: Condens. Matter **31**, 375802 (2019).

[10] F. D. M. Haldane, Physics letters a **93**, 464 (1983).

[11] F. D. M. Haldane, Physical review letters **50**, 1153 (1983).

[12] E. Lieb, T. Schultz, and D. Mattis, Annals of Physics **16**, 407 (1961).

[13] C. Paulsen, M. J. Jackson, E. Lhotel, B. Canals, D. Prabhakaran, K. Matsuhira, S. Giblin, and S. Bramwell, Nature Physics **10**, 135 (2014).

[14] C. Paulsen, S. Giblin, E. Lhotel, D. Prabhakaran, K. Matsuhira, G. Balakrishnan, and S. Bramwell, Nature communications **10**, 1 (2019).

[15] J. Chadwick, Nature **129**, 312 (1932).

[16] H. Von Halban and P. Preiswerk, CR Hebd. Séances Acad **203**, 73 (1936).

[17] D. P. Mitchell and P. N. Powers, Phys. Rev. **50**, 486 (1936).

[18] F. Bloch, Phys. Rev. **50**, 259 (1936).

[19] J. S. Schwinger, Phys. Rev. **51**, 544 (1937).

[20] O. Hahn and F. Strassmann, Naturwissenschaften **27**, 11 (1939).

[21] L. Meitner and O. R. Frisch, Nature **143**, 239 (1939).

[22] O. R. Frisch and J. A. Wheeler, Physics Today **20**, 43 (1967).

[23] C. G. Shull, Rev. Mod. Phys. **67**, 753 (1995).

[24] T. E. Mason, T. J. Gawne, S. E. Nagler, M. B. Nestor, and J. M. Carpenter, Acta Crystallogr. A **69**, 37 (2013).

[25] A. M. Weinberg, Science **109**, 245 (1949).

[26] A. A. Needell, Historical studies in the physical sciences **14**, 93 (1983).

[27] D. Hurst, Electrical Engineering **70**, 476 (1951).

[28] C. G. Shull and J. S. Smart, Phys. Rev. **76**, 1256 (1949).

[29] B. Brockhouse, Can J Phys. **33**, 889 (1955).

[30] B. N. Brockhouse and A. T. Stewart, Phys. Rev. **100**, 756 (1955).

[31] B. N. Brockhouse, Phys. Rev. **106**, 859 (1957).

[32] J. Hendrie, The brookhaven high flux beam research reactor (1964).

[33] P. Ageron, Endeavour **31**, 67 (1972).

[34] J. Finney, Europhysics News **20**, 119 (1989).

[35] T. Mason, D. Abernathy, I. Anderson, J. Ankner, T. Egami, *et al.*, Physica B: Condensed Matter **385**, 955 (2006).

[36] ISIS STFC, Annual review (2019) (2019).

[37] ISIS STFC, Idaaas: Isis data analysis as a service (2021).

[38] O. Arnold, J. Bilheux, J. Borreguero, A. Buts, S. Campbell, *et al.*, Nuclear Instruments and Methods in Physics Research Section A: Accelerators, Spectrometers, Detectors and Associated Equipment **764**, 156 (2014).

[39] Mantid Project, `https://github.com/mantidproject/mantid` (2021).

[40] R. Garoby, A. Vergara, H. Danared, I. Alonso, E. Bargallo, *et al.*, Physica Scripta **93**, 014001 (2017).

[41] H. Abele, Progress in Particle and Nuclear Physics **60**, 1 (2008).

[42] C. Patrignani, P. Richardson, O. Zenin, R. Zhu, A. Vogt, *et al.*, Chin. Phys. C **40**, 100001 (2016).

[43] G. Konrad and H. Abele, in *The 26th International Nuclear Physics Conference* (SISSA Medialab, 2017) p. 359.

[44] M. Blume, J. Appl. Phys **57**, 3615 (1985).

[45] J. Jensen and A. R. Mackintosh, *Rare earth magnetism* (Clarendon Press, 1991).

[46] IUCr, *International tables for crystallography. Vol. C. Mathematical, physical and chemical tables* (International Union of Crystallography, 1993).

[47] L. Van Hove, Phys. Rev. **95**, 249 (1954).

[48] D. B. Litvin and V. Kopský, Acta Crystallographica Section A **67**, 415 (2011).

[49] A. Glazer, M. Aroyo, and A. Authier, Acta Crystallogr. A **70**, 300–302 (2014).

[50] P. Buser and H. Karcher, in *Global Differential Geometry and Global Analysis* (Springer, 1981) pp. 82–93.

[51] J. A. Wolf, *Spaces of constant curvature*, 6th ed., Vol. 372 (American Mathematical Soc., 2011).

[52] IUCr, *International Tables for Crystallography, Volume B: Reciprocal Space* (Springer Science & Business Media, 2008).

[53] W. L. Bragg, Proceedings of the Royal Society of London. Series A, Containing papers of a mathematical and physical character **89**, 248 (1913).

[54] IUCr, *International Tables for Crystallography, Volume A: Space Group Symmetry*, edited by T. Hahn (Kluwer, Dordrecht, 2002).

[55] R. D. Johnson, L. C. Chapon, D. D. Khalyavin, P. Manuel, P. G. Radaelli, *et al.*, Phys. Rev. Lett. **108**, 067201 (2012).

[56] G. F. Koster, in *Solid state physics*, Solid State Physics, Vol. 5 (Elsevier, 1957) pp. 173–256.

[57] H. Hiller, The American Mathematical Monthly **93**, 765 (1986).

[58] M. A. Armstrong, *Groups and symmetry* (Springer Science & Business Media, 1997).

[59] C. Giacovazzo, H. L. Monaco, D. Viterbo, F. Scordari, G. Gilli, *et al.*, *Fundamentals of crystallography*, Vol. 7 (Oxford University Press, 2002).

[60] E. Kroumova, M. Aroyo, J. Perez-Mato, A. Kirov, C. Capillas, *et al.*, Phase Transitions: A Multinational Journal **76**, 155 (2003).

[61] M. S. Dresselhaus, G. Dresselhaus, and A. Jorio, *Group theory: application to the physics of condensed matter* (Springer Science & Business Media, 2007).

[62] C. Bradley and A. Cracknell, *The mathematical theory of symmetry in solids: representation theory for point groups and space groups* (Oxford University Press, 2009).

[63] P. Radaelli, *Symmetry in Crystallography: Understanding the International Tables*, IUCr texts on crystallography (Oxford University Press, 2011).

[64] A. Wills, Le Journal de Physique IV **11**, 133 (2001).

[65] S. Van Smaalen, *Incommensurate crystallography*, Vol. 21 (Oxford University Press, 2007).

[66] P. Babkevich, *Quantum Materials Explored by Neutron Scattering*, Ph.D. thesis, University of Oxford (2012).

[67] A. S. Wills, Phys. Rev. B **63**, 064430 (2001).

[68] S. W. Lovesey, *Theory of neutron scattering from condensed matter* (Clarendon Press, 1984).

[69] G. Bacon, *Fifty Years of Neutron Diffraction* (Adam Hilger, 1986).

[70] M. F. Collins, *Magnetic Critical Scattering* (Oxford University Press, New York, 1989).

[71] G. Shirane, S. M. Shapiro, and J. M. Tranquada, *Neutron scattering with a triple-axis spectrometer: basic techniques* (Cambridge University Press, 2002).

[72] G. L. Squires, *Introduction to the theory of thermal neutron scattering* (Courier Corporation, 1996).

[73] J. Schwinger, Phys. Rev. **73**, 407 (1948).

[74] L. L. Foldy, Rev. Mod. Phys. **30**, 471 (1958).

[75] L. Koester and A. Steyerl, *Neutron physics*, Vol. 80 (Springer, 2006).

[76] T. Welberry, M. Gutmann, H. Woo, D. Goossens, G. Xu, *et al.*, J. Appl. Crystallogr. **38**, 639 (2005).

[77] J. A. Paddison, J. R. Stewart, and A. L. Goodwin, J. Phys. Condens. Matter **25**, 454220 (2013).

[78] T. Proffen and R. Neder, J. Appl. Crystallogr. **30**, 171 (1997).

[79] R. B. Neder and T. Proffen, *Diffuse Scattering and Defect Structure Simulations: A cook book using the program DISCUS*, Vol. 11 (Oxford University Press, 2008).

[80] J. A. Paddison, Acta Crystallogr. A **75**, 14 (2019).

[81] R. Waite, *Neutron Scattering Studies of Spin-Density Waves in Itinerant Systems*, Ph.D. thesis, Bristol University (2021).

[82] A. T. Boothroyd, *Principles of Neutron Scattering from Condensed Matter* (Oxford University Press, 2020).

[83] E. Riordan, *Quantum spin systems and magnetic frustration investigated with high frequency AC susceptibility and muons*, Ph.D. thesis, Cardiff University (2020).

[84] S. Blundell, Magnetism in condensed matter (2003).

[85] F. Hippert, E. Geissler, J. L. Hodeau, E. Lelièvre-Berna, and J.-R. Regnard, *Neutron and X-ray Spectroscopy* (Springer Science & Business Media, 2006).

[86] L. Edwards, `LinkedUBs`, `mantid/Framework` (2018), accessed 27/10/2021.

[87] P. Wadley, V. Novák, R. Campion, C. Rinaldi, X. Martí, H. Reichlová, J. Železnỳ, J. Gazquez, M. Roldan, M. Varela, *et al.*, Nature communications **4**, 1 (2013).

[88] P. Wadley, V. Hills, M. Shahedkhah, K. Edmonds, R. Campion, V. Novák, B. Ouladdiaf, D. Khalyavin, S. Langridge, V. Saidl, *et al.*, Scientific reports **5**, 1 (2015).

[89] S. Yang, A. J. Ramirez-Cuesta, R. Newby, V. Garcia-Sakai, P. Manuel, S. K. Callear, S. I. Campbell, C. C. Tang, and M. Schröder, Nature chemistry **7**, 121 (2015).

[90] O. Benson, I. Da Silva, S. P. Argent, R. Cabot, M. Savage, H. G. Godfrey, Y. Yan, S. F. Parker, P. Manuel, M. J. Lennox, *et al.*, Journal of the American Chemical Society **138**, 14828 (2016).

[91] D. R. Harcombe, P. G. Welch, P. Manuel, P. J. Saines, and A. L. Goodwin, Phys. Rev. B **94**, 174429 (2016).

[92] M. Savage, I. Da Silva, M. Johnson, J. H. Carter, R. Newby, M. Suyetin, E. Besley, P. Manuel, S. Rudić, A. N. Fitch, *et al.*, Journal of the American Chemical Society **138**, 9119 (2016).

[93] N. Waterfield Price, R. D. Johnson, W. Saenrang, F. Maccherozzi, S. S. Dhesi, A. Bombardi, F. P. Chmiel, C.-B. Eom, and P. G. Radaelli, Phys. Rev. Lett. **117**, 177601 (2016).

[94] A. Agbelele, D. Sando, C. Toulouse, C. Paillard, R. Johnson, R. Rüffer, A. Popkov, C. Carrétéro, P. Rovillain, J.-M. Le Breton, *et al.*, Advanced Materials **29**, 1602327 (2017).

[95] F. Moreau, I. Da Silva, N. H. Al Smail, T. L. Easun, M. Savage, H. G. Godfrey, S. F. Parker, P. Manuel, S. Yang, and M. Schröder, Nature communications **8**, 1 (2017).

[96] Z. Lu, H. G. Godfrey, I. Da Silva, Y. Cheng, M. Savage, F. Tuna, E. J. McInnes, S. J. Teat, K. J. Gagnon, M. D. Frogley, *et al.*, Nature communications **8**, 1 (2017).

[97] N. Waterfield Price, R. D. Johnson, W. Saenrang, A. Bombardi, F. P. Chmiel, C. B. Eom, and P. G. Radaelli, Phys. Rev. Applied **8**, 014033 (2017).

[98] Y. Yan, D. I. Kolokolov, I. Da Silva, A. G. Stepanov, A. J. Blake, A. Dailly, P. Manuel, C. C. Tang, S. Yang, and M. Schröder, Journal of the American Chemical Society **139**, 13349 (2017).

[99] A. Biffin, R. D. Johnson, S. Choi, F. Freund, S. Manni, *et al.*, Phys. Rev. B **90**, 205116 (2014).

[100] D. D. Khalyavin, A. N. Salak, A. B. Lopes, N. M. Olekhnovich, A. V. Pushkarev, *et al.*, Phys. Rev. B **92**, 224428 (2015).

[101] S. Bennington, S. Campbell, T. Broome, D. Picton, and T. Beynon, J. Neutron Res. **11**, 93 (2003).

[102] O. Kirichek, C. Lawson, D. Jenkins, C. Ridley, and D. Haynes, Cryogenics **88**, 101 (2017).

[103] M. B. Stone, J. L. Niedziela, M. J. Loguillo, M. A. Overbay, and D. L. Abernathy, Review of Scientific Instruments **85**, 085101 (2014).

[104] S. Ikeda and J. M. Carpenter, Nuclear Instruments and Methods in Physics Research Section A: Accelerators, Spectrometers, Detectors and Associated Equipment **239**, 536 (1985).

[105] K. Lefmann and K. Nielsen, Neutron news **10**, 20 (1999).

[106] O. Young, A. R. Wildes, P. Manuel, B. Ouladdiaf, D. D. Khalyavin, *et al.*, Phys. Rev. B **88**, 024411 (2013).

[107] Y. F. Guo, A. J. Princep, X. Zhang, P. Manuel, D. Khalyavin, *et al.*, Phys. Rev. B **90**, 075120 (2014).

[108] N. Terada, D. D. Khalyavin, P. Manuel, T. Osakabe, P. G. Radaelli, *et al.*, Phys. Rev. B **89**, 220403 (2014).

[109] D. Billington, D. Ernsting, T. E. Millichamp, C. Lester, S. B. Dugdale, *et al.*, Sci. Rep. **5**, 12428 (2015).

[110] R. D. Johnson, D. D. Khalyavin, P. Manuel, A. Bombardi, C. Martin, *et al.*, Phys. Rev. B **93**, 180403 (2016).

[111] N. Terada, D. D. Khalyavin, P. Manuel, T. Osakabe, A. Kikkawa, *et al.*, Phys. Rev. B **93**, 081104 (2016).

[112] O. A. Petrenko, O. Young, D. Brunt, G. Balakrishnan, P. Manuel, *et al.*, Phys. Rev. B **95**, 104442 (2017).

[113] N. Terada, Y. Ikedo, H. Sato, D. D. Khalyavin, P. Manuel, *et al.*, Phys. Rev. B **96**, 035128 (2017).

[114] L. Ding, F. Orlandi, D. D. Khalyavin, A. T. Boothroyd, D. Prabhakaran, *et al.*, Crystals **8**, 88 (2018).

[115] S. R. Giblin, M. Twengström, L. Bovo, M. Ruminy, M. Bartkowiak, P. Manuel, J. C. Andresen, D. Prabhakaran, G. Balakrishnan, E. Pomjakushina, C. Paulsen, E. Lhotel, L. Keller, M. Frontzek, S. C. Capelli, O. Zaharko, P. A. McClarty, S. T. Bramwell, P. Henelius, and T. Fennell, Phys. Rev. Lett. **121**, 067202 (2018).

[116] N. Terada, Y. Ikedo, H. Sato, D. D. Khalyavin, P. Manuel, *et al.*, Phys. Rev. B **99**, 064402 (2019).

[117] K. J. Franke, P. R. Dean, M. C. Hatnean, M. T. Birch, D. Khalyavin, *et al.*, AIP Adv. **9**, 125228 (2019).

[118] C. J. Ridley, C. L. Bull, N. P. Funnell, S. C. Capelli, P. Manuel, *et al.*, J. Appl. Phys **125**, 015901 (2019).

[119] O. Young, G. Balakrishnan, P. Manuel, D. D. Khalyavin, A. R. Wildes, *et al.*, Crystals **9**, 488 (2019).

[120] S. Ishiwata, T. Nakajima, J. Kim, D. S. Inosov, N. Kanazawa, *et al.*, Phys. Rev. B **101**, 134406 (2020).

[121] O. Kirichek, J. Brown, D. Adroja, P. Manuel, G. Kouzmenko, R. Bewley, and R. Wotherspoon, in *Journal of Physics: Conference Series*, Vol. 400 (IOP Publishing, 2012) p. 052013.

[122] M. K. Jacobsen, C. J. Ridley, A. Bocian, O. Kirichek, P. Manuel, D. Khalyavin, M. Azuma, J. P. Attfield, and K. V. Kamenev, Review of Scientific Instruments **85**, 043904 (2014).

[123] T. Youngs, *JournalViewer: a desktop application for viewing and interrogating ISIS instrument journal files*, Tech. Rep. (ISIS, STFC Rutherford Appleton Lab, 2016).

[124] P. F. Peterson, S. I. Campbell, M. A. Reuter, R. J. Taylor, and J. Zikovsky, Nuclear Instruments and Methods in Physics Research Sec-

tion A: Accelerators, Spectrometers, Detectors and Associated Equipment **803**, 24 (2015).

[125] D. A. Keen, M. J. Gutmann, and C. C. Wilson, J. Appl. Crystallogr. **39**, 714 (2006).

[126] S. Rosenkranz and R. Osborn, Pramana **71**, 705 (2008).

[127] F. Ye, Y. Liu, R. Whitfield, R. Osborn, and S. Rosenkranz, J. Appl. Crystallogr. **51**, 315 (2018).

[128] R. Welberry and R. Whitfield, Quantum Beam Science **2**, 2 (2018).

[129] W. R. Busing and H. A. Levy, Acta Crystallogr. **22**, 457 (1967).

[130] M. D. Lumsden, J. L. Robertson, and M. Yethiraj, J. Appl. Crystallogr. **38**, 405 (2005).

[131] O. Kirichek, R. Down, P. Manuel, J. Keeping, and Z. Bowden, in *Journal of Physics: Conference Series*, Vol. 568 (IOP Publishing, 2014) p. 032011.

[132] R. Downa, O. Kirichek, P. Manuel, J. Keeping, and Z. Bowden, Physics Procedia **67**, 338 (2015).

[133] A. J. Schultz, M. R. V. Jørgensen, X. Wang, R. L. Mikkelson, D. J. Mikkelson, V. E. Lynch, P. F. Peterson, M. L. Green, and C. M. Hoffmann, Journal of Applied Crystallography **47**, 915 (2014).

[134] B. Sullivan, R. Archibald, P. S. Langan, H. Dobbek, M. Bommer, R. L. McFeeters, L. Coates, X. P. Wang, F. Gallmeier, J. M. Carpenter, *et al.*, Acta Crystallographica Section D: Structural Biology **74**, 1085 (2018).

[135] M. Iizumi, Japanese Journal of Applied Physics **12**, 167 (1973).

[136] B. Buras and L. Gerward, Acta Crystallogr. A **31**, 372 (1975).

[137] T. M. Michels-Clark, A. T. Savici, V. E. Lynch, X. Wang, M. Chodkiewicz, *et al.*, J. Appl. Crystallogr. **50**, 1559 (2017).

[138] E. H. Snell, H. D. Bellamy, and G. E. Borgstahl, Methods in enzymology **368**, 268 (2003).

[139] A. M. Glazer, *A Journey into Reciprocal Space*, 2053-2571 (Morgan & Claypool Publishers, 2017).

[140] J. Peters and W. Jauch, Science Progress **85**, 297 (2002).

[141] N. Niimura, S. Tomiyoshi, J. Takahashi, and J. Harada, J. Appl. Crystallogr. **8**, 560 (1975).

[142] C. Darwin, The London, Edinburgh, and Dublin Philosophical Magazine and Journal of Science **43**, 800 (1922).

[143] V. Petříček, M. Dušek, and L. Palatinus, Z. Kristallogr. Cryst. Mater **229**, 345 (2014).

[144] W. H. Zachariasen, Acta Crystallogr. **23**, 558 (1967).

[145] P. J. Becker and P. Coppens, Acta Crystallogr. A **30**, 129 (1974).

[146] L. Palatinus and G. Chapuis, J. Appl. Crystallogr. **40**, 786 (2007).

[147] G. Oszlányi and A. Sütő, Acta Crystallogr. A **64**, 123 (2008).

[148] P. W. Stephens, J. Appl. Crystallogr. **32**, 281 (1999).

[149] S. Geller, Z. Kristallogr. Cryst. Mater **125**, 1 (1967).

[150] K. Momma and F. Izumi, J. Appl. Crystallogr. **41**, 653 (2008).

[151] M. I. Aroyo, D. Orobengoa, G. de la Flor, E. S. Tasci, J. M. Perez-Mato, and H. Wondratschek, Acta Crystallographica Section A **70**, 126 (2014).

[152] C. Liu, Z. Xia, M. S. Molokeev, and Q. Liu, J. Am. Ceram. Soc **98**, 1870 (2015).

[153] M. Griffel and J. Stout, J. Am. Chem. Soc **72**, 4351 (1950).

[154] D. B. Litvin, Acta Crystallographica Section A **64**, 419 (2008).

[155] O. Nikotin, P. Lindgård, and O. Dietrich, J. Phys. Condens. Matter **2**, 1168 (1969).

[156] F. Keffer, Phys. Rev. **87**, 608 (1952).

[157] W. De Haas, B. Schultz, and J. Koolhaas, Physica **7**, 57 (1940).

[158] J. Stout and H. Adams, J. Am. Chem. Soc **64**, 1535 (1942).

[159] W. Jauch, A. Palmer, and A. J. Schultz, Acta Crystallogr. B **49**, 984–987 (1993).

[160] T. Chatterji, G. N. Iles, B. Ouladdiaf, and T. C. Hansen, J. Phys. Condens. Matter **22**, 316001 (2010).

[161] S. Diaz, S. de Brion, G. Chouteau, P. Strobel, B. Canals, *et al.*, J. Appl. Phys **97**, 10A512 (2005).

[162] E. Bertaut, G. Roult, A. Delapalme, G. Bassi, M. Mercier, *et al.*, Journal of Applied Physics **35**, 952 (1964).

[163] S. Diaz, S. de Brion, G. Chouteau, B. Canals, V. Simonet, *et al.*, Phys. Rev. B **74**, 092404 (2006).

[164] M. Matsuda, J. Chung, S. Park, T. Sato, K. Matsuno, *et al.*, EPL (Europhysics Letters) **82**, 37006 (2008).

[165] T. Mizoguchi, L. D. C. Jaubert, R. Moessner, and M. Udagawa, Phys. Rev. B **98**, 144446 (2018).

[166] E. V. Sampathkumaran and A. Niazi, Phys. Rev. B **65**, 180401 (2002).

[167] L. Edwards, H. Lane, F. Wallington, A. M. Arevalo-Lopez, M. Songvilay, *et al.*, Phys. Rev. B **102**, 195136 (2020).

[168] H. L. Stormer, D. C. Tsui, and A. C. Gossard, Rev. Mod. Phys. **71**, S298 (1999).

[169] R. B. Laughlin, Phys. Rev. B **23**, 5632 (1981).

[170] A. Vasiliev, O. Volkova, E. Zvereva, and M. Markina, NPJ Quantum Materials **3**, 18 (2018).

[171] E. Gibney and D. Castelvecchi, Nature **538**, 10.1038/nature.2016.20722 (2016).

[172] D. A. Tennant, T. G. Perring, R. A. Cowley, and S. E. Nagler, Phys. Rev. Lett. **70**, 4003 (1993).

[173] J. Villain, Physica B **79**, 1 (1975).

[174] I. Affleck, T. Kennedy, E. H. Lieb, and H. Tasaki, Phys. Rev. Lett. **59**, 799 (1987).

[175] M. Oshikawa, Phys. Rev. Lett. **84**, 1535 (2000).

[176] M. Oshikawa, M. Yamanaka, and I. Affleck, Phys. Rev. Lett. **78**, 1984 (1997).

[177] I. S. Jacobs, J. W. Bray, H. R. Hart, L. V. Interrante, J. S. Kasper, *et al.*, Phys. Rev. B **14**, 3036 (1976).

[178] M. Hase, I. Terasaki, and K. Uchinokura, Phys. Rev. Lett. **70**, 3651 (1993).

[179] T. Takagi and M. Mekata, J. Phys. Soc. Jpn. **64**, 4609 (1995).

[180] H. Kikuchi, Y. Fujii, M. Chiba, S. Mitsudo, T. Idehara, *et al.*, Phys. Rev. Lett. **94**, 227201 (2005).

[181] H. Kageyama, K. Yoshimura, K. Kosuge, M. Azuma, M. Takano, *et al.*, J. Phys. Soc. Jpn. **66**, 3996 (1997).

[182] H. Kageyama, K. Yoshimura, K. Kosuge, H. Mitamura, and T. Goto, J. Phys. Soc. Jpn. **66**, 1607 (1997).

[183] V. Hardy, M. R. Lees, A. Maignan, S. Hebert, D. Flahaut, *et al.*, J. Phys. Condens. Matter **15**, 5737 (2003).

[184] Y. B. Kudasov, Phys. Rev. Lett. **96**, 027212 (2006).

[185] E. V. Sampathkumaran and A. Niazi, Phys. Rev. B **65**, 180401(R) (2002).

[186] S. Niitaka, K. Yoshimura, K. Kosuge, M. Nishi, and K. Kakurai, Phys. Rev. Lett. **87**, 177202 (2001).

[187] V. Hardy, C. Martin, G. Martinet, and G. André, Phys. Rev. B **74**, 064413 (2006).

[188] A. Maignan, V. Hardy, S. Hebert, M. Drillon, M. R. Lees, *et al.*, J. Mater. Chem. **14**, 1231 (2004).

[189] K. Okamoto, T. Tonegawa, and M. Kaburagi, J. Phys. Condens. Matter **15**, 5979 (2003).

[190] K. C. Rule, A. U. B. Wolter, S. Süllow, D. A. Tennant, A. Brühl, *et al.*, Phys. Rev. Lett. **100**, 117202 (2008).

[191] S. Mitsuda, M. Mase, K. Prokes, H. Kitazawa, and H. Aruga Katori, Journal of the Physical Society of Japan **69**, 3513–3516 (2000).

[192] N. Terada, S. Mitsuda, K. Prokes, O. Suzuki, H. Kitazawa, and H. Aruga Katori, Physical Review B **70**, 174412 (2004).

[193] R. S. Fishman and S. Okamoto, Phys. Rev. B **81**, 020402(R) (2010).

[194] R. S. Fishman, Phys. Rev. Lett. **106**, 037206 (2011).

[195] B. Jasper-Tonnies and H. Muller-Buschbaum, Z. Anorg. Allg. Chem. **508**, 7 (1984).

[196] K. Mocała and J. Ziółkowski, Journal of Solid State Chemistry **69**, 299–311 (1987).

[197] M. Belaïche, M. Bakhache, M. Drillon, A. Derrory, and S. Vilminot, Physica B: Condensed Matter **305**, 270–273 (2001).

[198] H. Müller-Buschbaum and M. Kobel, Journal of Alloys and Compounds **176**, 39–46 (1991).

[199] M. Lenertz, A. Dinia, S. Colis, O. Mentré, G. André, *et al.*, The Journal of Physical Chemistry C **118**, 13981–13987 (2014).

[200] J. Szymanski and J. Scott, Canadian Mineralogist **20**, 271–279 (1982).

[201] P. Fazekas and P. W. Anderson, Philos. Mag. **30**, 423 (1974).

[202] C. Stock, L. C. Chapon, O. Adamopoulos, A. Lappas, M. Giot, *et al.*, Phys. Rev. Lett. **103**, 077202 (2009).

[203] M. Giot, L. C. Chapon, J. Androulakis, M. A. Green, P. G. Radaelli, *et al.*, Phys. Rev. Lett. **99**, 247211 (2007).

[204] R. L. Dally, R. Chisnell, L. Harriger, Y. Liu, J. W. Lynn, *et al.*, Phys. Rev. B **98**, 144444 (2018).

[205] R. L. Dally, Y. Zhao, Z. Xu, R. Chisnell, M. B. Stone, *et al.*, Nat. Commun. **9**, 2188 (2018).

[206] D. Khomskii, *Transition metal compounds* (Cambridge University Press, 2014).

[207] F. Wallington, A. M. Arevalo-Lopez, J. W. Taylor, J. R. Stewart, V. Garcia-Sakai, *et al.*, Phys. Rev. B **92**, 125116 (2015).

[208] M. Nandi, K. Nazir, B. Dilip, A. Midya, and M. Prabhat, J. Phys. Chem. C **118**, 1668 (2014).

[209] M. Markkula, A. M. Arevalo-Lopez, and J. P. Attfield, Journal of Solid State Chemistry **192**, 390 (2012).

[210] N. Hollmann, S. Agrestini, Z. Hu, Z. He, M. Schmidt, *et al.*, Phys. Rev. B **89**, 201101(R) (2014).

[211] M. Markkula, A. M. Arévalo-López, and J. P. Attfield, Phys. Rev. B **86**, 134401 (2012).

[212] M. Lenertz, J. Alaria, D. Stoeffler, S. Colis, A. Dinia, *et al.*, Phys. Rev. B **86**, 214428 (2012).

[213] P. M. Sarte, R. A. Cowley, E. E. Rodriguez, E. Pachoud, D. Le, *et al.*, Phys. Rev. B **98**, 024415 (2018).

[214] R. A. Cowley, W. J. L. Buyers, C. Stock, Z. Yamani, C. Frost, *et al.*, Phys. Rev. B **88**, 205117 (2013).

[215] P. M. Sarte, M. Songvilay, E. Pachoud, R. A. Ewings, C. D. Frost, *et al.*, Phys. Rev. B **100**, 075143 (2019).

[216] J. Ollivier, H. Mutka, and L. Didier, Neutron News **21**, 22 (2010), https://doi.org/10.1080/10448631003757573 .

[217] B. Kim, B. H. Kim, K. Kim, H. C. Choi, S.-Y. Park, *et al.*, Phys. Rev. B **85**, 220407(R) (2012).

[218] S. Kanetsuki, S. Mitsuda, T. Nakajima, D. Anazawa, H. A. Katori, and K. Prokes, Journal of Physics: Condensed Matter **19**, 145244 (2007).

[219] M. E. Fisher and W. Selke, Phys. Rev. Lett. **44**, 1502 (1980).

[220] I. Affleck, Journal of Physics: Condensed Matter **1**, 3047 (1989).

[221] H. Tasaki, *Physics and Mathematics of Quantum Many-Body Systems*, Graduate Texts in Physics (Springer International Publishing, Cham, 2020).

[222] W. Marshall, Proceedings of the Royal Society of London. Series A. Mathematical and Physical Sciences **232**, 48 (1955).

[223] E. Lieb and D. Mattis, Journal of Mathematical Physics **3**, 749 (1962).

[224] H. Bethe, Zeitschrift für Physik **71**, 205 (1931).

[225] B. S. Shastry, Journal of Physics A: Mathematical and General **25**, L249 (1992).

[226] K. Tanaka, K. Takeda, and T. Idogaki, Journal of magnetism and magnetic materials **272**, 908 (2004).

[227] S. Bachmann, S. Michalakis, B. Nachtergaele, and R. Sims, Communications in Mathematical Physics **309**, 835 (2012).

[228] S. Bravyi and B. Terhal, New Journal of Physics **11**, 043029 (2009).

[229] T. Hirano, H. Katsura, and Y. Hatsugai, Physical review B **78**, 054431 (2008).

[230] R. Fernández, J. Fröhlich, and A. D. Sokal, *Random walks, critical phenomena, and triviality in quantum field theory* (Springer Science & Business Media, 2013).

[231] S. Friedli and Y. Velenik, *Statistical mechanics of lattice systems: a concrete mathematical introduction* (Cambridge University Press, 2017).

[232] I. Affleck, Nuclear Physics B **257**, 397 (1985).

[233] Y. H. Matsuda, N. Abe, S. Takeyama, H. Kageyama, P. Corboz, *et al.*, Phys. Rev. Lett. **111**, 137204 (2013).

[234] K. Totsuka, Phys. Rev. B **57**, 3454 (1998).

[235] C. L. Henley, Phys. Rev. Lett. **62**, 2056 (1989).

[236] A. I. Smirnov, T. A. Soldatov, O. A. Petrenko, A. Takata, T. Kida, M. Hagiwara, A. Y. Shapiro, and M. E. Zhitomirsky, Phys. Rev. Lett. **119**, 047204 (2017).

[237] S. Agrestini, C. L. Fleck, L. C. Chapon, C. Mazzoli, A. Bombardi, *et al.*, Phys. Rev. Lett. **106**, 197204 (2011).

[238] K. Singh, C. Simon, E. Cannuccia, M.-B. Lepetit, B. Corraze, *et al.*, Phys. Rev. Lett. **113**, 137602 (2014).

[239] W. H. Ji, L. Yin, W. M. Zhu, C. M. N. Kumar, C. Li, *et al.*, Physical Review B **100**, 134420 (2019).

[240] C. Paulsen, *Introduction to Physical Techniques in Molecular Magnetism: Structural and Macroscopic Techniques-Yesa 1999* (Servicio de Publicaciones de la Universidad de Zaragoza, 2001).

[241] S. T. Bramwell and P. C. W. Holdsworth, Journal of Applied Physics **73**, 6096 (1993).

[242] I. A. Zaliznyak and S. H. Lee, *Modern Techniques for Characterizing Magnetic Materials* (John Wiley & Sons, UK, 2007).

[243] A. Guinier, *X-ray diffraction in crystals, imperfect crystals, and amorphous bodies* (W. H. Freeman, San Francisco, 1963).

[244] C. Stock, E. E. Rodriguez, N. Lee, F. Demmel, P. Fouquet, *et al.*, Phys. Rev. Lett. **119**, 257204 (2017).

[245] M. Oshikawa, Phys. Rev. Lett. **90**, 236401 (2003).

[246] J. Stephenson, J. Math Phys. **5**, 1009 (1964).

[247] H. Cho, J. B. Young, W. Kang, K. L. Campman, A. C. Gossard, *et al.*, Phys. Rev. Lett. **81**, 2522 (1998).

[248] S. Ihnatsenka and I. V. Zozoulenko, Phys. Rev. B **75**, 035318 (2007).

[249] A. P. Ramirez, A. Hayashi, R. J. Cava, R. Siddharthan, and B. Shastry, Nature **399**, 333 (1999).

[250] M. Udagawa and L. Jaubert, *Spin Ice*, Vol. 197 (Springer Nature, 2021).

[251] L. D. Jaubert and P. C. Holdsworth, Journal of Physics: Condensed Matter **23**, 164222 (2011).

[252] B. Tomasello, *A quantum mechanical study of the dynamical properties of spin-ice materials*, Ph.D. thesis, University of Kent, STFC (2014).

[253] S. Gao, *Neutron scattering investigation of the spin correlations in frustrated spinels*, Ph.D. thesis, Université de Genève, PSI (2017).

[254] U. Walter, Journal of Physics and Chemistry of Solids **45**, 401 (1984).

[255] B. C. den Hertog and M. J. P. Gingras, Phys. Rev. Lett. **84**, 3430 (2000).

[256] M. J. Gingras and B. C. den Hertog, Canadian journal of physics **79**, 1339 (2001).

[257] C. Castelnovo, R. Moessner, and S. L. Sondhi, Nature **451**, 42 (2008).

[258] C. L. Henley, Phys. Rev. B **71**, 014424 (2005).

[259] M. Twengström, P. Henelius, and S. T. Bramwell, Phys. Rev. Research **2**, 013305 (2020).

[260] T. Fennell, O. A. Petrenko, B. Fåk, S. T. Bramwell, M. Enjalran, T. Yavors'kii, M. J. P. Gingras, R. G. Melko, and G. Balakrishnan, Phys. Rev. B **70**, 134408 (2004).

[261] D. Pomaranski, L. Yaraskavitch, S. Meng, K. Ross, H. Noad, H. Dabkowska, B. Gaulin, and J. Kycia, Nature Physics **9**, 353 (2013).

[262] G. Sala, M. Gutmann, D. Prabhakaran, D. Pomaranski, C. Mitchelitis, J. Kycia, D. Porter, C. Castelnovo, and J. Goff, Nature Materials **13**, 488 (2014).

[263] J. Snyder, B. G. Ueland, J. S. Slusky, H. Karunadasa, R. J. Cava, and P. Schiffer, Phys. Rev. B **69**, 064414 (2004).

[264] C. Paulsen, S. Giblin, E. Lhotel, D. Prabhakaran, G. Balakrishnan, *et al.*, Nature Physics **12**, 661 (2016).

[265] F. Pobell, *Matter and methods at low temperatures*, Vol. 2 (Springer, 2007).

[266] J. Ekin, *Experimental techniques for low-temperature measurements: cryostat design, material properties and superconductor critical-current testing* (Oxford university press, 2006).